NOTE TO USERS

This reproduction is the best copy available.

UMI®

**University of Alberta**

# INTEGRATION OF GEOLOGIC INFORMATION INTO GEOSTATISTICAL MODELS

by

**Michael James Pyrcz** ©

A thesis submitted to the Faculty of Graduate Studies and Research in partial fulfillment of the requirements for the degree of **Doctor of Philosophy**.

in

Mining Engineering

Department of Civil and Environmental Engineering

Edmonton, Alberta
Fall 2004

Library and
Archives Canada

Published Heritage
Branch

395 Wellington Street
Ottawa ON K1A 0N4
Canada

Bibliothèque et
Archives Canada

Direction du
Patrimoine de l'édition

395, rue Wellington
Ottawa ON K1A 0N4
Canada

*Your file Votre référence*
*ISBN: 0-612-96005-6*
*Our file Notre référence*
*ISBN: 0-612-96005-6*

The author has granted a non-exclusive license allowing the Library and Archives Canada to reproduce, loan, distribute or sell copies of this thesis in microform, paper or electronic formats.

L'auteur a accordé une licence non exclusive permettant à la Bibliothèque et Archives Canada de reproduire, prêter, distribuer ou vendre des copies de cette thèse sous la forme de microfiche/film, de reproduction sur papier ou sur format électronique.

The author retains ownership of the copyright in this thesis. Neither the thesis nor substantial extracts from it may be printed or otherwise reproduced without the author's permission.

L'auteur conserve la propriété du droit d'auteur qui protège cette thèse. Ni la thèse ni des extraits substantiels de celle-ci ne doivent être imprimés ou aturement reproduits sans son autorisation.

In compliance with the Canadian Privacy Act some supporting forms may have been removed from this thesis.

Conformément à la loi canadienne sur la protection de la vie privée, quelques formulaires secondaires ont été enlevés de cette thèse.

While these forms may be included in the document page count, their removal does not represent any loss of content from the thesis.

Bien que ces formulaires aient inclus dans la pagination, il n'y aura aucun contenu manquant.

Canada

"Every day you may make progress.
Every step may be fruitful.
Yet there will stretch out before you an ever-lengthening, ever-ascending,
ever-improving path.
You know you will never get to the end of the journey.
But this, so far from discouraging, only adds to the joy and glory of the climb."
- Sir Winston Churchill

**We did it Tobes!**

# Acknowledgements

I thank Professor Clayton V. Deutsch for his energetic support. Dr. Deutsch was pivotal in my decision to enter graduate studies. Dr. Deutsch is an inexhaustible source of new ideas and a great mentor. Due to his efforts my Ph.D. has been a great learning experience.

The Government of Canada, the Provincial Government of Alberta and the University of Alberta provided essential monetary support through NSERC PGS A and B, iCORE A and B and Walter Johns awards during the entire duration of my Ph.D. The industry supporters of the Centre for Computational Geostatistics provided valuable feed back and support.

I would also like to acknowledge Professor Octavian Catuneanu who enthusiastically supported and encouraged my interests in sedimentology and sequence stratigraphy. I also appreciate the support of my colleges at the Centre for Computational Geostatistics, including Dr. Julian Ortiz who was always willing to discuss. ChevronTexaco and specifically Dr. Sebastien Strebelle provided an excellent opportunity for an internship.

My family has been a continual source of strength. Through my family, I retain an eternal perspective concerning these life challenges. My parents Edward and Sylvia Pyrcz taught me from an early age a love of the natural sciences and the joy of creativity. My two sons, Aidan and Clayton, have provided much needed comic relief during graduate studies. My wife, Tobi, has been indomitable. Tobi, there are no words to express my gratitude. In time you will see.

Finally, I thank everyone who fed me along the way.

# Table of Contents

**1 Problem Setting** **1**

1.1 The Approach . . . 5

1.2 Dissertation Outline . . . 6

**2 Reservoir Model Building** **9**

2.1 Basic Principles . . . 9

2.1.1 Quantitative Modeling Principles . . . 10

2.1.2 Clastic Sedimentological Principles . . . 11

2.1.3 Sequence Stratigraphic Principles . . . 11

2.1.4 Geologic Information Sources . . . 12

2.1.5 Physical Sedimentary Process and Depositional Systems . . . 14

2.1.6 Facies Models, Lithofacies and Architectural Elements . . . 16

2.1.7 Sequence Stratigraphy, Systems Tracts and Bounding Surfaces 17

2.1.8 Quantitative Dynamic Stratigraphy Models . . . 19

2.2 Geostatistical Techniques . . . 21

2.2.1 Random Variables and Random Functions . . . 23

2.2.2 Stationarity and Inference . . . 25

2.2.3 Data Conditioning . . . 27

2.2.4 Multiple Equally Likely to be Drawn Realizations . . . 27

2.2.5 Semivariogram Based Geostatistical Algorithms . . . 28

2.2.6 Training Image Based Multiple-point Geostatistics . . . 37

2.2.7 Surface Based Models . . . 39

2.2.8 Object Based Models . . . 40

2.2.9 Simulated Annealing . . . 43

2.2.10 Volume Variance Relations . . . 45

2.2.11 Nonstationary Statistics . . . 47

2.3 Advanced Geostatistical Models . . . . . . . . . . . . . . . . . . . . . 47

**3 Fluvial Reservoir Models** **49**
3.1 Fluvial Reservoirs . . . . . . . . . . . . . . . . . . . . . . . . . . . 49
3.1.1 Lithofacies and Architectural Elements . . . . . . . . . . . . . 50
3.1.2 Styles . . . . . . . . . . . . . . . . . . . . . . . . . . . . . . . 52
3.1.3 Sequence Stratigraphy . . . . . . . . . . . . . . . . . . . . . . 53
3.1.4 Reservoir Types . . . . . . . . . . . . . . . . . . . . . . . . . . 54
3.2 Streamline Based Stochastic Fluvial Model . . . . . . . . . . . . . . 55
3.2.1 The 3-D Streamline . . . . . . . . . . . . . . . . . . . . . . . . 56
3.2.2 Streamline Associations within Streamline Based Models . . 59
3.2.3 Streamline Operations . . . . . . . . . . . . . . . . . . . . . . 59
3.2.4 Fluvial Architectural Elements . . . . . . . . . . . . . . . . . . 69
3.3 Streamline Based Unconditional Algorithm . . . . . . . . . . . . . . 77
3.3.1 Event Schedule . . . . . . . . . . . . . . . . . . . . . . . . . . 77
3.3.2 `ALLUVSIM` Parameters . . . . . . . . . . . . . . . . . . . . . 83
3.3.3 Example `ALLUVSIM` Models of Reservoir Types . . . . . . . . 84
3.4 Conditional Streamline Based Simulation . . . . . . . . . . . . . . . 90
3.4.1 The Prior Streamline Based Simulation . . . . . . . . . . . . 92
3.4.2 Interpreted Well Data . . . . . . . . . . . . . . . . . . . . . . 93
3.4.3 Updating Streamline Associations to Honor Well Data . . . . 93
3.4.4 Iterative Procedure for Updating Streamline Associations . . 97
3.4.5 Correction for Unwarranted Well Intercepts . . . . . . . . . . 98
3.4.6 Example Conditional Streamline Based Models . . . . . . . . 98
3.5 Stochastic Inclined Heterolithic Strata . . . . . . . . . . . . . . . . . 9~~8~~9
3.5.1 Stochastic Inclined Heterolithic Strata Geologic Settings . . . 101
3.5.2 Stochastic Inclined Heterolithic Strata Geologic Models . . . 102
3.5.3 Example Stochastic Inclined Heterolithic Strata Model . . . . 103
3.6 Discussion . . . . . . . . . . . . . . . . . . . . . . . . . . . . . . . . 106

**4 Turbidite Reservoir Models** **109**
4.1 Deepwater Reservoirs . . . . . . . . . . . . . . . . . . . . . . . . . . 110
4.1.1 Small Scale Geometries . . . . . . . . . . . . . . . . . . . . . 111
4.1.2 Large Scale Geometries . . . . . . . . . . . . . . . . . . . . . 112
4.2 Hierarchical Trend Models . . . . . . . . . . . . . . . . . . . . . . . . 112

4.2.1 Construction of Hierarchical Trend Models . . . . . . . . . . 113
4.2.2 Correction for Global Areal and Vertical Trends . . . . . . . 127
4.3 Surface Based Models . . . . . . . . . . . . . . . . . . . . . . . . . . 132
4.3.1 Surface Templates and Candidate Surfaces . . . . . . . . . . 135
4.3.2 Placement of Candidate Surfaces . . . . . . . . . . . . . . . . . 136
4.3.3 Surface Acceptance Criteria . . . . . . . . . . . . . . . . . . . . 137
4.3.4 Conditioning by Stochastic Residual . . . . . . . . . . . . . . 138
4.3.5 Termination of Surface Based Simulation . . . . . . . . . . . 138
4.4 Surface Based Strataform Model . . . . . . . . . . . . . . . . . . . 139
4.4.1 Methodology . . . . . . . . . . . . . . . . . . . . . . . . . . . . . . 139
4.4.2 Demonstration . . . . . . . . . . . . . . . . . . . . . . . . . . . . 140
4.5 Surface Based Turbidite Model . . . . . . . . . . . . . . . . . . . . 143
4.5.1 Methodology . . . . . . . . . . . . . . . . . . . . . . . . . . . . . . 143
4.5.2 Demonstration . . . . . . . . . . . . . . . . . . . . . . . . . . . . 147
4.6 Turbidite Case Study . . . . . . . . . . . . . . . . . . . . . . . . . . 156
4.6.1 The Data . . . . . . . . . . . . . . . . . . . . . . . . . . . . . . . . 158
4.6.2 Geostatistical Work Flow . . . . . . . . . . . . . . . . . . . . . 161
4.6.3 Comments on the Surface Based Turbidite Model . . . . . . . 171
4.7 Discussion . . . . . . . . . . . . . . . . . . . . . . . . . . . . . . . . . 173

**5 Training Images** **175**
5.1 Multiple Point Techniques . . . . . . . . . . . . . . . . . . . . . . . 176
5.2 Training Image Library . . . . . . . . . . . . . . . . . . . . . . . . . 176
5.2.1 The Static Training Images . . . . . . . . . . . . . . . . . . . . 177
5.2.2 Correction of Global Category Proportions . . . . . . . . . . 190
5.2.3 Selection of the Appropriate Training Image . . . . . . . . . . 191
5.3 Turbidite Style Training Image Generating Algorithms . . . . . . . . 192
5.3.1 Turbidite Style Training Image Architectural Elements . . . . 192
5.3.2 Turbidite Dynamic Training Images in C++ . . . . . . . . . 193
5.3.3 Channel and Levee Complex . . . . . . . . . . . . . . . . . . . 194
5.3.4 Channelized Sheet Complex . . . . . . . . . . . . . . . . . . . . 199
5.3.5 Comments on Training Image Generating Algorithms . . . . 202
5.4 Associated Code for Training Image Library . . . . . . . . . . . . . 203
5.4.1 Extraction of Multiple-point Statistics from the Training Images 203

5.4.2 Model Operations . . . . . . . . . . . . . . . . . . . . . . . . . 209
5.5 Anticipated Applications . . . . . . . . . . . . . . . . . . . . . . . . . . . 211
5.5.1 Inference of Input Statistics . . . . . . . . . . . . . . . . . . . . 213
5.5.2 Comparative Flow Studies . . . . . . . . . . . . . . . . . . . . . 215
5.5.3 Documented "Type Models" . . . . . . . . . . . . . . . . . . . 215
5.5.4 Library for Scenario Based Uncertainty Study . . . . . . . . . 216
5.6 Discussion . . . . . . . . . . . . . . . . . . . . . . . . . . . . . . . . . 217

**6 Gridding and Building Blocks** **218**
6.1 Gridding . . . . . . . . . . . . . . . . . . . . . . . . . . . . . . . . . . 218
6.1.1 Regular Cartesian Grids . . . . . . . . . . . . . . . . . . . . . . 222
6.1.2 Irregular Grids . . . . . . . . . . . . . . . . . . . . . . . . . . . . 223
6.2 Concepts Related to Direct Sequential Simulation . . . . . . . . . . . 226
6.2.1 Local CCDF in Direct Space . . . . . . . . . . . . . . . . . . . 227
6.2.2 Accounting for Support Size in Direct Space . . . . . . . . . . 230
6.2.3 Accounting for Heteroscedasticity in Direct Space . . . . . . 234
6.3 Implementation with the Building Blocks Subroutines . . . . . . . . 234
6.3.1 Local CCDF Look Up Table . . . . . . . . . . . . . . . . . . . 235
6.3.2 Mean Covariance Calculation . . . . . . . . . . . . . . . . . . . 239
6.3.3 Nonstationary Covariance Table . . . . . . . . . . . . . . . . . 241
6.3.4 Search Considerations . . . . . . . . . . . . . . . . . . . . . . . 243
6.4 Applications of Simulation in Direct Space . . . . . . . . . . . . . . . 251
6.4.1 Direct Sequential Tartan Grid Simulation (TARTANSIM) with Radial Nested Grids . . . . . . . . . . . . . . . . . . . . . . . . 251
6.4.2 Atomic Grid Example . . . . . . . . . . . . . . . . . . . . . . . 264
6.5 Discussion . . . . . . . . . . . . . . . . . . . . . . . . . . . . . . . . . 266

**7 Concluding Remarks** **268**
7.1 Summary . . . . . . . . . . . . . . . . . . . . . . . . . . . . . . . . . . 268
7.1.1 Surface Based Simulation . . . . . . . . . . . . . . . . . . . . . 269
7.1.2 Streamline Based Simulation . . . . . . . . . . . . . . . . . . . 269
7.1.3 Hierarchical Trend Models . . . . . . . . . . . . . . . . . . . . . 269
7.1.4 Building Blocks for Direct Simulation to Irregular Grids . . . 269
7.1.5 Training Images . . . . . . . . . . . . . . . . . . . . . . . . . . . 270
7.1.6 Implementation . . . . . . . . . . . . . . . . . . . . . . . . . . . 270

7.2 Future Work . . . . . . . . . . . . . . . . . . . . . . . . . . . . . . 270
    7.2.1 Additional Depositional Settings . . . . . . . . . . . . . . . . 271
    7.2.2 Diagenesis . . . . . . . . . . . . . . . . . . . . . . . . . . . . . . 271
    7.2.3 Trend Models . . . . . . . . . . . . . . . . . . . . . . . . . . . . 271
    7.2.4 Improved Conditioning . . . . . . . . . . . . . . . . . . . . . . 272
    7.2.5 Surface Based Models . . . . . . . . . . . . . . . . . . . . . . . 273
    7.2.6 Implementation of Irregular Grids . . . . . . . . . . . . . . . 273
    7.2.7 Application with Flow Simulation . . . . . . . . . . . . . . . 274

**Bibliography** **275**

**A Algorithms and Abbreviations** **290**

# List of Tables

2.1 A summary of the available data and information for the construction of reservoir and resource models. . . . . . . . . . . . . . . . . . . . . . 15

3.1 Architectural elements proposed for fluvial depositional settings summarized from Miall (1996)[73]. . . . . . . . . . . . . . . . . . . . . . 51
3.2 A description of the `ALLUVSIM` parameter file. . . . . . . . . . . . . . 85
3.3 Morphological characteristics of McMurray formation paleochannels from Mossop and Flach (1983)[76]. . . . . . . . . . . . . . . . . . . . 106

4.1 The hierarchy of architectural elements in turbidites (adapted from Ghosh and Lowe, 1993)[41]). . . . . . . . . . . . . . . . . . . . . . . . . 110
4.2 A description of the `HIERTREND` parameter file. . . . . . . . . . . . 126
4.3 A description of the `SURFTREND` parameter file. . . . . . . . . . . . 128
4.4 A description of the `TRENDCOR` parameter file. . . . . . . . . . . . 133
4.5 A description of the `SURFSIM` parameter file. . . . . . . . . . . . . 141
4.6 A description of the `TURBSIM` parameter file. . . . . . . . . . . . . 148
4.7 A summary of the lithofacies identified by Cazzolo et al. (1985)[13]. 162
4.8 Lobe parameter distributions applied in the example case study. All units are in meters. . . . . . . . . . . . . . . . . . . . . . . . . . . 164

5.1 The distributions of stochastic geometry transforms applied to the primary grains. . . . . . . . . . . . . . . . . . . . . . . . . . . . . . 179
5.2 The parameters for the marked point process scenarios. . . . . . . . 179
5.3 The scenarios for the channel only ribbon sandbody training images. 185
5.4 The scenarios for the channel with levee ribbon sandbody training images. . . . . . . . . . . . . . . . . . . . . . . . . . . . . . . . . 185

5.5 The scenarios for the channel with levee and crevasse splay ribbon sandbody training images. . . . . . . . . . . . . . . . . . . . . . . . . 186
5.6 The scenarios for the surface based turbidite lobe training images. . . 188
5.7 The scenarios for the streamline based training images. . . . . . . . . 190
5.8 A summary of the `MPSTATS` parameter file. . . . . . . . . . . . . . . . 210
5.9 A summary of the `MODELOPS` parameters file. . . . . . . . . . . . . . 212

6.1 The parameters required to define a regular Cartesian grid. . . . . . 223
6.2 The parameters required to define a tartan grid. . . . . . . . . . . . 224

# List of Figures

1.1 Ideal core representation of a simple 2-D stratigraphic dataset. . . . 2

1.2 A possible deterministic model based on the core data and a fluvial depositional setting. . . . . . . . . . . . . . . . . . . . . . . . . . . 2

1.3 Two geostatistical realizations conditioned by the facies core data. . 4

2.1 The system tracts and major bounding surfaces relative to an idealized base level curve and rate of base level change curve. . . . . . . . 18

2.2 A schematic of a semivariogram model. . . . . . . . . . . . . . . . . 26

2.3 An example estimation problem. . . . . . . . . . . . . . . . . . . . . 29

2.4 An schematic of a prograding coastal setting where facies ordering is an important feature. . . . . . . . . . . . . . . . . . . . . . . . . 34

2.5 An example six point template for the calculation of multiple point statistics. . . . . . . . . . . . . . . . . . . . . . . . . . . . . . . . 38

2.6 An example surface based simulation. . . . . . . . . . . . . . . . . . 40

2.7 An example Possion point process with lobe primary grains. . . . . . 41

2.8 An example `FLUVSIM` object based fluvial model with channels, levees and crevasse splays . . . . . . . . . . . . . . . . . . . . . . . . . 42

3.1 A schematic of mean flow velocity vs. median sediments size and the stability fields for difference sand beds (adapted from Miall, 1996)[73] 53

3.2 A demonstration of the construction of a 2-D spline by combining two splines. . . . . . . . . . . . . . . . . . . . . . . . . . . . . . . 57

3.3 An illustration of the streamline initialization operator. . . . . . . . 60

3.4 Example channel streamlines calculated with the disturbed periodic model. . . . . . . . . . . . . . . . . . . . . . . . . . . . . . . . . 62

3.5 The migration of a channel streamline over 100 times steps (white to black). . . . . . . . . . . . . . . . . . . . . . . . . . . . . . . . 66

3.6 The migration of a channel streamline over twelve time steps and the evolving architectural element model. . . . . . . . . . . . . . . . . . . . 67
3.7 An illustration of the steps required in the streamline migration operator. . . . . . . . . . . . . . . . . . . . . . . . . . . . . . . . . 68
3.8 An illustration of the fluvial architectural elements applied in the streamline based model. . . . . . . . . . . . . . . . . . . . . . . . . 69
3.9 CH and LV element cross section and associated geometric parameters. 71
3.10 Crevasse splay architectural element geometric parameters. . . . . . 75
3.11 Example crevasse splay geometries calculated with the `ALLUVSIM` algorithm. . . . . . . . . . . . . . . . . . . . . . . . . . . . . . . . 76
3.12 Example areal trends in channel density and the resulting streamlines. 79
3.13 Example vertical trends in channel density and the resulting architectural element models. . . . . . . . . . . . . . . . . . . . . . . . 81
3.14 The effect of probability of avulsion and number of aggradation levels on `ALLUVSIM` models. . . . . . . . . . . . . . . . . . . . . . . . 82
3.15 An example `ALLUVSIM` PV type reservoir model. . . . . . . . . . . 86
3.16 An example `ALLUVSIM` CB type jigsaw reservoir model. . . . . . . . . 88
3.17 An example `ALLUVSIM` CB type labyrinth reservoir model. . . . . . . 89
3.18 An example `ALLUVSIM` distal SH type reservoir model. . . . . . . . 90
3.19 An example `ALLUVSIM` proximal SH type reservoir model. . . . . . . 91
3.20 A schematic of updating individual streamlines and entire streamline associations. . . . . . . . . . . . . . . . . . . . . . . . . . . . . 94
3.21 An illustration of methods for updating streamlines to well data. . . 96
3.22 An illustration of methods for correcting streamlines associations to remove unwarranted well intercepts. . . . . . . . . . . . . . . . . 99
3.23 An example conditional streamline based model from `ALLUVSIM`. . . 100
3.24 A schematic dip section of the morphology of IHS sets associated with meandering fluvial systems. . . . . . . . . . . . . . . . . . . . . . 101
3.25 A schematic of the sigmoidal channel profile calculation. . . . . . . . 104
3.26 Examples of the modified sigmoidal channel profile. . . . . . . . . . . 105
3.27 First realization of IHS sets generated with the `ALLUVSIM` algorithm and parameters based on the Mossop and Flach (1983)[76] study of the McMurray Formation. . . . . . . . . . . . . . . . . . . . . . . . 107

3.28 Second realization of IHS sets generated with the `ALLUVSIM` algorithm and parameters based on the Mossop and Flach (1983)[76] study of the McMurray Formation. . . . . . . . . . . . . . . . . . . . . . . . . 108

4.1 The internal and external geometry of turbidite lobes. . . . . . . . . 111
4.2 A drawing similar to the schematic illustration of compensational bedding from Mutti and Sonnino (Figure 2, 1981)[79]. . . . . . . . . 112
4.3 An schematic of a potential error in identification of architectural elements based on connected geo-objects. . . . . . . . . . . . . . . . 116
4.4 A schematic of the homotopic skeleton transform on two geo-objects. 117
4.5 A schematic of the application of a structural element for the dilation and erosion mathematical morphology operations. . . . . . . . . . . 117
4.6 A illustration of nonhomotopic and homotopic erosions. . . . . . . . 118
4.7 A schematic illustration of operations to construct a flow line. . . . . 119
4.8 A demonstration of the coordinate system describing vertical, longitudinal and transverse location within nested architectural elements. 120
4.9 Example porosity vertical trend functions for $2^{nd}$ and $3^{rd}$ hierarchical orders. . . . . . . . . . . . . . . . . . . . . . . . . . . . . . . 121
4.10 A potential suite of porosity trends that may be applied in the vertical, longitudinal and transverse directions for $2^{nd}$ and $3^{rd}$ order architectural elements. . . . . . . . . . . . . . . . . . . . . . . . . 122
4.11 A 1D example of the combination of $3^{rd}$ and $2^{nd}$ order vertical trend functionals. . . . . . . . . . . . . . . . . . . . . . . . . . . . . . 124
4.12 A schematic of a trend model cross section, areal and vertical, initial (dotted line) and target(solid line) trends and a multiplier window. . 130
4.13 A demonstration of the effect of window size on areal and vertical trend correction. . . . . . . . . . . . . . . . . . . . . . . . . . . . . 131
4.14 Schematics of two artifacts that may occur in surface based simulation. 134
4.15 A schematic of surface and object based simulation. . . . . . . . . . 135
4.16 Schematics of three example surface templates. . . . . . . . . . . . . 135
4.17 Three example candidate surfaces. . . . . . . . . . . . . . . . . . . . 136
4.18 Methods for vertical placement of surface geometries. . . . . . . . . . 137
4.19 An example realization of general surface based simulation. . . . . . 142

4.20 The lobe geometry applied in the `TURBSIM` algorithm as a surface template. . . . . . . . . . . . . . . . . . . . . . . . . . . . . . . 144
4.21 The construction of individual flow events within a lobe. . . . . . . . 145
4.22 An illustration of the addition of a stochastic residual to characterize fluctuations and to allow for conditioning to well data. . . . . . . . . . 146
4.23 A plan view of the $3^{rd}$ order lobe and the locations of the four vertical wells. . . . . . . . . . . . . . . . . . . . . . . . . . . . . . . 147
4.24 The lobe geometry, vertical well locations and sections for the demonstration of stochastic surface-based flow events within a lobe. . . . . 149
4.25 Two example realizations of flow events in a depositional lobe with hierarchical trend models. . . . . . . . . . . . . . . . . . . . . . . 150
4.26 A screen capture from Gocad of the first ten flow event surfaces. . . 151
4.27 A screen capture from Gocad of the first ten flow event surfaces with a cut away view to reveal internal structure. . . . . . . . . . . . . . . 151
4.28 A fence plot of the discretized architectural element model from Gocad.152
4.29 The initial areal trend model from the hierarchical trend model and the target areal trend based on conditioning. . . . . . . . . . . . . . 153
4.30 The initial vertical trend model from the hierarchical trend model and the target vertical trend based on conditioning. . . . . . . . . . 154
4.31 The areal and vertical trend of the corrected trend model. . . . . . . 155
4.32 The mismatch between the corrected and target areal and vertical trends . . . . . . . . . . . . . . . . . . . . . . . . . . . . . . . . 156
4.33 Long sections of the hierarchical trend model before and after correction to honor areal and vertical trend model. . . . . . . . . . . . . . 157
4.34 Fence diagrams of the initial and corrected surfaced-based models. . 158
4.35 A schematic of the initial bathymetry loosely based on a study of Cengio turbidite system Italy (Cazzolo et al., 1985)[13]. . . . . . . . 159
4.36 The distribution of synthetic porosity and permeability from well log. 160
4.37 The scatter plots of synthetic well permeability and porosity before and after Gaussian transform. . . . . . . . . . . . . . . . . . . . . . . 160
4.38 The locations of the North-South sections (A through D) and the long section (E). . . . . . . . . . . . . . . . . . . . . . . . . . . . . 161
4.39 Two surface realizations. . . . . . . . . . . . . . . . . . . . . . . . . 164
4.40 One surface realization (North-South sections *A* - *D*). . . . . . . . . 165

4.41 The porosity trends inferred from the lithofacies study of the Cengio Turbidite System, Italy (Cazzolo et al. 1985)[13]. . . . . . . . . . . . 166
4.42 Two porosity (percent) hierarchical trend models. . . . . . . . . . . . 167
4.43 A fence diagram of the first realization of the porosity hierarchical trend model. . . . . . . . . . . . . . . . . . . . . . . . . . . . . . . 167
4.44 Horizontal and vertical semivariograms of the Gaussian transform of the porosity residual. . . . . . . . . . . . . . . . . . . . . . . . . . 168
4.45 Two realizations of porosity (percent) constrained to the surface based hierarchical trend model and conditioned to well logs. . . . . . . . . 169
4.46 A fence diagram of the first porosity realization. . . . . . . . . . . . 169
4.47 Horizontal and vertical semivariograms of the Gaussian transform of the permeability well log data. . . . . . . . . . . . . . . . . . . . . 170
4.48 Two realizations of permeability correlated to the paired porosity realizations and conditioned to well logs. . . . . . . . . . . . . . . . . 170
4.49 A realization of permeability correlated to the paired porosity realization and conditioned to well logs. . . . . . . . . . . . . . . . . . 171
4.50 Porosity·thickness maps for two realizations of porosity (%m). . . . . 172

5.1 Summary of the training image library with schematic representations of the models. . . . . . . . . . . . . . . . . . . . . . . . . . . . 178
5.2 The nominal training image size, the level of discretization and the model origin. . . . . . . . . . . . . . . . . . . . . . . . . . . . . 178
5.3 The templates for the marked point processes. . . . . . . . . . . . . 180
5.4 The limits of the triangular distributions for scale, azimuth, dip and rake. . . . . . . . . . . . . . . . . . . . . . . . . . . . . . . . . 181
5.5 An example marked point training image - small lobes with a NTG ratio of 0.6. . . . . . . . . . . . . . . . . . . . . . . . . . . . . . 181
5.6 An example marked point training image - small ellipses with a NTG ratio of 0.8. . . . . . . . . . . . . . . . . . . . . . . . . . . . . . 182
5.7 A schematic of the `FLUVSIM` model (based on Deutsch and Tran (2002)[25]). . . . . . . . . . . . . . . . . . . . . . . . . . . . . . 183
5.8 An example `FLUVSIM` training image - channel only, channel width to thickness ratio of 20, low sinuosity and NTG of 0.8. . . . . . . . . . 183

5.9 An example `FLUVSIM` training image - channel and levee, channel width to thickness ratio of 50, high sinuosity and NTG of 0.4. . . . . 184
5.10 An example `FLUVSIM` training image - channel, levee and crevasse splay, width to thickness ratio of 100, median sinuosity and NTG of 0.2. . . . . . . . . . . . . . . . . . . . . . . . . . . . . . . . . . . . 184
5.11 The relationship between deviation, deviation correlation length and sinuosity in the `FLUVSIM` channel model. . . . . . . . . . . . . . . . . 187
5.12 An example surface based training image - large lobes, low correlation and NTG of 0.4. . . . . . . . . . . . . . . . . . . . . . . . . . . . 189
5.13 An example surface based training image - small lobes, high correlation and NTG of 0.8. . . . . . . . . . . . . . . . . . . . . . . . . . . 189
5.14 An example streamline based training image - high degree of amalgamation, channel width to thickness ratio of 20, median sinuosity and NTG of 0.2. . . . . . . . . . . . . . . . . . . . . . . . . . . . . . 190
5.15 An example streamline based training image - low degree of amalgamation, channel width to thickness ratio of 20, high sinuosity and NTG of 0.4. . . . . . . . . . . . . . . . . . . . . . . . . . . . . . 191
5.16 The lobe architectural element. . . . . . . . . . . . . . . . . . . . . . 194
5.17 A schematic of the channel / levee complex and channelized sheet complex turbidite styles. . . . . . . . . . . . . . . . . . . . . . . . . . 195
5.18 Nested streamline associations. . . . . . . . . . . . . . . . . . . . . . 197
5.19 The acceptance criteria applied to calculate the centroids for the nested streamline associations. . . . . . . . . . . . . . . . . . . . . . . 198
5.20 First example channel and levee complex training image. . . . . . . . 199
5.21 Second example channel and levee complex training image. . . . . . 200
5.22 The influence of source and primary azimuth distribution on streamline associations. . . . . . . . . . . . . . . . . . . . . . . . . . . . . . 202
5.23 Cross sections of two example channelized sheet complex training images. . . . . . . . . . . . . . . . . . . . . . . . . . . . . . . . . . . 203
5.24 A method for integrating a compensational stacking pattern into streamline association placement. . . . . . . . . . . . . . . . . . . . . 204
5.25 Example channelized sheet complex training image. . . . . . . . . . . 205
5.26 A schematic representation of the multiple point statistics calculated with the `MPSTATS` program. . . . . . . . . . . . . . . . . . . . . . . . 207

5.27 Example training image for the inference of statistics. . . . . . . . . . 214
5.28 Statistics inferred from the example training image. . . . . . . . . . . 214
5.29 A potential scenario tree for a reservoir model with uncertainty with respect to the depositional system, architectural elements and sandbody geometry. . . . . . . . . . . . . . . . . . . . . . . . . . . . . 217

6.1 Cross sections of stochastic mud drape models upscaled for flow simulation on regular Cartesian grids. . . . . . . . . . . . . . . . . . . . . 219
6.2 Plan views of streamline based stochastic models upscaled for flow simulation on regular Cartesian grids. . . . . . . . . . . . . . . . . . . 220
6.3 Cross sections of stochastic mud drape models upscaled for flow simulation on Voronoi grids. . . . . . . . . . . . . . . . . . . . . . . . . 221
6.4 An example regular Cartesian grid and the associated parameters. . 223
6.5 An example tartan grid and the associated parameters. . . . . . . . 224
6.6 An example tartan grid and the associated parameters; note the inclusion of two nested redial grids. . . . . . . . . . . . . . . . . . . . . 225
6.7 An example Voronoi grid and associated parameters. . . . . . . . . . 226
6.8 An schematic demonstrating the utilization of the link between global direct and Gaussian global distributions to construct the direct space local distribution from Gaussian space local distribution. . . . . . . . 228
6.9 Example $Y$ and $Z$ global distributions and the resulting ccdf table entries. . . . . . . . . . . . . . . . . . . . . . . . . . . . . . . . 230
6.10 Example redundant covariance calculations. . . . . . . . . . . . . . . 232
6.11 An example to demonstrate the sensitivity of kriging estimate to the number of bins in the semivariogram look up table. . . . . . . . . . . 233
6.12 The main `PRECDIST` subroutine flow chart. . . . . . . . . . . . . . . . 236
6.13 The transforms to move from $Y$ space to $Z$ space in the `PRECDIST` subroutine. . . . . . . . . . . . . . . . . . . . . . . . . . . . . . . 237
6.14 The `GETCDIST` subroutine flow chart. . . . . . . . . . . . . . . . . . . 238
6.15 The `PREGBAR` subroutine flow chart. . . . . . . . . . . . . . . . . . . . 240
6.16 The `CALCGBAR` subroutine flowchart. . . . . . . . . . . . . . . . . . . 242
6.17 An example tartan grid and well data to demonstrate the construction of a nonstationary covariance table. . . . . . . . . . . . . . . . . . . 244
6.18 The `NONSTATCOVTABLE` subroutine flowchart. . . . . . . . . . . . . . . 245

6.19 A variety of estimation settings that result in extreme weights. . . . 246

6.20 `TARTANSIM` applied to a regular. . . . . . . . . . . . . . . . . . . . . . . . . 247

6.21 `TARTANSIM` applied to a irregular grid with an isotropic semivariogram (spherical, range = 50) and a reference distribution. . . . . . . . . . . 248

6.22 The shadow template that is applied to filter screened data. . . . . . 249

6.23 Three `TARTANSIM` realizations with the same parameters, but with different kriging weight thresholds. . . . . . . . . . . . . . . . . . . 250

6.24 Example unconditional `SGSIM` realizations and the associated block averaged results. . . . . . . . . . . . . . . . . . . . . . . . . . . . . 256

6.25 Example unconditional `TARTANSIM` realizations. . . . . . . . . . . . . 257

6.26 Comparison of the mean covariance for unconditional `TARTANSIM` and `SGSIM`. . . . . . . . . . . . . . . . . . . . . . . . . . . . . . . . . 258

6.27 The data locations and Gaussian transformed distribution. . . . . . 258

6.28 Example conditional `SGSIM` realizations and the associated block averaged results. . . . . . . . . . . . . . . . . . . . . . . . . . . . . 259

6.29 Example unconditional `TARTANSIM` realizations. . . . . . . . . . . . . 260

6.30 The conditioning data locations and the e-type estimates over 201 realizations for both `TARTANSIM` and block averaged `SGSIM`. . . . . . 260

6.31 Three example local distributions of uncertainty compared between `SGSIM` block averaged and `TARTANSIM`. . . . . . . . . . . . . . . . . . 261

6.32 Comparison of the mean covariance for conditional `TARTANSIM` and `SGSIM`. . . . . . . . . . . . . . . . . . . . . . . . . . . . . . . . . 262

6.33 The nested radial grid format. . . . . . . . . . . . . . . . . . . . . . . 263

6.34 Example conditioned `TARTANSIM` realization with six nested radial grids. 263

6.35 An atomic grid provided by D. Hale, Landmark Graphics (2002)[46]. 264

6.36 A fine scale simulation and upscaled atomic grid. . . . . . . . . . . 265

6.37 The distributions at the support size of the fine regular grid and the Voronoi grid. . . . . . . . . . . . . . . . . . . . . . . . . . . . . . . 266

6.38 A direct simulation based on the LUSIM matrix method. . . . . . . 267

# Chapter 1

# Problem Setting

The inaccessibility of the subsurface generally results in a high degree of uncertainty in numerical models of geologic properties. Nevertheless, models are required for engineering design related to petroleum, mining, hydrogeology and geotechnical fields.

These models are an intermediate step to evaluate the response of the system to a transfer function. This transfer function may be the subsidence with respect to time after the construction of a dam or the flow of a contaminant through an aquifer. This thesis is focused on petroleum reservoir modeling; therefore, the transfer function is often flow simulation and the response variables may be flow rates and recovery.

There are a variety of information sources available. Seismic data provides extensive coverage, but at a coarse resolution. Well logs and core sampling give precise information, but with very small coverage. An example 2-D facies data set is shown in Figure 1.1. In most cases, data scarcity precludes the reliable use of purely deterministic techniques. A possible deterministic model is shown in Figure 1.2.

While deterministic models may appear realistic and account for some geologic information, they do not offer a model of the uncertainty due to incomplete information and they rarely show small-scale heterogeneity (Deutsch, 2003)[22].

Available information always has a limit in quality and resolution. This prevents the integration of small-scale heterogeneity into deterministic models with any degree of confidence. The omission of significant small scale features may bias the response variables. For example, thin and persistent mud drapes may form along accretion surfaces in inclined heterolithic strata sets. These mud drapes may form barriers and baffles to fluid flow in otherwise high quality reservoir sands. The omis-

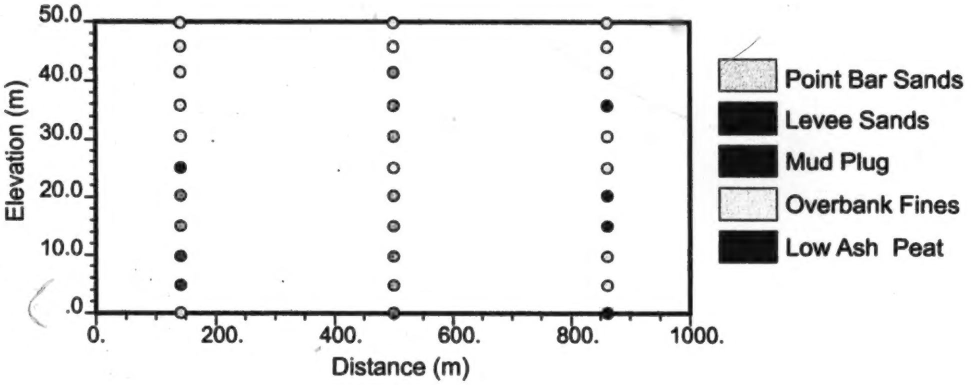

Figure 1.1: Ideal core representation of a simple 2-D stratigraphic dataset.

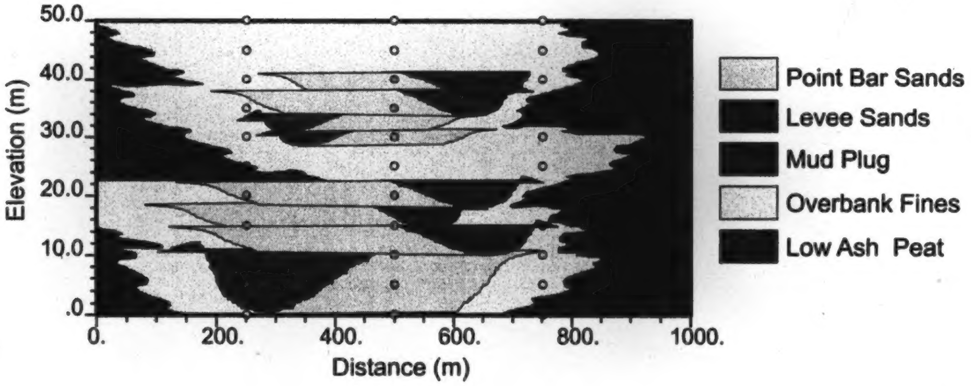
50.0
40.0
30.0
20.0
10.0
.0
Elevation (m)
0.
200.
400.
600.
800.
1000.
Distance (m)
Point Bar Sands
Levee Sands
Mud Plug
Overbank Fines
Low Ash Peat

Figure 1.2: A possible deterministic model based on the core data and a fluvial depositional setting.

sion of these mud drapes from a reservoir model will result in a biased assessment of recovery, connected volume and flow rates. Engineering design often requires models that reproduce both the small and large scale heterogeneity.

A measurement of uncertainty is required for optimized decision making. Stochastic models are required for these purposes. Stochastic processes allow for the efficient construction of multiple reservoir models that honor available conditioning while accounting for uncertainty in input model parameters and fluctuations due to a limited model size. Deterministic methods are impractical to construct multiple models to assess uncertainty. For example a number of geologists could construct reservoir models based on the available information, their unique experience and professional judgment. This would be cost prohibitive and would still miss important heterogeneity.

Unfortunately, stochastic geologic models are often unrealistic. Current methods for the construction of stochastic models often lack the flexibility to adequately integrate geologic information and to build models that reproduce the complex spatial features of many geologic setting. This weakness is due to the fact that most stochastic models are limited to the integration of statistics based on the two point semivariogram or relatively simple parametric objects.

A common complaint is that while the resulting stochastic models may honor a limited amount of statistical input they lack geologic realism. Statistics are applied, but the physics and processes behind the data and the complicated geometries and interrelationships are generally ignored. See Figure 1.3 for two typical semivariogram based geostatistical realizations that reproduce the statistics, as defined by the histogram and semivariogram, but lack geologic realism.

Geostatistics focusses on issues such as reproduction of statistics, models of uncertainty, computational efficiency and decision making after the application of a transfer function are the primary focus of research. While this is important, there is often a disconnect between geostatistical models and the underlying geology. There is a need for research on the further integration of geologic information into geostatistical models.

Clastic reservoirs are created by well understood physical laws. Base level, accommodation and sedimentation supply vary over a hierarchy of scales and generate characteristic depositional patterns. The resulting depositional units reflect a wealth of complex trends, geometries and interrelationships. The relevant details should

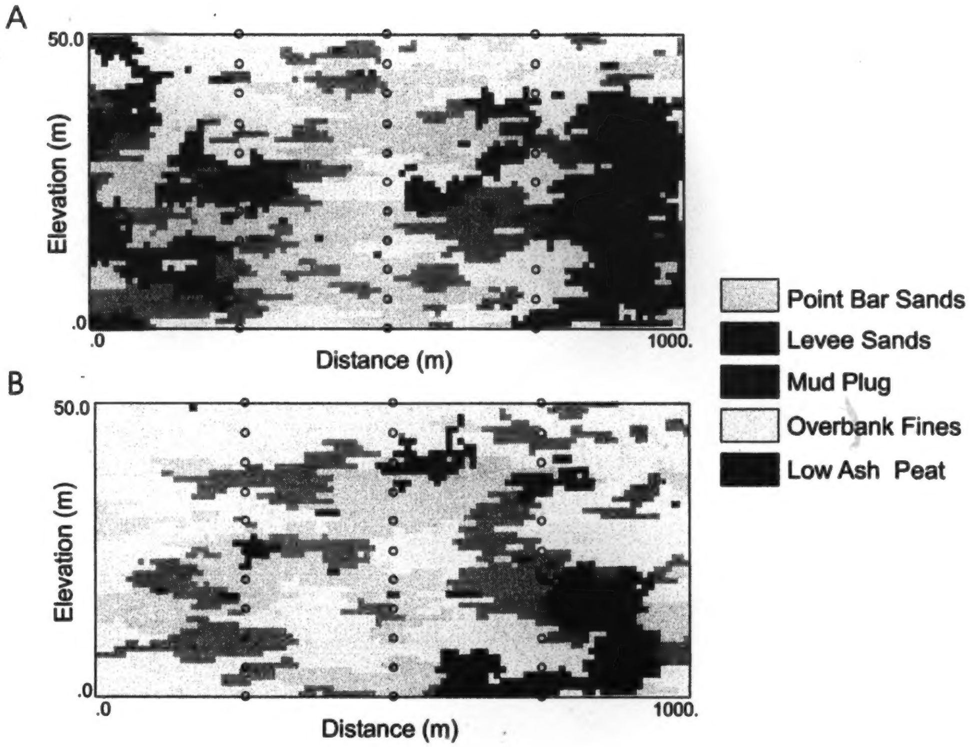

Figure 1.3: Two geostatistical realizations conditioned by the facies core data. A - realization #1 and B - realization #2. The facies geometries and interrelationships seen in deterministic model shown in Figure 1.2 are not reproduced.

be quantified and transferred to geostatistical models. Geologists have compiled a wealth of qualitative description that awaits quantification.

## 1.1 The Approach

This research develops methodologies and algorithms for improving the geologic realism of stochastic models. This problem has been addressed with integrated geological and geostatistical research. The result is a set of algorithms and methodologies as additions to the conventional tools such as those found in GSLIB (Deutsch and Journel, 1998)[23]. These tools address (**1**) building blocks for streamline based simulation for a variety of fluvial reservoir types, (**2**) surface based simulation and hierarchical trends for simulation of distal deepwater depositional environments, (**3**) static training image library and the building blocks for dynamic deepwater training image construction and (**4**) building blocks for direct simulation to unstructured grids.

A primary criteria of these developments is flexibility. Flexibility is preserved by: (**1**) flexible parametrization, (**2**) open source and (**3**) utilization of a building block framework.

Many of the developed algorithms are parameter rich. This may be an obstacle to practitioners who prefer a "black box" approach. This work and geostatistics in general should not be applied as a black box. The large number of parameters should improve the range of application of these tools.

With few exceptions, the code developed in this dissertation is publicly available. The format is similar to the Fortran code in GSLIB (Deutsch and Journel, 1998)[23]. In fact, some blocks of code have been taken directly from GSLIB programs, which is acknowledged.

It is hoped that this code will be adopted, applied and modified by other practitioners. The author or distributor does not accept responsibility to anyone for the consequences of using them or for whether they serve any particular purpose or work at all. This is research code.

The building blocks for streamline based simulation, deepwater training images and direct sequential simulation to irregular grids have been developed in this dissertation. These building blocks may be easily applied in the provided code, tailored or extracted for used as subroutines in new algorithms.

Models with geologically realistic features will improve model credibility. These improved models are expected to give more realistic assessment of response variables after the application of a transfer function and more correct assessment of uncertainty. This translates to improved engineering design and economic results. This will improve the quality and confidence of decisions made in the presence of geologic uncertainty.

These models are based on geometric and stochastic assumptions. Verification of models of natural systems is not possible. Validation is limited to ensuring that the model is consistent with the natural system (Oreskes, Shrader-Frechette and Belitz, 1994)[85]. This form of validation may be conducted by (**1**) careful identification of input parameters from the available geologic information and (**2**) ensuring that the modeling technique and associated assumptions construct a model that does not contradict the features observed and expected in the area of interest. These criteria are identified as internal and external objectivity respectively by Matheron (Translated by A. M. Hasofer, 1989)[69].

This research focuses on fluvial and deepwater petroleum reservoirs. Many of the methods and algorithms developed in this dissertation may be tailored to other geologic settings and mining resource and ground water contaminate studies.

A central theme of this dissertation is that the geostatistical professional should should seek further understanding of the underlying geology. The geostatistical modeling cannot be divorced from the geological analysis.

## 1.2 Dissertation Outline

Chapter 2 is an overview of concepts in reservoir model construction. The chapter is divided into three parts. Section 2.1 is a brief description of basic principles that are prerequisite to this thesis. This sections also serves to establish the working definition of controversial and esoteric terms for this dissertation. Section 2.2 is an overview of current methodologies in geostatistical techniques for reservoir modeling. Conventional semivariogram based, simulated annealing and object based paradigms along with more modern multiple-point and surface based methods are discussed. The additional topics of irregular grids and volume variance relations are covered. This material is prerequisite for the development of geostatistical models that further integrate geologic information.

Chapter 3 focuses on the construction of fluvial reservoir models. Section 3.1 provides a brief review of the architectural element approach to characterizing fluvial depositional systems, fluvial reservoir types and fluvial sequence stratigraphy. Section 3.2 proposes the streamline based simulation technique for the construction of fluvial stochastic models. This methodology is based on a set of building blocks for streamline based simulation. The architectural element approach and complicated channel streamline evolution are applied while preserving a strong degree of flexibility. Section 3.4 presents a methodology for efficient rule based conditioning of streamline based models. Another set of building blocks is presented to condition streamline based models. This method is demonstrated with a limited conditional streamline based model algorithm. Section 3.5 introduced the methodology for the application of the streamline based model for the calculation of stochastic inclined heterolithic strata. This model may be applied to assess the impact of heterogeneity related to the complicated geometries and trends associated with inclined heterolithic strata sets in petroleum reservoirs.

Chapter 4 focuses on the construction of deepwater reservoir models. Section 4.1 discusses recent research in turbidite heterogeneity and architectural element analysis and provides some specifics on small and large scale geometries of turbidite fans. Section 4.3 introduces a generalized surface based sequential simulation algorithm and related visualization program. These techniques were extended beyond initial work by Xie and Deutsch (2000)[140] in that the surfaces honor gradational, erosional contacts and missing data contacts. Section 4.2 introduces hierarchical trend models and an automatic trend fitting algorithm based on mathematical morphology operations. While hierarchical trend models may be applied to fluvial settings also, they are demonstrated in the surface based turbidite model in Section 4.5. This algorithm accounts for geometry and compensational stacking pattern of small scale turbidite flow event deposits within turbidite lobes. Section 4.6 demonstrates the application of the surface based turbidite model in a geostatistical work flow based on the Cengio, Italy turbidite fan system.

Chapter 5 explores the application of training images to improve the geologic realism of stochastic models. Section 5.1 discuses the dependence of multiple-point geostatistics on training images. Section 5.2 summarizes a suite of static training images in the first release of the training image library. This library is expected to grow over time. Section 5.4 presents a set of Fortran programs to tailor the training images and to calculate multiple-point statistics. Section 5.3 presents the building blocks for deepwater training images in C++. These building blocks are demonstrated with two distinct deepwater styles. Section 5.5 explores the many potential applications of the training image library.

Chapter 6 presents concepts and code required to perform simulation directly to irregular grids. The improved utilization of irregular grids fit to geologic heterogeneity and engineering constraints improves the ability of stochastic models to model heterogeneity and integrate data at a variety of support sizes. Section 6.1 provides a brief discussion on a variety of gridding schemes. Section 6.2 describes the direct sequential simulation algorithm that is required for simulation to irregular grids. Section 6.3 introduces a set of subroutines that are key building blocks for direct sequential simulation. Implementation details and procedures to improve CPU efficiency are covered. Section 6.4 presents two applications of the building blocks subroutines to directly simulate to tartan and Voronoi grids.

A list of the abbreviations and algorithms applied in this dissertation is included in Appendix A.

# Chapter 2

# Reservoir Model Building

This review describes the geologic and geostatistical concepts that are fundamental to this research. Section 2.1 is a brief description of basic principles that are prerequisite to this thesis. This sections also serves to establish the working definition of some key terms for this dissertation. Section 2.2 is an overview of current methodologies in geostatistical techniques for reservoir modeling. Conventional semivariogram, simulated annealing and object based paradigms along with more recent multiple-point and surface based methods are discussed. The additional topics of grids and volume variance relations are covered. This material is prerequisite for the development of geostatistical models that further integrate geologic information.

## 2.1 Basic Principles

Terminology is key to understanding the principles applied within this research. The terms that are applied within this dissertation are consistent with the most recent literature available. Some of these terms may have multiple meanings or may be esoteric. In the following discussion of basic principles, key terminology is identified by italics. For geologic terms not defined in the subsequent discussion the reader may refer to resources such as the Oxford Dictionary of Earth Sciences (Allaby and Allaby, 1999)[1]. For geostatistical terms the reader may refer to publications such as the Geostatistical Glossary and Multilingual Dictionary (Olea, 1991)[83].

### 2.1.1 Quantitative Modeling Principles

A *model* may represent any interpretation of a physical system. This may include an equation, a pseudo-process based framework or an image representing heterogeneity in the subsurface. In this dissertation the term model may refer to any one of these definitions. For example, a semivariogram model is a function representing the spatial continuity of a variable, a model may be a schedule of aggradation and avulsion derived from systems tract and a model may be a map of porosity in the subsurface.

An *approach* is a general paradigm for addressing a problem, while a *methodology* represents a series of steps or a work flow that is presented to accomplish a specific task. Methodologies may be classified within different approaches. Each one of these steps may be described as *techniques* and are coded as *algorithms*. For example, the task may be to calculate a 3-D porosity model based on a specific site. It may be decided to apply an object based approach over pixel based simulation. Then, the methodology may be designed with a series of techniques such as: (**1**) transform to proportional stratigraphic coordinates, (**2**) decluster sample data by cell declustering, (**3**) apply simulated annealing to model facies, (**4**) apply sequential Gaussian simulation to model porosity within facies. Each one of these techniques may be accomplished with coded algorithms such as those provided with GSLIB (Deutsch and Journel, 1998)[23].

The space that is the target of study in geostatistics is commonly referred to as the *area of interest* (AOI). The AOI may represent any geometry, scale and dimensionality. In this thesis the AOI will always refer to a 3-D geologic volume at reservoir scale. *Conditioning data* refers to any information that is available with regard to the AOI. The different types of information sources are discussed in Section 2.1.4. Conditioning that includes direct measures of the property of interest with uncertainty limited to measurement error is denoted as *hard data*, while conditioning that provides an indirect and uncertain measure is denoted as *soft data*.

Stochastic models honor hard conditioning data (e.g. well data) exactly and input statistics within *ergodic fluctuations*. These fluctuations in model statistics are due to the modelling of a limited domain and the assumption of an infinite domain inherent to geostatistical methods. When the available statistics are based on preferential sampling the statistics are *clustered* and when the samples do not sample the entire underlying property distribution the statistics are *spatially biased*.

### 2.1.2 Clastic Sedimentological Principles

*Facies* identification is a technique of rock characterization and grouping by composition, grain size, texture etc. Specific features such as grain size trends or *grading* are diagnostic. Normal grading indicates that the grain size is fining upward and reverse grading indicates that the grain size is coarsening upward. Facies may grouped together as *architectural elements* that are genetically related. Architectural elements have unique lithology, scale, internal geometry and eternal form (Miall, 1996) [73]. A *depositional system* is a three dimensional collection of process-related facies that represent a paleo-geomorphic setting (Galloway, 1989)[39].

Direction and location within a depositional system may be described as *proximal* or *distal*. Proximal is applied to sediment of sedimentary environment near the source of the deposit or as the direction towards the source and away from the basin. Distal is applied to sediment of sedimentary environment furthest from the source or as the direction towards the basin and away from the source.

### 2.1.3 Sequence Stratigraphic Principles

*Base level* is an idealized surface that divides denudation above and deposition below. *Accommodation* is space available below base level for the accumulation of sediments. *Sequence stratigraphy* is the analysis of cyclic sedimentation in response to variations in base level, sediment supply and accommodation (Posamentier and Allen, 1999)[94].

The basic unit of sequence stratigraphy is the depositional system. Collections of contemporaneous depositional settings are grouped as *systems tracts*. A systems tract is a linkage of related depositional systems, forming a subdivision of a sequence (Brown and Fisher, 1977)[10]. A *sequence* is a relatively conformable succession of genetically related systems tracts bounded by unconformities or their correlative conformities (Mitchum, 1977)[75].

### 2.1.4 Geologic Information Sources

This brief summary identifies the geologic information sources and their associated scales of observation, resolution and coverage, application and limitations. The focus is on the application of information to reservoir characterization. The following review is based on Miall (2000)[74].

#### Core

Core samples usually have a diameter of about 10 centimeters. Coverage is limited with only about a trillionth of the reservoir sampled. In practice, only meters to a few 10's of meters of core is available for a single well, since the collection of core represents a significant interruption in drilling.

Core is used to assess present lithofacies, reservoir quality, calibrate well logs and establish geologic time through biostratigraphy. Lithofacies and small to medium-scale structures observed in core aid in identifying depositional system and architectural elements. Core provides a direct measurement of reservoir properties that may be used to calibrate well logs to improve well log inferred reservoir properties.

#### Well Logs

There are a suite of logging tools that measure rock properties such as electrical resistivity, sonic velocity, gamma radioactivity and image logs. These logging tools have vertical resolutions from centimeters to about a meter with a similar depth of penetration away from the well.

Coverage is generally good along the wells, but the limited number of wells results in low overall coverage. Well logs are applied to identify facies and to infer reservoir properties. The response of a lithology to a specific tool is not unique; therefore, multiple logs are jointly analyzed to improve identification. Logs provide relative measures that readily identify vertical grading and bounding surfaces, but require calibration from core for improved inference of reservoir quality and depositional setting.

#### Cuttings

The well cuttings are generally less than one centimeter in length and are collected as the well is being drilled. Cuttings provide immediate information that may aid in directing drilling and provide information on lithology, texture and microfossils. Differences in density and rock caving in the well result in depth distortions and mudstones are preferentially dissolved and washed away. This reduces the quality of this information.

### Outcrop

Outcrops provide excellent exposure with extents from tens to hundreds of kilometers and heights up to hundreds of meters. The resolution of observation is limitless, but outcrops do not provide coverage of the actual reservoir.

Outcrops may provide valuable analogue information for reservoir characterization. Reservoir heterogeneity, including architectural element geometry and interrelationships and related distribution of petroleum properties, may be inferred from outcrop. The application of statistics from an outcrop entails a strong assumption of stationarity (see 2.2.2), since information is borrowed from a different site with its own unique depositional history. Also, 3-D architecture may be difficult to infer from outcrop, unless exposure is available in a variety of orientations and with close spacing. Features observed in outcrop may be a function of surface weathering and unloading.

### Seismic

The scale and resolution of seismic is variable. The contribution of seismic is limited by detection and tuning effects. The following description of seismic is based on Bertram and Milton (1996)[3] and Sharma (1986)[110].

The resolvable limit of seismic is a function noise, the quality of data and the interpreter's skill. The rule of thumb is that the resolvable limit is $\frac{1}{4}\lambda$ where $\lambda$ is the wave length of the p-wave. Resolution decreases with depth due to increased sonic velocity with depth and the preferential filtering of the high frequencies of the sweep.

$$\lambda = \frac{v}{f} \tag{2.1}$$

where $\lambda$ is the wavelength, $v$ is the sonic velocity and $f$ is dominant reflected frequency. The increase in velocity and decrease in frequency with depth increase wavelength and diminish resolution. Example vertical resolvable limits are shown below.

- Shallow loosely consolidated sandstone
  - $v$ of about 1800 m/s, 60 Hz, $\frac{1}{4}\lambda = 7.5$ meters
- Deeper Paleozoic carbonate
  - $v$ of about 4500 m/s, 15 Hz, $\frac{1}{4}\lambda = 75$ meters

Seismic is applied to characterize the reservoir geometry and to a limited extent internal geometry. Seismic properties such as acoustic impedance, amplitude and sonic velocity may be applied as soft, large scale information to aid in the inference of lithology and petroleum properties. The primary limitation of seismic is its resolution and inherent error due to difficulties in the time to depth conversion and correlation to petrophysical properties including saturation.

#### Well Test

Well test or pressure transient analysis is an attempt to solve an inverse problem. The flow rate transient and reservoir properties are the inputs and the pressure transient is the output. Given this input and output inference is made concerning the unknown reservoir properties. There are a variety of test types including draw down, buildup, injection, fall off, interference and drill stem tests. The type of test applied is based on study objectives and practical limitations. From this data, details on the character of the system are extracted. This information is at the scale of the area of influence of the well. Coverage may be extensive, depending on the well coverage. Well tests may indicate the effective permeability or conductivity near the well, the reservoir pressure may aid in the inference of reservoir extent, presence of faults and barriers to flow. Well tests provide very coarse information on subsurface heterogeneity since pressure transmission is inherently diffusive (Horne, 1995)[48].

### 2.1.5 Physical Sedimentary Process and Depositional Systems

Reservoirs form in a variety of depositional systems. Clastic depositional settings represent a major proportion of world reservoirs (55% of oil and 75% of gas reser-

| Type | Resolution | Scale | Coverage | Application |
|---|---|---|---|---|
| Core | $\simeq \infty$ | 10 cm dia. | V. Low | Sample / Calibration |
| Well Log | 10 cm | 1 $m^3$ | Low | Vertical Trends, Surfaces |
| Cuttings | $\simeq \infty$ | 1 cm | Low | Direct Drilling / Units |
| Outcrop | $\simeq \infty$ | 1000's $m^2$ | None | Analogue Info. |
| Seismic | $10m$ | $10m^3$ | $\leq$ Complete | Trends, Secondary, Surfaces |
| Well Test | $10 - 100m$ | $10 - 100m$ | Medium | Reservoir Quality |

Table 2.1: A summary of the available data and information for the construction of reservoir models. These values represent approximate measures. Greater detail is provided in the text.

voirs, although carbonates account for a greater proportion of total production (Boggs, 2001)[5]). The following are some major clastic depositional settings.

- *Aeolian* - deposition dominated by wind, typically in arid areas with low vegetation
- *Colluvial and Alluvial Fans* - deposition in proximal settings due to rock erosion and channel flow.
- *Fluvial* - deposition dominated by rivers
- *Deltaic* - sediments at the intersection of a river and a standing body of water. The deposition is controlled by a balance of river, tidal and wave influence.
- *Lacustrine* - Low energy sediments in lakes
- *Estuarine* - A coastal body of water where fresh and salt water mix resulting from the drowning of a river valley due to base level rise.
- *Deepwater* - sediments transported to the continental slope and abyssal plane by turbidity currents and debris flows.

Each one of these depositional systems has unique heterogeneities that are a result of physical sedimentary processes at a hierarchy of scales. For example, alluvial deltas form at the intersection of rivers and standing bodies of water. The reduction of velocity systematically reduces stream competency. The sedimentation of coarse to fine grained materials leads to a characteristic reverse grading, and the regression of the shoreline due to sedimentation leads to overall progradation. The morphology at a variety of scales is a function of sediment supply, relative density, tidal, wave and river forces. Overviews of morphologies and the responsible sedimentary processes for a variety of depositional settings are provided by many authors including Allen and Allen (1990), Galloway and Hobday (1996), Miall (2000), Reading (1996) and Walker and James (1992)[2, 39, 74, 104, 136].

This dissertation directly deals with the characterization of reservoirs in the fluvial and deepwater environments (see Chapter 3 and Chapter 4). In each of these chapters more information will be provided on their associated heterogeneities.

### 2.1.6 Facies Models, Lithofacies and Architectural Elements

The functional definition of facies model is a generalized model that captures the essence of depositional setting, lithofacies and architectures (see 2.1.2). Facies models are adapted to a specific site in an hierarchical fashion. The present lithofacies are identified. Then, the process-related assemblages of lithofacies, architectural elements, are identified.

Lithofacies are classified based on bedding, grain size, texture and sedimentary structures. A variety of lithofacies schemes have become standard for each depositional system. These are not exhaustive as types are added and customized to fit a specific site (Miall, 1996)[73].

The architectural elements are defined as components within the deposition that are characterized by a distinct facies assemblage, internal geometry and external form. Architectural elements are generally larger than individual facies units and are smaller than a channel fill (Miall, 1996, p. 89)[73]. Architectural elements have a predictable form and morphology and are characteristic of the associated sedimentary processes. Fluvial architectural elements include lateral accretion, crevasse splays, down stream accretion deposits etc. A list of fluvial architectural elements is included in Table 3.1. The architectural element method is more demanding than traditional lithofacies methods. The identification of large scale geometries requires good exposure and sufficient data (Miall, 1985)[72].

### 2.1.7 Sequence Stratigraphy, Systems Tracts and Bounding Surfaces

This review of the principles and concepts of sequence stratigraphy is based on Catuneanu (2003) and Galloway and Hobday (1996)[12, 39]. The working definition of sequence stratigraphy is the analysis of cyclic sedimentation patterns that are present in stratigraphic successions, as they develop in response to variations in sediment supply and space available for sediment accumulation (Posamentier and Allen, 1999)[94](see Section 2.1.3).

Sequence stratigraphy principles are independent of scale. The sequence stratigraphy paradigm is applied to integrate information on heterogeneity at a variety of scales within reservoirs.

Bounding surfaces identified by the Exxon Production Research model are maximum regression, maximum flooding, basal surface of forced regression, subaerial unconformity and correlative conformity (Van Wagoner et al, 1990)[133]. These salient surfaces segment the sediments into system tracts such as lowstand, transgressive, highstand, and falling stage. Each system tract has unique characteristics with respect to the bounding surfaces, change in accommodation, preservation potential of sediments and the nature of the sediments.

The following description of system tracts is adapted from Catuneanu (2003)[12]. The system tracts and major bounding surfaces relative to an idealized base level curve is shown in Figure 2.1.

#### Lowstand Systems Tract

The lowstand systems tract (LST) is bounded by the subaerial unconformity and its correlative conformity at its base and above by the maximum regressive surface. Although base level is rising during this systems tract, sedimentation results in normal regression (NR). This system tract represents the coarsest component of both terrigenous and marine settings. The terrigenous sediments reach maximum progradation and fluvial incising and shelf erosion delivers coarse sediments to the marine setting. Coarse sediments in deepwater form turbidite reservoir rock and fluvial systems form amalgamated channel sand complex reservoirs due to poor preservation potential of overbank fines. Preservation of lowstand sediments in fluvial and deepwater is high due to the subsequent transgressive system tract.

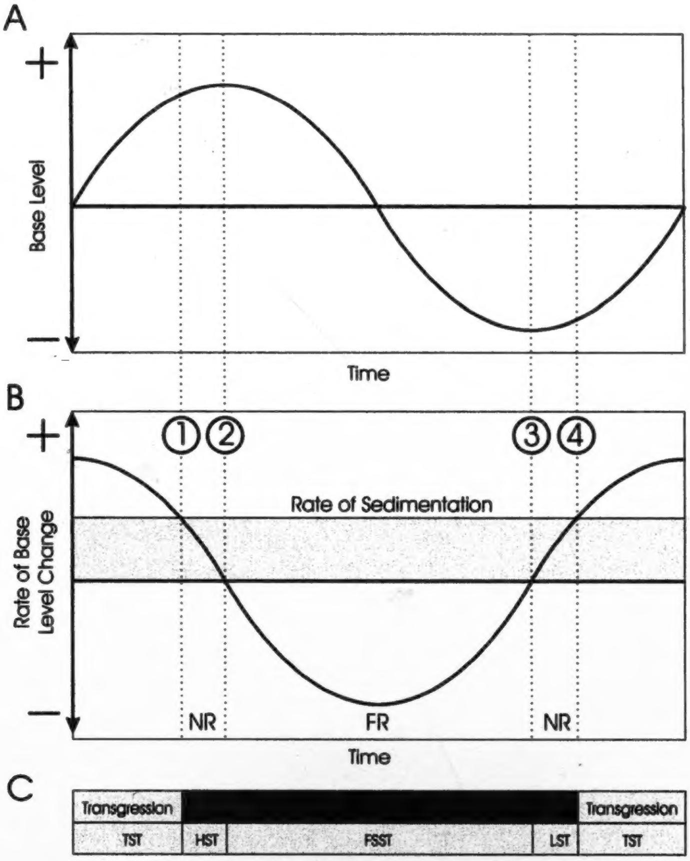
A
+
Base Level
−
Time
B
+
①②
③④
Rate of Sedimentation
Rate of Base Level Change
−
NR
FR
NR
Time
C
Transgression
Transgression
TST
HST
FSST
LST
TST

Figure 2.1: The system tracts and major bounding surfaces relative to an idealized base level curve and rate of base level change curve. A - the base level curve, B - the rate of change in base level and the rate of sedimentation and C - the T-R and depositional sequence IV models. The surfaces are enumerated; (**1**) maximum flooding surface, (**2**) basal surface of forced regression, (**3**) subaerial unconformity and correlative conformity and (**4**) maximum regression surface (adapted from Catuneanu (2003)[12]).

#### Transgressive Systems Tract

The transgressive systems tract (TST) is bounded by the maximum regression surface at its base and the maximum flooding surface at its top. Base level rise outpaces coastal sedimentation and shoreline transgression results.

Accommodation is created and the preservation potential of transgressive systems tract is high. Fluvial systems aggrade in response to rising base level and preserve channels and associated architectural elements embedded in over bank fines. There is general fining upward trend due to a decrease in stream gradient. Coastal systems aggrade and preserve back stepping foreshore, estuarine facies and barrier island systems. Deepwater systems are starved as terrigenous sediments are deposited along the coast and on the shelf, resulting in compressed layers.

#### Highstand Systems Tract

The highstand systems tract (HST) is bounded by the maximum flooding surface at its base and by the basal surface of forced regression at its top. Base level rise is slowing and is outpaced by sedimentation resulting in normal regression.

Accommodation is created at a slower pace. Fluvial systems reach their lowest energy and the slow rise in base level may result in laterally connected reservoir sands, although subsequent falling stage system tract may reduce the preservation potential of fluvial and shallow marine deposits. Limited sediments are transported to the deepwater and form the initial component of a coarsening upward trend.

#### Falling Stage Systems Tract

The falling stage systems tract (FSST) is bounded by the basal surface of forced regression at its base and by the subareal unconformity and its correlative conformity at its top. Base level is falling resulting in forced regression (FR).

Fluvial systems incise and and coastal systems rapidly prograde with offlapping shoreface lobes and shelf macroforms. Large amounts of terrigenous sediments are delivered to the deepwater and form extensive submarine fan complexes.

### 2.1.8 Quantitative Dynamic Stratigraphy Models

Some geologists have approached quantitative subsurface models with a reliance on depositional related processes with quantitative dynamic stratigraphy (QDS) models. QDS models are based on initial and boundary conditions and on a continuum of relationships including established fundamental laws, approximations, empirical relationships to poorly defined gross empirical relationships (Cross and Harbaugh, 1990)[18]. These are forward and dynamical models since they construct the subsurface in sequential time steps and the current state is a function of all previous states.

QDS models based directly on fundamental laws and first principles are generally called deductive models. Deduction models assume that processes at small scales of observation have a significant impact on the heterogeneity at the large scale. Rule-based models assume that important lower level dynamics may be synthesized through a series of rules (Paolo, 2000)[90].

A QDS clastic sediment model may consider variables such as tectonics, eustasy, and sediment supply. These variables are input to mathematical models based on physical laws that describe sedimentological processes such as particle settling velocities, compaction, tectonic deflection, fluid flow, and erosion. These models are process based since they are based on physical processes. These coupled equations with initial and boundary conditions generate quantitative models of depositional systems that are able to reproduce the wealth of geometries and relationships observed in the sedimentological record (Cross and Harbaugh, 1990)[18].

There are two significant limitations to the predictive power of QDS models: (**1**) they are limited in their spatial precision and (**2**) the initial and boundary conditions are not known. The limit in precision is due to limited model resolution or discretization errors and simplification of the physical processes. For example, it not possible to apply Navier-Stokes equation to track the settlement of every grain in suspension. Increasing computing power may improve resolution, but will not aid in identifying the initial and boundary conditions. It is not possible to calculate the initial and boundary conditions given the current state because of the chaotic nature of most non-linear dynamic models (or forward models) (Tetzlaff, 1990, Gleick, 1987) [124, 42].

The practical consequence of chaos is a high sensitivity of the model outcome to the initial and boundary conditions. Infinitesimal perturbations in these model parameters may result in vastly different outcomes. This chaotic nature and the high computational requirements of QDS models preclude the application of an iterative method to converge on initial and boundary conditions that reproduce a realistic level of site specific conditioning.

Attempts have been made to produce conditional QDS models. Tetzlaff (1990) [124] proposes a methodology for reproducing conditioning by making an observation based on geologic knowledge and data, and pseudo-inverse modeling to get distributions of possible initial conditions. Pseudo-inverse modeling is trial and error forward modeling in an attempt to reproduce the geologic observations. These distributions of initial conditions are then applied in forward modeling and a rejection criteria is applied to filter out model realizations that deviate too greatly from the geologic observations. This method would not be plausible when detailed conditioning is available.

Although QDS models are not appropriate for detailed reservoir modeling, QDS models are useful for refining conceptual models and exploring the link between coupled geomorphological processes and the preserved sediments (Paola, 2000)[90]. In some cases, sedimentological features were discovered in QDS models and then were confirmed in geology (Cross and Harbaugh, 1990)[18]. QDS models may also be applied to reproduce large scale field observations in an approximate manner.

## 2.2 Geostatistical Techniques

This dissertation is concerned with the further integration of geological information into geostatistical models for petroleum geology than currently permitted by commonly applied methods. The following introduction to geostatistics is based on the short coarse by Deutsch (2003)[22]. Geostatistics is a branch of applied statistics that focuses on (**1**) the geologic nature of the data, (**2**) the spatial relationships between the data, and **3**) the size support and the precision of the data.

Geostatistical techniques have been widely applied to a variety of fields interested in spatial modeling including forestry, fisheries, agriculture, environmental, mining and petroleum. The following are the key applications of geostatistics (adapted from Deutsch (2003)[22]).

1. Geostatistic algorithms aid in the construction of quantitative models for the geologic area of interest. Geostatistic tools allow for the integration of multiple types and scales of conditioning and geologic information into numeric subsurface models.

2. Geostatistic algorithms are well suited for estimation and inference based on the limited conditioning data and a measure of the spatial structure and the correlation between the data.

3. Geostatistical algorithms allow for quantification of uncertainty locally and globally through the calculation of multiple equiprobable realizations.

4. Geostatistical algorithms allow for improved sample design through the assessment of the impact on model uncertainty of additional sampling or sample configuration.

5. Geostatistical algorithms allow for simulation of quantitative geologic models that mimic some of the spatial features expressed in the underlying geologic phenomenon. These models may be subjected to transfer functions such as flow simulation for the quantification of uncertainty in response variables, such as flow rates.

6. The measure of uncertainty from a geostatistical study allows for uncertainty analysis, sensitivity studies and the optimized decision making through the application of a loss function.

Correct application of geostatistics requires the recognition of its limits.

1. While geostatistical characterization may improve the utilization of available data it does not replace the need for good additional data.

2. Geostatistical models are based on a large number of model decisions and implicit assumptions. The goodness of the resulting models is dependent on the use of sound professional judgement and a fundamental understanding of the associated tools and algorithms; geostatistics does not function well as a black box.

3. Geostatistical characterization does not save time. On the contrary, a geostatistical study may represent an additional work load beyond the conventional geologic studies. Good geostatistical models require significant amounts of professional time.

Fundamental concepts related to geostatistical models include: **(1)** random variables and random functions, **(2)** stationarity and inference, **(3)** data conditioning and (4) multiple equiprobable realizations. A review of each of these concepts follows.

### 2.2.1 Random Variables and Random Functions

Reviews the random function concept is provided in geostatistical references such as Deutsch (2002), Deutsch and Journel (1998), Goovaerts (1997), Issaks and Srivastava (1989) and Journel and Huijbregts (1978) [21, 23, 43, 51, 59]. The following is a brief summary.

There is an inaccessible true value at all unsampled locations. A random variable (RV) is a mathematically convenient method for characterizing our lack of knowledge or ignorance with regard to this inaccessible truth. A RV is a variable that may take a variety of outcomes based on a probability distribution. $Z(\mathbf{u})$ denotes the RV and $z(\mathbf{u})$ denotes an outcome at spatial location defined by location vector $\mathbf{u}$.

A RV is characterized by its associated cumulative distribution function (cdf).

$$F(z_1 \dots z_V) = Prob(Z_1(\mathbf{u}) \leq z_1, \dots, Z_V(\mathbf{u}) \leq z_V) \tag{2.2}$$

where $z_1, \dots, z_V$ are the outcomes for variables $1, \dots, V$ at location $\mathbf{u}$.

A random function (RF) is a set of RV at any number of locations and is applied to characterize the associated joint distribution. Complete characterization of the RF requires the spatial law, which is the set of all possible distribution functions for all possible combinations of locations, $\mathbf{u}_1 \dots \mathbf{u}_N$, and all combinations possible outcomes, $z_1 \dots z_V$.

$$F(\mathbf{u}_1 \dots \mathbf{u}_N, z_1 \dots z_N) = Prob(Z_1(\mathbf{u}_1) \leq z_1, \dots, Z_V(\mathbf{u}_N) \leq z_V) \tag{2.3}$$

where locations $\mathbf{u}_1, \dots, \mathbf{u}_N$ are jointly considered.

The first-order moment of the RF is the mathematical expectation. The expected value is defined for the RV $Z(\mathbf{u})$ as follows:

$$E\{Z(\mathbf{u})\} = \int_{-\infty}^{\infty} z dF(\mathbf{u}; z) \tag{2.4}$$

The second-order moments considered in geostatistics include the variance, the covariance and the semivariogram. The variance is a commonly applied measure of spread in conventional statistics. The variance is defined for the RV $Z(\mathbf{u})$ as follows:

$$Var\{Z(\mathbf{u})\} = E\{[Z(\mathbf{u}) - m(\mathbf{u})]^2\} \tag{2.5}$$

The covariance is a two-point statistic based on RV's at locations $\mathbf{u}_1$ and $\mathbf{u}_2$. The covariance is defined as follows:

$$C(\mathbf{u}_1, \mathbf{u}_2) = E\{[Z(\mathbf{u}_1) - m(\mathbf{u}_1)][Z(\mathbf{u}_2) - m(\mathbf{u}_2)]\} \tag{2.6}$$

where $C(\mathbf{u}_1, \mathbf{u}_2)$ is the covariance between locations $\mathbf{u}_1$ and $\mathbf{u}_2$.

The link between the semivariogram and covariance will be discussed in Section 2.2.2. The semivariogram is defined as follows:

$$\gamma(\mathbf{u}_1, \mathbf{u}_2) = \frac{1}{2}E\{[Z(\mathbf{u}_1) - Z(\mathbf{u}_2)]^2\} \tag{2.7}$$

where $\gamma(\mathbf{u}_1, \mathbf{u}_2)$ is the semivariogram between locations $\mathbf{u}_1$ and $\mathbf{u}_2$. The semivariogram may be calculated over a range of distances and directions to infer the spatial structure of the available data.

In practical applications only lower moments (generally the first and second order moments) of the RF are inferred from data and modeled directly. The higher order moments up to the complete spatial law is usually based on an underlying model, such as the multi-Gaussian (MG) model. The indicator formalism offers an alternative approach to characterize the bivariate character of an RF.

### Indicator Formalism

The indicator formalism is covered in Deutsch (2002), Deutsch and Journel (1998) and Goovaerts (1997) [21, 23, 43]. Indicator techniques are concerned with the following binary transform of the RF $Z(\mathbf{u})$.

$$i(\mathbf{u}; z_k) = \begin{cases} 1 & if\ Z(\mathbf{u}) \leq z_k \\ 0 & otherwise \end{cases} \tag{2.8}$$

where $z_k$ is a threshold value for thresholds $k = 1, \ldots, K$ and $Z(\mathbf{u})$ is the RV at location $\mathbf{u}$. This represents a probability coding of hard data. Soft data may be directly coded as probabilities and constraints in the indicator formalism. Constraint coding is shown below.

$$i(\mathbf{u}; z_{lower}, z_{upper}) = \begin{cases} 1 & Z(\mathbf{u}) \le z_{lower} \\ undefined & Z(\mathbf{u}) \in (z_{lower}, z_{upper}] \\ 0 & Z(\mathbf{u}) > z_{upper} \end{cases} \tag{2.9}$$

where $z_{upper}$ and $z_{lower}$ are the upper and lower threshold values and $Z(\mathbf{u})$ is the RV at location $\mathbf{u}$.

The semivariogram of the indicator transform or indicator semivariogram may be calculated for any threshold.

$$\gamma(\mathbf{u}_1, \mathbf{u}_2; z_k) = \frac{1}{2}E\{[i(\mathbf{u}_1; z_k) - i(\mathbf{u}_2; z_k)]^2\} \tag{2.10}$$

where $\gamma(\mathbf{u}_1, \mathbf{u}_2; z_k)$ is the indicator semivariogram between locations $\mathbf{u}_1$ and $\mathbf{u}_2$ for threshold, $z_k$.

### 2.2.2 Stationarity and Inference

This discussion on stationary and inference is based on fundamental references on geostatistics including Deutsch, 2002; Deutsch and Journel 1997; Goovaerts 1997; Isaaks and Srivastava, 1989, Journel and Huijbregts, 1978)[21, 23, 43, 51, 59]. Stationarity is a modeling decision. Repetitive samples are required to infer any statistic. This is not available in the spatial setting. Once a specific location, $\mathbf{u}$, is sampled (**1**) there is no other samples available and (**2**) there is no need for inference since that location $\mathbf{u}$ is sampled and is known. Stationarity is the decision to accept samples at other locations as replicates for the inference of statistics. This amounts to an assumed invariance of the considered statistic with respect to location within the space or subset of the space. Stationarity of an RF and all its moments may be represented as follows:

$$F(\mathbf{u}_1 \ldots \mathbf{u}_N; z_1 \ldots z_V) = F(\mathbf{u}_1 + \mathbf{h} \ldots \mathbf{u}_N + \mathbf{h}; z_1 \ldots z_V) \tag{2.11}$$

Stationarity of the first and second-order moments of the RF this may be represented as follows (Deutsch,2002).

$$E\{Z(\mathbf{u})\} = m, \ \forall \ \mathbf{u} \in A \tag{2.12}$$

$$Var\{Z(\mathbf{u})\} = E\{[Z(\mathbf{u}) - m(\mathbf{u})]^2\} = \sigma^2, \ \forall \ \mathbf{u} \in A \tag{2.13}$$

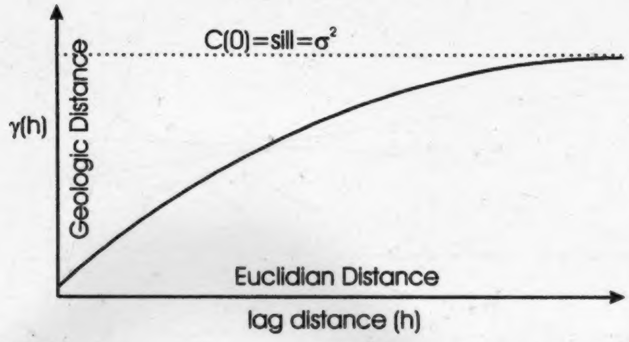

Figure 2.2: A schematic of a semivariogram model. The semivariogram quantifies the relationship between Euclidian distance and geologic distance or change.

$$C(\mathbf{h}) = E\{[Z(\mathbf{u}) - m(\mathbf{u})][Z(\mathbf{u}+\mathbf{h}) - m(\mathbf{u}+\mathbf{h})]\},\ \forall\ \mathbf{u}, \mathbf{u}+\mathbf{h} \in A \tag{2.14}$$

$$\gamma(\mathbf{h}) = \frac{1}{2}E\{[Z(\mathbf{u}) - Z(\mathbf{u}+\mathbf{h})]^2\},\ \forall\ \mathbf{u}, \mathbf{u}+\mathbf{h} \in A \tag{2.15}$$

where $A$ is the study area. With this assumption of second-order stationarity the link between the variance, covariance and semivariogram may be made.

$$C(\mathbf{h}) = \sigma^2 - \gamma(\mathbf{h}) \tag{2.16}$$

where $C(\mathbf{h})$ is the stationary covariance function, $\sigma^2$ is the stationary variance and $\gamma(\mathbf{h})$ is the stationary semivariogram.

The stationary semivariogram model may be seen as a function that characterizes the relationship between lag distance (Euclidian distance) and geologic distance; since geologic distance may viewed as the change in sediments (see Figure 2.2). Higher order moments are considered by multiple-point geostatistics (see Section 2.2.6).

The decision of stationarity represents an assumption for pooling samples and an export license of the inferred statistics over the area of interest. Inference would not be possible without this decision.

Stationarity is a property of the RF model and is not a feature of the underlying spatial phenomenon. Stationarity is a decision and not a hypothesis; therefore, it cannot be tested. Its appropriateness may be judged based on an understanding of the underlying spatial phenomenon. Too strong of a decision of stationarity may result in the masking of important spatial features, while too weak of a decision of stationarity may result in too few data for reliable statistical inference. The goal is to assemble the greatest number of relevant data for reliable predictive statements (Deutsch, 1992)[19]. Geostatistical simulation algorithms calculate multiple realizations of RF models that are able to honor inferred stationary statistics and a variety of conditioning. See Section 2.2.11 for a discussion on geostatistical algorithms that account for nonstationary statistics.

### 2.2.3 Data Conditioning

Without data there would be less difficulty in reproducing the complicated geometries and interrelationships for the construction of reservoir models. Quantitative dynamic stratigraphy (QDS) models are able to reproduce many of the geometries and relationships observed in the rock record. Section 2.1.8 reviews the difficulties in conditioning QDS models to a realistic level of data for a reservoir study.

Geostatistical methods are able to reproduce various levels of geometric complexity while allowing for conditioning to a wide variety of site specific data. The kriging and indicator kriging algorithms at the heart of pixel based simulation may be conditioned to measured hard data. The exactitude property of kriging ensures that the hard data are reproduced at the data locations and reproduced at other locations in a statistical sense (Deutsch and Journel, 1998)[23]. Inexact soft data may be directly coded into the indicator framework and applied directly as constraint conditioning. Local variable mean or proportion models may be constructed from site data and geologic information

### 2.2.4 Multiple Equally Likely to be Drawn Realizations

Simulation is the process of drawing realizations or outcomes from a RF model. Multiple, equally likely to be drawn, realizations are the key to the characterization of local and global uncertainty with simulated geostatistical models. The space of model uncertainty may explored at two levels; **(1)** change of the random number seed and **(2)** change of the model parameters.

Multiple realizations may be calculated with constant model parameters and different random number seeds. The variability between the resulting models is known as ergodic fluctuations (see Section 2.1) and is a function of the simulation technique, the density of the conditioning and the range of correlation relative to the area being modeled. The magnitude of these fluctuations may be predicted based on volume-variance relations (Deutsch and Journel, 1998 and Goovaerts, 1997)[23, 43] (see Section 2.2.10).

Fixing all of the modeling parameters may unrealistically limit the resulting space of uncertainty. For example, there may be significant uncertainty with regard to the stationary histogram and semivariogram. In this situation, the common practice is to apply a scenario based method. A variety of cases are assigned to each model parameter with associated probability. For each realization a suite of model parameters is drawn before simulation (Pyrcz et. al, 2004)[103].

### 2.2.5 Semivariogram Based Geostatistical Algorithms

The semivariogram is at the heart of traditional geostatistics. The experimental semivariogram is the expected square difference of a RF at locations separated by a lag vector, **h** (see Section 2.15). The following is a description of some traditional pixel based geostatistical techniques: (**1**) kriging, (**2**) sequential Gaussian simulation, (**3**) truncated Gaussian and (**4**) indicator kriging and simulation.

#### Kriging

The following is a brief discussion of kriging. This algorithm is known as the best linear unbiased estimator (Deutsch and Journel, 1998)[23]. The algorithm is derived and the properties of estimation are discussed (this derivation is found in Journel and Huijbregts (1978)[59] among others).

The classical estimation problem is the illustrated in Figure 2.3. Inference is required at an unknown point given some local samples or conditioning.

The variable at an unsampled location may be estimated as a linear combination of the available conditioning data.

$$Y^*(\mathbf{u}) = \sum_{i=1}^{n} \lambda_i \cdot Y(\mathbf{u}_i) \tag{2.17}$$

where $Y^*(\mathbf{u})$ is the estimate, $Y(\mathbf{u}_i)$ are conditioning data $i = 1, \ldots, n$, $\mathbf{u}$ is the location being estimated, $\mathbf{u}_i$ are the locations of the conditioning data with associated weights, $\lambda_i$, $i = 1, \ldots, n$.

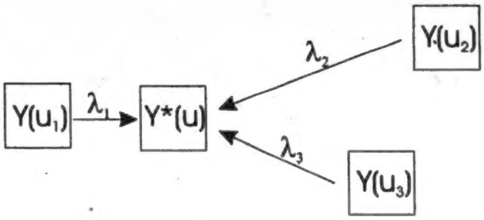

Figure 2.3: An example estimation problem. $Y$ is the RF with any nonstationary trend, $m(\mathbf{u})$, removed, $Y(\mathbf{u}) = Z(\mathbf{u}) - m(\mathbf{u})$.

The error variance, $\sigma_E^2$, may defined as the expected square difference between the estimate and the inaccessible true value, $E\{[Y^*(\mathbf{u})-Y(\mathbf{u})]^2\}$, with its expansion shown below.

$$\begin{aligned}
\sigma_E^2 &= E\{[Y^*(\mathbf{u})]^2\} - 2\cdot E\{Y^*(\mathbf{u})\cdot Y(\mathbf{u})\} + E\{[Y(\mathbf{u})]^2\} \qquad (2.18)\\
&= \sum_{i=1}^{n}\sum_{j=1}^{n}\lambda_i\lambda_j E\{Y(\mathbf{u}_i)\cdot Y(\mathbf{u}_j)\} - 2\cdot\sum_{i=1}^{n}\lambda_i E\{Y^*(\mathbf{u})\cdot Y(\mathbf{u}_i)\} + C(0)\\
&= \sum_{i=1}^{n}\sum_{j=1}^{n}\lambda_i\lambda_j C(\mathbf{u}_i,\mathbf{u}_j) - 2\cdot\sum_{i=1}^{n}\lambda_i C(\mathbf{u},\mathbf{u}_i) + C(0)
\end{aligned}$$

The optimum weights are those that minimize the error variance. These weights may be calculated by setting the partial derivative of the error variance to the weights, $\lambda_i$ to 0 as shown below.

$$\frac{\partial\left[\sum_{i=1}^{n}\sum_{j=1}^{n}\lambda_i\lambda_j C(\mathbf{u}_i,\mathbf{u}_j) - 2\cdot\sum_{i=1}^{n}\lambda_i C(\mathbf{u},\mathbf{u}_i) + C(0)\right]}{\partial\lambda_i} = 0\ , i = 1,\ldots,n \qquad (2.19)$$

The result is a solution for the weights, known as the simple kriging equations.

$$\sum_{j=1}^{n}\lambda_j C(\mathbf{u}_i,\mathbf{u}_j) = C(\mathbf{u},\mathbf{u}_i) \qquad (2.20)$$

The matrix representation is shown below.

$$\begin{bmatrix} C(\mathbf{u}_1,\mathbf{u}_1) & \cdots & C(\mathbf{u}_1,\mathbf{u}_n)\\ \vdots & \ddots & \vdots\\ C(\mathbf{u}_n,\mathbf{u}_1) & \cdots & C(\mathbf{u}_n,\mathbf{u}_n)\end{bmatrix}\cdot\begin{bmatrix}\lambda_1\\ \vdots\\ \lambda_n\end{bmatrix} = \begin{bmatrix} C(\mathbf{u},\mathbf{u}_1)\\ \vdots\\ C(\mathbf{u},\mathbf{u}_n)\end{bmatrix} \qquad (2.21)$$

The left matrix accounts for redundancy between the conditioning data and the right matrix accounts for the closeness to the location to be estimated. Note that the measure of 'closeness' or 'redundancy' is based on the covariance, a measure of geologic similarity and not Euclidian distance. The volumes of the location being estimated and conditioning data may be explicitly accounted for in the kriging system by replacing the covariance values, $C$, with volume average covariance values, $\overline{C}$. The volume average covariances represent the integration of the covariance function over the volumes considered (see Equation 2.22).

$$\overline{C}(V(\mathbf{u}), v(\mathbf{u}')) = \frac{1}{V \cdot v} \int_{V(\mathbf{u})} dy \int_{v(\mathbf{u}')} C(y - y\prime) dy\prime \tag{2.22}$$

where $\overline{C}(V(\mathbf{u}), v(\mathbf{u}'))$ is the average covariance between volume $V$ at location $\mathbf{u}$ and volume $v$ at location $\mathbf{u}'$. Additional discussion of the application of volume average covariances and semivariograms is presented in Section 2.2.10.

The solution to the simple kriging system is the weights $\lambda_i, i = 1, \ldots, n$. The simple kriging estimator is shown below.

$$z^*_{SK}(\mathbf{u}) - m(\mathbf{u}) = \sum_{i=1}^{n} \lambda_i [z(\mathbf{u}_i) - m(\mathbf{u}_i)] \tag{2.23}$$

where $z^*_{SK}$ is the simple kriging estimate, $i = 1, \ldots, n$ are the available data, $\lambda_i$ are the simple kriging weights, $Z(\mathbf{u}_i)$ are the data values and $m(\mathbf{u}_i)$ is the nonstationary trend component. The simple kriging variance expressed as:

$$\sigma^2_{SK} = \sigma^2 - \sum_{i=1}^{n} \lambda_i C(\mathbf{u}_i, \mathbf{u}) \tag{2.24}$$

The following are some additional properties of kriging.

1. A unique solution exists to the kriging system if the covariance function is positive definite.

2. The kriging estimate minimizes the error variance.

3. The kriging estimate is unbiased, $E\{Y(\mathbf{u})^* - Y(\mathbf{u})\} = 0$.

4. The kriging estimate is exact. At the precise conditioning location, $\mathbf{u}_i$, the weight $\lambda_i = 1$ and all other weights, $\lambda_j, j = 1, \ldots, n, i \neq j$ are equal to zero.

5. The kriging variance assumes homoscedasticity, since the kriging variance is independent of the kriging estimate. The impact of sample selection may be assessed prior to sampling.

Kriging is not intended for the construction of maps. While the kriging estimates individually are the best linear unbiased estimate, jointly they do not correctly represent the variability of the underlying phenomenon. Simulation may be applied to calculate maps that honor the conditioning data and the correct spatial structure.

### Sequential Gaussian Simulation

Sequential Gaussian simulation (`SGSIM`) is a commonly applied simulation algorithm available in GSLIB (Deutsch and Journel, 1998)[23]. `SGSIM` corrects for the smoothness of the kriging estimates through the addition of a random residual.

The stationary variance is $C(0) = \sigma^2$ and the variance of the kriging estimate is $Var\{Y^*(\mathbf{u})\} = C(0) - \sigma^2_{SK}$, where $\sigma^2_{SK}$ is the kriging variance; therefore, the missing variance is the kriging variance. The missing variance may be added back as a random residual, $R(\mathbf{u})$. The random residual has a mean of zero to maintain unbiasedness and a variance equal to the kriging variance.

$$Y_{simulation}(\mathbf{u}) = Y^*(\mathbf{u}) + R(\mathbf{u}) \qquad (2.25)$$

The simulation is conducted sequentially to ensure that the covariance is correct between simulated values, $Y_{simulation}(\mathbf{u}_\beta)$ where $\beta = 1, \ldots, n$ and there are $n$ simulated locations. Some of the important properties of sequential Gaussian simulation are discussed below (adapted from Deutsch, 2003[22]).

1. The global histogram is reproduced within ergodic fluctuations by back transformation after simulation.
2. The semivariogram in Gaussian space is reproduced within ergodic fluctuations.
3. Multiple equally likely to be drawn realizations are available by changing the random number seed. These realizations do not account for uncertainty within the input statistics. This uncertainty should be accounted for explicitly (Pyrcz et. al, 2004)[103].

4. The Gaussian distribution is a maximum entropy model (Journel and Alabert, 1988; Journel and Deutsch, 1993)[56, 58]. This results in maximum disorder beyond the semivariogram and maximum disorder of the extremes. This feature will remove connected features in high and low values. For example, this may result in the removal of potential conduits or barriers to flow in the model.

### Cosimulation

There are a variety of methods available for the cosimulation of multiple related variables. These methods reproduce the histogram and semivariogram of each variable and the cross relationship.

Cokriging is the application of kriging with multiple variables. For example, permeability may be estimated with permeability and porosity data available. The cokriging system of equations is similar to the simple kriging equations shown in Equation 2.21 with the addition of covariances between the primary and secondary variables and autocovariances for the secondary variables on the left hand side, weights for the secondary data and covariances between the estimated location and the secondary variable on the right hand side.

Full cokriging is based on the linear model of coregionalization (LMC) for direct and cross covariances. The equation for the cross-semivariogram is shown below.

$$\gamma_{Z,Y}(\mathbf{h}) = \frac{1}{2}E\{[Z(\mathbf{u}) - Z(\mathbf{u}+\mathbf{h})] \cdot [Y(\mathbf{u}) - Y(\mathbf{u}+\mathbf{h})]\} \qquad (2.26)$$

where $\gamma_{Z,Y}(\mathbf{h})$ is the cross-semivariogram between variables $Z$ and $Y$ for lag vector $\mathbf{h}$.

The LMC assumes that each variable is a combination of a set of common components. Positive definite semivariogram models for the direct and cross for each variable are constrained by the LMC. Full cokriging is not usually used due to (**1**) difficulties in the inference of a LMC model, (**2**) the restrictions of the LMC and (**3**) there is usually no real advantage to considering all secondary data because of screening.

Collocated cokriging is based on assumption that only the collocated secondary data is relevant. If only collocated secondary data are considered then the cross relationship may be fully characterized by the linear correlation coefficient, $\rho_{s,p}(0)$ where the cross semivariogram is assumed as follows.

$$\gamma_{p,s}(\mathbf{h}) = \sqrt{\frac{\sigma_s^2}{\sigma_p^2}} \cdot \rho_{p,s}(0) \cdot \gamma_{p,p}(\mathbf{h}) \tag{2.27}$$

where $\gamma_{s,p}(\mathbf{h})$ is the cross semivariogram between the primary and secondary variable, $\sigma_s^2$ is the variance of the secondary variable, $\sigma_p^2$ is the variance of the primary variable and $\rho_{s,p}(0)$ is the correlation between the primary and secondary variable and $\gamma_{p,p}(\mathbf{h})$ is the direct semivariogram of the primary variable.

Cosimulation by collocated cokriging is commonly applied due to its simplicity. Neither of the previous methods is able to reproduce complicated multivariate relationships, such as nonlinear features and constraints.

Stepwise conditional transform has been reintroduced by Leuangthong (2003)[61]. The stepwise transformation removes correlation between variables and enables the independent simulation of each variable. A back transform is applied to replace the original correlation after simulation. This algorithm allows for the reproduction of complicated multivariate relationships.

### Gaussian Truncated Simulation

Gaussian truncated simulation (`GTSIM`) represents an extension of continuous variable simulation to categorical variables (Matheron et al., 1987)[70]. The categorical variable is represented by a truncated continuous RF, where the thresholds are assigned based on the probability of each category and the ordering is based on the interaction of the categories in the underlying phenomenon. Categorical data are transformed to continuous values before simulation. Truncation is applied as a post processing step. Complicated interrelations and varying spatial continuities between categories may be reproduced through the application of pluri-Gaussian truncated simulation. In pluri-Gaussian truncated simulation. Multiple variables are cosimulated and the multivariate distribution is truncated.

A strength of `GTSIM` is that ordering relationships may be reproduced. Facies ordering is a common feature in many depositional settings. For example, a prograding coastal system tract would demonstrate a natural transition from marine to non-marine facies (see Figure 2.4).

A method of modeling large scale facies associations in shoreface reservoirs with `GTSIM` has been presented by MacDonald and Aasen (1995)[67]. Their proposed model reproduces facies ordering and the integrated effect of base level changes

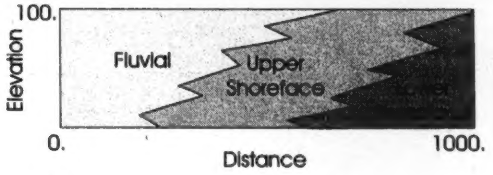

Figure 2.4: An schematic of a prograding coastal setting where facies ordering is an important feature. Facies include from fluvial sands, upper shoreface sands and lower shoreface sands. Units are in meters.

on bivariate distribution of aggradation and progradation angles. Their method illustrates the integration of a variety of sequence stratigraphic concepts into a stochastic modeling framework.

### Indicator Kriging and Simulation

As mentioned before, the multivariate Gaussian model is a maximum entropy model and this can be undesirable. The indicator techniques can be applied to control the spatial correlation of the extremes with the limitation that only linear features may be captured by the two-point indicator semivariograms. Also, the indicator techniques are well suited to model categorical variables with unique correlation structures. The following is a brief review of the indicator kriging and sequential indicator simulation methods based on Deutsch (2002), Deutsch and Journel (1997), Goovaerts (1997)[21, 23, 43].

The indicator approach does not make any assumptions with regard to the character of the local conditional cumulative distribution functions (ccdf). The continuous ccdf or categorical pdf is estimated directly at a set of thresholds or categories $k = 1, \ldots, K$.

$$F(\mathbf{u}; z_k) = Prob\{Z(\mathbf{u}) \leq z_k\} \tag{2.28}$$

$$F(\mathbf{u}; z_k) = Prob\{Z(\mathbf{u}) \in z_k\} \tag{2.29}$$

The weights for the indicator estimate are found by solving a simple kriging system as shown below for each threshold or category.

$$\sum_{j=1}^{n} C(\mathbf{u}_i, \mathbf{u}_j; z_k) \cdot \lambda_j = C(\mathbf{u}, \mathbf{u}_i; z_k) \tag{2.30}$$

where $\mathbf{u}$ is the location to be estimated, $\mathbf{u}_i$ and $\mathbf{u}_j$ are the locations of conditioning with two indices and $\lambda_j$ are the simple kriging weights and $z_k$ is the associated threshold. The matrix representation is shown below (compare to the simple kriging system in Equation 2.21).

$$\begin{bmatrix} C(\mathbf{u}_1, \mathbf{u}_1; z_k) & \cdots & C(\mathbf{u}_1, \mathbf{u}_n; z_k) \\ \vdots & \ddots & \vdots \\ C(\mathbf{u}_n, \mathbf{u}_1; z_k) & \cdots & C(\mathbf{u}_n, \mathbf{u}_n; z_k) \end{bmatrix} \cdot \begin{bmatrix} \lambda_1 \\ \vdots \\ \lambda_n \end{bmatrix} = \begin{bmatrix} C(\mathbf{u}, \mathbf{u}_1; z_k) \\ \vdots \\ C(\mathbf{u}, \mathbf{u}_n; z_k) \end{bmatrix} \tag{2.31}$$

The indicator kriging estimator with a stationary mean of the indicator RF may be expressed as follows.

$$i(\mathbf{u}; z_k)^*_{SK} = \sum_{\alpha=1}^{n} \lambda_\alpha(\mathbf{u}; z_k) i(u_\alpha; z_k) + \left[1 - \sum_{\alpha=1}^{n} \lambda_\alpha(\mathbf{u}; z_k)\right] F(z_k) \tag{2.32}$$

where $F(z_k)$ is the global cdf or pdf value for the threshold or category $z_k$.

The probability for each threshold or category is estimated separately; therefore, there is no constraint to enforce order relations. Order relations are the requirement for a continuous ccdf to be monotonically increasing and for a categorical pdf to sum to 1.0 and exist between 0.0 and 1.0. The former issue is corrected by taking the average of a forward and reverse correction and the latter is corrected by standardization (Deutsch and Journel, 1998)[23].

Sequential indicator simulation (`SISIM`) proceeds by applying indicator kriging to directly estimate the local ccdf, then a value is drawn and used as conditioning for the simulation of subsequent locations.

### Example Semivariogram Based Geostatistical Work Flow

The following is a generic description of the common geostatistical modeling work flow. Actual work flows will vary in complexity and may include a hierarchy of work flows depending on the goals of the study and the information available. This discussion is brief; Deutsch (2002)[21] provides detailed discussion on geostatistical work flows and trade craft.

The geostatistical work flow begins with data analysis. A large component of the study includes data cleaning. The data scale is reconciled and coördinates are transformed to account for stratigraphic correlation style. The primary data is often hard well data. Large scale information may be available from well tests and seismic. Analogue information may be available from similar settings and outcrops and knowledge concerning the geologic setting. Univariate distributions are checked for form and outliers. Representativeness is improved with declustering and debiasing. Bivariate and multivariate relationships between variables and variable constraints may be checked and characterized. The spatial behavior of the data, trends and spatial correlation styles, are characterized. Goovaerts (1997, pp. 9-56) and Isaaks and Srivastava (1989, pp. 10-65)[43, 51] provide a detailed description of the techniques and tools commonly applied in data analysis.

The coordinate system may be rotated to the principal correlation directions (major horizontal, minor horizontal and vertical) and the data coordinates may be transformed based on a stratigraphic correlation style (e.g. onlap, proportional and truncation) (Deutsch, 2002, pp. 85-92)[21].

Semivariograms are modeled to characterize the spatial behavior of facies categories and reservoir properties in the translated/rotated coordinate system. Positive definite semivariogram models are constructed with the aid of the experimental semivariograms, analogous sites, and geologic knowledge. Deutsch and Journel (1998, pp, 24-32) and Isaaks and Srivastava (1989, pp. 369-399)[23, 51] describe procedures for semivariogram modeling. These models provide a valid measure of correlation for any direction and distance.

Facies may be modeled by `SISIM`, that honors the facies categories at the data locations, the global proportions, vertical and areal trends and the spatial correlation as characterized by indicator semivariogram models. Reservoir properties are modeled on a by-facies basis with `SGSIM` or `SISIM` that honors the continuous properties at the data locations, the global distributions and the spatial correlation as characterized by semivariogram models. The reservoir properties are merged together into a single model based on the facies models. Multiple facies and property realizations are applied as a measure of local and global uncertainty. These simulation work flows are described in Deutsch (2002, pp. 21-26)[21].

This common work flow leads to models that honor the conditioning data, univariate distributions and trends and spatial correlation as quantified by two-point semivariograms. Multiple-point statistics beyond the two-point statistic, the semivariogram, are not explicitly modeled and are determined by implicit model assumptions (e.g. multiGaussian maximum entropy model). Some genetic features may be captured indirectly by facies and property trend models, although in general these common methods are not easily adapted to reproduce complicated morphologic features.

### 2.2.6 Training Image Based Multiple-point Geostatistics

Conventional geostatistics is limited to two-point statistics. These techniques are unable to directly reproduce complicated geometries and curvilinear features that are often present in reservoir geology. The omission of these features may result in numerical reservoir models that misrepresent the reservoir response qualified by flow simulation. For example, effective permeability is very sensitive to connectivity of extremes and this is not limited to linear features. This limitation has motivated research in geostatistical methods that integrate multiple-point statistics beyond the semivariogram.

The development of geostatistical algorithms that explicitly account for multiple-point statistics (MPS) is not new. These techniques were pioneered by Journel and Alabert (1989)[57] and were applied in simulated annealing by Deutsch (1992)[19]. Strebelle (2002)[120] provides a review of the evolution of these multiple-point geostatistical algorithms and a proposed efficient noniterative algorithm called single normal equation simulation (`SNESIM`).

A multiple point statistic is defined by a template of $n$-points. An example multiple-point template is shown in Figure 2.5. The conditional probabilities of an outcome at the first template location $z(\mathbf{h}_1)$ given all possible outcomes at the other locations within the template are calculated. This is accomplished by translating this template over the available conditioning data and counting the frequency of all configuration $z_1(\mathbf{h}_1), \ldots, z_n(\mathbf{h}_n)$. This conditional probability is stated below.

$$Prob\{z_1(\mathbf{h}_1)|z_2(\mathbf{h}_2), ..., z_n(\mathbf{h}_n)\} \tag{2.33}$$

where $\mathbf{h}_1$ is assumed as a null vector and $\mathbf{h}_2, \ldots, \mathbf{h}_n$ are vectors that define the template configuration. $z_1(\mathbf{h}_1), \ldots, z_n(\mathbf{h}_n)$ are the outcomes at each template location.

Inference of consistent or positive definite multiple-point statistics is not possi-

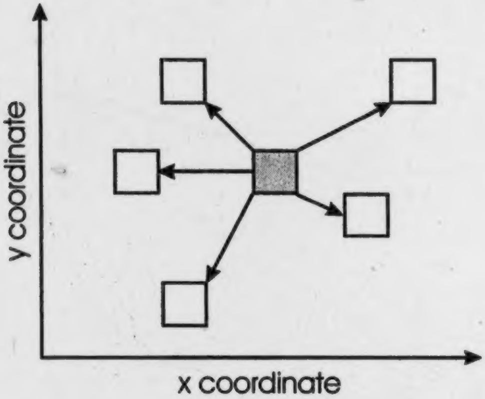

Figure 2.5: An example six point template for the calculation of multiple point statistics.

ble given the sparseness of conditioning in most practical settings. This is overcome by extracting n-point statistics from exhaustive training images that have the features that are expected in the actual phenomenon. These training images may be unconditional simulations or conceptual models.

Since the multiple-point statistics capture lower order statistics there is no need to explicitly model the semivariogram. The semivariogram and histogram are implicitly imported from the training image. The conditional probabilities assigned by this technique are analogous to those assigned by kriging if all the pertinent neighbouring locations are included in the search template

The size of the template determines the level of information extracted from the training image. The goal is to capture the essence of the geology and not to transport idiosyncrasies unique to the training image (Strebelle and Journel, 2000)[121]. Also the available memory becomes a limiting factor since for a template with n-points and $K$ categories $K^n$ conditional categories are stored (see Chapter 5.1 for further discussion on training images).

The simultaneous characterization of small and large scale features would require a large template. The required number of template cells is reduced by working with the multiple grids concept (Tran, 1994)[127]. Templates for each scale are applied to the training image. If features vary greatly between scales, a different training image may be needed at each scale, although this may introduce inconsistency.

Currently applied MPS techniques are limited to categorical variables. It would be difficult to infer the full continuous n-point distributions. A suggested alternative for continuous variables is to bin the continuous property and then to simulate within each bin a posteriori (Strebelle and Journel, 2000)[121].

There are limitations associated with the approach. MPS slavishly attempts to reproduce features from the training image that may be different from the site being characterized. The choice of training image and the size of the template are difficult decisions that have a large impact on the resulting models. This results in the need for sensitivity analysis.

The 3-D geologic morphologies that can be handled by this technique are limited. Multiple-point statistics may reproduce curvilinear features, but not the complicated geometries and interrelationships reproduced in surface and object based models (see Sections 2.2.7 and 2.2.8 respectively).

#### Multiple Point Correction

An engineering correction for the inability of two-point statistics to capture nonlinear connectivity was proposed by Deutsch and Gringarten (2000)[44]. This method relies on accounting for the non-linear connectivity/continuity by increasing the semivariogram range. This method results in greater connectivity and a practical engineering match for flow simulation results.

The corrected semivariogram range is found by calibration based on dispersion variances calculated over various support sizes. Calibration is accomplished by correcting the semivariogram such that the final model dispersion variances closely match the dispersion variances calculated from the reference image. This method is suitable for improving the performance of traditional semivariogram based models, although the resulting realizations do not integrate nonlinear heterogeneity.

### 2.2.7 Surface Based Models

Surface based models have recently been introduced. These models are generated by simulating stratigraphically or sedimentologically significant surfaces and then simulating facies and properties between simulated surfaces.

Xie and Deutsch (2000)[140] addressed methods for stochastically generating surfaces that honor the available data, rules based on volume filling and types of stratal termination and the reproduction of within unit trends. These methods

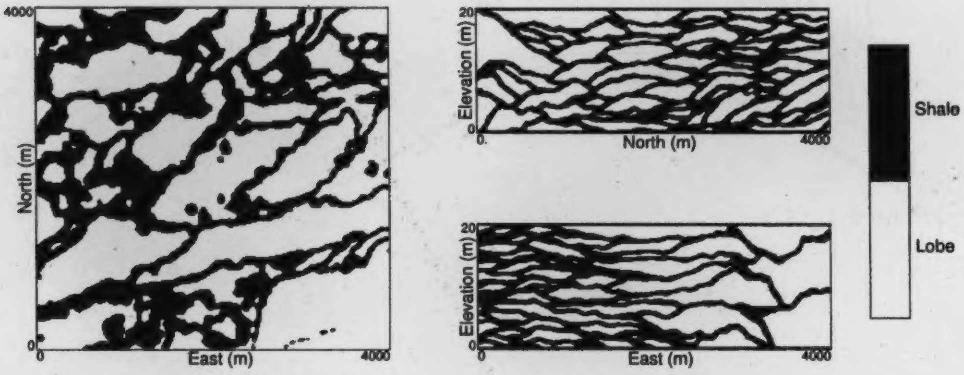

Figure 2.6: An example surface based simulation. Cross sections have ×75 vertical exaggeration. Note a stratigraphic transformation was applied to set a constant thickness. The actual feature thins towards the southeast.

have been shown to generate surfaces that mimic the appearance of actual geologic bounding surfaces in an example outcrop with tabular units.

The surfaces are based on a geometric template determined from the geologic setting. The surfaces are stochastically positioned and then neighbouring conditioning is checked. If the mismatch is below a tolerance the surface is corrected to honor the data and if the mismatch is too large the surface is discarded. Surfaces are generated until the volume of interest is filled (see Figure 2.6 for an example surface based simulation).

Parameterized trends are modeled from the available geologic information. These trends may be set to conform to the stochastic surfaces. The residuals are simulated and then added to the trend to realizations.

The application of surface based models has been extended in this dissertation to model general tabular stratigraphy with gradational and erosional surfaces and compensational cycles in a distal turbidite lobe. The associated algorithm allows for the reproduction of surface geometries, stacking patterns and hierarchical trends. This work is developed in Chapter 4.

### 2.2.8 Object Based Models

Object based models are very efficient at reproducing distinct geologic geometries, such as filled fluvial channels and turbidite lobes systems. The object based methods

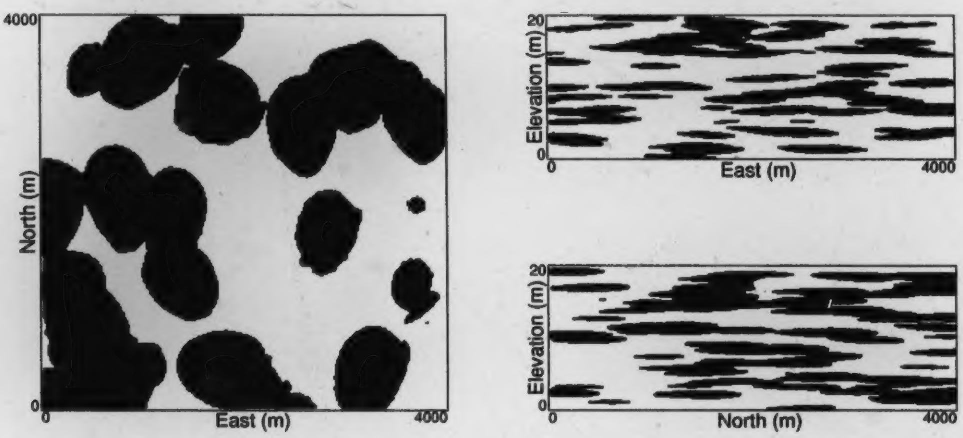

Figure 2.7: An example Possion point process with lobe primary grains.

simulate the RF on a by-object basis. Key properties of these objects are (**1**) they mimic geologic morphologies and (**2**) they are parameterized so that they may be scaled, translated and rotated as required by the applied algorithm and (**3**) the objects are positioned in the AOI often without a direct connection to sequence.

Object based methods are closely related to stochastic geometry (Stoyan et al, 1987)[119]. The simplest object based models are based on Poisson point processes and primary grains. A Poisson point process with or without stationary intensity may be applied to position germs. Primary grains, or parameterized objects, are then positioned relative to the germs (see Figure 2.7 for an example). More complicated object based models are now discussed.

Interest in North Sea fluvial reservoirs led to the development of object based models for fluvial facies and geometries (Clemensten et al., 1990; Gundesø and Egeland, 1990; Omre, 1992; Stanley et al., 1990)[14, 45, 84, 114]. This initial work has been further refined by others (Georgsen and Omre, 1993; Hatløy, 1995; Hove et al., 1992; Tjelmeland and Omre, 1993; Tyler et al., 1992)[40, 47, 49, 126, 128, 129].

`FLUVSIM` (Deutsch and Wang, 1996; Deutsch and Tran, 2002)[28, 25] is a convenient public domain fluvial object based algorithm. The algorithm generates stochastic channel streamlines and fits stochastic channel and related architectural element geometries to these streamlines. The `FLUVSIM` geologic model is based on ribbon sandbodies from typically low net-to-gross systems with primary reservoir quality encountered in sinuous to straight channels and secondary reservoir rock

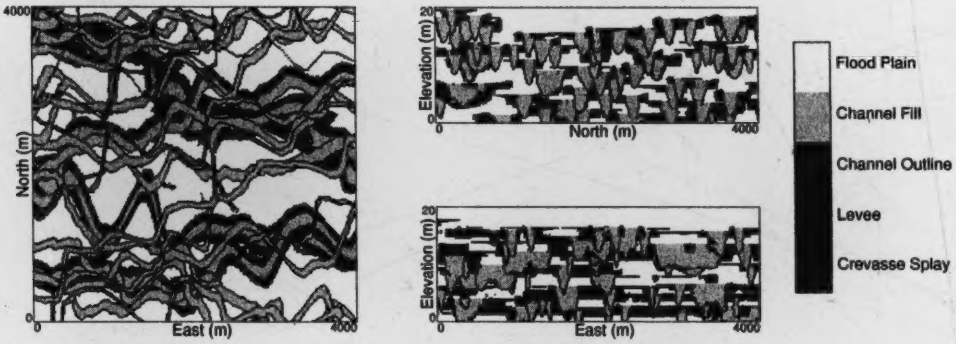

Figure 2.8: An example `FLUVSIM` object based fluvial model with channels, levees and crevasse splays

based on levees and crevasse splays embedded in overbank fines (Galloway and Hobday, 1996; Miall, 1996)[39, 73].

The algorithm initially performs a calibration to determine the scale of the levee and crevasse splay required to approximately match the prior architectural element proportions. The channels and associated elements are added randomly until the global NTG ratio is met. Simulated annealing (see Section 2.2.9) is applied to honor global, vertical and areal trends and to match conditioning data.

Algorithms such as `FLUVSIM` are excellent at building stochastic fluvial ribbon models, but are sometimes considered inefficient at honoring a realistic level of conditioning. Given the complicated geometry of the objects and the possible intersection with multiple wells, convergence may be CPU intensive. Simulated annealing does not provide prior information on the rate of convergence and the determination of optimum anneal schedule is currently a difficult problem (see Section 2.2.9).

These difficulties in conditioning spurred research in direct object modeling. Visuer et al. (1998)[132] and Shmaryan and Deutsch (1999)[111] developed methods to directly simulate object based fluvial models. The algorithms segment the well data into unique channel and nonchannel facies and then fit channels through the segments. Additional wells that are close to a placed channel may be included. The channels are parameterized (Wietzerbin and Mallet, 1993)[138] by a set sections fit along the center line. The Shmaryan method proceeds from the top down and is able to reproduce vertical and horizontal proportions. Channels are added until the vertical proportion is met. Artificial sand intervals are added to force channels to honor areal trends. Visuer (2001)[131] increased the object complexity with the addition of simulated piecewise linear avulsion surfaces which constrain the channel dip and the channel spacing and overlap. Further development in object based fluvial models are presented in Chapter 3.

### 2.2.9 Simulated Annealing

Simulated annealing (Deutsch, 1992; Deutsch and Journel, 1998)[19, 23] is an iterative optimization algorithm. An initial model is seeded, an objective function is calculated and random perturbations are applied. Perturbations that reduce the objective function are accepted and perturbations that increase the objective function are conditionally accepted with a probability based on a annealing schedule. Each of these steps are discussed in greater detail.

The model is initialized. In the pixel based paradigm the initial image is white noise with the correct continuous or categorical global pdf. In the object based paradigm, objects are randomly positioned until the global pdf is matched. It is intuitive that an image closer to optimum would reduce the CPU intensity of the algorithm, but a high initial temperature is required to avoid local optimal solutions and this high temperature removes initial features (Deutsch and Journel, 1998)[23].

The objective function quantifies the level of mismatch in the model statistics. Simulated annealing is very flexible since any statistic may be incorporated into the objective function. The objective function takes the following form.

$$O = \sum_{i=1}^{N} \omega_i O_i \tag{2.34}$$

where $N$ is the number of statistics applied in the objective function, $\omega_i$ is the weight and $O_i$ is the objective value from the $i^{th}$ statistic. The objective values is the mismatch between the target and the current values of a statistic. The calculation of the objective function for a histogram and semivariogram are demonstrated below.

$$O_{histogram} = \sum_{i=1}^{n_q} |F_Z^*(q_i) - F_Z(q_i)| \tag{2.35}$$

where $n_q$ is the number of quantiles considered, $F^*$ is the current cdf and $F$ is the target cdf.

$$O_{variogram} = \sum_{i=1}^{n_{\mathbf{h}}} |\gamma^{*}(\mathbf{h}_i) - \gamma(\mathbf{h}_i)| \qquad (2.36)$$

where $n_{\mathbf{h}}$ is the number of lags considered, $\gamma^{*}$ is the current semivariogram and $\gamma$ is the target variogram.

In the pixel based paradigm the perturbations are commonly random swaps of pixels. This ensures that the global distribution is preserved. In object based techniques the perturbations may include translations, rotations, scaling, removal and addition of objects. For example, the FLUVSIM algorithm applies the following perturbations; (**1**) replace a channel, (**2**) add a channel, (**3**) remove a channel and (**4**) shift a channel to honor a particular well interval (Deutsch and Tran, 2002).

The probability of accepting a perturbation that increases the objective function is determined from the Boltzmann equation for Gibbs free energy, which is a function of temperature.

$$P\{accept\} = \begin{cases} 1 & if O_{new} \leq O_{old} \\ e^{\frac{O_{old}-O_{new}}{t}} & otherwise \end{cases} \qquad (2.37)$$

where $t$ is the temperature.

Analogous to metallurgy, the annealing schedule is a schedule of temperatures applied to the particular optimization problem. The common practice is to begin with a high temperature and to decrease the temperature over time. Too fast of a cooling will lock the model in a local minimum and too slow of a cooling will increase the CPU intensity of the algorithm.

The selection of an efficient annealing schedule is a implementation difficulty to for simulated annealing. There is currently no technique for a priori precise determination of the appropriate schedule and the number of iterations to converge. Deutsch (1992)[19] indicated that there is a critical temperature at which convergence may be more rapid and Deutsch and Norrena (2000)[82] demonstrated the application of critical temperatures to improve the rate of convergence.

The recent increase in CPU speed has made simulated annealing more appealing. The flexibility of simulated annealing may be useful in the integration of geologic information into stochastic models.

### 2.2.10 Volume Variance Relations

Detailed reviews of volume variance relations are available in many geostatistical references including Deutsch (2002), Deutsch (2003), Deutsch and Journel (1998), Goovaerts (1997), Issaks and Srivastava (1989) and Journel and Huijbregts (1978) [21, 22, 23, 43, 51, 59]. Variance is a function of sample volume. As volume increases the variance decreases; it is easier to predict the average porosity over a large volume than over a small volume of a reservoir.

Volumes associated with estimation and simulation must be considered. This relationship may be quantified with the application of volume averaged covariance (see Equations 2.22) and semivariogram values.

Dispersion variance is a general form of variance that accounts for size support. This measure may be applied to characterize the volume variance relation of an RF for change of support size. The dispersion variance of volumes $v$ within the larger volume $V$ is written as:

$$D^2(v, V) = E\{[z_i - m_i]^2\} \tag{2.38}$$

where $z_i$ is at support size $v$ and $m_i$ is at support size $V$. If $v$ is at point support, $\cdot$, then the dispersion variance is the variance.

$$D^2(\cdot, V) = \sigma^2 \tag{2.39}$$

The dispersion variance may be represented in terms of average covariance and semivariogram values as follows:

$$D^2(v, V) = \overline{C}(v, v) - \overline{C}(V, V) \tag{2.40}$$

$$D^2(v, V) = \overline{\gamma}(V, V) - \overline{\gamma}(v, v) \tag{2.41}$$

Dispersion variances are additive. This property may be utilized for change of support. This is characterized by Krige's relation.

$$D^2(v, A) = D^2(v, V) + D^2(V, A) \tag{2.42}$$

where the dispersion variance of data with support $v$ within $A$ is equal to the dispersion variance of support size $v$ with $V$ added to the dispersion variance of support size $V$ within $A$. For example, if the support size was changed from $v$ to $V$ the variance of $V$ with $A$ may be calculated. The variance at the current support size is $D^2(v, A)$ and the dispersion variance between support sizes $v$ and $V$ may be found with Equation 2.40 or 2.41.

### Power Law Averaging

Power law averaging may be applied to scale up properties that do not average linearly (Deutsch et al., 2002)[21]. Specific methodologies for scaling up small scale permeability measurements have been discussed by Corbett (1993)[16]. The following review is based on Deutsch et al., (2002)[21]. Implicit to linear estimation (see Equation 2.17) and average covariance values (see Equation 2.22) is the assumption of arithmetic averaging, that is, the variable averages linearly. Power law averaging effectively transforms the directional permeability to a variable that averages linearly. The general formula for power law averaging of the continuous variable $K$ is written:

$$K_{eff} = \left[ \frac{1}{v} \int_{v} k(\mathbf{u})^{\omega} d\mathbf{u} \right]^{\frac{1}{\omega}} \tag{2.43}$$

where $v$ is the volume over which the average is calculated, $k(\mathbf{u})$ is the permeability at location $\mathbf{u}$ within the volume, and $\omega$ is an exponent of averaging. The effective permeability, $K_{eff}$, of a 3-D network of blocks must take a value between the harmonic and arithmetic average of the constituent permeabilities, depending on their spatial arrangement. The lower-bound harmonic average can be seen as a power average with $\omega$ = -1; this is representative of flowing through a series of alternating permeability layers. The upper-bound arithmetic average can be seen as a power average with $= +1$; this represents parallel flow through alternating permeability layers. The geometric average is obtained at the limit when $\omega = 0$.

The averaging power for each site must be calibrated. The calibration process for a single geological model is straightforward. The numerical model of small-scale permeabilities is subjected to flow simulation with specified boundary conditions to obtain the true effective permeabilities: $K_X$, $K_Y$, and $K_Z$. The directional averaging exponents, $\omega_X$, $\omega_Y$ and $\omega_Z$, are chosen such that the power-law average matches the flow simulation results.

To account for uncertainty and fluctuations in the geological models, the calibration process is repeated for multiple realizations of the same geological model. Once an assemblage of directional values have been calculated, the resulting distributions can be checked. The mean value provides a single estimate for $\omega$ in a given direction, and the distribution provides the uncertainty in $\omega$ for the geological model.

### 2.2.11 Nonstationary Statistics

Nonstationary statistics have been applied to conventional geostatistical algorithms in order to integrate complicated and nonlinear features. Simple kriging with the removal of a nonstationary trend component is commonly applied in geostatistical studies. Ordinary kriging (OK) and universal kriging have a limited capability to automatically fit trends.

A variety of approaches have been applied to further utilize nonstationary statistics. Complicated surface anchored trend models which model nonstationary means have been demonstrated by Xie and Deutsch (2000)[140]. Nonstationary correlations have been applied to nickel laterite deposits by Lyall and Deutsch (2000)[66]. Nonstationary semivariogram parameters (directions and ranges) have been demonstrated by Xu (1996)[142]. Although, it is difficult to calculate a nonstationary semivariogram without a training image and there are theoretical challenges in modeling the interdependent direction angles (azimuth, dip and rake).

## 2.3 Advanced Geostatistical Models

An alternative approach to the traditional geologic and geostatistical methodologies is to focus on synthesizing complicated geometries and interrelationships in a geostatistical framework. Sedimentological processes are not directly modeled, but the resulting characteristic patterns are integrated into stochastic models.

Geostatistical methods such as object-based, surface-based and training image based MPS offer excellent opportunities integrated geologic information in a flexible manner and to constrain the final models to conditioning such as hard well data, trends and global distributions. These models are typically not dynamic, although some limited dynamic processes are introduced and developed in this dissertation. This includes compensational cycles in Chapter 4 and the bank retreat meander operation in Chapter 3.

This dissertation includes; (**1**) advanced geostatistical algorithms for the simulation of characteristic architectural element geometries tailored to fluvial and deepwater depositional settings and conditioning (**2**) proposed methods and work flows with demonstrations and supplemental utilities and (**3**) building blocks for geostatistical simulation to unstructured grids.

# Chapter 3

# Fluvial Reservoir Models

Fluvial deposits are of interest in resource exploration. Hydraulic processes result in the sorting, concentration and preservation of economic minerals and good quality reservoir sands in characteristic patterns. These patterns should be accounted for in stochastic models for improved resource modeling.

This chapter focuses on the construction of fluvial reservoir models. Section 3.1 provides a brief review of the architectural element approach to characterizing fluvial depositional systems, fluvial reservoir types and fluvial sequence stratigraphy. Section 3.2 proposes the streamline based simulation technique for the construction of fluvial stochastic models. This described algorithm applies a flexible suite of building blocks. Section 3.4 presents a methodology for updating streamline based models to honor local conditioning. This method is demonstrated with a conditional streamline based model algorithm. Section 3.5 introduces the application of the streamline based model for the calculation of stochastic inclined heterolithic strata models. This model may be applied to assess the impact of heterogeneity related to the complicated geometries and trends in inclined heterolithic strata sets.

## 3.1 Fluvial Reservoirs

Fluvial depositional settings host major petroleum reserves, some major fields include Prudhoe Bay in Alaska, Bren in the North Sea and Daqing in China. Fluvial processes result in the deposition of good quality reservoir sands with characteristic geometries. The importance and predictibility of fluvial environments have made this setting a prime target of research. Section 2.2.8 reviewed the development of object based methods. Much of this work has been focused on fluvial reservoirs.

### 3.1.1 Lithofacies and Architectural Elements

A wealth of qualitative information on fluvial sedimentology is available. This includes general information on potential geometries and features within alluvial sediments. Hydraulic and geomorphological studies provide a variety of empirical relationships between gradient, depth of the channel, flow velocity, types of channel bedforms and sinuosity. This information is based on flume experiments, surface and near surface surveys.

Sedimentological and sequence stratigraphy studies have revealed a catalog of characteristic geometries and interrelationships in the alluvial deposits. For example, alluvial fans have a proximal to distal trend of debris flow dominant to water-laid dominant and the lowstand and highstand systems tracks have lower rates of generation of accommodation and result in preserved amalgamated channel sediments. These studies are often based on outcrops or seismic studies.

Fluvial studies are conducted in a hierarchical fashion. The lithofacies are identified. Then, the process-related assemblages of lithofacies, architectural elements, are identified and their geometries and interrelationships are characterized.

Lithofacies are classified based on bedding, grain size, texture and sedimentary structures. Miall (1996, p. 79)[73] has proposed a lithofacies scheme for fluvial deposits. This scheme includes facies such as matrix supported massive gravel (Gmm), and sand, fine to very coarse may be pebbly (St). This fluvial lithofacies scheme is not intended as an exhaustive list and other types may be added to fit a specific site.

Fluvial architectural elements may be classified based on the nature of bounding surfaces, external geometry, scale, lithology and internal geometry (Miall, 1985)[72]. Architectural elements are generally larger than individual facies units and are smaller than a channel fill (Miall, 1996, p. 89)[73]. They include lateral accretion, crevasse splays and down stream accretion deposits. Miall's (1996, p. 93)[73] proposed list of fluvial architectural elements is included in Table 3.1.

Interpretation of architectural elements is more quantitative than traditional lithofacies methods. Architectural studies consider the processes and the resulting 3-D architectures. The identification of large scale geometries requires good exposure and sufficient data, yet their interpretation is more diagnostic of fluvial processes

| Architectural Element | Symbol | Geometry |
|---|---|---|
| Channel Fill | CH | Finger, Lens or Sheet |
| Gravel Bars and bedforms | GB | Lens or Tabular |
| Sandy Bedforms | SB | Lens or Tabular |
| Downstream-accretion macroform | DA | Lens |
| Lateral-accretion macroform | LA | Wedge |
| Scour Hollows | HO | Scoop |
| Sediment Gravity Flows | SG | Lobe or Sheet |
| Laminated Sand Sheet | LS | Sheet |
| Levee | LV | Wedge |
| Crevasse Channel | CR | Ribbon |
| Crevasse Splay | CS | Lens |
| Floodplain Fines | FF | Sheet |
| Abandoned Channel | FF(CH) | Ribbon |

Table 3.1: Architectural elements proposed for fluvial depositional settings summarized from Miall (1996)[73]. The first eight architectural elements (up to and including LS) are within channel fills. The remaining are architectural elements associated with the overbank environment.

and the resulting sediments than investigation of lithofacies alone.

### Scale and Fluvial Deposits

Channel dynamics and deposits have been studied at scales ranging over five orders of magnitude (Bristow and Best, 1993)[9]. A large degree of self similarity has been identified over these scales. This work assumes a nominal observation scale at the size of an individual architectural element. Current fluvial stochastic object based models and training images are constructed on a by architectural element basis (Deutsch and Tran, 2002; Deutsch and Wang, 1996; Viseur et al, 1998)[23, 28, 132].

## 3.1.2 Styles

The familiar geomorphologic classification of rivers (meandering, braided, anastomosed, and straight) is based only on geomorphology, and hence surface features; therefore, this scheme is unsuitable for sedimentological studies. Geomorphology does not uniquely constrain the preserved sediments. For example, two rivers of the same geomorphologic class may result in significantly different preserved sediments.

Modern fluvial studies classify fluvial systems (ancient or contemporary) based on process-related *fluvial styles*(Miall, 1996, p. 89)[73]. For each fluvial style there are characteristic architectural elements and lithofacies relationships.

The fluvial styles classification is based on channel controls. These controls include discharge, channel slope and sediment load. These channel controls have a direct influence on the formation and migration of ripples and bedforms (see Figure 3.1) and thus on the formation and preservation of lithofacies and architectural elements.

This paradigm shift from geomorphological classes to fluvial styles recognizes a continuum of possible settings. In characterizing this continuum there is a compromise between coarse discretization with very few fluvial styles resulting in vague facies models and very fine discretization with each fluvial setting modeled as an unique system. The currently applied discretization of this continuum includes sixteen common fluvial styles. The fluvial styles method retains the flexibility to recognize intermediate cases that display characteristics of more than one of the fluvial styles.

The link between the ancient and contemporary examples remains weak. For

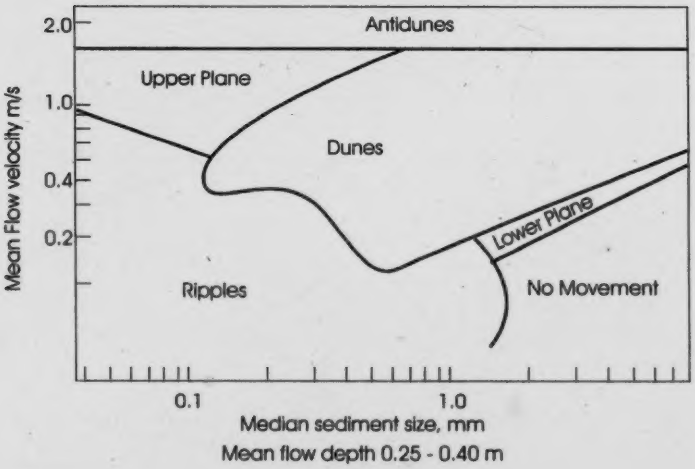

Figure 3.1: A schematic of mean flow velocity vs. median sediments size and the stability fields for difference sand beds (adapted from Miall, 1996)[73]

example there are some fluvial styles that are only found in the ancient record (Miall, 1996, p.202)[73]. The matter is complicated by the fact that the fluvial style may be transient with respect to time due to changes in the channel controls such as discharge, channel slope and sediment load.

### 3.1.3 Sequence Stratigraphy

Fluvial deposition and incision are dependent on the graded profile. A stream with this profile is at equilibrium, sediments are carried by a stream without aggradation or incision. The graded profile is a function of discharge and sediment load. These stream parameters are dependent on the competing allogenic controls of climate, eustasy and tectonics and autogenic controls such as channel migration and avulsion. Cycles in these controls result in significant sedimentological cycles (Brayshaw et al., 1996; Catuneanu, 2003; Emery and Myers, 1996; Miall, 2000)[8, 12, 35, 74]. These cycles are key to the pattern of heterogeneity in fluvial reservoirs.

Eustasy is a dominant control for distances up to a hundreds of kilometers inland (e.g. Mississippi River about 200 kilometers). Eustatic change results in the formation of systems tracts as discussed in Section 2.1.7. The destruction of accommodation during the falling stage system tract may result in a hiatus in the terrestrial sediment record. Subaerial unconformities result as river channels incise and paleosols form in the interfluve. During the transgressive system track accommodation space is rapidly created and this results in rapid aggradation of river channels and a high preservation potential for overbank environments and the potential for poorly connected reservoir sands.

During low and highstand system tracts, accommodation is generated at a lower rate than during the transgressive system tract. The net result is the lateral amalgamation of sandstone units and good reservoir sands (Catuneanu, 2003)[12]. The preservation potential is lower for overbank fines.

Source area denudation and coastal aggradation reduce fluvial gradients. Also, the highstand systems tract is often eroded by the formation of the subaerial unconformity during the falling stage systems tract. The net result is a sequence of fluvial deposits with a fining upward trend, decreasing channel amalgamation, decreasing reservoir quality bounded between unconformities. Progradation and retrogradation of the system may significantly affect trends.

### 3.1.4 Reservoir Types

The interplay between fluvial style and systems tract results in distinct fluvial reservoir styles. These types are (**1**) layer cake reservoirs, (**2**) jigsaw reservoirs and (**3**) labyrinth reservoirs (Weber and van Geuns, 1990)[137].

Layer cake reservoirs are amalgamated and laterally extensive. They are often associated with gravel dominated fluvial styles. These reservoirs are modeled as tabular units generally without barriers and baffles. Jigsaw reservoirs are composed of amalgamated channels with occasional low permeability barriers and baffles. These reservoirs generally form with gravel to sand dominated fluvial styles. Labyrinth reservoirs include complex associations of lenses and pods with limited connectivity. These reservoirs generally form in fine grained meandering and anastomosing styles.

Miall (1996)[73] identifies three types of fluvial reservoir style (**1**) paleo-valley shoestring reservoirs (PV type), (**2**) sheet reservoirs (SH type) and (**3**) channel and bar bodies (CB type). A single reservoir may demonstrate a mixture of these types.

The PV type is typified by a collection of many shoe string ribbon sand bodies. These channels may be straight to highly sinuous and may contain estuary components. These reservoirs may extend for tens of kilometers along the channels and a few kilometers across with a thickness of several tens of meters. Important examples include fields in the Mannville, Alberta and Blackwell, Texas. SH type reservoirs generally form gravel dominated fluvial styles. This style is analogous to the layer cake reservoir style. Important oil provinces include the North Viking Graben, the North Slope of Alaska. The CB type reservoirs include the jigsaw and labyrinth reservoir types discussed previously. Important examples include Citronelle field, Texas and Daqing field, China.

A flexible streamline baseb modeling technique is now presented and demonstrated. This technique may be applied to model any one of these fluvial reservoir styles and to better integrate information derived from fluvial style and systems tract. A major advantage of this algorithm is ability to reproduce complicated associations of architectural elements found in the CB type (e.g. LA element lenses, streamline bifurication and FF(CH) elements). While SH type reservoirs may express complicated associations, these features may not have a significant impact on reservoir response since SH type reservoirs are often very well connected (Miall, 1996)[73].

## 3.2 Streamline Based Stochastic Fluvial Model

Analysis of the fluvial styles (see Section 3.1.2) and systems tracts (see Section 3.1.3) demonstrates the great variety in fluvial deposition. Stochastic modeling of fluvial reservoirs requires tools that are more flexible than current algorithms to integrate information related to fluvial style and sequence stratigraphy framework.

A variety of approaches have been applied to construct iterative and non-iterative object-based stochastic models of meandering fluvial depositional systems. The techniques reviewed in Section 2.2.8 are well suited to PV reservoir types with low sinuosity but lack the ability to reproduce CB and SH reservoir types. A flexible building block approach is presented for the construction of PV, CB and SH fluvial reservoir type models and training images.

The basic building block of this model is the *streamline*. A streamline represents the central axis of a flow event. This concept is general and may represent confined or unconfined, fluvial or debris flows.

Groupings of streamlines form *streamline associations*. Streamline associations are interrelated by process. For example a streamline association may represent a braided stream or meander migration. Fluvial architectural elements are attached to streamlines and architectural element interrelationships are characterized by streamline associations. This is a logical technique for constructing fluvial models since all architectural elements are related to "flow events" and may be characterized by streamlines.

This building block methodology may be applied to generate a variety of fluvial models that may be applied as training images. In Section 3.3 a flexible unconditional algorithm is developed and in Section 3.4 a limited conditional algorithm is developed. These techniques are extended in Section 5.3 for the development of dynamic deepwater training images.

### 3.2.1 The 3-D Streamline

The direct application of a cubic spline function to represent the plan view projection of a fluvial flow event is severely limited. As a function, a spline represented as $f^s(x)$ may only have a single value for any value $x$. In graphical terms, a function may not curve back on itself. This precludes the direct use of a spline function (i.e. channel streamline characterized by locations $x$, $f^s(x)$) to characterize high sinuosity channel streamlines.

A solution is to fit a separate cubic spline to characterize each coordinate ($x$, $y$ and $z$) with respect to distance along the spline ($s$). This allows for high sinuosity streamlines to be modeled. A 2-D spline with a sinuosity of 1.4 is demonstrated in Figure 3.2.

The advantages of this streamline technique are: (**1**) continuous interpolation of streamline location in Cartesian coordinates at any location along the streamline, (**2**) relatively few parameters required to describe complicated curvilinear paths, (**3**) manipulation of splines is much more computationally efficient than modifying geometries and (**4**) other properties such as geometric parameters and longitudinal trends may be stored as continuous functions along the streamline. These issues will be discussed in further detail below.

Geometries attached to raster pathways are highly susceptible to discretization artifacts. These artifacts are often manifested in the form of lines radiating from the raster pathway in plan view and steps in the resulting geometry. It is difficult to calculate reliable streamline properties such as curvature from a raster pathway. The resulting values will not be continuous along the streamline path. A spline by construction is a continuous function. Since each coordinate is continuous the resulting composite streamline is continuous. Geometries may be attached to a 3-D

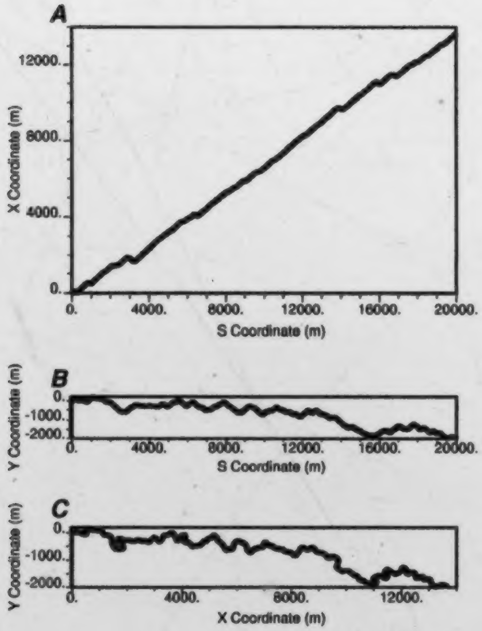

Figure 3.2: A demonstration of the construction of a 2-D spline by combining two splines. A - the $X$ spline relative to length along the spline $S$, B - the $Y$ spline relative to the length along the spline $S$ and C - the resulting 2-D spline in the $X-Y$ plane.

spline without discretization artifacts and are only limited in their resolution by the model grid.

Complicated 3-D spline-based streamlines require very few parameters. The parameters include a table of the $x$,$y$,$z$ and properties values and the first derivative of the splines representing $x$,$y$,$z$ and properties splines at each *streamline control node.* The number of control nodes required depends on the length and complexity of the spline. For problems with highly sinuous streamlines and lengths at reservoir scale less than a hundred control nodes are required to ensure well behaved splines. Complicated curvilinear geometries and interrelationships are represented with minimal storage requirements.

The 3-D spline allows for efficient calculation of the nearest location along a streamline to any location within the model volume. A nested search strategy is applied. First the nearest control node is located. Then finer intervals along the 3-D spline are checked for an interval of the streamline centered on the nearest control node.

It is more computationally efficient to modify 3-D streamlines than geometries. The control nodes of a 3-D spline may be freely translated, rotated or otherwise modified. The only requirement is that the first derivatives of the spline location parameters is recalculated after modification. This operation is very fast. The calculation of complicated geometries generally requires a high level of computational intensity or simplification. In the streamline based models the geometric construction is postponed to the end of the algorithm. This results in very fast calculation and manipulation of complicated geometric morphologies and associations.

Any properties may be attached to the 3-D spline and interpolated along the length of the spline. In the fluvial streamline based model, the channel width, local curvature, relative thalweg location and local azimuth are included in the 3-D spline. Other information including architectural element type and additional property trends may be included. These properties are calculated at the control nodes and then splines are fit as with the location parameters. A single streamline with all its associated properties is denoted as $\kappa_{i,j}$ where $j$ is the streamline index within a streamline association with index $i$.

### 3.2.2 Streamline Associations within Streamline Based Models

A streamline association is a grouping of interrelated 3-D splines. Streamline associations are characterized by their internal structure and interrelationship or stacking patterns. The internal structure is the relation of streamlines within the streamline association. The external structure is the interrelationship between streamline associations. Streamline associations may be tailored to reproduced features observed in each fluvial reservoir style.

Internal structures include streamline nesting, branching streamlines with common origin or streamlines representing steps in meander migration. Nesting may be reproduced with point processes introduced in Section 2.2.8. A technique for reproducing nested channels in deepwater is shown in Section 5.3.3. Branching and meandering associations are reproduced with streamline operations described in Section 3.2.3.

A variety of stacking patterns may exist in the fluvial depositional setting. Compensation is common in dispersive sedimentary environments such as proximal alluvial fans, vertical stacking with little migration is common in anastomosing reaches and interrelated channel belts often form in incised valleys. These patterns include important information with regard to the heterogeneity of a reservoir and should be included in fluvial models. Stochastic processes may be applied to mimic these features. A technique for reproducing compensational stacking in deepwater depositional systems is shown in Section 5.3.4.

### 3.2.3 Streamline Operations

A suite of streamline operations is presented. These operations allow for streamline based models to be constructed by the creation and modification of streamlines. These operations include (**1**) initialization, (**2**) avulsion, (**3**) aggradation and (**4**) migration.

#### Streamline Initialization

The streamline initialization operator is applied to generate an initial streamline or to represent channel avulsion proximal of the model area. Given the source and target locations and channel sinuosity this operator generates a realistic streamline from the source with a length (head to tail) equal to the spacing between the

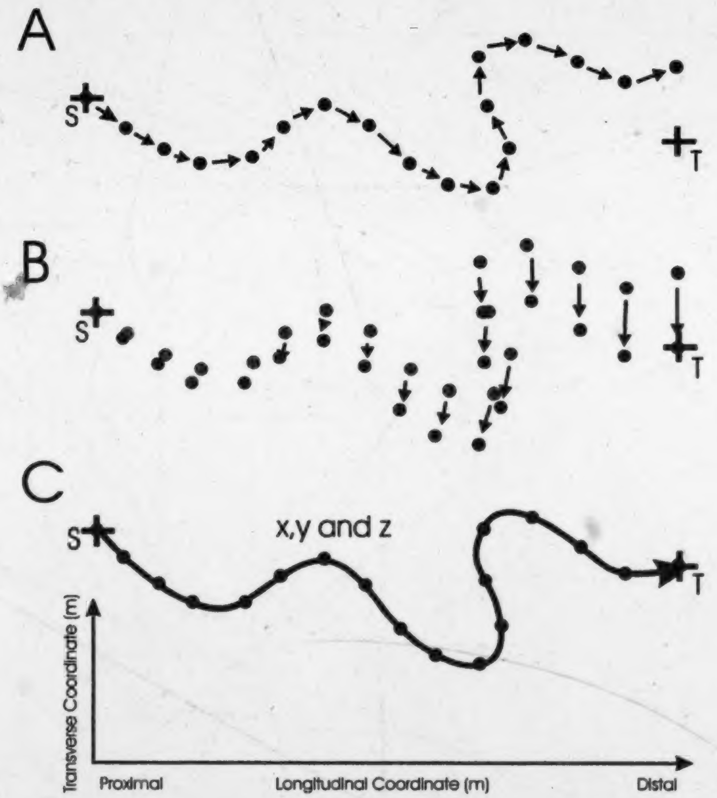

Figure 3.3: An illustration of the streamline initialization operator: A - apply process to generate realistic channel represented by regularly spaced control nodes, B - apply a smooth translation to correct to the target location and C - fit a 3-D spline. Note **S** is the source location and **T** is the target location.

source and target, then a smooth translation is applied to correct the location of the streamline control nodes to honor the target location (see Figure 3.3).

A model is required to represent channel streamline morphology. For example the `FLUVSIM` algorithm constructs streamlines as an one dimensional RF centered on a linear axis with a Gaussian distribution for displacement parameterized by amplitude and correlation length. There are a variety of methods available to generate meandering channel streamlines (Ferguson, 1976)[36]. Some methods are based on the regular wave-form models. The following is an example.

$$\phi(\mathbf{s}_i) = \omega \cdot sin\left(\frac{2\pi\mathbf{s}_i}{\lambda}\right) \quad i = 1, \ldots, n \tag{3.1}$$

where $\phi(\mathbf{s}_i)$ is the orientation of segment $i$, $\lambda$ is the wavelength, $\omega$ is the maximum deviation from principle channel direction and $\mathbf{s}_i$ is the specific segment of $n$ segments along the streamline.

This model is fully determined by wavelength and the maximum deviation terms that may be directly related to sinuosity. While this parametrization is straightforward, these models do not mimic actual river meanders. While hydraulic morphology does tend towards regularity, nonstationary in the host material and topography disrupt this regularity.

Streamlines may also be based on random walk models. These methods attempt to capture the irregularity of meandering streamlines by setting the segment orientation as a RV. The simple random walk model is shown below.

$$\phi(\mathbf{s}_i) = \phi(\mathbf{s}_{i-1}) + \varepsilon(\mathbf{s}_i) \tag{3.2}$$

where $\phi(\mathbf{s}_i)$ is the orientation of segment $i$, $\phi(\mathbf{s}_{i-1})$ is the orientation of segment $i$ and $\varepsilon(\mathbf{s}_i)$ is a disturbance value independently drawn from a distribution, often normally distributed $N(0, \sigma^2)$. This model is not realistic, since it lacks the periodicity observed in actual river channels (Ferguson, 1976)[36].

The disturbed dampened harmonic model developed by Ferguson (1976)[36] provides a realistic streamline model.

$$\phi(\mathbf{s}) + \frac{2h}{k}\frac{d\phi(\mathbf{s})}{ds} + \frac{1}{k^2}\frac{d^2\phi(\mathbf{s})}{ds^2} = \varepsilon(\mathbf{s}) \tag{3.3}$$

where $k$ is related to the primary wavelength $k = 2\pi/\lambda$, $h$ is the dampening factor $(0 < h < 1)$ and $\varepsilon(\mathbf{s})$ is the disturbance value. The physical analogue for this model is a pendulum dampened by air resistance and continuously hit by rocks. The discrete approximation of this model may be applied to efficiently calculate streamlines with intuitive parameters and with periodicity and irregularity observed in fluvial channels.

Sinuosity is related to the dampening factor, $h$, the wavelength through $k$, and the variance of the disturbance RV, $\varepsilon$. Decrease in dampening results in more regularity and higher sinuosity. Decrease in the disturbance variance increases the regular periodicity of the model. Given a nominal wavelength and level of periodicity a calibration may be performed to find the required dampening factor to get a required sinuosity. A series of channels are generated with varying sinuosities in

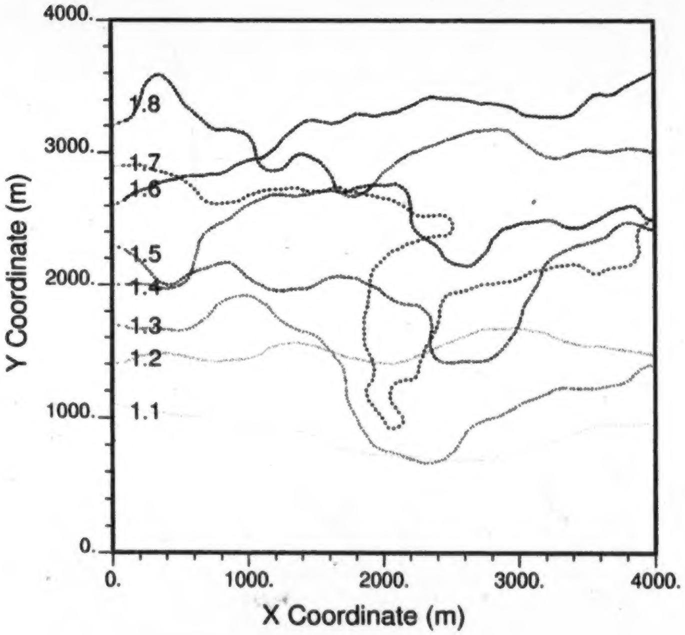

Figure 3.4: Example channel streamlines calculated with the disturbed periodic model. From bottom to top sinuosity = 1.1, 1.2, . . . , 1.8.

Figure 3.4. The disturbed dampened harmonic model is applied in the streamline initialization operator, although any model may be used.

### Streamline Avulsion

There are two types of avulsion; (**1**) change in channel path within an active channel system and (**2**) abandonment of an active channel system and activation of a previously inactive system. The first type of avulsion includes neck cut offs (an entire meander loop is abandoned) and chute channels (the channel cuts across the point bar. This type of avulsion is handled within the migration operation by checking for nonadjacent control nodes that are within a channel width of each other.

The second type of avulsion is the process of channel abandonment and the establishment of a new channel outside the active channel. Unless otherwise specified the term avulsion in this dissertation refers to this type. The frequency of avulsion is related to channel confinement, loading index, and the availability of accommodation outside the channel. In alluvial fans and deltas, avulsion is associated with the large scale switching between sedimentary lobes (Miall, 1996)[73]. Within model avulsion is handled with the streamline avulsion operator. Avulsion proximal of the model is handled by spontaneously initializing a new channel with the streamline initialization operator (a drawing of the previously constructed streamlines that honor morphology, areal trend, source and azimuth distribution information).

The avulsion operator creates a copy of a specific channel streamline, selects a location along the streamline, generates a new downstream channel segment with same streamline sinuosity and the same geometric parameter distributions. The geometric parameters (e.g. channel width) of the new streamline are corrected so that the properties are continuous at the avulsion location. The initial azimuth is specified as the azimuth of the tangent at the avulsion location. There is no constraint to prevent the avulsed streamline from crossing the original streamline distal of the avulsion location.

The original and avulsed streamlines may be related to each other sequentially or in parallel. Considered sequential, one channel replaces the next as described above. Architectural elements such as LV and CS may partially or completely replace the CH and FF(CH) elements related to the original streamline. Considered in parallel, both channels are coeval, this operator could be applied to approximate braiding patterns with the limitation that the streamlines branch and cross basinward but do not merge.

In the current implementation the location of avulsion may be specified or unspecified. If the location is unspecified then an avulsion location is drawn from the distribution of streamline control nodes weighted by the curvature at each node. This rule integrates the concept that avulsion is more likely to occur at locations of high curvature.

### Streamline Aggradation

Aggradation occurs when a channel deposits sediments in the channel and over bank environments. This process is represented by a incremental increase in the elevation of a streamline. The current implementation is to add a specified constant value to the elevation, $z$, parameter for all control nodes.

Fluvial systems are continually adjusting to their changing equilibrium profile. This profile shifts under the influence of allogenic (e.g. eustasy discussed in Section 3.1.3) and autogenic (e.g. sediment supply) forces. This process is further complicated by internal feedbacks. Aggradation in a location may reduce the sediment load and hence the loading index downstream and this may result in local erosion.

A model of these complex coupled processes would require a full forward deductive model (refer back to Section 2.1.8). The building blocks for streamline based simulation are not designed for implementation in a true forward model. The following limitations are present; (**1**) topography is not modeled or altered; therefore, while a negative aggradation decreases streamline elevation, there is no true mechanism for eroding underlying architectural elements. In the current implementation channels remove elements from above to prevent floating residual LV and CS elements. (**2**) Aggradation occurs as monotonically increasing streamline elevation constrained only by a user provided vertical trend model. There is no consideration of the previously mentioned autogenic or allogenic considerations. This is advantageous since a vertical trend may be observable from available well data and it would be difficult to reproduce a precise vertical trend with a full deductive model.

### Streamline Migration

The streamline migration operator is based on the bank retreat model. The application of the bank retreat model for realistic channel meander migration has been proposed by Howard (1992)[50], applied to construct fluvial models by Sun et al. (1996)[123] and extended to construct meandering fluvial models that approximately honor global proportions, vertical and horizontal trends by Lopez et al. (2001)[65].

The bank retreat model assumes that a stream is at equilibrium; the cut bank erosion is equal to the point bar deposition. The rate of meander migration is assumed to be a function of the near bank velocity. The near bank velocity is calculated along the channel streamline with the following equation (Sun et al., 1996)[123]:

$$\tilde{u}_{sb}(\mathbf{s}) = -b(\mathbf{s})u_{s_0}\tilde{C}(\mathbf{s}) + \frac{bC_f}{u_{s_0}}\left[\frac{u_{s_0}^2}{gh_0^2} + (A'+2)\cdot\frac{u_{s_0}^2}{h_0^2}\right]\cdot\int_0^\infty exp\left(\frac{-2C_f}{h_0}\right)\cdot\tilde{C}(\mathbf{s}-\mathbf{s}')d\mathbf{s}' \tag{3.4}$$

where $\tilde{u}_{sb}(\mathbf{s})$ is the near bank velocity, $b(\mathbf{s})$ is the channel half width, $\tilde{u}_{s_0}$is the stream mean velocity, $\tilde{C}(\mathbf{s})$ is the local channel curvature, $C_f$ is the friction coefficient, $g$ is the gravitational constant, $h_0$ is the average depth of channel, $A$ is a positive factor describing the scour factor and **s** is the coordinate along the streamline. The integration component accounts for the upstream inertial effects on the near bank velocity.

The migration of each control node normal to the channel is calculated as function of the near bank velocity and the "erodability" of the host material (Sun et al., 1996)[123]:

$$\zeta(\mathbf{s}) = E(\mathbf{s}) \cdot \tilde{u}_{sb}(\mathbf{s}) \tag{3.5}$$

where $\zeta(\mathbf{s})$ is the channel migration distance, $E(\mathbf{s})$ is the local erosion coefficient and $\tilde{u}_{sb}(\mathbf{s})$ is the near bank velocity calculated in Equation 3.4.

Time steps are applied to model the channel migration. As the channel migrates, an underlying facies model is modified with the formation of channel, point bar and abandoned channel architectural elements. The erosion coefficient grid is modified as a function of facies. After each time step there is a check for chute and neck cutoffs (refer back to discussion on within channel avulsion) and control nodes are added where they are widely spaced. An example streamline with 100 time steps is shown in Figure 3.5.

A 2-D image demonstrates the meandering of a channel and the modification of the underlying architectural element model (see Figure 3.6). While channel migration increases sinuosity, periodic neck cutoffs reduce the sinuosity.

The streamline migration operator is based on an efficient implementation of the bank retreat model (Sun et al., 1996)[123]. The migration operators takes an initialized streamline (a set of control nodes and location and property splines) and (**1**) calculates the curvature and first derivative of curvature from the spline fit streamline, (**2**) calculates the near bank velocity with the discrete approximation of Equation 3.4, (**3**) calculates the relative migration and standardizes this migration to a user supplied maximum migration, (**4**) migrates the control nodes and (**5**) checks for neck and chute cutoffs. If chute or cutoff occurs the abandoned channel segments are removed and CH and CH(FF) element is generated. (**6**) Then, a new set of regularly spaced control nodes are assigned by spline interpolation. These steps are illustrated in Figure 3.7.

Key implementation differences from the original work from Sun et al. (1996)[123] include (**1**) elimination of the erosion coefficient matrix, (**2**) integration of 3-D splines for location and properties, (**3**) application of various architectural elements.

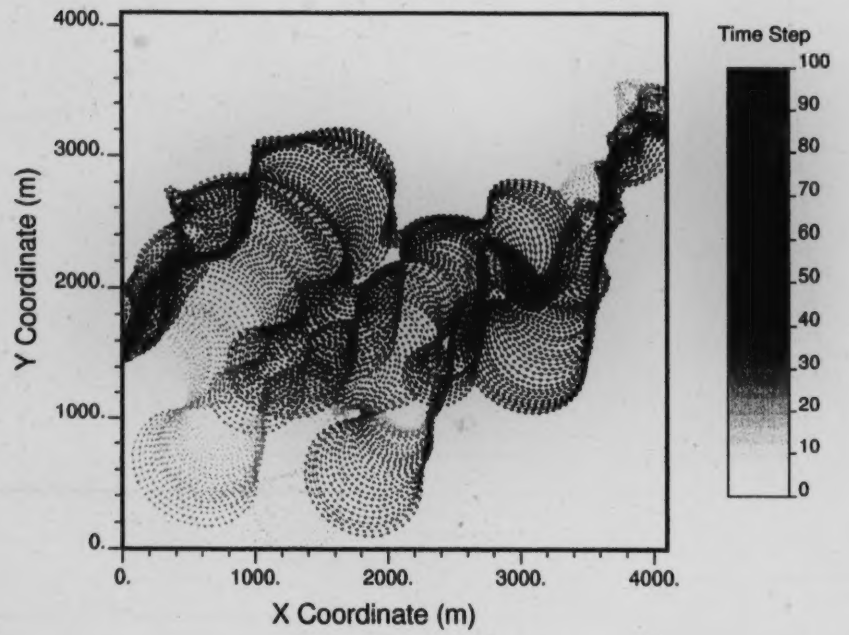

Figure 3.5: The migration of a channel streamline over 100 times steps (white to black). The source and target locations are kept constant. Note the neck cut offs. The end points are constrained.

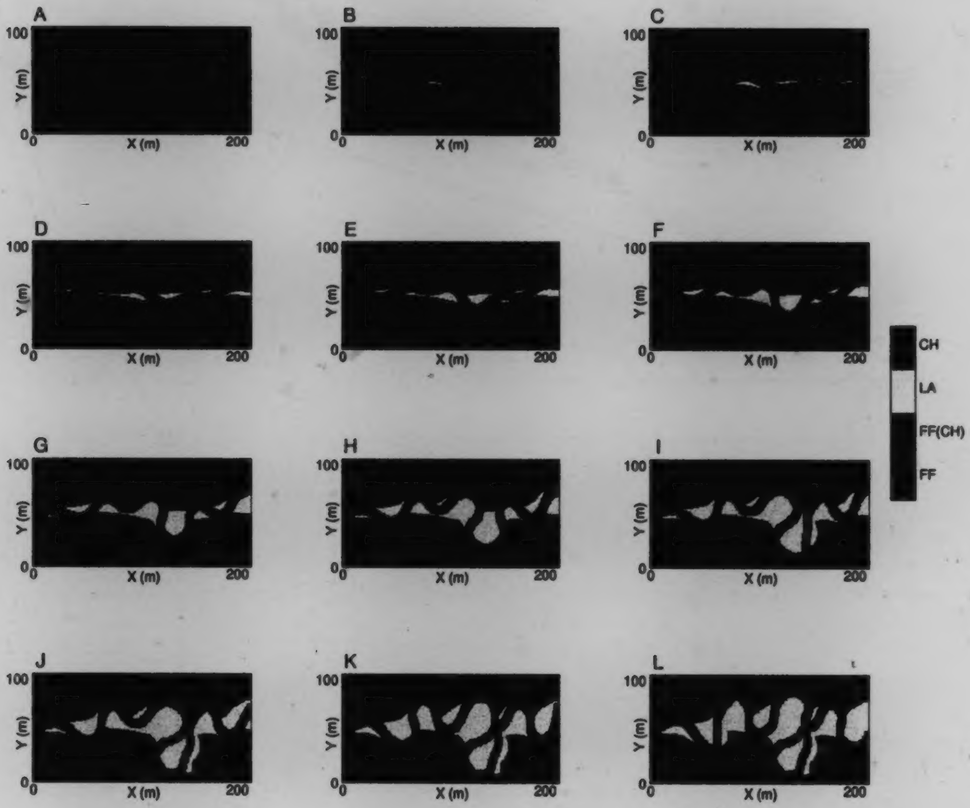
A
B
C
D
E
F
G
H
I
J
K
L
100
Y (m)
0
0
X (m)
200
CH
LA
FF(CH)
FF

Figure 3.6: The migration of a channel streamline over twelve time steps and the evolving facies model. A to L - note the formation of LA elements and increasing streamline sinuosity. J - a neck cutoff occurs and the oxbow lake is coded as abandoned channel fill (CH element capped with FF(CH) element).

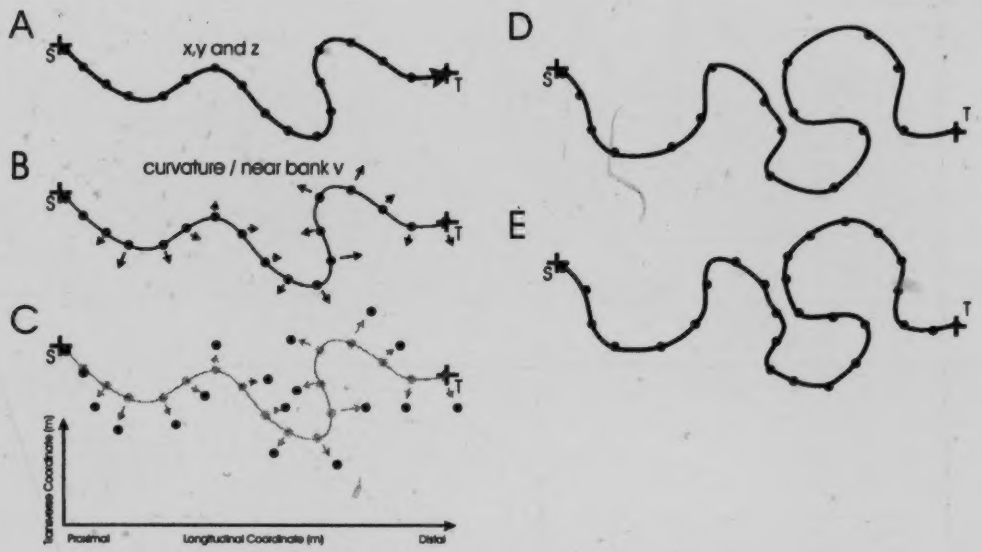
A
x,y and z
S
T
B
curvature / near bank v
S
T
C
S
T
Transverse Coordinate (m)
Proximal
Longitudinal Coordinate (m)
Distal
D
S
T
E
S
T

Figure 3.7: An illustration of the steps required in the streamline migration operator: A - the initial streamline 3-d spline and control nodes, B - the curvature, near bank velocity and migration are calculated at control nodes, C - the nodes are migrated, D - a new 3-D spline is fit to the migrated control nodes and E - a new set of regularly spaced control nodes are assigned by spline interpolation. Note $S$ is the source location and $T$ is the target location.

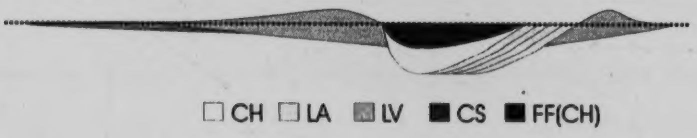

Figure 3.8: An illustration of the fluvial architectural elements applied in the streamline based model.

Instead of local erosion coefficients, a uniform erosion coefficient is applied that is calibrated for each migration step such that the maximum migration matches a specified value. This standardization of the migration rates removes the significance of hydraulic parameters such as friction coefficient, scour factor and average flow rate, since only the relative near bank velocity along the streamline is significant. Hydraulic parameters are replaced by the maximum spacing of accretion surfaces. The spacing of mud draped along accretionary surfaces is observable in well logs and cores, while paleo-hydraulics are often not a reliable source of information in reservoir studies (Miall, 1996)[73].

In addition, the utilization of 3-D splines allows for improved computational efficiency and well behaved local curvature functions (refer back to Section 3.2.1). The available architectural elements are now discussed.

### 3.2.4 Fluvial Architectural Elements

The available architectural elements include (**1**) CH, (**2**) LA, (**3**) LV, (**4**) CS, (**5**) FF(CH) and (**6**) FF (refer back to Table 3.1 and see illustration in Figure 3.8). The geometries and associated parameters are discussed for each element.

#### Channel Fill (CH) Elements

The CH element is applied in two modes; (**1**) to represent channel fill architectural elements in abandoned channels with or without the presence of FF(CH) elements and (**2**) as the geometry of the active channel for each time step. As an active channel the CH element geometry constrains the geometries of other architectural elements. LV, CS and FF(CH) elements are anchored to CH elements and LA elements are assigned as then abandoned CH element after meander migration.

The geometry of the CH element is parameterized by a streamline, relative thalweg location, stochastic depth and a width to depth ratio. The cross section channel geometry is based on the following equations (see Equations 3.6 to 3.8) from Deutsch and Wang (1996)[28]. The relative thalweg is calculated as a function of channel curvature.

$$a(\mathbf{s}) = \begin{cases} \frac{W(\mathbf{s})}{2}\left(1 - \frac{|C_v(\mathbf{s})|}{C_v^l}\right) & C_v(\mathbf{s}) < 0 \\ \frac{W(\mathbf{s})}{2}\left(1 - \frac{|C_v(\mathbf{s})|}{C_v^r}\right) & C_v(\mathbf{s}) > 0 \\ \frac{W(\mathbf{s})}{2} & C_v(\mathbf{s}) = 0 \end{cases} \tag{3.6}$$

where $a(\mathbf{s})$ is the location of the thalweg, $C_v^l$ and $C_v^r$ are the maximum channel curvature in the clockwise and counter clockwise directions and $C_v(\mathbf{s})$ is the local curvature. The channel cross section geometry is defined by Equation 3.7 for a thalweg closer to the left bank and by Equation 3.8 for a thalweg closer to the right bank.

$$d(\mathbf{w},\mathbf{s}) = 4 \cdot t(\mathbf{s}) \cdot \left(\frac{\mathbf{w}}{W(\mathbf{s})}\right)^{b(\mathbf{s})} \cdot \left[1 - \left(\frac{\mathbf{w}}{W(\mathbf{s})}\right)^{b(\mathbf{s})}\right] \tag{3.7}$$

where $b(\mathbf{s}) = -ln(2)/ln[a(\mathbf{s})]$.

$$d(\mathbf{w},\mathbf{s}) = 4 \cdot t(\mathbf{s}) \cdot \left(\frac{\mathbf{w}}{W(\mathbf{s})}\right)^{c(\mathbf{s})} \cdot \left[1 - \left(1 - \frac{\mathbf{w}}{W(\mathbf{s})}\right)^{c(\mathbf{s})}\right] \tag{3.8}$$

where $c(\mathbf{s}) = -ln(2)/ln[1 - a(\mathbf{s})]$ and $d(\mathbf{w},\mathbf{s})$ is a function describing the channel cross section, $t(\mathbf{s})$ is the local channel thickness, $W(\mathbf{s})$ is the local channel width and $\mathbf{w}$ and $\mathbf{s}$ are the locations transverse and along the streamline respectively.

Fluvial channel profiles are a function of stream loading index, gradient and the properties of the host material. Wide channels and easily eroded host material typically have shallow channel margins, while narrow channels in mud and peat may have vertical to oversteep channel margins (Miall, 1996)[73]. Modern meandering channels demonstrate a shifting thalweg and asymmetry in cross section (Ritter et al., 2002)[137]. Stream profiles may be complicated and highly irregular (Ritter et al., 2002)[106], although this geometry is consistent with the general form of the observed geometry in a meandering stream (Easterbrook, 1969)[34] (see Figure 3.9).

The CH element parameters; thalweg location, depth and width to depth ratio are calculated at control nodes along the streamline. Cubic splines are fit to these properties to allow for a smooth transition along the streamline and efficient interpolation at any streamline location.

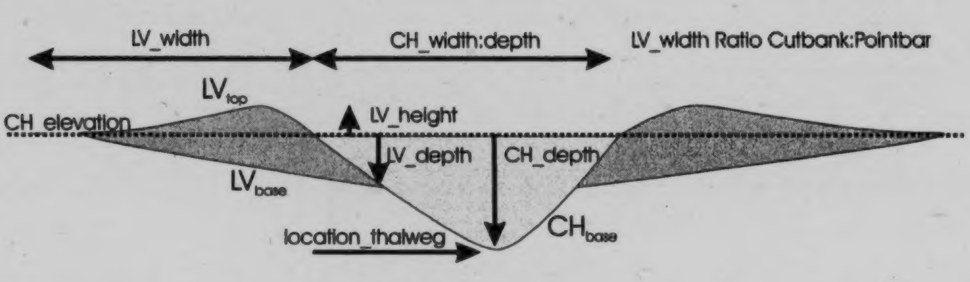

Figure 3.9: Channel and levee elements cross section and associated geometric parameters. Note the LV geometry is eclipsed by the channel geometry.

By applying a variety of streamline operations this single CH geometry may be applied to construct a variety of reservoir geometries. For example, a set of nested or isolated CH elements may be generated to construct shoe string reservoirs or isolated FF(CH) elements may form barriers or baffles as in jigsaw reservoirs.

The CH element average width to depth ratio and average depth are drawn from a Gaussian distributions specified in the parameter file. This information may be assessed from well data and analog information related to fluvial style. Typically gravel dominated styles are characterized by shallow streams and high width to depth ratios and fine grained systems have lower width to depth ratios (Colinson, 1996; Miall, 1996)[15, 73].

Conservation of cross sectional area is honored in the current implementation. The approximate cross sectional area is found by integrating the channel cross section equation (see Equation 3.7).

$$Area = 4 \cdot \bar{t} \cdot \overline{W} \cdot \left[ \frac{1}{b+1} - \frac{1}{2 \cdot b + 1} \right] \tag{3.9}$$

where $\bar{t}$ is the mean depth, $\overline{W}$ is the mean width and $b$ is a function of thalweg location as described in Equation 3.7. For the approximate channel cross sectional area calculation a centered thalweg is assumed.

The channel width along the streamline is represented as a correlated RF with mean calculated from the drawn average CH element average width and width to depth ratios. The standard deviation of width for a channel is specified in the parameter file. Depositional settings with fairly regular gradients will result in low variance in CH element width.

Given the CH element width and thalweg along the streamline, the corresponding

CH element depth is calculated such that the CH element cross sectional area is constant (simple manipulation of Equation 3.9). The CH element area as a function of thalweg location has a symmetric solution about the centered thalweg case $a = 0.5$; therefore, only Equation 3.7 was integrated for thalweg closer to the right hand side the $a$ value is corrected, $a' = 1 - a$.

### Lateral Accretion (LA) Elements

An advantage of the application of the bank retreat method for channel streamline migration is the generation of realistic LA geometries. The lateral accretion deposits are represented as the volume of channel abandoned during channel migration. The complicated geometries of LA elements have been demonstrated by Diaz-Molina, (1993) and Willis (1993)[32, 139]. LA elements are characterized by wedge channel fills distributed along the inside of meander bends. These elements are formed during channel migration towards the cut bank.

An example of evolving point bar architectural elements is shown in Figure 3.6. The combination of a realistic model of channel migration and a realistic channel cross section results in realistic LA geometries. The application of the streamline based fluvial model to construct stochastic LA is explored in Section 3.5.

### Levee (LV) Elements

Significant reservoir quality facies may be represented by levees. LV elements form as the accumulation of multiple flooding events separated by hiatus and subaerial erosion. The internal LV geometry is composed of overlapping lenses that have dips of two to ten degrees and are thinning and finning away from the channel axis (Miall, 1996, p. 172)[73]. LV elements may be represented as a set of nested lobes and lenses (i.e. many small CS elements (Collinson, 1996)[15]). The external geometry of LV elements is characterized by a wedge that are thickest adjacent to the channel and thinning toward the over bank (Collinson, 1996; Galloway and Hobday, 1996, Miall, 1996)[15, 39, 73]. LV elements may extend for large distances from the channel (e.g. up to a one kilometer)(Miall, 1996)[73].

The LV geometry and associated parametrization were shown in Figure 3.9. The equations for the LV top and base are shown in Equations 3.10 and 3.11 respectively.

$$LV_{top}(\mathbf{d},\mathbf{s}) = LV_{height}(\mathbf{s}) \cdot \left[\frac{\mathbf{d}}{LV_{width}(\mathbf{s}) \cdot F}\right] \cdot exp^{\left[\frac{-\mathbf{d}}{LV_{width}(\mathbf{s}) \cdot F}\right]} + CH_{elev}(\mathbf{s}) \quad (3.10)$$

$$LV_{base}(\mathbf{d},\mathbf{s}) = CH_{elev}(\mathbf{s}) - LV_{depth}(\mathbf{s}) \cdot \left[\frac{LV_{width}(\mathbf{s}) \cdot F - \mathbf{d}}{LV_{width}(\mathbf{s}) \cdot F}\right] \quad (3.11)$$

where $z_{top}(\mathbf{s},\mathbf{d})$ is the top elevation of the LV element and $z_{base}(\mathbf{s},\mathbf{d})$ is the elevation of the base of the LV element at a location s along the streamline and location **d** orthogonal from the channel edge. $CH_{elev}(\mathbf{s})$, $LV_{depth}(\mathbf{s})$, $LV_{width}(\mathbf{s})$ and $LV_{height}(\mathbf{s})$ are the elevation of the channel and the depth, width and height of the LV element at the nearest location along the streamline, s. At locations with negative thickness (i.e. $z_{base}(\mathbf{s},\mathbf{d}) > z_{top}(\mathbf{s},\mathbf{d})$) no LV element is placed. $F$ is a scaling factor described below.

The distribution of LV elements may not be uniform along the channel axis. Typically LV elements are more pronounced on the cut bank. This information is integrated with a LV width scaling factor, $F$, that scales the LV width to account for LV asymmetry on channel bends. The current implementation is applied to calculate the $F$ multiplier with the following equations.

$$F_{pointbar}(\mathbf{s}) = 1.0 - LV_{asym} \cdot \frac{c(\mathbf{s})}{|c_{max}|} \quad (3.12)$$

$$F_{cutbank}(\mathbf{s}) = 1.0 + LV_{asym} \cdot \frac{c(\mathbf{s})}{|c_{max}|} \quad (3.13)$$

where $LV_{asym}$ is a value between 0 and 1 that parameterizes the strength of the levee asymmetry, $c(\mathbf{s})$ is the local curvature along the streamline and $c_{max}$ is the maximum curvature along the streamline. A $LV_{asym}$ value of 0 results in symmetric LV elements and a $LV_{asym}$ value of 1 results in no LV element on the point bar side and double width of LV element on the cut bank side at the location along the streamline with greatest curvature.

### Crevasse Splay (CS) Elements

CS elements may also have significant reservoir quality. CS elements differ from LV in their genesis. They form from a significant local breach in the LV element as opposed to general flooding and represent sedimentation over a shorter time scale.

This tapping of the channel results in the availability of the coarser component of channel sediment load than available during LV element construction.

The internal geometry of CS elements may include low angle accretion surfaces with fining away from the channel axis and coarsening upwards associated with lateral progradation (Miall, 1996)[73]. CS element external geometry is commonly identified as discrete lobes with fingers extending beyond the lobe. CS elements extend beyond natural levees onto the floodplain. In flood prone settings the CS elements may extend over ten kilometers in length and five kilometers in width and may form amalgamated aprons along the channel. A CS element may have a thickness of less than a meter to several meters and may form amalgamated successions of tens of meters (Collinson, 1996; Galloway and Hobday, 1996, Miall, 1996)[15, 39, 73].

For each streamline the number of CS elements is drawn from a Gaussian distribution with mean and standard deviation supplied by the user. The location of each CS element along the streamline is drawn from a distribution of streamline locations, weighted by the curvature. Crevasse splays more likely occur at locations with high curvature since high near bank velocities erode the confining LV elements. The CS elements are modeled as a series of lobes fit to low sinuosity streamlines initiated from the crevasse location with initial azimuth normal to the channel streamline towards the cut bank.

The number of lobes and the lobe parameters (see Figure 3.10) are drawn from Gaussian distributions with user supplied mean and standard deviation. Fewer large lobes reproduce sheet geometries while many thin lobes reproduce inter fingering. The lobes within the CS element have the same areal geometry as the lobe element applied in Section 4.5. This geometry taken from `LOBESIM` algorithm by Deutsch and Tran (1999)[26]. Four example of CS elements constructed with the `ALLUVSIM` algorithm (discussed in Section 3.3) are shown in Figure 3.11.

### Abandoned Channel (FF(CH)) Elements

In jigsaw reservoirs FF(CH) elements may be barriers or baffles to flow and may have significant control on reservoir response. FF(CH) elements represent low energy channel fills that are muddy sand to pure mud (Miall, 1996)[73]. They form due to rapid channel abandonment. If channel abandonment is very abrupt (i.e. rapid avulsion, neck cut-off) then there is a strong contrast between the FF(CH) and CH

6

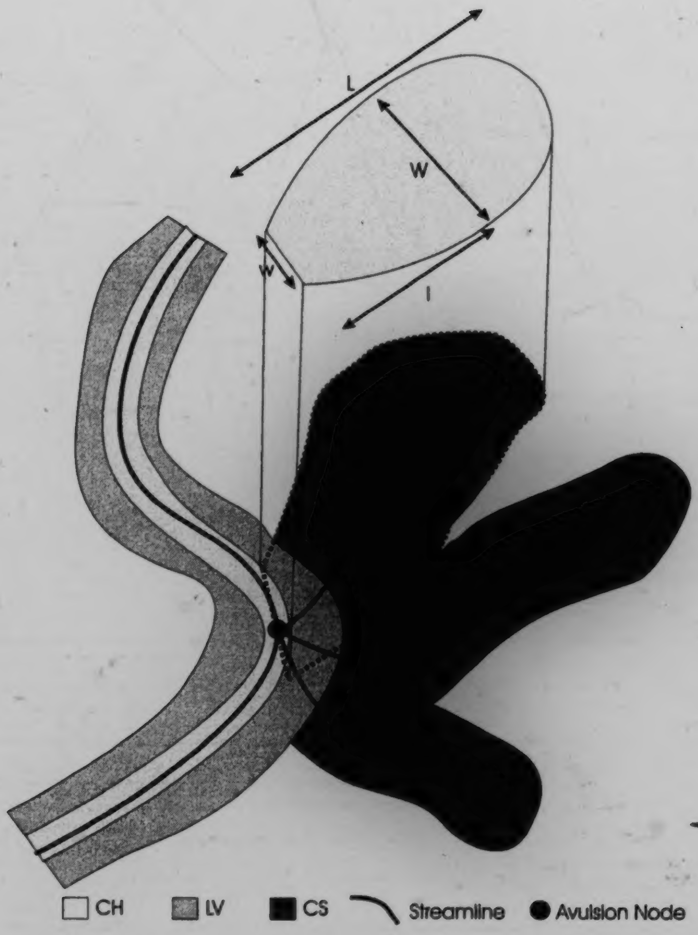
L
W
w
l
CH
LV
CS
Streamline
Avulsion Node

Figure 3.10: Crevasse splay architectural element geometric parameters. $L$ is the length of the lobe, $l$ is the length along the streamline where the lobe has its maximum width, $W$ and $w$ is the width along the proximal edge.

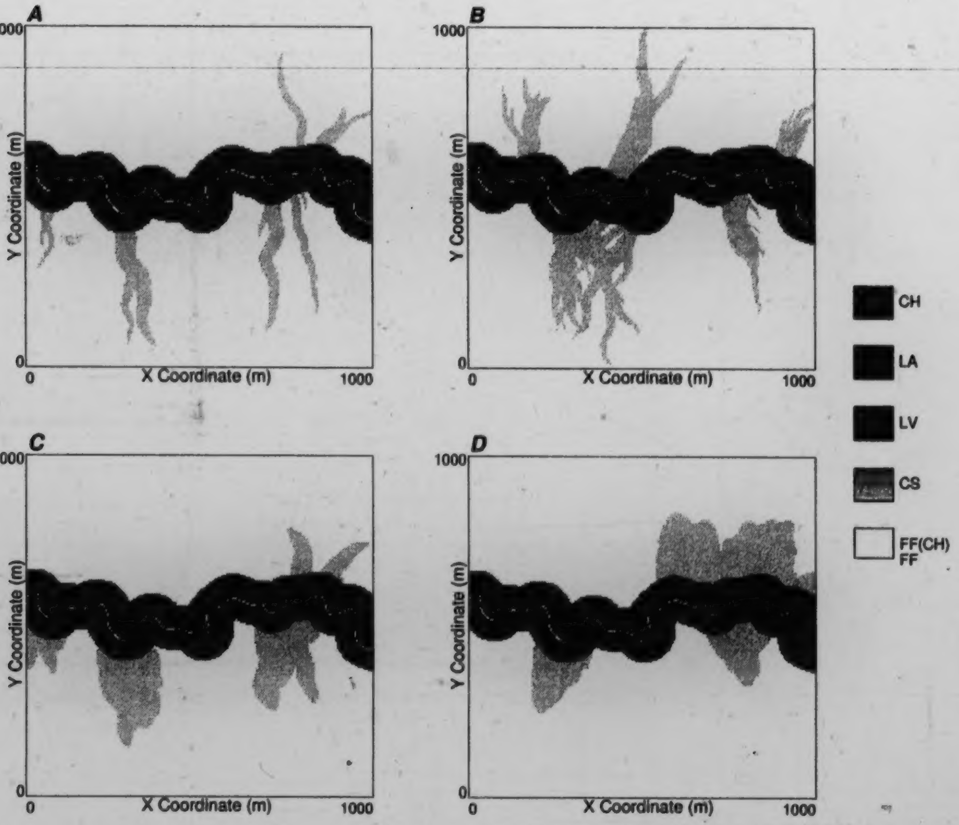
A
B
C
D
1000
0
Y Coordinate (m)
X Coordinate (m)
1000
CH
LA
LV
CS
FF(CH)
FF

Figure 3.11: Example crevasse splay geometries calculated with the **ALLUVSIM** algorithm: A - isolated interfingered elements, B - amalgamated lobe and interfingered elements, C - isolated lobe elements and D - amalgamated lobe elements.

elements. Slow abandonment leads to fining upward fills (Galloway and Hobday, 1996)[39].

In the current implementation FF(CH) elements form; (**1**) in oxbow lakes when meander migration has cut off a reach, (**2**) in the channel reaches distal of avulsion locations and (**3**) in the last channel placed for a level or within a level.

The user specifies the distribution of the proportion of abandoned channels fill with FF(CH) elements. For a proportion of 0 the abandoned channel is coded as CH element and for a proportion of 1 the entire abandoned channel is coded as FF(CH) element. For a proportion between 0 and 1 the contact between the FF(CH) and CH elements is calculated with the following equation.

$$FFCH_{elev} = P_{mud} \cdot (CH_{elev} - CH_{base}) + CH_{base} \tag{3.14}$$

where $P_{mud}$ is the proportion of FF(CH) element and $CH_{elev}$ and $CH_{base}$ are the elevations of the top and base of the abandoned channel respectively. Note this assumes a proportional contact between FF(CH) and CH elements.

#### Overbank Fines (FF) Elements

FF elements are not modeled directly. The model space is initialized as FF element. Other architectural elements displace FF elements during model construction.

## 3.3 Streamline Based Unconditional Algorithm

The streamline based approach (refer back to Section 3.2) and the building blocks for streamline base simulation (refer back to Sections 3.2.3 and 3.2.4) are demonstrated with a Fortran program called `ALLUVSIM`. This algorithm applies the previously identified building blocks to construct flexible unconditional stochastic fluvial models. These models may be applied as training images as discussed later in Chapter 5. In Section 3.4 a conditional model is presented based on these building blocks.

### 3.3.1 Event Schedule

The application of building blocks based on streamline operators and associated architectural elements allows for a large degree of flexibility. An algorithm could be written to read in a precise schedule of flow events expressed as a list of streamline operators and associated architectural elements with all required geometric parameters. This would enable a practitioner to custom build a wide variety of synthetic fluvial models.

The `ALLUVSIM` algorithm is able to reproduce a wide variety of reservoir styles with limited parametrization. This algorithm may reproduce braided, avulsing, meandering channels and may reproduce geometries and interrelationships of any reservoir type (PV, SH or CB) and fluvial style within any systems tract. The algorithm is supplied with areal and vertical trends, distributions of geometric parameters, probabilities of events and architectural elements. Further implementation details are discussed.

### Areal Channel Density Trends

Analogue, well test and seismic information may indicate areal trends in reservoir quality. Although seismic vertical resolution is often greater than the reservoir thickness, seismic attributes calibrated to well data may indicate a relative measure of local reservoir quality. Well tests may provide areal information on the distribution of reservoir quality and may significantly constrain model uncertainty (Corbett et al., 1998)[17]. Analogue information such as reservoir type may indicate a confined PV type or a more extensive and uniform SH type reservoir. If the net facies are associated with CH, LV and CS elements then this areal trend information may be integrated by preferentially placing streamlines in areal locations with high reservoir quality.

The technique for honoring areal trends is to (**1**) construct a suite of candidate streamlines with the desired morphology, (**2**) superimpose each streamline on the areal trend model and calculated average relative quality and (**3**) for each streamline initialization draw from this distribution of candidate streamlines (without replacement) weighted by the average quality index. This technique is efficient since the construction of hundreds or thousands of streamlines is computationally fast.

This technique is demonstrated in Figure 3.12. 30 streamlines are drawn from a suite of 500 candidate streamlines for three different areal trends. Note the control of the areal trend on the drawn streamlines.

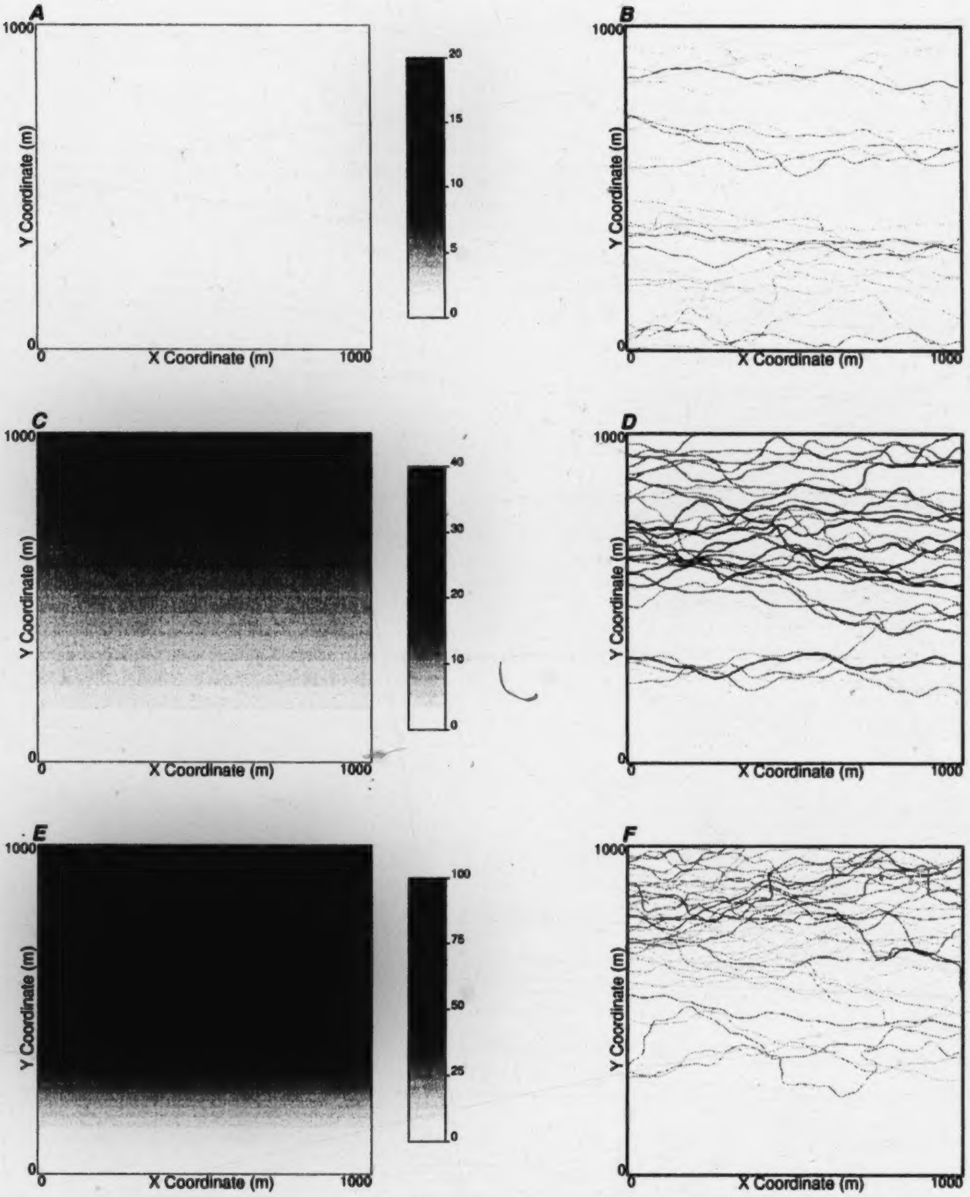

Figure 3.12: Example areal trends in channel density and the resulting streamlines. A and B - no areal trend supplied, C and D - a linear trend increasing in the y positive direction and E and F - a second order trend increasing in the y positive direction. Note areal trend is a relative measure without units.

### Vertical Channel Density Trends and Aggradation Schedule

Well data and analogue information may provide information on vertical trends in reservoir quality. Well logs calibrated by core are valuable sources of vertical trend information. Often identification of systems tract and fluvial style will provide analogue information concerning potential vertical trends.

These trends may be honored by constraining the aggradation schedule. The current implementation is to apply the trend within a user defined number of constant elevation levels. Streamlines and associated architectural elements are generated at the lowest level until the NTG indicated by the vertical trend is reached for the model subset from the base of the model, $z_0$, to the elevation of the first level, $z_1$. Then the aggradation operator is applied to aggrade to the next level and the process is repeated through all user defined levels. For the highest level, $z_n$, the model is complete when the global NTG ratio is reached. Fluvial aggradation and erosion is discussed in the description of the aggradation operator in Section 3.2.3.

The assignment of a few constant elevation levels to model aggradation is a simplification, although this technique does allow for the flexibility to reproduce a variety of aggradation patterns. For example, few levels result in a stepped system with amalgamated reservoir elements separated by FF elements. The assignment of many levels and an overall low NTG results in isolated PV type shoestring or CB type labyrinth reservoirs. The assignment of many levels with an overall high NTG results in a amalgamated CB type jigsaw reservoirs.

The number of aggradation levels impacts the vertical trend reproduction. The assignment of few levels results in coarse reproduction of the vertical trend. Taken to the limit, the application of a single level would not reproduce a vertical trend. The assignment of many levels may allow for more precise reproduction of the vertical trend. With minor modification more complicated schedules may be applied that allow for continuous aggradation as opposed to discrete levels. Three example vertical trends with cross sections from the resulting models are shown in Figure 3.13. It is recommended that the number of aggradation levels be chosen based on the observed vertical stacking in the fluvial reservoir. Then, the avulsion probability may be adjusted to reproduced observed CH, LA and FF(CH) element proportions.

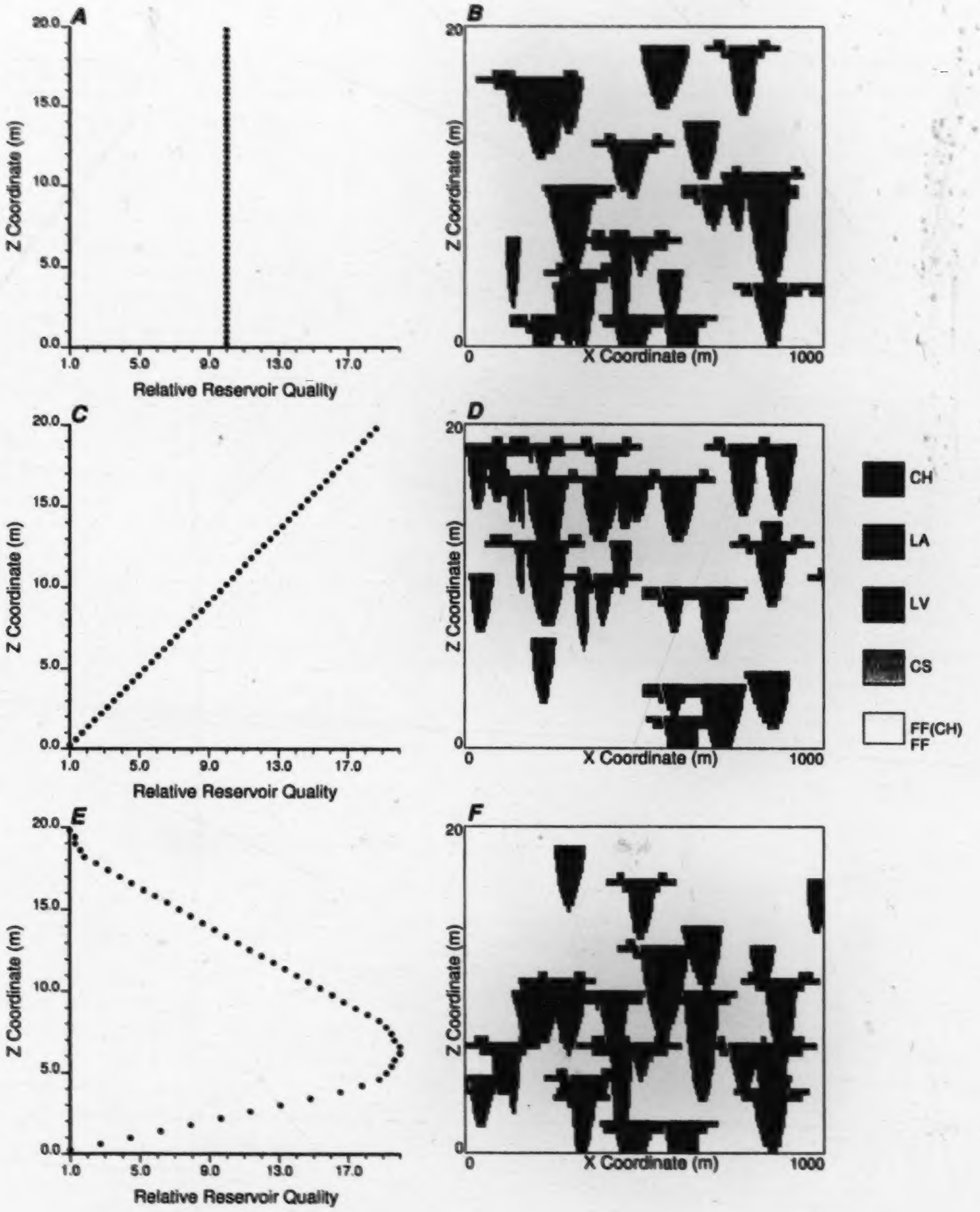

Figure 3.13: Example vertical trends in channel density and the resulting architectural element models. A and B - no areal trend supplied, C and D - a linear trend increasing in the y positive direction and E and F - a second order trend increasing in the y positive direction. The source locations are drawn from a uniform distribution along the proximal edge. Note vertical trend is a relative measure without units.

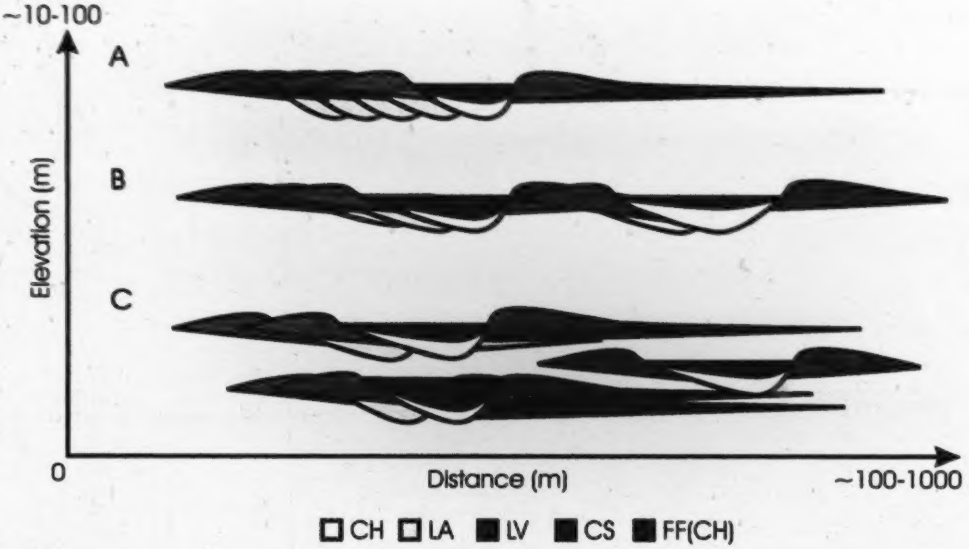

Figure 3.14: The effect of probability of avulsion and number of aggradation levels on `ALLUVSIM` models. A - few aggradation levels and low avulsion probability result in well developed LA elements, B - few levels and high avulsion probability result amalgamated reservoir punctuated by FF(CH) elements and C - many aggradation levels and low probability of avulsion results in isolated LA element lenses or PV type shoestring reservoirs.

### Channel Pattern and Avulsion Schedule

The streamlines are generated sequentially from the base to the top of the model. Streamlines are modified through (**1**) streamline avulsion proximal of model, (**2**) streamline avulsion and (**3**) streamline migration with streamline initialization generating the first streamline on each level (refer back to Section 3.2.3).

The probabilities of avulsion events for each time step are user defined. The selection of low avulsion probabilities results in well developed LA elements with FF(CH) element baffles as seen in CB type labyrinth fluvial reservoirs. The application of a high probability of avulsion results in braided SH type reservoir. A schematic illustration of the impact of avulsion probability and number of aggradation levels on `ALLUVSIM` models is shown in Figure 3.14.

#### Channel Pattern and Source and Azimuth Distributions

The source location (position along the proximal edge of the model) and the general azimuth of each streamline are drawn from Gaussian distributions parameterized by user supplied mean and standard deviation. The application of a small source standard deviation results in point source of flow events on the proximal edge while the application of a large source standard deviation results in an apron source. The application of a small azimuth standard deviation results in parallel to subparallel channels while a large azimuth standard deviation results in a more dispersive pattern.

Channel patterns from braided SH type alluvial fan reservoirs may be reproduced with a small source standard deviation and a large azimuth deviation. While a large source standard deviation and small azimuth deviation may reproduce the channel patterns observed in PV type reservoirs. A schematic illustration of the influence of source and azimuth distributions on channelized sheet complex deepwater models is shown in Figure 5.22.

### 3.3.2 `ALLUVSIM` Parameters

An example `ALLUVSIM` parameter file is shown below. These parameters include input trend files, schedule information and geometric parameter distributions. In Table 3.2 each of these parameters are discussed in greater detail.

```
Parameters for ALLUVSIM
 1.  horitrend.dat         -file with the horizontal trend
 2.  1                     - htcol
 3.  verttrend.dat         -file with the vertical trend
 4.  1                     - vtcol
 5.  200 3 2.0 10.0 13.0   -num. streamlines and levels,level elevations
 6.  0.30                  -NTG target
 7.  100 10                -channel table,fine search
 8.  0.0 0.0               -prob. of prox. avulsion,prob. of avulsion
 9.  90.0   1.0            -CH element:azimuth*
 10. 500.0 50.0            - source location*
 11. 4.0 0.5 0.2           - depth*
 12. 2 20.0 2.0            - width:depth*
 13. 1.3 0.2               - sinuosity*
 14. 2.0 0.1               -LV Element:depth*
 15  160.0 5.0             - width*
 16. 1.5 0.2               - height*
```

```
17. 0.3 0.1              - asymmetry factor*
18. 0.3 0.1              - thinning factor*
19. 50.0 20.0            -CS Element:length
20. 2 2                  - number of CS / streamline*
21. 10 2                 - number of lobes / CS*
22. 300.0 100.0          - lobe length*
23. 150.0 30.0           - lobe maximum width*
24. 50.0 10.0            - lobe length to maximum width*
25. 150.0 30.0           - lobe proximal width*
26. 0.000 0.000          - height:width*
27. 0.010 0.005          - depth:width*
28. 0.5  0.1             -FF(CH) Element:proportion of channel fill*
29. 50.0 20.0            -maximum migration step*
30. 200 2.5 5.0          -nx,xmn,xsiz
31. 200 2.5 5.0          -ny,ymn,ysiz
32. 50 0.20 0.4          -nz,zmn,zsiz
33. 69069 0.05           -random number seed,color_incr
34. alluvsim.out         -file for output facies file
35. streamline.out       -file for output streamlines

* mean and standard deviation of associated Gaussian distribution
```

### 3.3.3 Example `ALLUVSIM` Models of Reservoir Types

The algorithm that applies the previously described building blocks is called `ALLUVSIM`. The following are five example `ALLUVSIM` models that are based on PV, CB and SH reservoir types. These models demonstrate the flexibility of the streamline based fluvial technique and provide suggestions for parameter assignment to construct models of each reservoir type.

#### PV Type Shoe String Reservoir Model

The PV type reservoirs are the basis for simulated annealing object based stochastic models such as `FLUVSIM` (Deutsch and Wang, 1996; Deutsch and Tran, 2002)[28, 25] and direct object based algorithms developed by Viseur et al. (1998)[132] and Shmaryan and Deutsch (1999)[111]. The `ALLUVSIM` algorithm offers improvements over these algorithms with (**1**) more realistic channel sinuosity, (**2**) improved architectural element models and (**3**) the ability to model evolution of the fluvial system with interrelated streamline associations.

Each of these algorithms is based on a channel streamline RF along a line.

| Line | Description |
|---|---|
| 1 | input file with relative horizontal trend in channel density. The file should be in GEOEAS format and GSLIB grid convention. |
| 2 | column number for the horizontal trend. |
| 3 | input file with relative vertical trend in channel density. |
| 4 | column number for the vertical trend. |
| 5 | the maximum number of streamlines in the model (set as large), the number of levels and a list of level elevations. |
| 6 | the target NTG fraction. |
| 7 | the number of streamlines in look up table and the correlation length of the CH width RF. |
| 8 | the probability of avulsion proximal of the model and avulsion within the model. |
| 9-13 | the geometric parameters for CH element. |
| 14-18 | the geometric parameters for LV element. |
| 19-27 | the geometric parameters for CS element. |
| 28 | the geometric parameters for FF(CH) element. |
| 29 | the maximum migration step. |
| 30-32 | the regular grid parameters. |
| 33 | the random number seed and the element code increment for differentiation of individual architectural elements. |
| 34 | the output file with the architectural element model. |
| 35 | the output file with the streamlines: index, x, y and z. |

Table 3.2: A description of the `ALLUVSIM` parameter file. Further details on these parameters is found in the text.

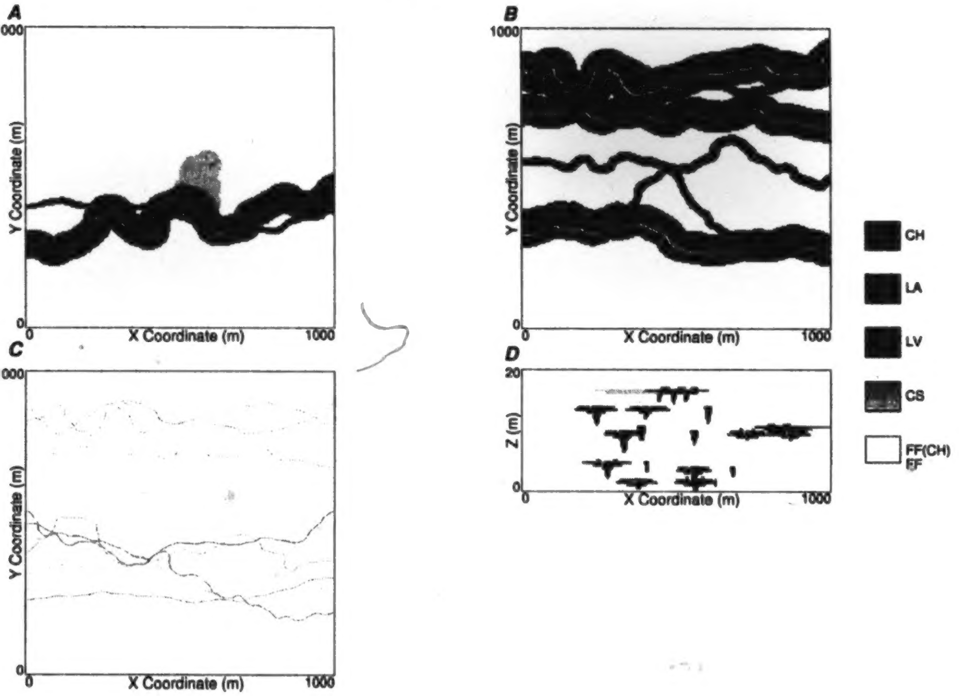

Figure 3.15: An example `ALLUVSIM` PV type reservoir model. A - plan section (z=5m), B - plan section (z=10m), C - all streamlines (grey scale from 1=white to n=black) and D - cross section (x=10m). Note grey scale assignment for architectural elements is varied to aid in differentiating amalgamated elements.

Sinuosity is parameterized by maximum departure and correlation range. While this technique is efficient, it is not a realistic model of channel sinuosity. High sinuosity is reproduced as a short wavelength streamline that is similar to a scribbled line. The `ALLUVSIM` algorithm provides direct control over sinuosity and results in realistic sinuosity patterns for low to high sinuosities.

The `ALLUVSIM` algorithm provides realistic models of CH, LA, LV, CS and FF(CH) element geometries. The most significant improvements are the addition of LA elements related to channel migration and a flexible CS parametrization that allows for interfingered and sheet geometries. An example low NTG PV type reservoir model is shown in Figure 3.15.

The previously mentioned algorithms retain greater flexibility in being conditional to any architectural elements identified at well locations. The current implementation of `ALLUVSIM` honors vertical and areal channel density trends, but not well data. The `ALLUVSIMCOND` algorithm discussed in Section 3.4 honors channel intercepts at wells.

### CB Type JigSaw Reservoir Model

The CB and SH type reservoirs are not addressed with current stochastic fluvial models. As discussed in Section 3.1.4 these reservoir types are important targets and the related heterogeneities may have an impact on reservoir response. The jigsaw reservoir type is characterized by high NTG with no major gaps. These reservoirs form from coarse grained meandering and braided fluvial styles. In these coarse grained systems the channels typically have high width to depth ratios. An example jigsaw reservoir model is shown in Figure 3.16. Note the braided and meandering streamline associations and the formation of FF(CH) baffles. The high NTG and poor preservation of FF elements is accomplished with a high NTG and few aggradation levels. This would be indicative of the LST or HST.

### CB Type Labyrinth Reservoir Model

CB type labyrinth reservoirs (Section 3.1.4) are also not well modeled with currently available algorithms. These reservoirs are characterized by poorly connected associations of CH and LA element pods and lenses. These reservoirs often originate from fine grained and anastomosing fluvial styles. An example models is shown in Figure 3.17. Note the meandering and braided features in the streamlines. The isolated channel associations may be indicative of a high rate of accommodation generation characteristic of the TST. These are formed in the model by applying a low NTG, many aggradation levels and low probability of avulsion to allow for significant LA element development.

### SH Type Reservoir Model

The SH type reservoir models are discussed in Section 3.1.4. While early exploration may indicate these reservoirs are uniform further study often indicates features similar to CB type reservoirs (Miall, 1996)[73]. Two SH type reservoir models are shown. In Figure 3.18 a SH type model based on a distal setting is shown. The streamline associations show a high degree of meandering and little avulsion. In

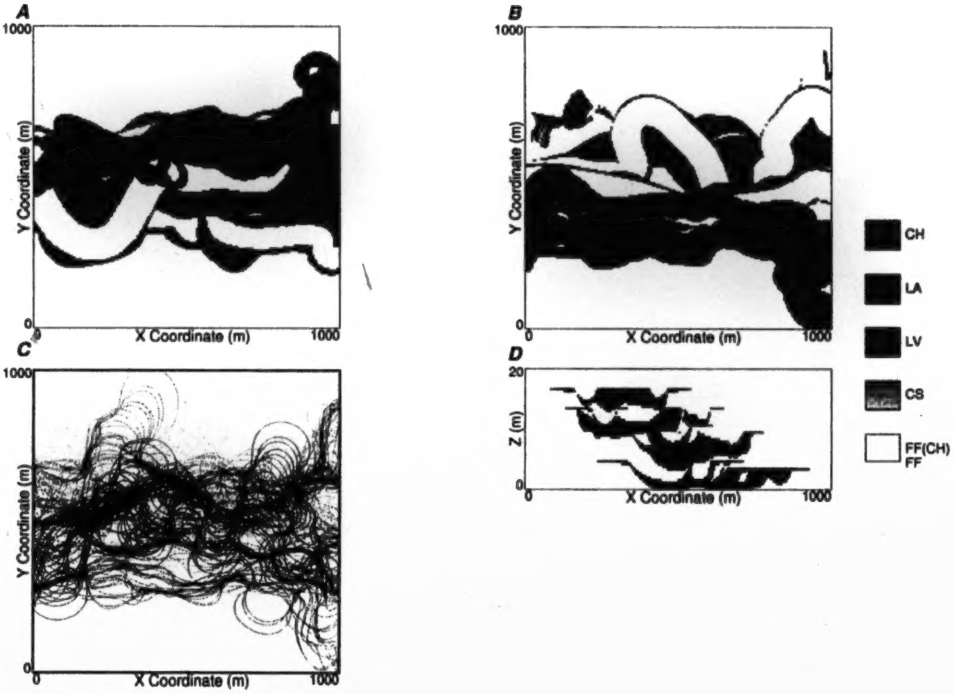

Figure 3.16: An example `ALLUVSIM` CB type jigsaw reservoir model. A - plan section (z=5m), B - plan section (z=10m), C - all streamlines (grey scale from 1=white to n=black) and D - cross section (x=10m). Note grey scale assignment for architectural elements is varied to aid in differentiating amalgamated elements. Note the meandering and braided features in the streamlines.

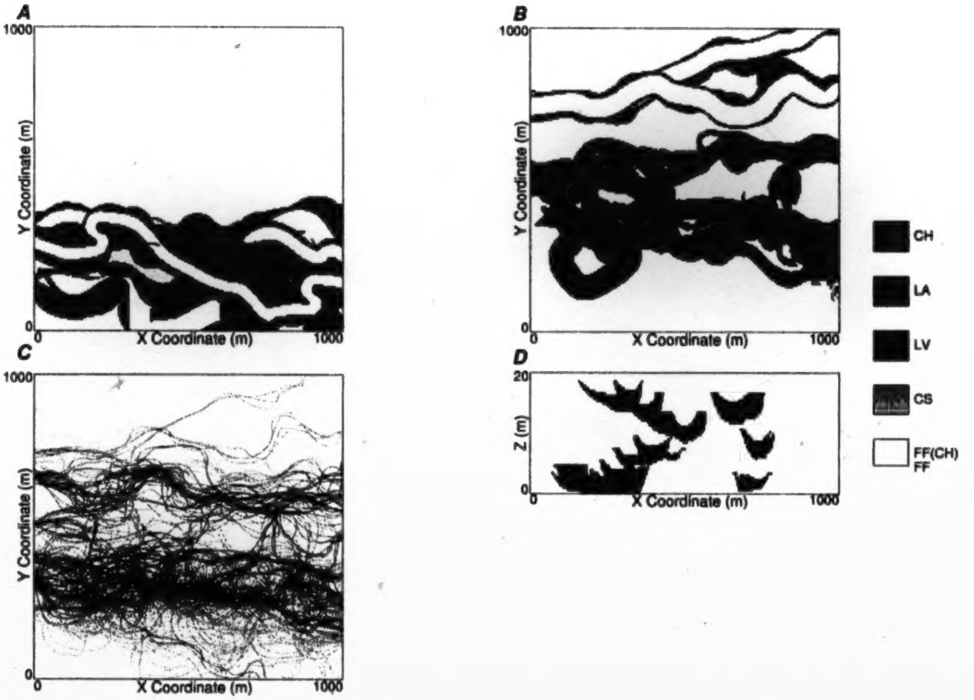

Figure 3.17: An example **ALLUVSIM** CB type labyrinth reservoir model. A - plan section (z=5m), B - plan section (z=10m), C - all streamlines (grey scale from 1=white to n=black) and D - cross section (x=10m). Note grey scale assignment for architectural elements is varied to aid in differentiating amalgamated elements.

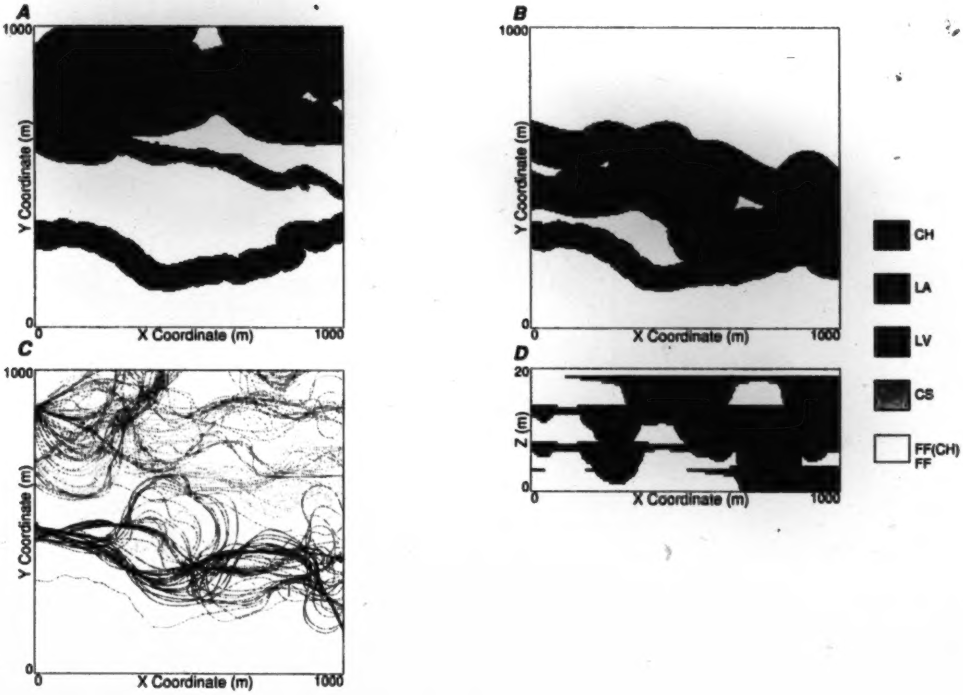

Figure 3.18: An example **ALLUVSIM** distal SH type reservoir model. A - plan section (z=5m), B - plan section (z=10m), C - all streamlines (grey scale from 1=white to n=black) and D - cross section (x=10m). Note grey scale assignment for architectural elements is varied to aid in differentiating amalgamated elements.

Figure 3.19 a SH type model based on a proximal setting is shown such as an alluvial fan. The streamline associations show a high degree of avulsion and braiding and a dispersive pattern. SH reservoir type models are generated with high NTG and many time steps to allow for amalgamate net facies.

## 3.4 Conditional Streamline Based Simulation

The **ALLUVSIM** algorithm is unconditional. This section presents a technique for updating streamline based simulation with a reasonable level of well conditioning. Additional building blocks for this technique are added to the building blocks for streamline based models. A demonstration algorithm similar to **ALLUVSIM** is presented. This algorithm, **ALLUVSIMCOND**, constructs conditional streamline based

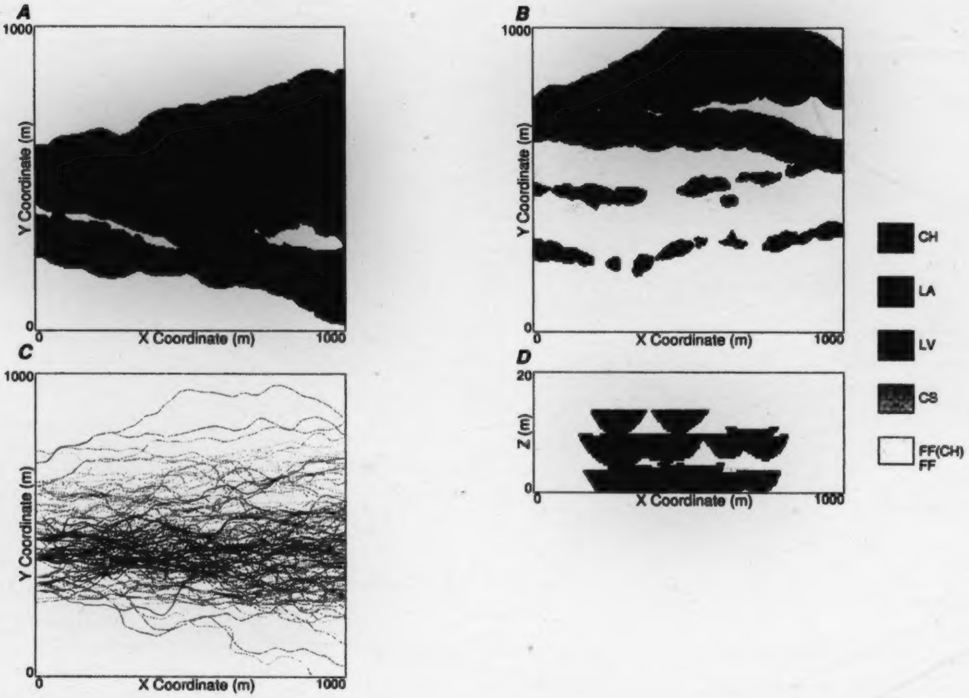

Figure 3.19: An example `ALLUVSIM` proximal SH type reservoir model. A - plan section (z=5m), B - plan section (z=10m), C - all streamlines (grey scale from 1=white to n=black) and D - cross section (x=10m). Note grey scale assignment for architectural elements is varied to aid in differentiating amalgamated elements.

models. These models are conditioned to identified channel fill elements, denoted as CH′, without differentiation of CH, LA or FF(CH) elements. These techniques are further developed in Pyrcz and Deutsch (2004)[97].

There are a variety of available methods that may be applied to condition complicated geologic models; (**1**) dynamically constrain model parameters during model construction to improve data match (Lopez et al., 2001)[65], (**2**) posteriori correction with kriging for conditioning (Ren et al.,2004)[105], (**3**) pseudo-reverse modeling (Tetzlaff, 1990) [124], (**4**) apply as a training image for multiple-point geostatistics (Strebelle, 2002)[120] and (**5**) direct fitting of geometries to data (Visuer et. al., 1998 and Shmaryan et. al., 1999)[132, 111]. Each of these techniques has significant limitations either in efficiency, robustness or the ability to retain complicated geometries and interrelationships.

In Section 3.2.1 the advantages of the streamline based simulation are discussed. These advantages include a flexibility and computational efficiency. This paradigm is amenable to a new method for the construction of conditional models. In this section a method, *updating streamline based simulation*, is developed and presented.

The essence of a streamline based model is associations of streamlines with associated geometric parameters and identified architectural elements. A prior model of streamline associations may be updated to reproduce well observations. The proposed procedure is; (**1**) construct the prior streamline based model conditioned by all available soft information, (**2**) interpret well data and identify CH′ element intervals, (**3**) sequentially update streamline associations to honor identified CH′ element intervals and (**4**) correct for unwarranted CH′ intercepts. This technique entails the translation of large-scale elements to honor small scale data; therefore, it is only suitable for settings with sparse conditioning data. Settings with dense data will be intractable and may result in artifacts.

### 3.4.1 The Prior Streamline Based Simulation

Streamline based models are very flexible. In Section 3.3.3 the `ALLUVSIM` algorithm is applied to construct a variety of fluvial reservoir type models. This flexibility allows for the direct integration of information related to fluvial style, systems tract and fluvial reservoir type.

Architectural element information from available well, production and seismic data, analog information and professional judgment may be integrated through the geometric and streamline association parameters. In addition, these models may be conditioned directly to areal and vertical trends in reservoir quality (see Section 3.3.1).

### 3.4.2 Interpreted Well Data

The hard data from wells are identified CH′ element intervals. CH′ elements are typically identified by erosional bases and normal grading. CH′ element fills often occur in multistory and multilateral configurations. CH′ elements often erode into previously deposited CH′ elements to form amalgamated elements (Collinson, 1996, Miall, 1996)[15, 73].

The geologic interpretation of well data is performed prior to the updating step. The input data includes the areal location for each vertical well and a list of CH′ element intervals with base and original top (prior to erosion). The geologic interpretation is often uncertain, especially with amalgamated CH′ elements. Alternate geologic interpretations may be applied to account for this uncertainty.

### 3.4.3 Updating Streamline Associations to Honor Well Data

The model is updated by modifying streamline associations to honor CH′ element intercepts. For each CH′ element interval identified in the well data the following steps are performed. (**1**) The horizontal position is corrected such that the CH′ element intercept thickness is within tolerance of the CH′ element interval thickness. (**2**) Then the vertical location is corrected such that the CH′ element intercept top matches the top of the CH′ element interval. Entire streamline associations are corrected to preserve the relationships between streamlines within a streamline association. For example, if a streamline association includes a set of streamlines related by meander migration, the entire set of streamlines defining representing a point bar is shifted. If individual streamlines were modified independently this would change the nature of the streamline association (see Figure 3.20).

The CH′ element intervals are sequentially corrected. The intervals are corrected in a random order. For each interval the nearest streamline $\kappa_{i,j}(\mathbf{s})$ is found and the nearest location on the streamline is found $\kappa_{i,j}(\mathbf{s}^0)$. The "distance" calculation includes user defined anisotropy factors to account for anisotropy in the geology.

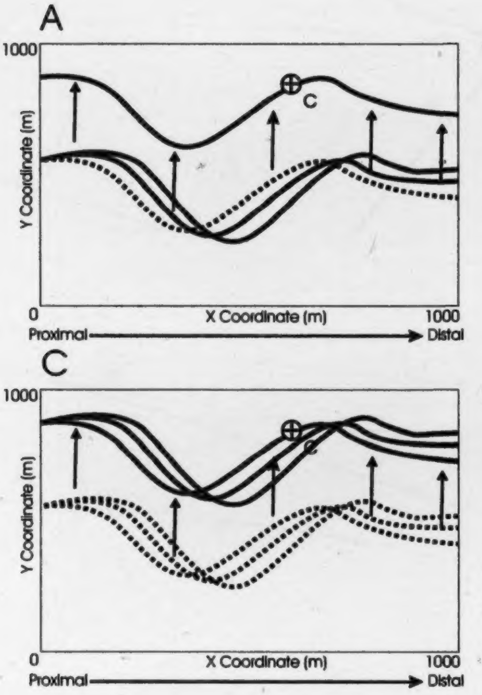
A
B
C
D
1000
Y Coordinate (m)
0
X Coordinate (m)
1000
Proximal
Distal
C

Figure 3.20: A schematic of updating individual streamlines and entire streamline associations. A - the correction is applied to the nearest streamline and C - the correction is applied to the entire streamline association. B and D - a braided streamline association. B - the correction is applied to the nearest streamline and D - the correction is applied to the entire streamline association. Modification of individual streamlines does not preserve interrelationships within streamline associations.

$$\Delta = \sqrt{\left(\frac{\Delta_x}{a_x}\right)^2 + \left(\frac{\Delta_y}{a_y}\right)^2 + \left(\frac{\Delta_z}{a_z}\right)^2} \tag{3.15}$$

where $\Delta_x$, $\Delta_y$ and $\Delta_z$ are the distance of separation in the horizontal ($x$ and $y$) and vertical ($z$) directions and $a_x$, $a_y$ and $a_z$ are anisotropy ranges.

The nearest streamline association is checked for previous conditioning. To prevent artifacts, a buffer distance, $\tau$, is set such that a streamline association may not be updated at a location $\mathbf{s}_i^0$ that is too close to any previously updated location. Closely spaced updates may lead to a discontinuities in the streamline association. This rule may be expressed as:

$$|\mathbf{s}_i^0 - \mathbf{s}_j^0| > \tau \; \forall \; j = 1, \ldots, i-1 \tag{3.16}$$

where $\mathbf{s}_i^0$ is the location along the streamline association closest to the hard data and $\mathbf{s}_j^0 \; \forall j = 1, \ldots, i-1$ is all previous conditioning applied to this streamline association.

If there is previous conditioning, an additional acceptance criteria is applied to prevent unrealistically large vertical undulation within a streamline association.

$$|z(\mathbf{s}^0) - z_{CH_i}| > \tau_z \tag{3.17}$$

where $z(\mathbf{s}^0)$ is the elevation (accounting for stratigraphic coordinates) of the of the streamline closest to the hard data, $z_{CH_i}$ is the elevation of the CH$'$ element interval and $\tau_z$ is the maximum streamline deviation in the vertical direction.

The criteria controls the level of vertical modification that may be applied in a streamline association. A small $\tau_z$ will result in constant z coordinate streamlines. This should be the case since any irregularities should be handled with stratigraphic transformations prior to model construction. A small $\tau_z$ will also limit the frequency of a single streamline association being conditioned by more than one interval. A large $\tau_z$ allows for greater flexibility in conditioning but may result in an unrealistic level of independent undulation between streamline associations.

There are three possible cases; (**1**) there is no previous conditioning, (**2**) the streamline association has been previously updated and passes both criteria in Equation 3.16 and 3.17 and (**3**) the streamline association has been previously updated and fails the criteria in Equation 3.16.

In the first case, the streamline association may be freely translated in the transverse direction to honor the specific conditioning. Since there is no longitudinal

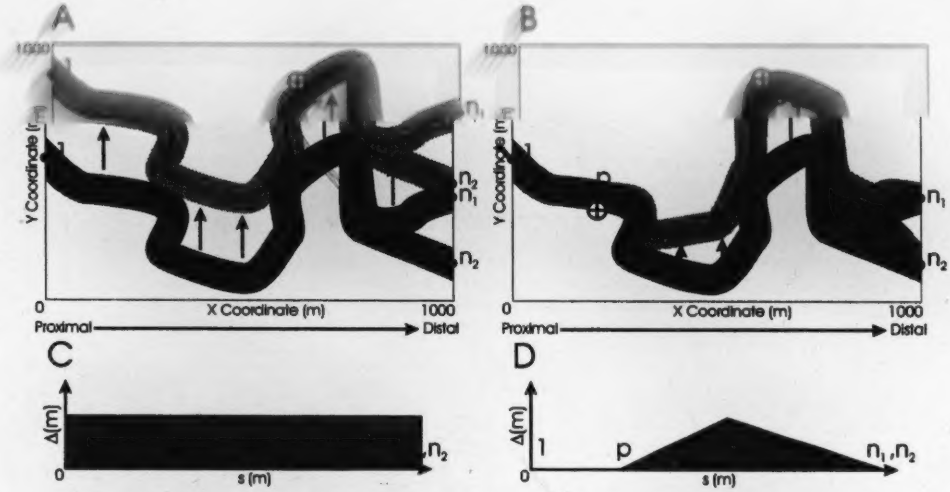

Figure 3.21: An illustration of methods for updating streamline associations to well data. For this example there are two streamlines in the streamline association representing an avulsion event that are corrected to honor conditioning data (c). A - the case with no previous conditioning. The streamline is translated in the lateral direction to honor the CH′ interval. B - the case with previous conditioning. The streamline is translated with a triangular difference distribution with the streamline held constant at the control node of previous conditioning ($p$) and beyond ($p \rightarrow 1$) and at the last control nodes ($n_1$ and $n_2$). C - the transverse correction with respect to location along the streamline (s). D - the smooth correction applied with respect to location along the streamline.

component to the translation there is no need to extrapolate to the proximal or distal edges of the model (see A and C in Figure 3.21).

For the second case, a smooth correction method is applied to the streamline associate (see B and D in Figure 3.21). A step vector is constructed oriented from $\mathbf{s}_i^0$ to the location of the well interval. The scale of the step of the sense is determined by an iterative procedure described later.

For the third case the streamline association is rejected and the next closest streamline association is then considered.

### 3.4.4 Iterative Procedure for Updating Streamline Associations

Modifications of streamline associations has an impact on CH′ element geometry. It would be difficult to directly calculate the precise translation of a streamline to result in the correct interval thickness at a well location. A simple iterative method is applied to correct the well intercept thickness. The thickness of the CH′ element from a streamline association is calculated at the vertical well location. The error is calculated, if the thickness is less than indicated by the conditioning then the streamline association is shifted towards the well location. If the thickness is greater than indicated by the conditioning then the streamline association is shifted away from the well location. The parameters for this iterative technique are the initial step size, the dampening factor and the thickness tolerance.

$$s^i = s^0 \cdot (1 - \delta)^{(i-1)} \tag{3.18}$$

where $s^n$ is the $i^{th}$ step size, $s^0$ is the initial step size and $\delta$ is the dampening factor (between 1.0 and 0.0). The limit of the sum of infinite steps may be calculated to represent the maximum distance a streamline association may be shifted given an initial step size, $s^0$, and dampening factor, $\delta$.

$$\sum_{i=1}^{\infty} s^i = \frac{s^0}{\delta} \tag{3.19}$$

By setting the initial step size to the maximum channel width and the maximum migration as the model extent transverse to the primary flow direction the required dampening factor may be calculated.

The thickness tolerance may be set to a fraction of the vertical model resolution. When the difference between the interval from well conditioning and the CH′ element intercept is less than the tolerance the convergence criteria is satisfied. The closest node, $\kappa_{i,j}(\mathbf{s}^0)$, is locked and is not modified by subsequent updating.

Once the CH′ element intercept thickness is corrected then the vertical location is corrected by applying a vertical shift to the streamline association. The procedure is repeated for all identified CH′ element intercepts. If there is no previous conditioning the entire streamline association is shifted vertically. If there is previous conditioning then a smooth correction is applied (similar to the smooth correction applied for the horizontal correction). It is possible that CH′ elements may intercept wells where such intercepts are not indicated. These unwarranted intercepts are corrected.

### 3.4.5 Correction for Unwarranted Well Intercepts

The correction for unwarranted CH′ element intercepts applies a robust iterative technique. For each unwarranted CH′ element intercept the associated streamline association is checked for conditioning. If the streamline association is not anchored to conditioning data then the streamline association may be translated in the direction transverse to the primary flow direction. If the streamline association is anchored to conditioning data then the smooth modifications may be applied. These modification are the same as applied in the previously indicated first and second cases for updating.

The streamline association is modified until the thickness of the unwarranted CH′ element intercept reaches zero. For each iteration the step size of the modification is increased and the direction is reversed. This method is robust since it does not become trapped with complicated streamline associations. This methodology is illustrated in Figure 3.22 with a complicated setting.

### 3.4.6 Example Conditional Streamline Based Models

The `ALLUVSIMCOND` algorithm was applied to construct a conditional CH′ element model. The streamlines include braided low to high sinuosity morphology. A single well is included with two CH′ element intervals identified. Cross sections and streamline plan views of the prior and updated models are shown in Figure 3.23. The morphology of the streamlines is preserved while the well intercepts are honored.

## 3.5 Stochastic Inclined Heterolithic Strata

Inclined heterolithic strata (IHS) are of special interest in CB type reservoirs since they (**1**) are often a dominant component of these reservoirs, (**2**) often include a large component of good reservoir quality, (**3**) have inherent patterns of heterogeneity that may have a significant impact on reservoir response and (**4**) they have complicated geometries that are often difficult to model. The `ALLUVSIM` algorithm is applied to generate realistic models of IHS set geometries.

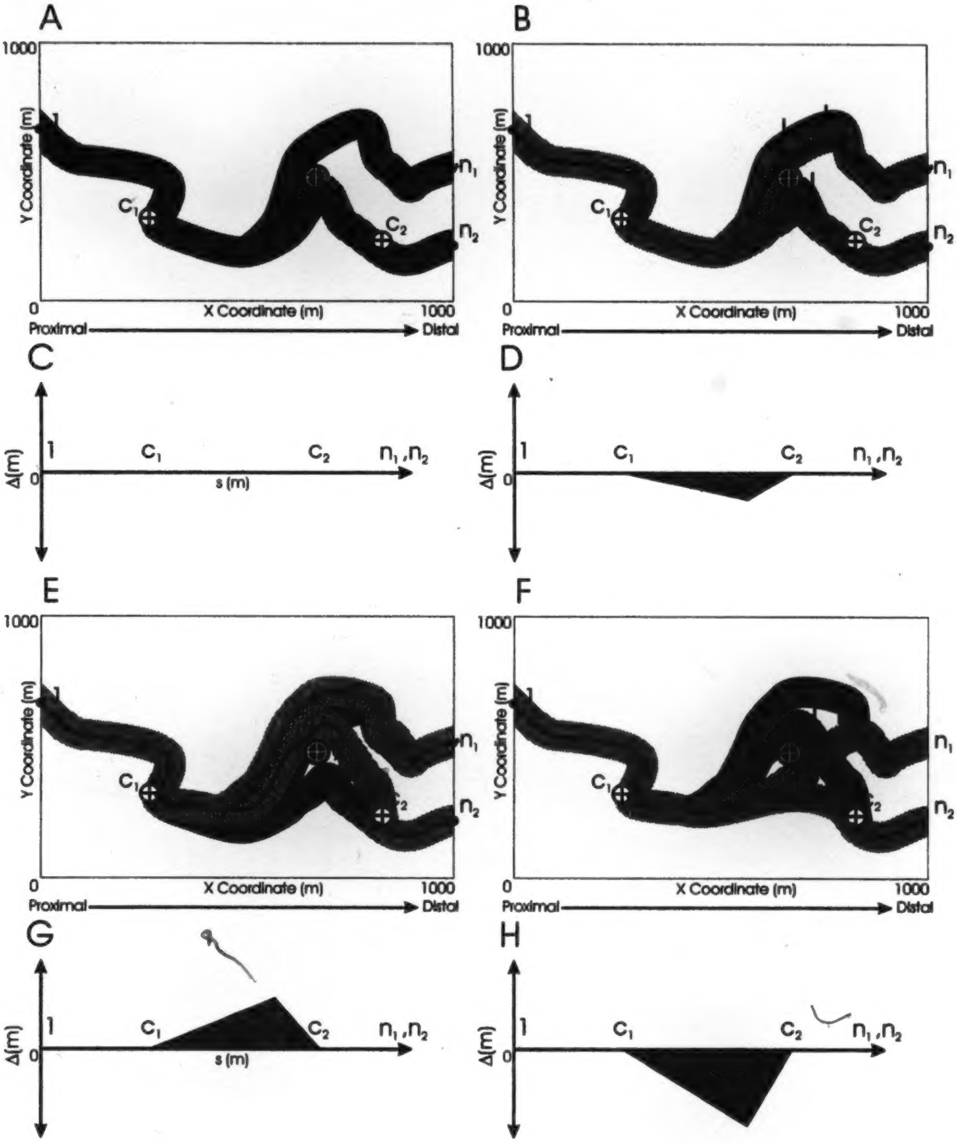
A
B
C
D
E
F
G
H
1000
0
Y Coordinate (m)
X Coordinate (m)
Proximal
Distal
1
C1
C2
n1
n2
Δ(m)
s (m)
n1,n2

Figure 3.22: An illustration of methods for correcting streamlines associations to remove unwarranted well intercepts. The two streamlines are related by avulsion in the streamline association and there are two previously conditioned locations ($C_1$ and $C_2$). A and C - the initial streamline association prior to correction. B and D - the first smooth modification. E and G - the second iteration. F and H - the third iteration removes all unwarranted intercepts with this streamline association.

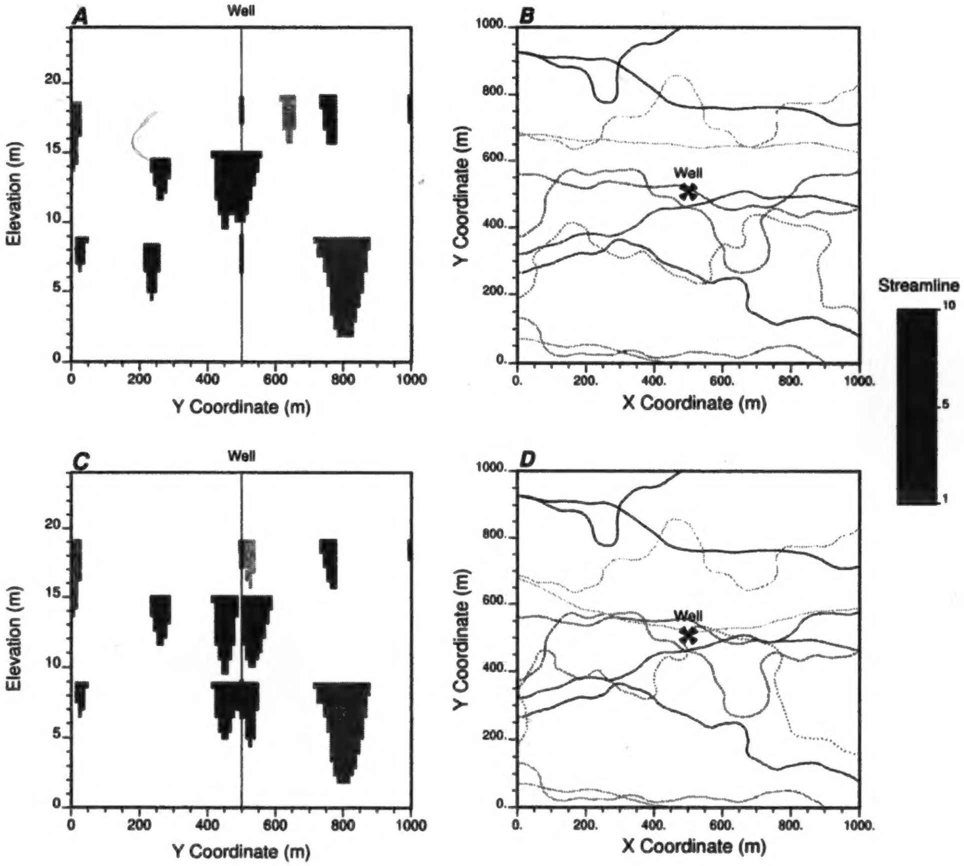

Figure 3.23: An example conditional streamline based model from `ALLUVSIM`.

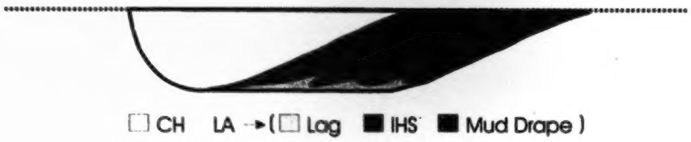

Figure 3.24: A schematic dip section of the morphology of IHS sets associated with meandering fluvial systems. Adapted from Thomas et al. (1987)[125]. Compare to the architectural element model in the `ALLUVSIM` algorithm (see Figure 3.8).

### 3.5.1 Stochastic Inclined Heterolithic Strata Geologic Settings

Two examples of reservoir settings that have significant components of IHS sets are the McMurray Formation (Mossop and Flach, 1983, Thomas et al., 1987)[76, 125] and Daqing Oil Field, China (Jin et al., 1985, Thomas et al., 1987)[53, 125]. In both of these examples the IHS sets developed from a meandering fluvial depositional setting. IHS sets have also been identified in deltaic channels, estuarine channels, low sinuosity streams and deepwater channels (Thomas et. al., 1987)[125].

IHS sets are characterized as siliciclastic sedimentary sequences that are parallel to sub parallel strata that possess original dips. These strata generally result from the lateral growth of large-scale bedforms such as point bars (LA element). Individual beds are characterized as growth units separated by accretionary surfaces (Thomas et. al., 1987)[125].

These accretionary surfaces are preserved at intervals along the growth of lateral accretion elements and are recognized in geomorphology by the surface expression of meander scrolls in point bars. These surfaces are the result of cycles in autogenic controls that influence the loading index of a river. Traditional models recognize coarse and fine grained couplets occurring between these surfaces. These fine grained sediments are often associated with estuaries during the transgressive systems tract. There may be hierarchies of accretionary surfaces.

A schematic of a typical IHS morphology for a mixed to suspended load meandering river is shown in Figure 3.24. This model is adapted from Thomas et al. (1987)[125] and is similar to the *simple point-bar model* from Galloway and Hobday (1996)[39].

IHS sets demonstrate a variety of characteristic trends and features. For example Thomas et. al. (pg. 133-134, 1987)[125] identified seven possible grain size fining trends associated with IHS deposits. These grain size trends include fining upwards, fining distal and fining perpendicular to the IHS sets. Often mud drapes are preserved along the accretionary surfaces. These features may have a significant control of the porosity and permeability distributions and flow performance.

The mud drapes along accretionary surfaces and associated property trends often have significant impact on reservoir response. This has been confirmed in a recent analog study based on high resolution ground penetrating radar and outcrop to model a single IHS set (Li and White, 2003)[63]. The impact of IHS morphologies on water flooding in the Daqing field is discussed by Jin et al., (1985)[53]) and on stream assisted gravity drainage (SAGD) in the McMurray Formation by Smith, (1985)[113].

These features should be included in stochastic models with IHS sets present. Yet, the geometry of accretionary surfaces in IHS sets is complicated. The geometry is the result of channel geometry and the meander evolution of low to high sinuous channels. These geometries have been discussed by authors such as Diaz-Molina (1993), Thomas et al. (1987) and Willis (1993))[32, 125, 139]. IHS deposits often include hierarchies of composite sets with vertical and lateral stacking. Lateral stacking results in imbricated IHS sets. These are caused by large-scale flooding and associated high rates of bank erosion. Vertical stacking is caused by system aggradation resulting in subsequent IHS sets with erosional / truncated contacts with the older IHS sets.

### 3.5.2 Stochastic Inclined Heterolithic Strata Geologic Models

Li and White (2003)[63] demonstrated methodologies for simulating mud drapes along accretionary surfaces with a single simple IHS set. The `ALLUVSIM` algorithm provides an opportunity to capture the complicated geometries resulting from laterally and vertically stacked IHS composite sets in a realistic manner. These models are unconditional. They may be applied as training images. These models were developed in Pyrcz and Deutsch (2004)[102].

The `ALLUVSIM` algorithm was modified for the construction of IHS geometry models. **(1)** The CH profile was modified to reproduce sigmoidal accretionary surface geometries. **(2)** The base of each CH element is stored, eroded and written to a file. **(3)** Only channel fill elements are considered.

### Sigmoidal Geometries

A variety of sigmoidal geometries are often observed in IHS sets (see mixed and suspended load IHS profiles in Thomas et al., 1987[125]). A multiplicative component was added to the CH element profile (see Equations 3.7 and 3.8). This multiplier is based on a parabola constrained to unity at the thalweg and the point bar edge of the channel and to a maximum sigmoidal multiplier ($0 > i > 1$) at the mid point.

$$F = 1 + i \cdot \left\{ \left[ \frac{\mathbf{w} - \frac{W(\mathbf{s})}{2} \cdot (1 + a(\mathbf{s}))}{\frac{W(\mathbf{s})}{2} \cdot (1 - a(\mathbf{s}))} \right]^2 - 1 \right\} \tag{3.20}$$

where $W(\mathbf{s})$ is the channel width and $a(\mathbf{s})$ is the thalweg location at location $\mathbf{s}$ along the streamline and $\mathbf{w}$ is the location normal to the streamline.

The application of the sigmoidal multiplier is illustrated in Figure 3.25 and example channel profiles are shown in Figure 3.26. The result is a simple parameterized CH element profile that may reproduce a variety of accretionary surface geometries.

### Erosion Rules

For the specific construction of IHS set models `ALLUVSIM` algorithm was modified to store the bases of all CH elements. These surfaces were post-processed to reproduce erosion rules based on the sequence of streamline evolution. Accretionary surfaces are eroded by younger accretionary surfaces.

### Architectural Elements

The levees and crevasse splay elements are not considered in this model. These elements are often eroded by subsequent channels in settings dominated by amalgamated lateral accretion deposits and the exclusion improves computational efficiency.

## 3.5.3 Example Stochastic Inclined Heterolithic Strata Model

An example stochastic IHS model was constructed based on the study of IHS sets in the McMurray Formation by Mossop and Flach (1983)[76]. This study identifies geometric parameters that may be reproduced with this model such as accretionary surface dips and IHS set thickness and also includes paleo-flow information such as

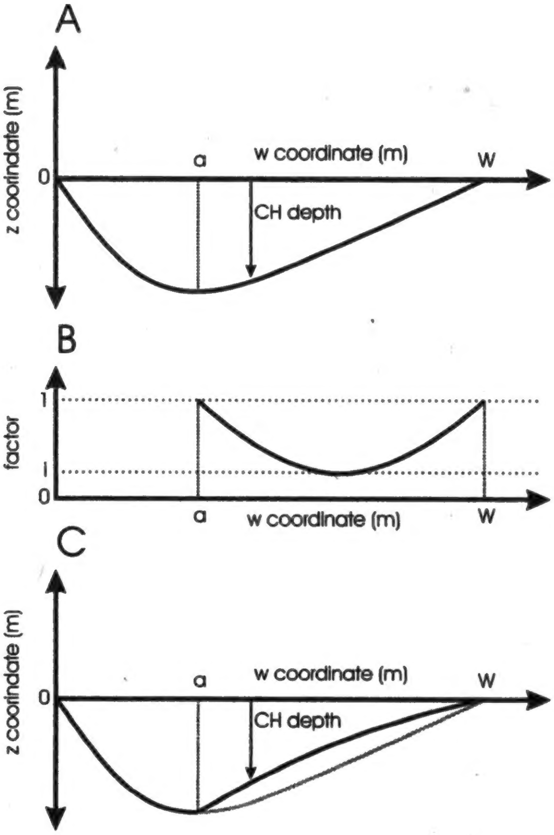
A
z coorindate (m)
0
a
w coordinate (m)
W
CH depth
B
factor
1
1
0
a
w coordinate (m)
W
C
z coorindate (m)
0
a
w coordinate (m)
W
CH depth

Figure 3.25: A schematic of the sigmoidal channel profile calculation. A - channel profile based on Equation 3.7. B - sigmoidal multiplier applied to CH depth. C - modified channel profile. Note *a* is the thalweg location and *W* is the channel width.

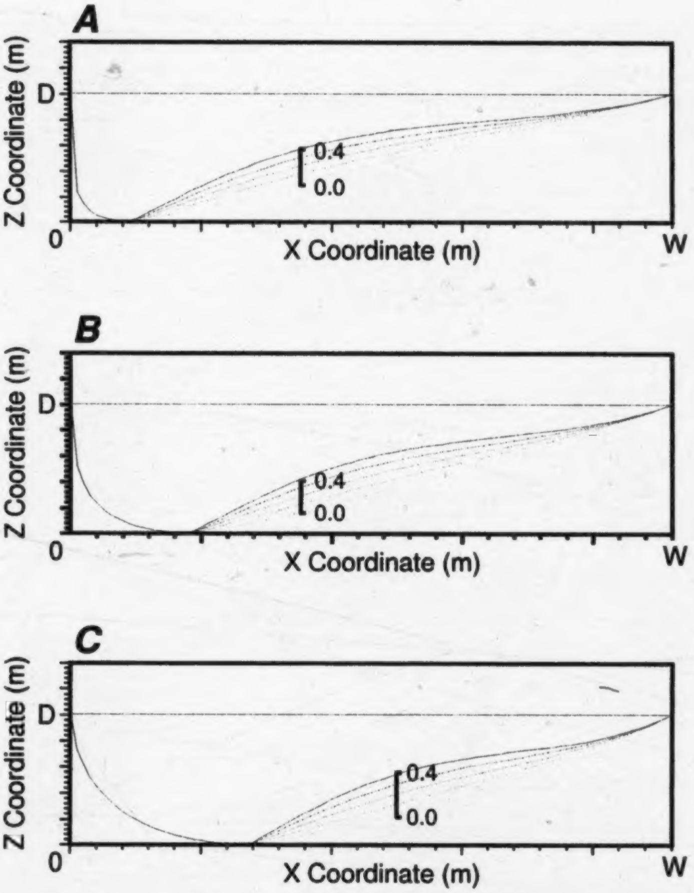

Figure 3.26: Examples of the modified sigmoidal channel profile. A - thalweg location $a = 0.1$ and intensities $i = 0.0, 0.1, \ldots, 0.4$. B - thalweg location $a = 0.2$ and intensities $i = 0.0, 0.1, \ldots, 0.4$. C - thalweg location $a = 0.4$ and intensities $i = 0.0, 0.1, \ldots, 0.4$. Note $W$ is the channel width and $D$ is the channel depth.

| Parameter | Value |
|---|---|
| Channel Depth | $25 - 40\ m$ |
| Channel Width:Depth | 16 |
| Sinuosity | 1.6 |
| Sinuosity Wavelength | $2500\ m$ |
| Accretionary Surface Dip | $4^0$ |
| Maximum Isopach IHS Bed Thickness | $2.0\ m$ |
| Maximum Channel Migration | $30\ m$ |

Table 3.3: Morphological characteristics of McMurray formation paleochannels from Mossop and Flach (1983)[76].

channel width to depth ratio, channel depth and channel sinuosity. These parameters are shown in Table 3.3. The maximum IHS bed thickness (isopach) is combined with the accretionary surface dip to calculate the maximum channel migration for each migration step.

$$\Delta_{max} = \frac{T_{max}}{sin\phi} \tag{3.21}$$

where $\Delta_{max}$ is the maximum channel migration step, $T_{max}$ is the maximum IHS bed thickness and $\phi$ is the dip of the accretionary surfaces.

Two realizations were calculated with these parameters. A plan view of the migrating channel streamlines and three cross sections are shown in Figures 3.27 and 3.27.

## 3.6 Discussion

This chapter has developed a new paradigm for the construction of stochastic fluvial models. The streamline based models have been shown to be (**1**) adaptable to the continuum of fluvial reservoir styles, (**2**) conditional to areal and vertical trends and well observations, (**3**) able to construct realistic models of fluvial architecture and (**4**) computationally efficient.

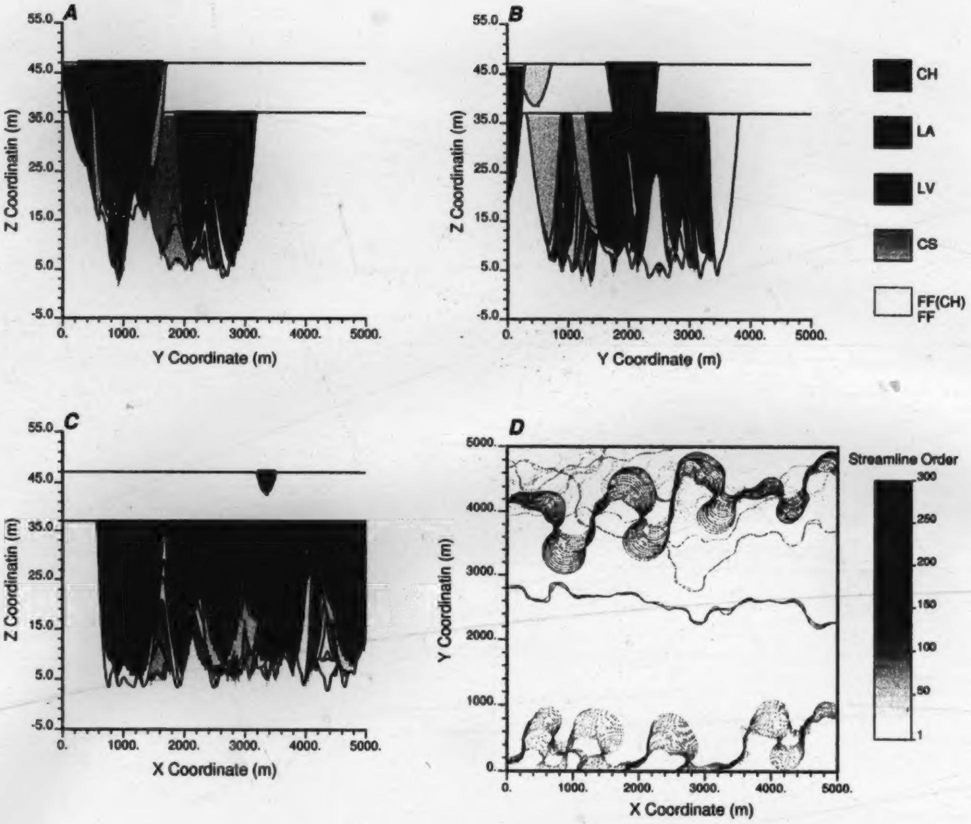

Figure 3.27: First realization of IHS sets generated with the `ALLUVSIM` algorithm and parameters based on the Mossop and Flach (1983)[76] study of the McMurray Formation. A - cross section at $X = 1500$ meters, B - cross section at $X = 4000$ meters, C - long section at $Y = 2500$ meters and D - all of the streamlines applied to construct this model. Few streamlines were generated for visualization. In the McMurray Formation IHS sets are more extensive and FF is poorly preserved.

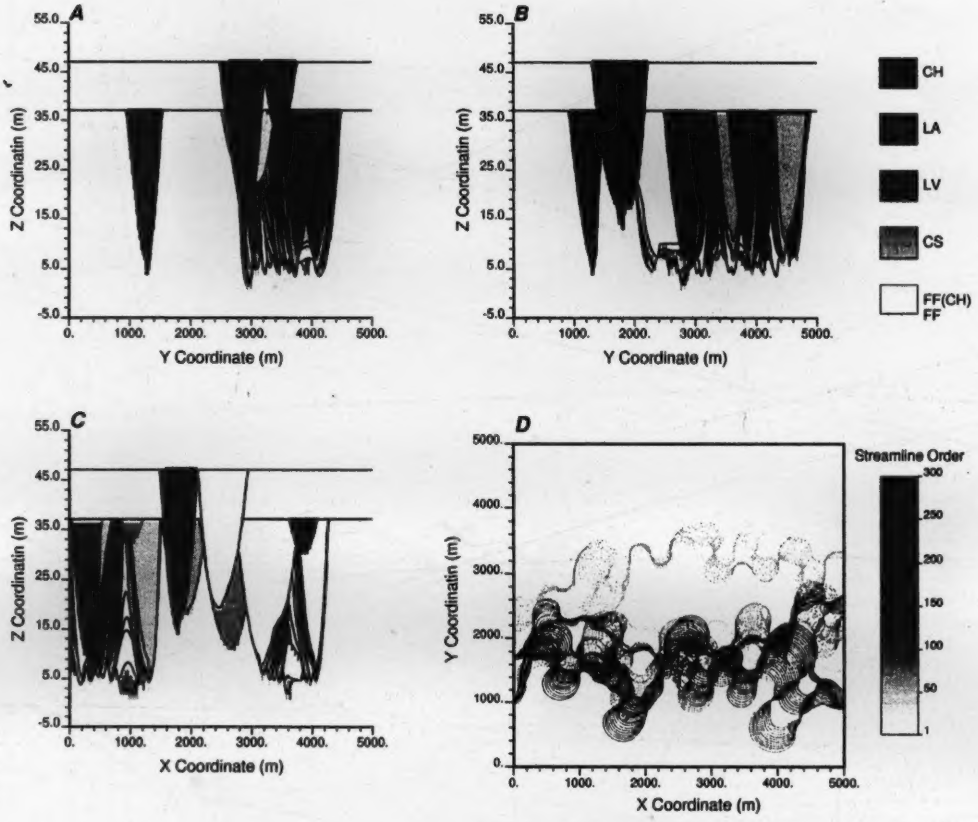

Figure 3.28: Second realization of IHS sets generated with the `ALLUVSIM` algorithm and parameters based on the Mossop and Flach (1983)[76] study of the McMurray Formation. A - cross section at $X = 1500$ meters, B - cross section at $X = 4000$ meters, C - long section at $Y = 2500$ meters and D - all of the streamlines applied to construct this model. Few streamlines were generated for visualization. In the McMurray Formation IHS sets are more extensive and FF is poorly preserved.

# Chapter 4

# Turbidite Reservoir Models

Surface based simulation applied to deepwater depositional systems is developed in this chapter. Surface based simulation is amenable to settings with hierarchies of strataform sediments such as distal turbidites lobes. A technique called "hierarchical trends" is developed for the construction of associated surface-constrained property trends including features such as mud drapes and normal grading. These features may result in geologic barriers and baffles to flow and may have a significant impact on oil and gas production.

Section 4.1 discusses turbidite heterogeneity and architectural element analysis and provides some details on geometry of turbidite lobes. Section 4.2 introduces hierarchical trend models and an automatic trend fitting algorithm based on mathematical morphology operations. Section 4.3 introduces a generalized surface based sequential simulation algorithm and a related visualization program. These techniques were extended beyond initial surface based simulation work by Xie and Deutsch (2000)[140] in that the surfaces honor gradational, erosional contacts and missing data contacts. A surface based simulation algorithm tailored to distal turbidite lobes is developed in Section 4.5. This algorithm accounts for the geometry and stacking pattern of small scale turbidite flow event deposits within turbidite lobes. Section 4.6 demonstrates the application of the stochastic surface based turbidite model in a geostatistical workflow based on the Cengio, Italy turbidite fan system.

| Rank | Architectural Elements |
|---|---|
| $1^{st}$ Order | Beds (i.e. $T_a$, $T_b$, $T_c$, $T_d$, $T_e$) |
| $2^{nd}$ Order | Single, Sediment Unit / Flow Event Deposit |
| $3^{rd}$ Order | Channel / Lobe Fill |
| $4^{th}$ Order | Channel / Lobe Complex |
| $5^{th}$ Order | Multi-story Channel / Lobe Stack |
| $6^{th}$ Order | Fan Complex |

Table 4.1: The hierarchy of architectural elements in turbidites (adapted from Ghosh and Lowe, 1993)[41]).

## 4.1 Deepwater Reservoirs

Turbidite systems represent important exploration targets. There has been a rapid increase in exploration in both convergent and passive margins in the last 20 - 30 years (Stow and Mayall, 2000)[117]. The concept of architectural elements has been recently extended to the turbidite setting. Ghosh and Lowe (1993)[41] constructed a hierarchy of process based architectural elements (see Table 4.1) and Pickering et al. (1995)[92] presented a scheme focused on internal and external geometry.

The Ghosh and Lowe (1993)[41] scheme is applied in this chapter. Individual homogeneous components are identified as $1^{st}$ order architectural elements. These may be individual components of the Bouma sequence ($T_a$ - $T_e$) (Bouma, 1962)[6] and other coarser components. The $2^{nd}$ order architectural elements are composed of single or multiple $1^{st}$ order elements that represent products of individual flow events. $3^{rd}$ and $4^{th}$ order architectural elements represent reservoir scale features such as lobes or channel levee systems. $5^{th}$ and $6^{th}$ order architectural elements are at basin scale.

There has been a great deal of research into the internal and external geometries and stacking patterns of architectural elements associated with turbidites (Johnson et al., 2001; Satur et al., 2000; Shanmugam, G., 2000; Stow and Johansson, 2000; Stow and Mayall, 2000)[54, 108, 109, 116, 117]. Stochastic methodologies are required that reproduce architectural elements while accounting for the inherent uncertainty. An approach using stochastic surface based simulation is introduced in Section 4.5 to model architectural elements associated with compensational cycles

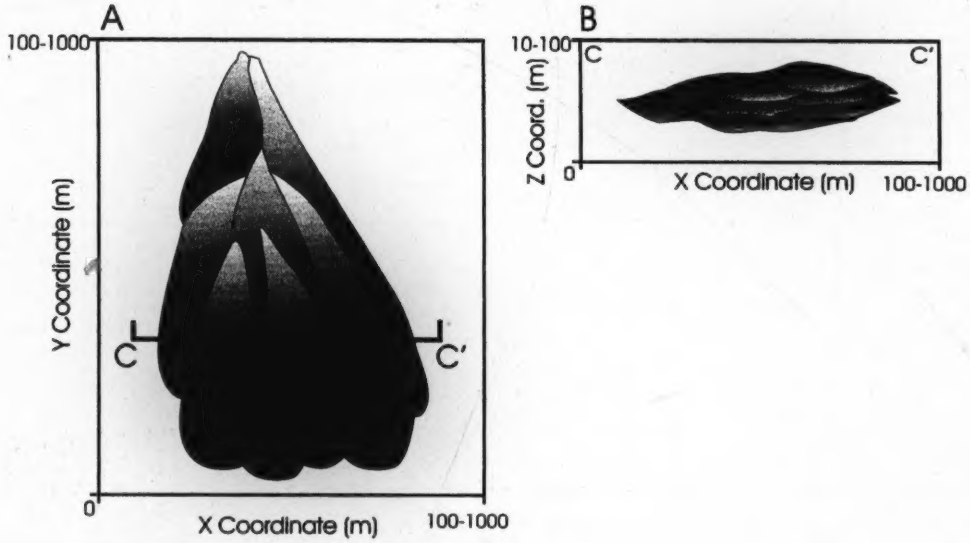

Figure 4.1: The internal and external geometry of turbidite lobes: A - plan view and B - cross section. The internal geometry is based on flow events with a compensational stacking pattern.

in distal planar lobes. This new algorithm is a generic tool that functions under a variety of facies model assumptions; therefore, it is independent of the recent debate concerning deep-sea clastic terminology, origin and nature (Shanmugan, 2000)[109].

### 4.1.1 Small Scale Geometries

Small scale geometries are represented by $1^{st}$ and $2^{nd}$ order architectural elements (Ghosh and Lowe, 1993)[41]. These elements have a thickness of less than a meter to a few meters and are generally below the resolvable limit of seismic, but may impose significant control on the reservoir response (Jensen et al., 1994; Satur et al., 2000; Slatt et al., 1998)[52, 108, 112]. These elements are referred to as flow event deposits in this chapter.

Stow and Johansson (2000)[116] noted that the small scale geometries (**1**) often mimic the large scale geometry and (**2**) often display a variety of stacking patterns, such as compensational bedding. For example, a lobe may be filled by flow events with lobe geometry and compensational cycles (see Figure 4.1).

Compensation cycles are defined as a main characteristic of ancient sandstone

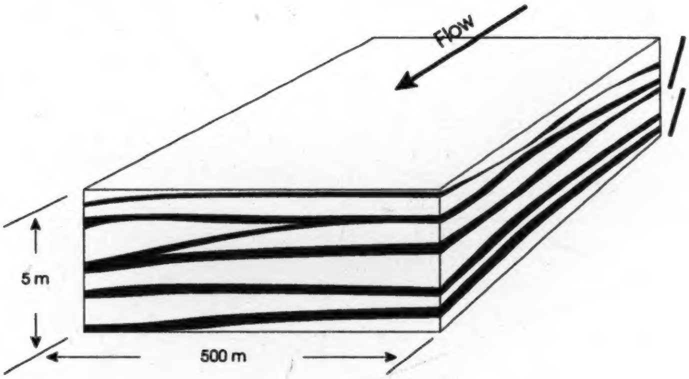

Figure 4.2: A drawing similar to the schematic illustration of compensational bedding from Mutti and Sonnino (Figure 2, 1981)[79].

lobes (Mutti and Normark, 1987; Mutti and Normark, 1991; Galloway and Hobday, 1996; Stow et al., 1996)[77, 78, 39, 118] and are considered ubiquitous in distal lobes (Mutti and Sonnino, 1981)[79]. These cycles are the result of preferential filling of topographic lows. In vertical section, compensational cycles are identified as multiple thickening upward sequences. These cycles are illustrated schematically in Figure 4.2.

### 4.1.2 Large Scale Geometries

Large-scale sand bodies in distal turbidites have been characterized as massive sand facies associations (MSFA) by Stow and Johansson (2000)[116] or a sandy frontal splay (Posamentier, 2003)[93] and are classified as $3^{rd}$ and $4^{th}$ order architectural elements by Ghosh and Lowe (1993)[41]. They include reservoir scale lobes (Stow and Johansson, 2000)[116] and may be correlated in well log and characterized by seismic survey. These elements are referred to as lobes in this chapter. These geometries may be characterized with hierarchical trend models (see Section 4.2) and surface based simulation (see Sections 4.3 and 4.5).

## 4.2 Hierarchical Trend Models

There is a hierarchy of controls on sedimentation in the deepwater (see scheme developed by Bouma (2000)[7]). These controls constrain trends within reservoir properties. For example turbidite lobes are commonly recognized by their $2^{nd}$ order fining upward trends on the order of decimeters to a few meters (Bouma, 1962)[6]. Over the $3^{rd}$ order architectural elements allogenic controls such as eustacy become significant. Since the majority of turbidite deposition occurs during the FSST and LST these systems are often prograding and exhibit coarsening upward trends (Catuneanu, 2003)[12].

The combined influence of this hierarchy of controls results in hierarchies of superimposed trends. Geostatistical models may be applied to calculated models of hierarchies of architectural elements (Deutsch and Wang, 1996)[28]. The surface based techniques described in Sections 4.3 and 4.5 may be applied to construct hierarchical turbidite models, yet there is no efficient technique available to integrate the information related to hierarchical trends. Manual methods to construct these hierarchical trend models are not feasible given the likely large number of architectural elements and simulated models. A flexible methodology is required to automatically construct trend models based on architectural element models and trend models as various scales.

The proposed technique is to (**1**) construct trend models that capture features within a hierarchy of architectural elements and then (**2**) correct this trend model to honor global features such as global mean, areal and vertical trends that are based on well data and large scale production and seismic information.

### 4.2.1 Construction of Hierarchical Trend Models

The steps in constructing hierarchical trend models are to (**1**) calculate the significant coordinates at each hierarchical order, (**2**) determine relative trend functions with respect to the significant depositional directions for the calculation of trend components and (**3**) combine the trend components to calculate the composite trend model at all locations.

#### Calculation of Depositional Coordinates for Hierarchical Trend Models

For the construction of a hierarchical trend model, the location relative to the primary sedimentation axis must be determined for each nested hierarchy and for each location in the model. This coordinate system is distinguished from regular Cartesian coordinates by the qualifier *depositional coordinates*. This axis represents the central axis of flow in a turbidite lobe in a submarine setting. A potential coordinate transform is illustrated below.

$$\mathbf{u} \rightarrow (\mathbf{u}_l^i, \mathbf{u}_t^i, \mathbf{u}_v^i) \;\; i = 1, \ldots, n^o \tag{4.1}$$

where $n^o$ is the number of hierarchical orders (superscript $i$) considered and $\mathbf{u}_l^i$ and $\mathbf{u}_t^i$ are proportional or absolute measures from the flow axis at each hierarchical order in the longitudinal (subscript $l$) and transverse (subscript $t$) directions. $\mathbf{u}_v^i$ is the proportional measure between the top and base of the architectural element or absolute measure from the bottom or top of the architectural element (subscript $v$). The choice between proportional and absolute measure (reflecting onlap and truncation) depends on the setting. Proportional measurements are assumed for the following work. This is reasonable in the low energy distal deepwater given the lack of erosion and shallow gradients. In this case, trend functions may be modeled for a set range $[0, 1]$ in proportional units. The following is a description of general techniques for calculating depositional coordinates for different scenarios of available information.

### Additional Details on the Calculation of Depositional Coordinates

The technique for calculating depositional coordinates depends on the available information. Three cases are discussed. (**1**) Primary flow axis and architectural elements are provided by the modeling algorithm. In this case the depositional coordinates may be directly calculated. This is the case with distal turbidite lobe model proposed in Section 4.5 and streamline based simulation discussed in Section 3.2. (**2**) The hierarchy of architectural elements are available but there is no information available with respect to primary flow axis. This is the case with geostatistical methods that simulate architectural elements directly such as object and surface based models. (**3**) There is no information available related to hierarchies of architectural elements. This is the case with pixel based geostatistical models.

Depositional coordinates may be obtained directly from the modeling algorithm, if the algorithm utilizes channel centerlines or primary flow axis to generate architectural elements. This is the easiest technique as the primary flow axis and associated architectural elements are known and the depositional coordinates may be calculated by scanning through the models and calculating the distance measures relative to the flow axis and the base and top of the architectural element. Also, errors in the calculation of architectural elements and axis of flow are avoided (see discussion below).

When flow axis or architectural element information is not available, then methods to automatically identify architectural elements and primary flow axis with mathematical morphology operations may be applied.

Mathematical morphology operations are widely applied to image processing as an automated tool for analyzing large data sets often associated with imagery (satelite, aerial photgraphy, quality control in manufacturing). Mathematical morphological operations include erosion, dilation, opening, closing, distance functions and skeleton transforms. These operations are performed with specified structural elements. The series of operations and structural elements are chosen in order to assess significant image features (Matheron, 1975; Stoyan, Kendall and Mecke, 1987, p. 19; Vincent, 1993, p. 255)[68, 119, 130].

### Automatic Identification of Architectural Elements

The architectural elements may be approximated by geo-objects with an efficient method for connectivity calculation developed by Deutsch (1998)[20]. This case is most problematic as error may occur in the identification of architectural elements and this will reduce the reliability of the calculated flow axis. For example, contacts without change in lithofacies category are not recognized and architectural elements may be incorrectly joined (see Figure 4.3). User intervention is required to ensure that the architectural elements that are calculated are representative of the geologic setting. This approach would likely be laborious and ambiguous.

### Automatic Identification of Primary Flow Axis

The primary flow axis may be automatically calculated with the skeleton transform of mathematical morphology. Image cleaning may be required prior to the skeleton transform if the architectural elements have holes or are not contiguous. These features will interfere with the subsequent skeleton transform. The skeleton transform is homotopic; therefore, holes and connected components in the original set are retained in the skeleton (Vincent, 1993, p. 279)[130] (see Figure 4.4 for a demonstration). This cleaning may be accomplished by mathematical morphology

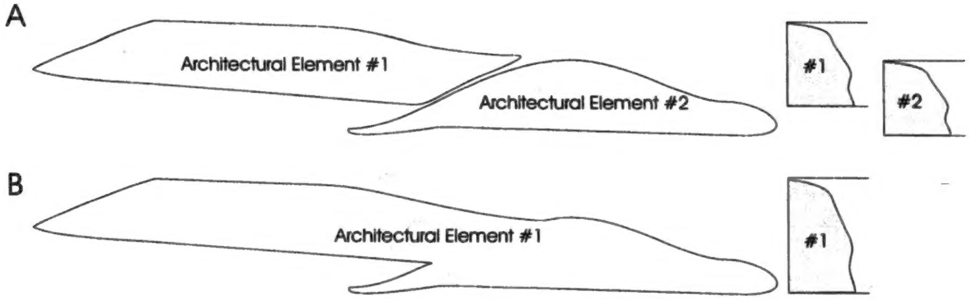

Figure 4.3: An schematic of a potential error in identification of architectural elements based on connected geo-objects. Multiple geo-objects may be incorrectly combined. A - the correct interpretation. B - the incorrect interpretation. This error results in an incorrect application of the trend model.

operations such as opening (erosion and then dilation) to remove disconnected fragments and then closing (dilation then erosion) to remove holes (Stoyan, Kendall and Mecke, 1987)[119] or by `MAPS` (Deutsch, 1998a)[20].

A calibration is required to select the appropriate structural element, so that the resulting architectural elements best describe the underlying geology and result in well behaved skeletons. During the opening operation, too large of an element will eliminate geo-objects and remove details while too small of an element will leave isolated fragments. In the closing operation, too large of an element will remove geo-object detail while too small of an element will leave holes in the geo-objects (a demonstration of dilation and erosion is shown in Figure 4.5).

Once the image cleaning is complete then the skeleton transform is applied. The steps include: (**1**) calculation of a distance function, (**2**) selection of anchor points and (**3**) homotopic erosion (Vincent, 1993, p. 279)[130].

The distance function (the city block distance from the edge of the architectural elements) is calculated for each of the architectural elements. From this distance function crest points are identified. These crest points are chosen as locations with one or no other adjacent cells with a larger distance value. Then crest points are selected as anchor points such that there are no two adjacent anchor points.

Then, homotopic erosion is applied to the architectural element with the anchor points preserved. For computational efficiency, a look up table indexing of all possible neighbourhood configurations is calculated a-priori and erosion config-

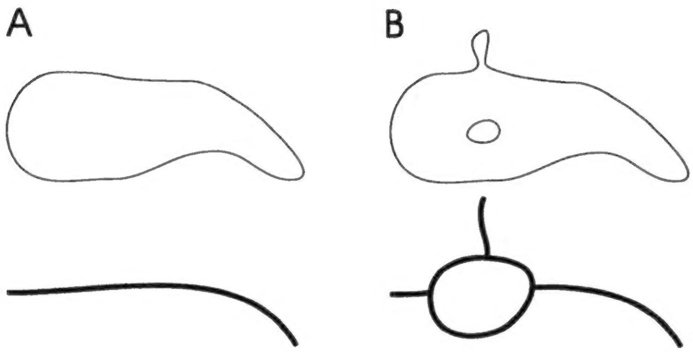

Figure 4.4: A schematic of the homotopic skeleton transform on two geo-objects: A - a clean geo-object results in a well behaved primary flow axis, B - a poorly behaved geo-object results in a poorly behaved primary flow axis.

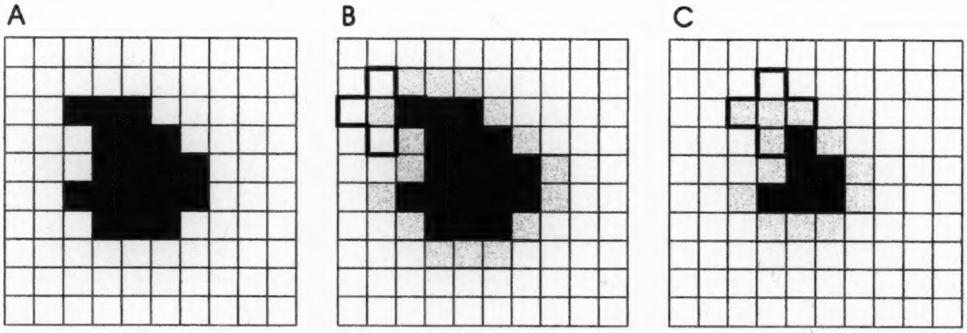

Figure 4.5: A schematic of the application of a structural element for the dilation and erosion mathematical morphology operations. A - the original image. B - the original image is dilated with the indicated structural element. The structural element (dark lines) is scanned over the original image and if any part of the element coincides with the object (dark grey) the cell at the origin (dashed box) is added to the object (light grey). C - the original image is eroded with the indicated structural element. The structural element is scanned over the original image and if any part of the element is outside the object (white) the cell at the origin is removed (light grey).

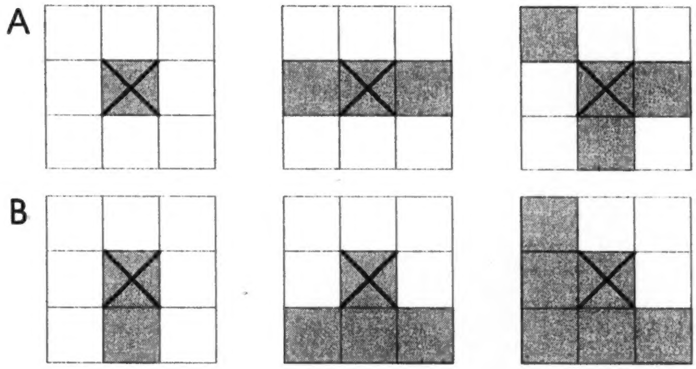

Figure 4.6: A illustration of erosions: A - nonhomotopic and B - homotopic. For each, the crossed out pixel will be reset to white.

urations that result in homotopic modification are flagged (see example homotopic and nonhomotopic erosions in Figure 4.6). The skeleton is constructed by eroding non-anchor point pixels that do not modify the homotopy. To avoid discretization artifacts, a spline is then fit to the skeleton and is extrapolated to the architectural element edges. These steps are illustrated in Figure 4.7.

The spline flow lines may be applied to determine the relative lateral and transverse location [0,1] for all locations and for all architectural elements. Where 0 is assigned to locations on the flow line and 1 is assigned to locations on the edge of the architectural element. An example of this calculation for a turbidite $2^{nd}$ and $3^{rd}$ order nested lobes (deepwater hierarchy as defined by Ghosh and Lowe, 1993)[41] in Table 4.1) with the associated flow lines and relative location vectors is shown in Figure 4.8.

### Relative Trend Functions

Relative trend functions are constructed with respect to location defined by vertical, longitudinal and transverse depositional coordinates. They are constructed with a mean of 1.0 for consistency. These trend functions represent multipliers that will be applied to the average property. The key components of the trend functions are the shape and the relative magnitude of variability within the trend functional. The lower the relative variability, the less impact the specific trend function will have on the final composite trend model. In the limit case of no variability, a trend

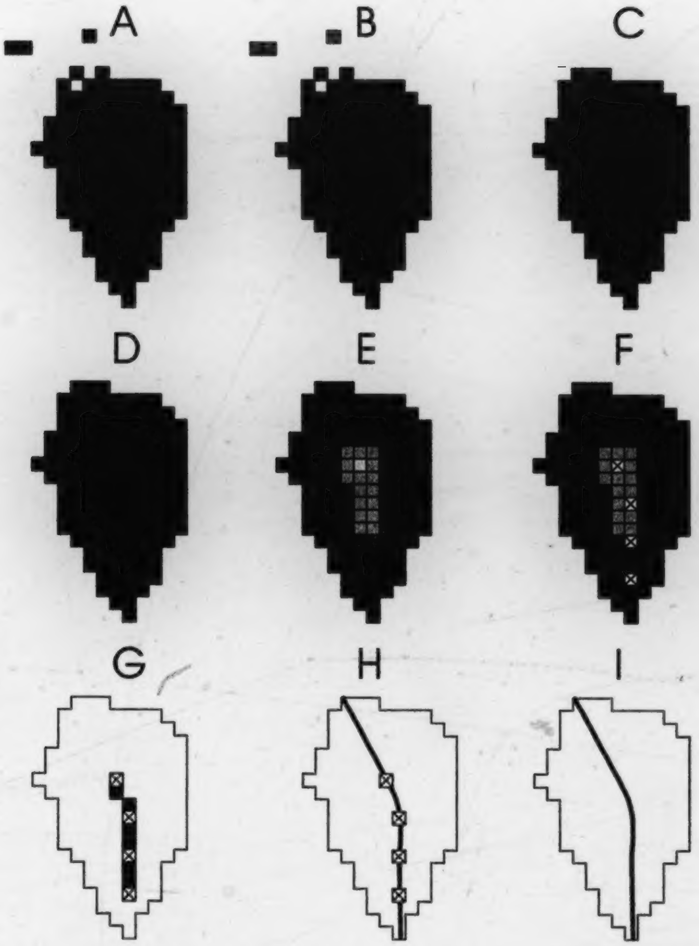

Figure 4.7: A schematic illustration of operations to construct a flow line: A - original object, B - opened to remove isolated blocks, C - closed to remove voids within the object, D - corrected object, E - distance function, F - anchor points selected, G - homotopic erosion to calculated skeleton, H - spline fit to skeleton and extrapolated to the object boundaries, and I - object and spline skeleton.

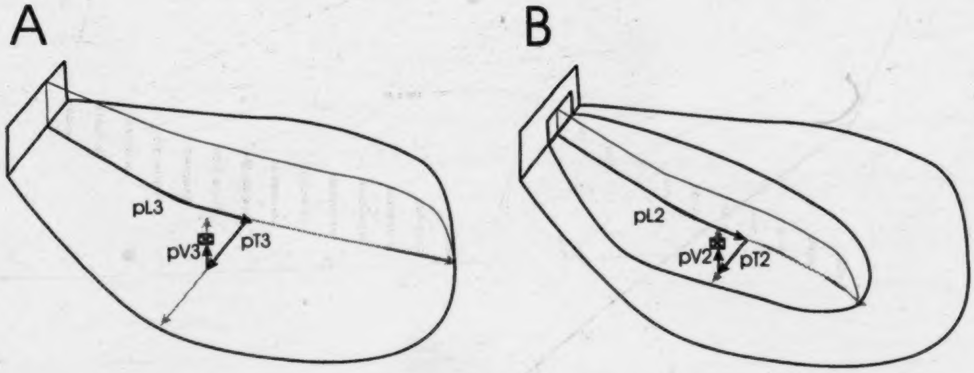

Figure 4.8: A demonstration of the depositional coordinate system describing vertical, longitudinal and transverse location within nested architectural elements (A - lobe scale and B - flow event scale). The striped section represents the primary flow axis at each scale.

function is constant 1.0. In this case, the specific order and direction does not have any impact on the final composite trend model. Calibration and expert judgment is required to set the relative importance of the directional and order trends and their associated shapes. Analog information such as outcrops and depositional processes may provide a general model for trend form and significance for each direction and scale. Well logs may provide specific information on vertical trends at each scale.

A 1-D example with two scenarios of trend functions for two hierarchical orders and resulting composite trends are shown in Figure 4.9. The methodology for combining trend functions will be discussed in the next subsection.

Example porosity trend functions for $2^{nd}$ and $3^{rd}$ order lobes (discussed in Section 4.1) are shown in Figure 4.10. These trends indicate a fining towards the peripheries and distal of the sand bodies. These longitudinal and transverse trends are supported by the turbidity models of Mutti et al. (2002)[80] and the lobe mound description of Hobday and Galloway (1996)[39]. Bouma's (2000)[7] description of a rapid fining at the sides and terminus is the basis for the form of the longitudinal and transverse trends. For individual $2^{nd}$ order elements there is a fining upward trend consistent with Bouma sequence turbidites (Bouma, 2000; Dudley, Rehmer and Bouma, 2000) [7, 33]. The system may be prograding resulting in a coarsening upward over the $3^{rd}$ order elements (Pickering et al, 1995, Catuneanu, 2003)[92, 12].

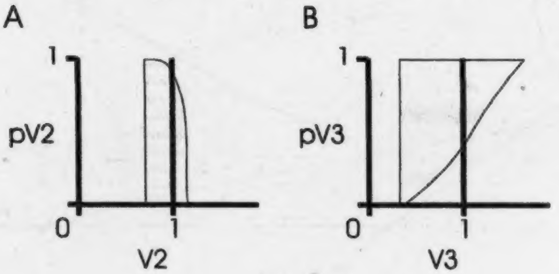

Figure 4.9: Example porosity (units relative to the global mean) vertical trend functions for: A - $2^{nd}$ and B - $3^{rd}$ hierarchical orders. Note they each have distinct shapes. Since the $3^{rd}$ order has greater variability it will have more influence on the final composite trend model. These vertical trends are similar to vertical turbidite lobe trends identified by Stow et al. (1996)[118].

This nested vertical trend is similar to the vertical facies succession for turbidite lobes identified by Hobday and Galloway (1996)[39].

### Combining the Trend Components

The trend functions for each depositional direction and hierarchy form the trend components that must be combined to calculate a composite trend value at all locations. This is analogous to the problem of merging areal and vertical trends into a full three-dimensional trend model discussed by Deutsch (2002)[21].

A convenient method based on the assumption of conditional independence between the trend functions for each direction and at each hierarchical order is shown in Equation 4.2. This may not be an acceptable assumption in all settings.

$$trend(\mathbf{u}) = \overline{\phi} \cdot \prod_{\ell=1}^{L} V^{\ell}(\mathbf{u}_V^{\ell}) \cdot L^{\ell}(\mathbf{u}_L^{\ell}) \cdot T^{\ell}(\mathbf{u}_T^{\ell}) \qquad (4.2)$$

where $\mathbf{u}$ is a location vector, $\overline{\phi}$ is the global average property and $V^{\ell}(\mathbf{u}_V^{\ell})$, $L^{\ell}(\mathbf{u}_L^{\ell})$, $T^{\ell}(\mathbf{u}_T^{\ell})$ are the local trend multipliers for each hierarchical order, $\ell = 1, \ldots, L$.

These techniques do not have an unbiasedness constraint or explicit control over the variability in the final composite trend model. The trend distribution may be scaled to the representative global mean and the variance that represents an appropriate balance of variance allocated to trend and residual.

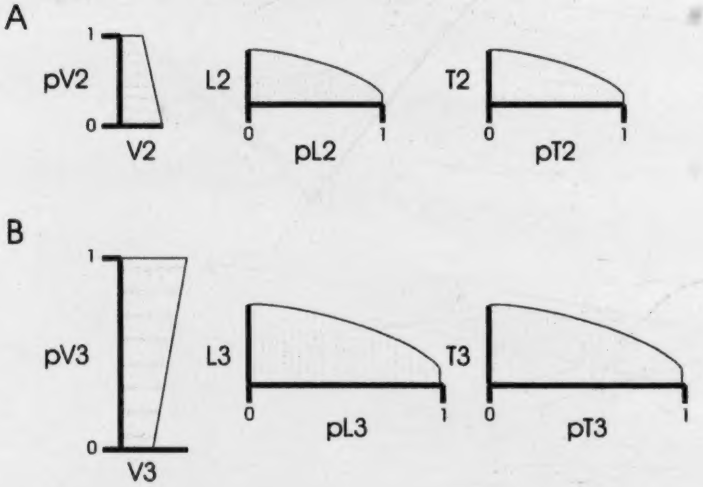

Figure 4.10: A potential suite of porosity trends that may be applied in the vertical, longitudinal and transverse directions for $2^{nd}$ and $3^{rd}$ order architectural elements. Individual flow events ($2^{nd}$ order) may be characterized by fining upward sequences while $3^{rd}$ groups may coarsen upwards due to progradation. Fining may occur in both basin ward (longitudinal) and away from the flow line (transverse). The $pV^2$, $pV^3$, $pL^2$, $pL^3$, $pT^2$ and $pT^3$ axes are the relative locations and the $V^2$, $V^3$, $L^2$, $L^3$, $T^2$ and $T^3$ axes are the trend functions centered on 1.0. See references provided in text for support.

$$m'(\mathbf{u}) = \sqrt{\frac{\sigma^2_{m_t}}{\sigma^2_{m_i}}}(m(\mathbf{u}) - \overline{m}_i) + \overline{m}_t \tag{4.3}$$

where $m'(\mathbf{u})$ is the scaled trend value at location $\mathbf{u}$, $\sigma^2_{m_t}$ and $\sigma^2_{m_i}$ are the target and initial variance of the trend model, $\overline{m}_t$ and $\overline{m}_i$ are the target and initial global mean of the trend model and $m(\mathbf{u})$ is the initial trend value at location $\mathbf{u}$. This is analogous to the affine correction discussed in Section 6.3.1.

This balance of variability between trend and residual is represented in Equation 4.4. In general the covariance between the trend and residual should be low.

$$\sigma^2_Z = \sigma^2_{m'} + \sigma^2_R + 2 \cdot C(R, m') \tag{4.4}$$

where $\sigma^2_Z$ is the variance of the property of interest, $\sigma^2_{m'}$ is the variance of the trend, $\sigma^2_R$ is the variance of the residual and $C(R, m')$ is the covariance between the residual and the trend.

A 1-D example was constructed to illustrate the combination of $3^{rd}$ and $2^{nd}$ order vertical trend functions (see Figure 4.11). The initial trend functions were set as linear with values varying between 0.7 and 1.3 for the $3^{rd}$ order and 0.95 to 1.05 for the $2^{nd}$ order. These trend functions are fit to a vertical profile with identified $3^{rd}$ and $2^{nd}$ order elements. The trend model standard deviation controls the variability of the trend model (see scenarios with standard deviations of 0.01, 0.02, 0.04, 0.06 and 0.08 in Figure 4.11) and the relative scale of the trend functions controls the influence of each hierarchy on the composite trend model (see scenarios with the range of $3^{rd}$ trend function set to [1.0,1.0], [0.9,1.1], [0.7,1.3], [0.5,1.5] and [0.3, 1.7] in Figure 4.11).

The application of hierarchical trend models allows for integration of data from a variety of sources. Seismic attributes may provide coarse information on areal trends over large scale architectural elements. Outcrops and well logs may provide information on vertical trends at a variety of scales. These trends may be characterized in a sequential manner from large scale to small scale. Large scale trends may be identified and removed. Then vertical trends within smaller scale architectural elements may be identified from the residual. Most reservoir settings lack short scale information on horizontal heterogeneity. Analog information, such as outcrops and conceptual process models may be utilized to inform longitudinal and transverse trends at a variety of architectural elements scales.

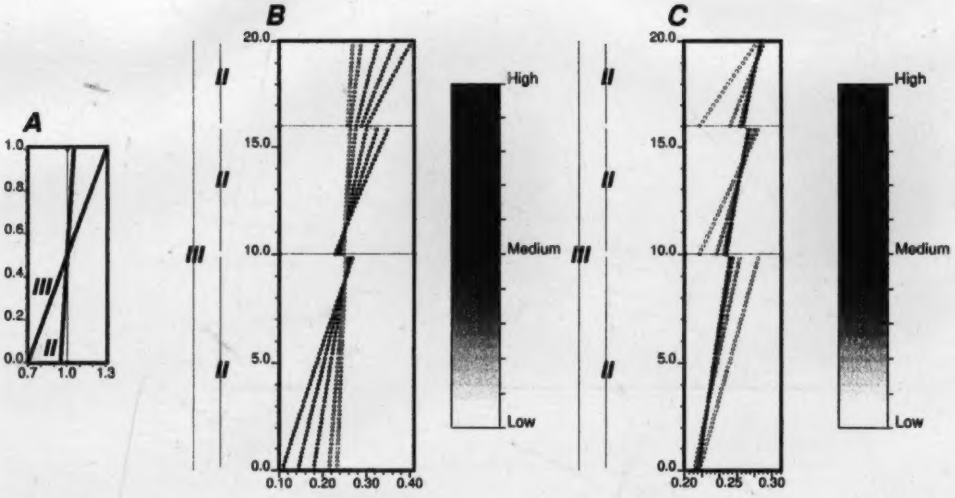

Figure 4.11: A 1D example of the combination of $3^{rd}$ and $2^{nd}$ order vertical trend functions: A - the initial trend functions set as linear with values varying between 0.7 and 1.3 for the $3^{rd}$ order and 0.95 to 1.05 for the $2^{nd}$ order. These trend functions are fit to a vertical profile with identified $3^{rd}$ and $2^{nd}$ order elements. The following were varied: B - trend model variance and C - the relative scale of the trend functions.

The hierarchical trend modeling technique is an efficient technique for combining trends in principle depositional directions defined along curvilinear primary axis of flow. The form of trend components will be integrated directly from the previously discussed information sources. This information may inform the relative scale of each trend component. The results should be scrutinized by professional judgement. An example hierarchical trend model constructed for a turbidite case study is shown in Section 4.6.

### Hierarchical Trend Model Construction Programs

Two Fortran programs were written to automatically calculate hierarchical trend models. `HEIRTREND` calculates trend models for any categorical model with no specification of the architectural elements. The architectural elements are approximated as connected geo-objects and the flow axis is approximated with the skeleton transform as described in method three (see Section 4.2.1). The program parameters are shown below and description of each parameter is included in Table 4.2.

```
Parameters for HIERTREND
1.  maps.out               -file with categories
2.  1 10                   -column
3.  -1.0 10000.0           -trimming limits
4.  100 0.5 1.0            -nx,xmn,xsiz
5.  100 0.5 1.0            -ny,ymn,ysiz
6.  40  0.5 1.0            -nz,zmn,zsiz
7.  0.0 50.0 0.0           -source location
8.  5 5 2                  -structural element
9.  trend.dat              -trend file
10. 1 2 3 4 5 6 7          -lprop,lz3,lz2,lt3,lt2,ll3,ll2
11. hiertrend.out          -output file
12. 10.0 2.5               -target: mean,st.dev. (optional)
```

`SURFTREND` calculates trend models for surface based models with $2^{nd}$ order architectural elements specified by bounding surfaces within a model of a $3^{rd}$ order architectural element. The $2^{nd}$ order elements are cleaned by erosion and dilation to improve interpretability and the flow axis is calculated by the skeleton transform as described in method two (see Section 4.2.1). An example parameter file for the `SURFTREND` program is included below and an explanation for each parameter is provided in Table 4.3. Code modifications are required to apply this code to more

| Line | Description |
|---|---|
| 1 | input file. The file should be in GEOEAS format and GSLIB grid convention with any number of categories. |
| 2 | column number with the associated categorical data. |
| 3 | trimming limits. Data outside of these limits are considered non-net. |
| 4-6 | parameters describing the model regular grid (see Figure 5.2). |
| 7 | the relative source location used for longitudinal depositional coordinates and to extrapolate flow axis splines. |
| 8 | the dimension in number of cells of the structural element applied for image cleaning. |
| 9 | the data file with the trend functionals for each direction and scale. |
| 10 | the columns with the proportional measure (0-1) and the trend functionals in each direction and at each scale. |
| 11 | the output file with the hierarchical trend model in GEOEAS format and GSLIB grid convention. |
| 12 | the target mean and standard deviation for affine correction of trend model. Not used if left empty. Only the mean is corrected if just one value entered. |

Table 4.2: A description of the `HIERTREND` parameter file.

than two hierarchical orders.

```
Parameters for SURFTREND
1.  turbsim.out          -file with surfaces
2.  1                    -column
3.  100 25.0   50.0      -nx,xmn,xsiz
4.  100 25.0   50.0      -ny,ymn,ysiz
5.  200 70.125 0.25      -nz,zmn,zsiz
6.  0.0 50.0 0.0         -source location
7.  5 5 10               -structural element
8.  trend.dat            -file with trend
9.  1 2 3 4 5 6 7        -prop,z3,z2,l3,l2,t3,t2
10. surfTrendReal1.out   -output file
11. 10.0 2.5             -target: mean,st.dev. (optional)
```

### 4.2.2 Correction for Global Areal and Vertical Trends

The procedure for the construction of hierarchial trend models is not constrained to reproduce model scale areal and vertical trends. Often large scale information from seismic or well test provides information on areal trends. Vertical trends are often assessed from well log and core and analog information. This information must be integrated into the hierarchical trend model. The problem of direct integration of this information during hierarchical trend construction is difficult. A post-processing technique is introduced that corrects trend models to honor areal and vertical trends.

The applied method is to randomly visit locations $\mathbf{u}^\ell$ within the trend model, and check the difference between the current and target, vertical and areal trend.

$$\delta_z = m_z^t(\mathbf{u}_z) - m_z^c(\mathbf{u}_z) \tag{4.5}$$

$$\delta_{x,y} = m_{x,y}^t(\mathbf{u}_{x,y}) - m_{x,y}^c(\mathbf{u}_{x,y}) \tag{4.6}$$

where $\delta_{x,y}$ and $\delta_z$ are the mismatch in the areal and vertical trends, $m_{x,y}^t(\mathbf{u}_{x,y})$ and $m_z^t(\mathbf{u}_z)$ are the areal and vertical trend targets and $m_{x,y}^c(\mathbf{u}_{x,y})$ and $m_z^c(\mathbf{u}_z)$ are the current areal and vertical trends. If both the areal and vertical trends are consistently below or above the target then a window of local factors is applied to increase or decrease the local trend values by a small random amount. The user sets the maximum absolute magnitude of the local factors and a uniform random

| Line | Description |
|---|---|
| 1 | input file with the surfaces. The file should be in GEOEAS format and GSLIB grid convention with the surfaces ordered from bottom to top. |
| 2 | column number with the surface elevations. |
| 3-5 | parameters describing the model regular grid (see Figure 5.2). |
| 6 | the relative source location used for longitudinal depositional coordinates and to extrapolate flow axis splines. |
| 7 | the dimension in cells (n × n) of the structural element applied for image cleaning. |
| 8 | the data file with the trend functionals for each direction and for the global (3) and category hierarchies (2). |
| 9 | the columns with the proportional measure (0-1) and the trend functions in each direction and for each order. |
| 10 | the output file with the hierarchical trend model in GEOEAS format and GSLIB grid convention. |
| 11 | the target mean and standard deviation for affine correction of trend model. Not used if left empty. Only the mean is corrected if just one value entered. |

Table 4.3: A description of the `SURFTREND` parameter file.

number [0, 1] is drawn to scale this maximum magnitude for each iteration. The absolute magnitude of the local factors is a function of distance from the center of the window ($\mathbf{u}$) with the maximum magnitude at the center and the factors reach 0.0 in a continuous manner at the peripheries of the local window (see Equation 4.7 and schematic of local factor window in Figure 4.12).

$$\lambda(\mathbf{u}') = 1 - \sqrt{\left(\frac{d_x}{r_x}\right)^2 + \left(\frac{d_y}{r_y}\right)^2 + \left(\frac{d_z}{r_z}\right)^2} \tag{4.7}$$

where $\lambda(\mathbf{u}')$ is the weight at location $\mathbf{u}'$ within the template with distance components $d_x$, $d_y$ and $d_z$ in $x$, $y$ and $z$ coordinates from the center of the template. The template size is defined by the distance from the center to the extent, $r_x$, $r_y$ and $r_z$.

By visiting many locations the trend model is gradually modified to honor the target vertical and areal trend while retaining the small scale features from the hierarchial trend model. The algorithm terminates when all values in the current vertical and areal trend models are within a tolerance of the target. A schematic in Figure 4.12 shows a cross section of a trend model and the areal and vertical trends, actual and target and the smooth multiplier window.

The user specifies parameters such as the maximum magnitude, size of the local factor window and the convergence tolerance. Relatively small factors will slow the rate of convergence while large factors may result in artifacts such as dimples in the corrected trend model. A demonstration with a variety of window sizes is shown in Figure 4.13. A large window size results in a smooth correction, while a small window size may add small scale features to the trend model. The algorithm terminates when the difference between the target and current areal and vertical trends is below the convergence tolerance for all areal locations and horizontal slices. A small tolerance requires more iterations to reach convergence, but results in a more precise match to the target areal and vertical trends.

The inputs for this algorithm are the trend model, mask file, target areal and vertical trends and the size of the moving window. An example parameter file for the `TRENDCOR` program is included below and an explanation for each parameter is provided in Table 4.4. The application of this method for hierarchical trend model construction is demonstrated in Section 4.5.2.

```
Parameters for TrendCor
1.  surftrend.out        -file with trend model
```

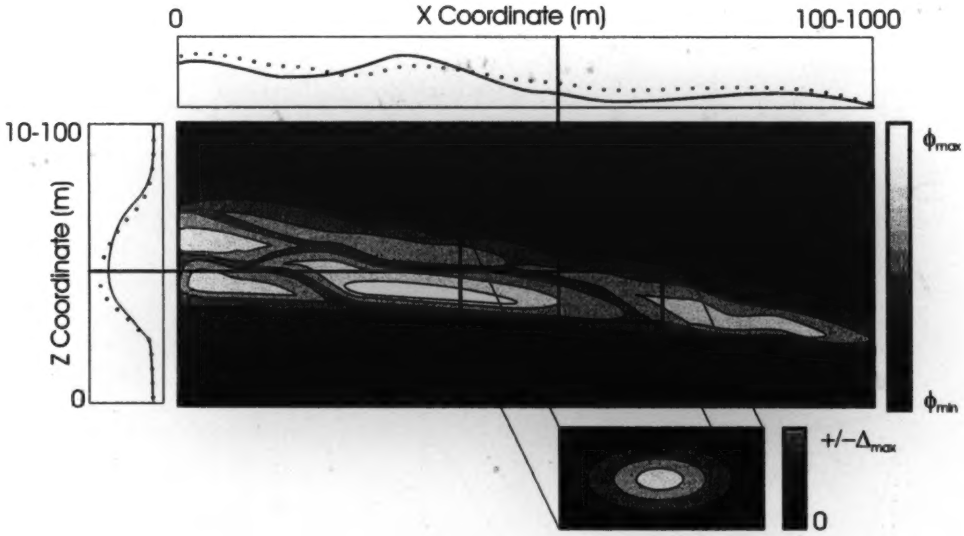
0
X Coordinate (m)
100-1000
10-100
Z Coordinate (m)
0
$\phi_{max}$
$\phi_{min}$
$+/-\Delta_{max}$
0

Figure 4.12: A schematic of a trend model cross section, areal and vertical, initial (dotted line) and target(solid line) trends and a multiplier window. The indicated location has a too large trend value in both the areal and vertical and so the smooth factor window is set to reduce the trend.

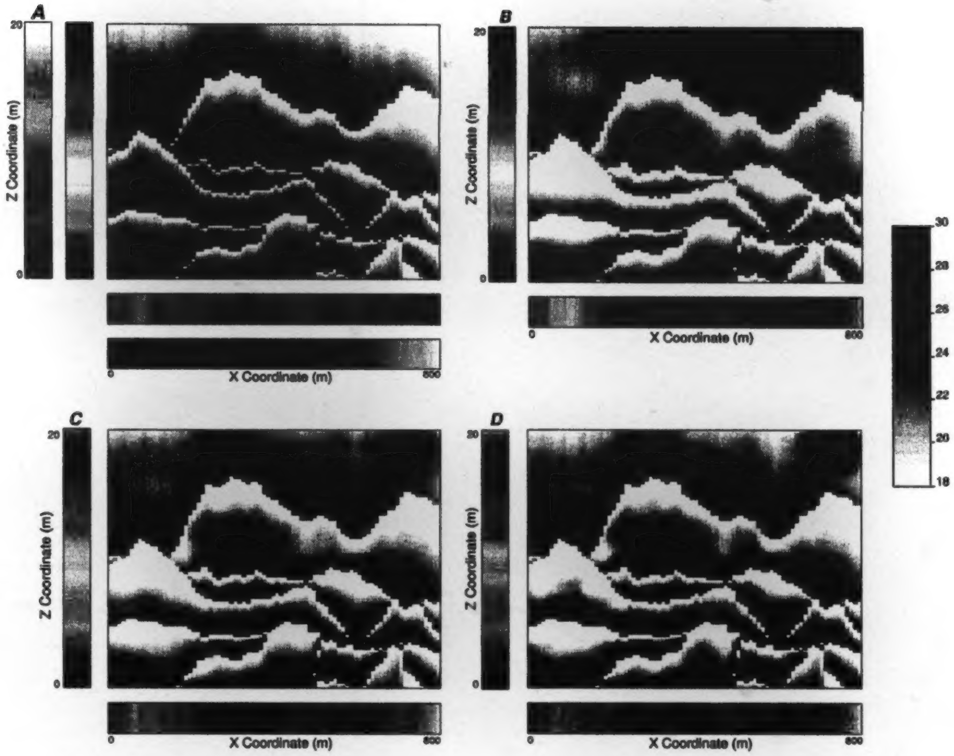

Figure 4.13: A demonstration of the effect of window size on areal and vertical trend correction. A cross section from a trend model based on stochastic surfaces is applied. A - the original trend model and associated initial vertical and areal trends (furthest) and the target vertical and areal trends (nearest). B - the correction was applied with a 200 × 4 meter window size. A cross section of the corrected model and associated vertical and areal trends are shown. C - the correction was applied with a 100 × 2 meter window size. A cross section of the corrected model and associated vertical and areal trends are shown. D - the correction was applied with a 50 × 1 meter window size. A cross section of the corrected model and associated vertical and areal trend are shown. Units are in percent porosity.

```
2.  -1.0 100.0            -trimming limits
3.  mask.dat              -file with mask (0-not masked)(optional)
4.  100 100 96            -nx,ny,nz
5.  targetareal.out       -target areal trend map
6.  2                     -column number
7.  verttrendtarget.out   -target vertical trend profile (bot-top)
8.  2                     -column number
9.  20 20 10 1.1          -cx,cy,cz,window size,max factor
10. 69069 5000 0.01 100   -random number seed,max inter,max miss
11. trendcor.out          -corrected trend output
12. arealcor.out          -corrected vertical trend output
13. vertcor.out           -corrected areal trend output
```

## 4.3 Surface Based Models

A general description of surface based simulation was provided in Section 2.2.7. Surface based simulation may be seen as a variation on object based simulation, although it has some key implementation differences. Surface based simulation focuses on the surfaces that divide the objects as opposed to the objects themselves. A surface is denoted:

$$\left\{\mho^{\ell}_{\psi^{\ell}}(\mathbf{u}),\ \ \forall\ \mathbf{u}\in A_2\right\} \tag{4.8}$$

where $\mho^{\ell}_{\psi^{\ell}}(\mathbf{u})$ is a surface parameterized by a suite of geometric parameters $\psi^{\ell}$ defined at location $\mathbf{u}$, $A_2$ is the projection of the area of interest $A$ on to a 2-D plane (commonly the horizontal plane in model space after a rotation to align the model with the dip of the strata bound sediments). In the proposed procedure, the surfaces are generated in order from the initial surface $\ell = 0$ at the bottom to $\ell = L$ the top surface.

Surface based simulation may be applied in a dynamic mode; the current surface $\mho^{\ell}_{\psi^{\ell}}(\mathbf{u})$ is a function of the previous surfaces $\mho^{i}_{\psi^{\ell}}(\mathbf{u}), i = 0, \ldots, \ell - 1$. The nature of the current object, defined by bounding surfaces, is dependent on the form of the previous objects.

This dynamic nature may be utilized to improve geologic realism by reproducing interrelationships between elements, but this feature also makes these models more susceptible to artifacts. These artifacts include (**1**) constrained horizontal placement may pile up elements in a subset of the model and result in unrealistic relief and (**2**)

| **Line** | **Description** |
|---|---|
| 1 | input file with the trend model. The file should be in GEOEAS format and GSLIB grid convention. |
| 2 | column number with the surface elevations. |
| 3 | file with mask. Any other value than 0 will flag associated location as masked. |
| 4 | parameters describing the size of the model (see Figure 5.2). |
| 5-6 | a 2-D model (nx by ny) with the target areal trend and column number. |
| 7-8 | a 1-D vector (nz) with the target vertical trend ordered from bottom to top and column. |
| 9 | the size of the smooth factor window and maximum factor. When reduction is required one is subtracted from this value. |
| 10 | the random number seed, the maximum number of iterations and the convergence threshold. When all layers and columns within the trend model are within this fraction of the target the algorithm is terminated. |
| 11 | the output file with the corrected 3-D trend model. The file is in GEOEAS format and GSLIB grid convention. |
| 12 | the output file for the corrected 2-D areal trend for checking. |
| 13 | the output file for the corrected 1-D vertical trend for checking. |

Table 4.4: A description of the `TRENDCOR` parameter file.

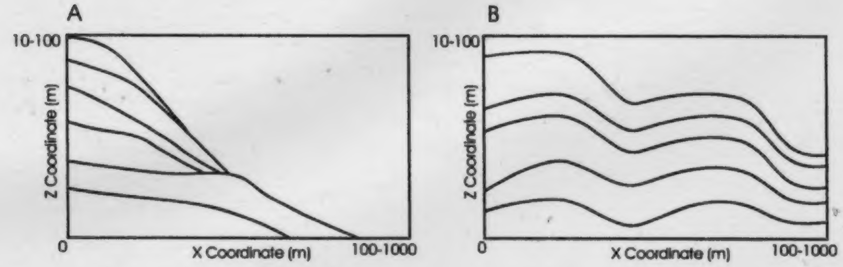

Figure 4.14: Schematics of two artifacts that may occur in surface based simulation. The surfaces may be: A - trapped in a subset of the model. This occurs if the element geometric distributions are small relative to the model size and the horizontal positioning is constrained. B - features in previous surfaces may persist in an unrealistic manner.

features in previous surfaces may persist in an unrealistic manner (see Figure 4.14). Specific methodologies are developed that utilize the dynamic feature but are robust and resistent to the formation of artifacts.

Surface based models are not well suited to constructing models with multiple lithofacies with unique geometries. These models are better left to object based methods (see Chapter 3 for further discussion on object based modeling approaches). Finally, to avoid computationally expensive geometric calculations each surface should exist over the entire model and have an unique solution at all locations, $\mho^{\ell}_{\psi^{\ell}}(\mathbf{u}) \ \forall \ \mathbf{u} \in A_2$; therefore, surfaces are coincidental with previous surface where an element pinches out and surfaces do not fold over on themselves. A schematic of a surface based realization compared to an object based realization is shown in Figure 4.15.

Surface based methods may be applied to a variety depositional settings. This chapter develops and demonstrates surface based methods tailored to turbidite lobes. The general methodology is to **(1)** generate a surface geometry, **(2)** place the surface geometry within the model, **(3)** check for agreement and surface intersections observed in well data and regenerate if the surface does not meet the acceptance criteria and **(4)** calculate a stochastic residual to honor well data precisely and to reproduce surface rugosity. This procedure is repeated until all conditioning is honored and the area of interest is filled. The following is an overview of these steps. Specific implementation details will be presented with the applications (see Sections 4.4 and

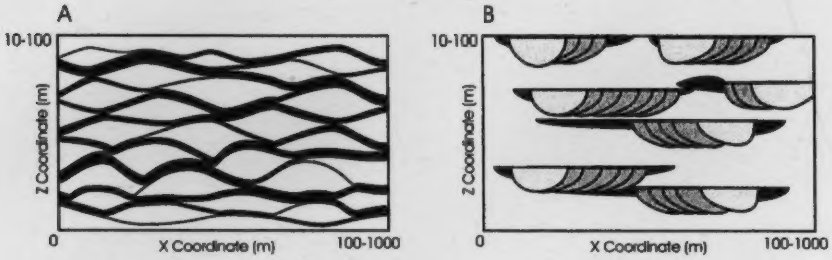

Figure 4.15: A schematic of: A - surface based simulation and B - object based simulation. The surfaces have been offset vertically to emphasize that the surfaces exist over the entire areal extent of the model area. Note: the object based simulation could not be represented efficiently by these surfaces.

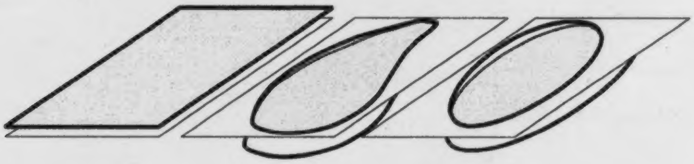

Figure 4.16: Schematics of three example surface templates. Note the surfaces are shown truncated by a plane, which might be a previous surface.

4.5).

### 4.3.1 Surface Templates and Candidate Surfaces

Surfaces with common geometric structures are frequently observed in clastic reservoirs. For example, stratiform sediments are expressed in parallel to subparallel surfaces, inclined heterolithic strata sets are composed of onlapping sigmoidal surfaces (Diaz-Molina, M., 1993; Willis, B.J., 1993)[32, 139], channel bedforms may be expressed as down stream accreting bars (Miall, 1996) [73] and turbidite frontal splays often occur as stacked lobes (Stelting at al., 2000)[115]. These characteristic geometries may be described by a surface template. Three example surface templates are shown in Figure 4.16.

Candidate surface may be constructed by scaling a surface template by geometric parameters. A candidate surface is denoted by $\mho'_{\psi'}(\mathbf{u})$.

Geometric parameters may be represented as RVs with distributions informed

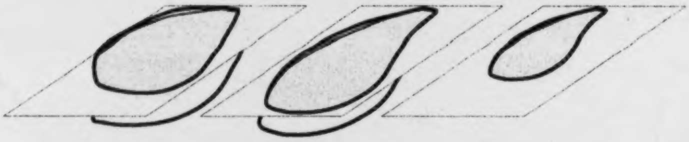

Figure 4.17: Three example candidate surfaces based on the lobe surface template in Figure 4.16. The length and width are varied. Note the surfaces are shown truncated by a plane.

from well data, analog information and based on the processes related information. Possible geometric parameters that may be quantified include length, width, length:width ratio, maximum thickness, thickness:width ratio and sinuosity. A schematic is shown in Figure 4.17 of three candidate surfaces based on the lobe template from Figure 4.16.

### 4.3.2 Placement of Candidate Surfaces

The placement algorithm should: (**1**) respect geologic information with respect to the interrelationship of the architectural elements described by the surfaces, (**2**) avoid artifacts in the resulting surfaces (see Figure 4.14), (**3**) result in a reasonable probability of the candidate surface being accepted and (**4**) be computationally efficient.

Architectural elements may have a variety of stacking relationships. Stacking styles may include aggradation, progradation, retrogradation, shingled, compensational or a combination of these styles. The style should determine the position and orientation of a candidate surface $\mathfrak{S}'_{\psi'}(\mathbf{u})$ relative to all previous surfaces $\mathfrak{S}^i(\mathbf{u}), i = 0, \ldots, \ell - 1$.

Placement includes the determination of attitude and location. The areal location may be a function of previous surfaces as is the case in `TURBSIM` (see Section 4.5) or may be independent of the previous surfaces (see the `SURFSIM` algorithm in Section 4.4). The methodology for determining areal location of the candidate surface should avoid piling surfaces in a subset of the model (refer back to Figure 4.14). Vertical placement is the determination of the vertical position of the candidate surface $\mathfrak{S}'_{\psi'}(\mathbf{u})$ relative to the previous surface $\mathfrak{S}^{\ell-1}_{\psi^{\ell-1}}(\mathbf{u})$. This placement methodology will determine the thickness and attitude of the element. The placement algorithm

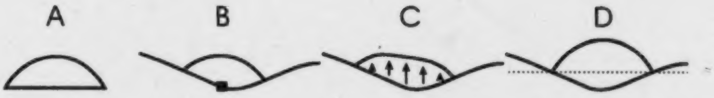

Figure 4.18: Methods for vertical placement of surface geometries: A - the candidate surface $\mho'_{\psi'}(\mathbf{u})$, B - the anchor point method is to anchor a specific location on the candidate surface onto the previous surface $\mho^{\ell-1}_{\psi^{\ell-1}}(\mathbf{u})$, C - the additive method is to add the thickness enclosed by the surface geometry to the previous surface and D - the moving window average method is to place the surface geometry with a datum determined as a smooth moving window average of the previous surface.

should be tailored to the specific application to reproduce features observed in the geology.

Some example vertical placement methods are (**1**) anchor point, (**2**) additive and (**3**) moving window average. Figure 4.18 illustrates these methods with an example of a lobe candidate surface on irregular bathymetry. The additive method for vertical placement may distort the geometry of the elements and result in the unrealistic persistence of features from previous surfaces artifact shown in Figure 4.14. The anchor point and moving window average methods are more robust but require the setup of parameters such as the location of the anchor and the size of the moving window for averaging.

### 4.3.3 Surface Acceptance Criteria

The candidate surface is compared with available well data. Mismatch is the difference between the surface contacts from wells and the candidate surface $\mho'_{\psi'}(\mathbf{u})$ intercepts at the wells.

$$\left|\mho'_{\psi'}(\mathbf{u}_i) - \phi(\mathbf{u}_i)\right| \leq \tau,\ \forall\, i = 1, \ldots, n \tag{4.9}$$

where $\mho'_{\psi'}(\mathbf{u}_i)$ is the surface and $\phi(\mathbf{u}_i)$ is the conditioning data at well location $\mathbf{u}_i$ for wells, $i = 1, \ldots, n$ and $\tau$ is the maximum allowable mismatch.

If a candidate surface has failed the acceptance check, it may be corrected or rejected and regenerated. The application of a correction to geometric parameters may result in artifacts. Given the speed with which a new candidate surface may be calculated, regeneration is preferred to correction. If the geometries are large relative to the data spacing this problem may become intractable. For the common deepwater reservoir settings with few, widely spaced wells this technique is practical.

### 4.3.4 Conditioning by Stochastic Residual

After a geometric surface has been accepted, a conditional stochastic residual $R^{\ell}(\mathbf{u}), \quad \forall \quad \mathbf{u} \in A_2$ is calculated. The stochastic residual: (**1**) may be based on any stochastic model, (**2**) should have a mean of 0.0 so the surface vertical location is not biased and (**3**) should have a correlation and total variance that reflects the short scale fluctuation of the associated surfaces observed in the sedimentological record. The addition of a stochastic residual may be represented as:

$$\mathcal{U}^{\ell}_{\psi^{\ell}}(\mathbf{u}) = \mathcal{U}'_{\psi^{\ell}}(\mathbf{u}) + R(\mathbf{u}) \tag{4.10}$$

where $\mathcal{U}'_{\psi'}(\mathbf{u})$ is the candidate surface, $R(\mathbf{u})$ is the conditional residual and $\mathcal{U}^{\ell}_{\psi^{\ell}}(\mathbf{u})$ is the $\ell^{th}$ surface for all locations within $A_2$.

The Gaussian model may be applied to calculate a conditional stochastic residual. Gaussian simulation is reviewed in Section 2.2.5. If Gaussian features such as maximum discontinuity of the extremes are deemed inappropriate, then indicator simulation (see Section 2.2.5) or simulated annealing (see Section 2.2.9) may be applied. `SGSIM` from GSLIB was converted to a subroutine to simulate 2-D for the surface based algorithms in this chapter. Figure 4.22 demonstrates the conditioning of a surface geometry with conditional stochastic residual.

### 4.3.5 Termination of Surface Based Simulation

There are two cases; (**1**) the top surface is deterministic and (**2**) the top surface is uncertain and should be modeled stochastically. For the first case, the algorithm terminates when the last surface $\mathcal{U}^{\ell}_{\psi^{\ell}}(\mathbf{u})$ exceeds the top surface $\mathcal{U}^{L}_{\psi^{L}}(\mathbf{u})$. The last surface is truncated by the top surface. For the second case, the algorithm terminates when the average elevation of the last surface $\mathcal{U}^{\ell}_{\psi^{\ell}}(\mathbf{u})$ reaches the average elevation of the top of the AOI within a tolerance. Then the last surface is accepted as a realization of the top surface.

Due to the dynamic nature of the surface based approach, it is not possible to directly constrain the algorithm to honor a top surface. This problem may lead to artifacts in the form of poor consistency between the top surface and the previous surfaces. This problem should be minimized by careful selection of the model methodology and input parameters. The resulting realizations may be screened to remove surface based realizations with poor agreement with the top surface. One method to check for consistency would be to compare the distribution of thickness for the top unit with the thickness distributions of previous units. Also, a visual check may be performed to check the correlation style at the top surface. An erosional surface at the top of the reservoir will reduce or remove issues related to consistency with the top surface.

## 4.4 Surface Based Strataform Model

The technique for constructing surface based models outlined in Section 4.3 was applied to construct surface based strataform models. The following is a discussion of the specific details related to methodology and a demonstration based on a sheet turbidite example.

### 4.4.1 Methodology

A Fortran program was written to calculate stochastic surface based realizations that honor surface geometry and erosional and gradational well contacts for strataform deposits. This program is called `SURFSIM`. This algorithm assumes near parallel bedding; therefore, the surface template is a plane (see A in Figure 4.16) although any geometry may be applied by modifying the code. The vertical location is chosen such that an average thickness (drawn from a lognormal distribution with a user defined average and standard deviation) is honored. Rozman (2000)[107] conducted a study of deepwater strataform bed thickness distributions indicating distributions similar to lognormal. The `SURFSIM` algorithm with planar geometries may be applied to model sheet architectural elements in distal fine grained turbidites (Carr and Gardner, 2000)[11].

The conditional stochastic residual is calculated with a 2-D version of the `SGSIM` algorithm from GSLIB that is called as a subroutine. The correlation structure is defined by traditional semivariogram parameters and the sill is set as the maximum amplitude of the residual and as the threshold for the acceptance criteria.

The parameters include well data, grid definition and simulation parameters (search and semivariogram) for the 2-D simulation of the residual. An example parameter file is included below and an explanation for each parameter is provided in Table 4.5.

```
Parameters for SURFSIM
1.  well.dat             -file with data
2.  1 2 3 4 5 6 7 8      - well,x1,y1,z1,x2,y2,z3,code
3.  5.0 2.0              -layer thickness:mean,st.dev.
4.  top.out              -file with top surface
5.  bot.out              -file with bottom surface
6.  1                    -number of realizations to calculate
7.  100 0.5 1.0          -nx,xmn,xsiz
8.  50 0.5 1.0           -ny,ymn,ysiz
9.  150 0.5 1.0          -nz,zmn,zsiz
10. surfsim.out          -file for simulation output (surfaces)
11. surfsimgrid.out      -file for simulation output (grid)
12. 1                    -debugging level:0,1,2,3
13. surfsim.dbg          -file for debugging output
14. 69069                -random number seed
15. 12                   -number of simulated nodes to use
16. 1 3                  -multiple grid search(0=no, 1=yes),num
17. 10.0 10.0            -maximum search radii (hmax,hmin)
18. 0.0                  -angle for search ellipsoid
19. 51 51                -size of covariance lookup table
20. 0.0                  -nst, nugget effect
21. 1 5.0 0.0            -it,cc,ang1
22.   10.0 10.0          -a_hmax, a_hmin
```

### 4.4.2 Demonstration

For a demonstration of the `SURFSIM` program a synthetic data set was constructed with two wells with erosional and conformable contacts and intervals with no information. Surfaces were simulated with geometries similar to the sand sheet architectural elements of Fan 2 of the Permian Lower Bushy Canyon Formation, West Texas (Carr and Gardner, 2000[11]). A layer thickness distribution (lognormal$\{1.0, 0.2\}$ in meters) and a smooth residual semivariogram consisting of a single spherical structure with a range of 500 meters were applied. These parameters are consistent with second order architectural elements from Ghosh and Lowe (1993)[41]. A cross section of the surface realization is shown in Figure 4.19.

Erosional and conformable contacts are honored by setting rules in the conditioning and post processing of surfaces. For conditioning the rules are:

| **Line** | **Description** |
|---|---|
| 1 | input file with well data. The file should be in GEOEAS format. |
| 2 | column numbers for the well, x, y, z location and marker code. The x2, y2, z2 are used for no information intervals. The codes are 0-erosional, 1-gradational and 2-no information. |
| 3 | the mean and standard deviation of the thickness of the parallel beds. |
| 4-5 | the files with the top and bottom surfaces in GEOEAS format and GSLIB grid convention. |
| 6 | the number of surface realizations to calculate. Realizations stacked in the same output file. |
| 7-9 | the regular grid parameters. The z parameters are required for the pixel based output for visualization. |
| 10 | the surfaces output. The surfaces output is a regular grid in x and y with elevation for the z coordinate. |
| 11 | the gridded output. Each grid node is assigned a layer number. |
| 12 | the debugging level. |
| 13 | the file for debugging information |
| 14 | the random number seed. |
| 15-22 | simulation search and semivariogram parameters. |

Table 4.5: A description of the `SURFSIM` parameter file.

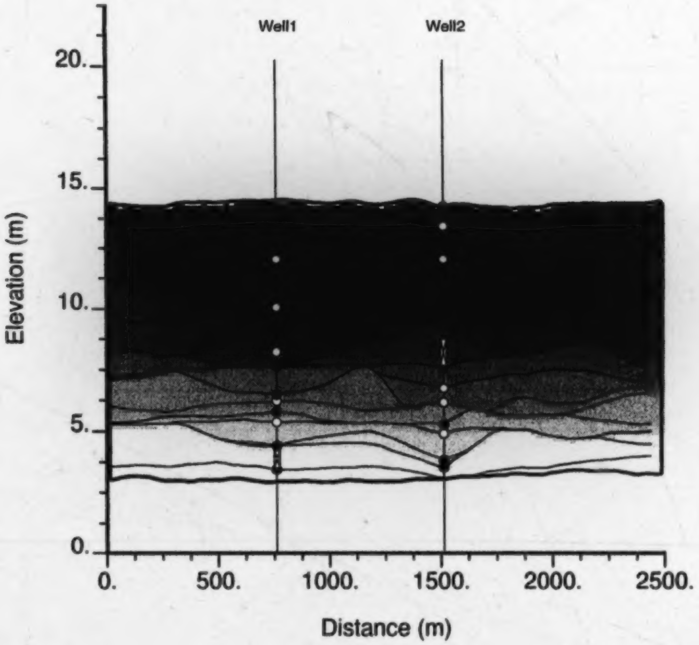

Figure 4.19: A cross section through a realization of stochastic surfaces that honor surface geometry and erosional (solid dots) and conformable (circles) surface contacts and segments with no information. Compare to outcrop photomosaic in Figure 8 from Carr and Gardner, 2000[11]

1. a single surface may only honor erosional or conformable contacts
2. if an erosional surface does not have an erosional contact available at a well then the surface is conditioned to a intersect a random location above the well
3. if a conformable surface does not have an available conformable contact at a well location then the surface is conditioned to a random location below the well.

For surface postprocessing the rules are:

1. an erosional surface truncates all previous surfaces
2. a conformable surface onlaps all previous surfaces

The `SURFSIM` algorithm is shown to reproduce features observed in a strataform setting while honoring well data. In the next section the surface based method is applied to reproduce stacking patterns.

## 4.5 Surface Based Turbidite Model

The previously described tools (see Sections 4.3 and 4.2) are now tailored to model the deepwater geologic setting described in Section 4.1. The hierarchial trend model and stochastic surface-based simulation approach is shown to model compensational cycles within turbidite lobes. This algorithm honors the geometries and interrelationships between the flow events, while also honoring a realistic level of conditioning data. This algorithm is demonstrated within a geostatistical work flow with property models constrained to honor trends based on compensational cycles for improved reservoir models. Integration of this geologic information may result in better models of reservoir response and an improved assessment of uncertainty. This work was originally developed in Pyrcz and Deutsch (2003)[96] and Pyrcz and Deutsch (2004)[101].

### 4.5.1 Methodology

Reservoir scale lobe geometry is established from the available data. A measurement of uncertainty is assigned based on data accuracy and this uncertainty may be accounted for as simulated fluctuations in the reservoir geometry. The lobe geometry defines the original bathymetry and the reservoir extents.

The surface template is a lobe with a convex upward geometry. This geometry is taken directly from the `LOBESIM` algorithm by Deutsch and Tran (1999)[26]. An illustration of this geometry is shown in Figure 4.20.

The placement methodology explicitly accounts for the compensational stacking pattern expected in this setting. The algorithm accomplishes this by mimicking the processes involved in the formation of flow event depositional units within a lobe.

The algorithm proceeds by generating stochastic flow event deposits defined by bounding surfaces. These flow event deposits have geometry based on parameter distributions from conditioning and analogue information. The calculation of the stochastic flow events requires two steps. First, the geometry is generated and then a stochastic residual is added. The geometric construction and placement considers factors such as: **(1)** source location, **(2)** bathymetry, **(3)** flow path and

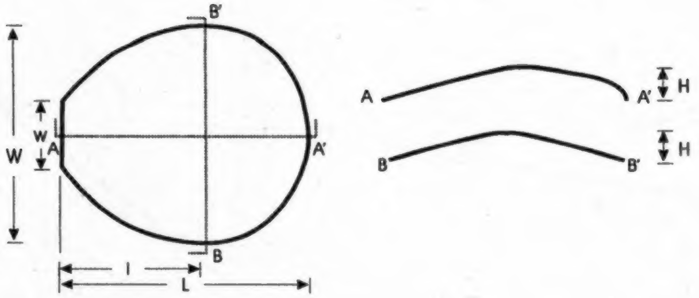

Figure 4.20: The lobe geometry applied in the `TURBSIM` algorithm as a surface template. Surface geometries are generated by varying the parameters l, L, w, W and H through a height to width ratio.

(**4**) characteristic geometry. The stochastic residual accounts for fluctuations within the bounding surfaces and is conditioned to well data.

The source location represents the entry location of a flow event into the lobe, where a feeding channel loses its confined character. The source is stochastically located along the proximal margin of the lobe prior to each flow event. The source location is drawn from a probability distribution with the probability inversely proportional to the elevation of the margin; therefore, flow events are more likely to enter in the lowest parts of the proximal margin of the lobe. Avulsion does not occur within the lobe (Posamentier, 2003)[93].

The bathymetry is initialized as the base of the lobe geometry defined by available data. If this surface is uncertain then multiple realizations of original bathymetry may be applied. Subsequent flow events modify this bathymetry, which affects the path of subsequent flow events (the influence of bathymetry on flow paths has been discussed by Liu and William (2000)[64]). Flow paths are set to follow the path of steepest gradient. The length of the flow path is based on a stochastically drawn lobe geometric parameters (refer back to Figure 4.20). The flow event deposit surface geometry is anchored to the flow path.

The geometric parameter distributions for the flow events are assigned based on available data. Well logs and analog studies may be applied to assess element thickness. Since flow events are below seismic resolution and are often difficult to correlate between widely spaced wells it is difficult to infer areal geometric parameters from site specific information. Outcrop studies may lack the ability to resolve

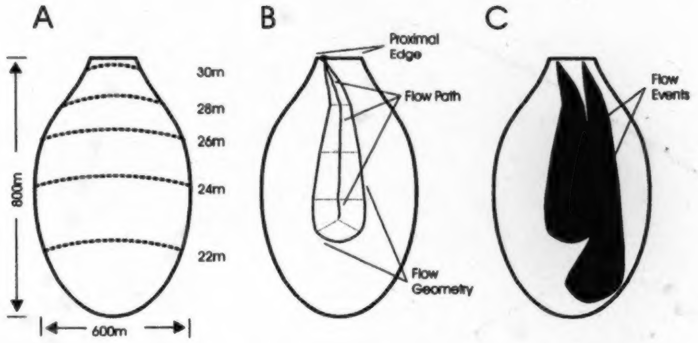

Figure 4.21: The construction of individual flow events within a lobe: A - a lobe geometry and bathymetry are defined, B - a stochastic flow events are generated, characterized by flow path and flow geometry and C - subsequent flow events are generated until the lobe is filled.

full 3-D architectures (Miall, 2000)[74], although canyon and butte type exposures and ground penetrating radar may provide information on flow event geometric distributions. This surface based turbidite lobe model is based on the assumption that the $2^{nd}$ order flow events mimic the geometries of the better resolved reservoir scale $3^{rd}$ order lobes (Stow and Johansson, 2000)[116]. Geometric information such as flow event length distributions may be inferred based on consistency with the $3^{rd}$ order lobe.

See Figure 4.21 for a schematic illustrating the construction of geometry of individual flow events within a lobe.

Histogram and semivariogram models characterize the stochastic residual. The semivariogram model defines the smoothness of the residual. The residual is simulated by a 2-D version of sequential Gaussian simulation (`SGSIM`) from the geostatistical library (GSLIB) (Deutsch and Journel, 1998)[23]. In deepwater settings it would be expected that the surfaces would have low rugosity. Nevertheless, this step allows for the conditioning of the surfaces.

The `SGSIM` realization is conditioned to neighbouring well data. This process is demonstrated in Figure 4.22. If the surface geometry contradicts data outside a tolerance then the geometry is recalculated. The algorithm terminates when the mean elevation of the surface is within a tolerance of the mean top elevation of the top of the lobe geometry.

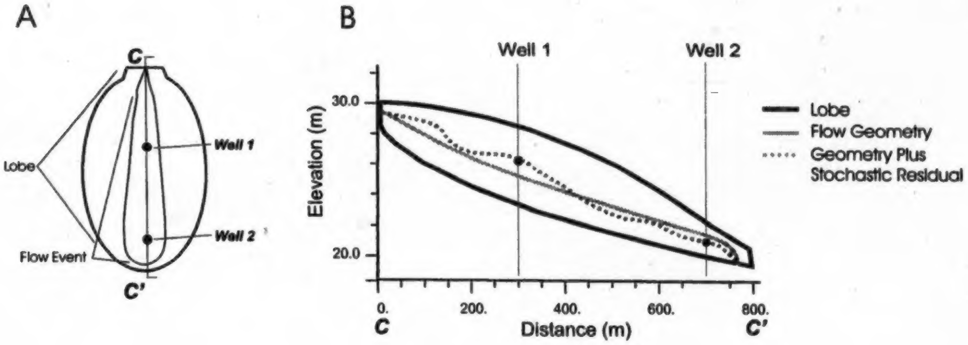
A
B
C
C'
Lobe
Flow Event
Well 1
Well 2
Elevation (m)
30.0
20.0
0.
200.
400.
600.
800.
C
Distance (m)
C'
Lobe
Flow Geometry
Geometry Plus Stochastic Residual

Figure 4.22: An illustration of the addition of a stochastic residual to characterize fluctuations and to allow for conditioning to well data: A - plan view and B - cross section $C - C'$ with lobe, flow geometry and the surface realization conditional to well data.

### The `TURBSIM` Parameters

`TURBSIM` is a Fortran program that applies the previously outline methodology. The associated parameter file is shown below. Note the inputs include well data, bounding surfaces (top is optional), flow event deposit parameters and simulation parameters for the 2-D simulation subroutine modified from GSLIB. An explanation of the `TURBSIM` parameters is provided in Table 4.6.

```
Parameters for TURBSIM
 1. wells.dat               -file with data
 2. 1 2 3 4 5 6 7 8         - well,x1,y1,z1,x2,y2,z3,code
 3. topsurf.out             -top surface
 4. 1                       - dynamically set top(1=yes,0=no)
 5. botsurf.out             -bottom surface
 6. 0                       -debugging level:0,1,2,3
 7. none                    -file for debugging output
 8. turbsim.out             -file for simulation output
 9. 4000 2000               -ML,SL
10. 2000 1000               -Ml,Sl
11. 2000 1000               -MW,SW
12. 1000 500                -Mw,Sw
13. 0.1 0.05                -Mhwratio,Shwratio
14. 1 120                   -number of realizations,max num of surfaces
15. 100 25.0 50.0           -nx,xmn,xsiz
16. 100 25.0 50.0           -ny,ymn,ysiz
17. 0.0 20.0                -zmin,zmax
```

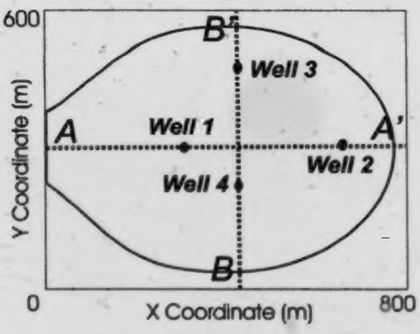

Figure 4.23: A plan view of the $3^{rd}$ order lobe and the locations of the four vertical wells.

```
18. 69069                -random number seed
19. 12                   -number of simulated nodes to use
20. 1 3                  -multiple grid search (0=no,1=yes),num
21. 1000.0 1000.0        -maximum search radii (hmax,hmin)
22. 0.0                  -angle for search ellipsoid
23. 201 201              -size of covariance lookup table
24. 1 0.0                -nst,nugget effect
25. 1 1.0 0.0            -it,cc,ang1
26.   1000.0 1000.0      -a_hmax, a_hmin
```

### 4.5.2 Demonstration

The following is a demonstration of the construction of deepwater surface based models with hierarchical trend model and a posteriori correction to honor areal and vertical trends from large scale information. Multiple surface-based realizations were calculated based on the flow event and lobe geometry shown in Figure 4.21. The surfaces were conditioned to four wells (see Figure 4.23). Two realizations are shown in Figure 4.24. A hierarchical trend model based on the simulated architectural elements was calculated and is shown in Figure 4.25. The surfaces were loaded into Gocad for visualization. A screen capture of the first ten surfaces is shown in Figure 4.26, and the same surfaces are shown in Figure 4.27 with a cut away to expose the stacking pattern of the surfaces. A fence plot of all the $2^{nd}$ order elements is shown in Figure 4.28.

The hierarchical trend models reproduce the trends within hierarchies of architectural elements. For example, the individual flow events, $2^{nd}$ order lobes show a

| Line | Description |
|---|---|
| 1 | input file with well data. The file should be in GEOEAS format and GSLIB grid convention with any number of categories. |
| 2 | column numbers for the well, x, y, z location and marker code. The x2, y2, z2 are used for no information intervals. The codes are 0-erosional, 1-gradational and 2-no information. |
| 3 | the file with the initial top surface in GEOEAS format and GSLIB grid convention.. |
| 4 | if top is set dynamically, the last simulated surface is set as the top, otherwise the last simulated surface is truncated by the top of the lobe from the top file. |
| 5 | the files with the bottom surfaces in GEOEAS format and GSLIB grid convention. |
| 6 | the debugging level (0=no debugging information, 3=all surface statistics and simulation processes are written out. |
| 7 | the file for the debugging output |
| 8 | the surfaces output. The surfaces output is regular grid in x and y with elevation for the z coordinate. |
| 9-13 | the mean and standard deviation for Gaussian distribution of the lobe geometric template parameters L,l,W,w and height to width ratio (hwratio). |
| 14 | the number of surface realizations to calculate and the maximum number of surfaces to calculate (may be set small for initial setup and then set large when calculating surface realizations. |
| 15-17 | the regular grid parameters. The z parameters are required for the pixel based output for visualization. |
| 18 | the random number seed |
| 19-26 | simulation search and semivariogram parameters. |

Table 4.6: A description of the `TURBSIM` parameter file.

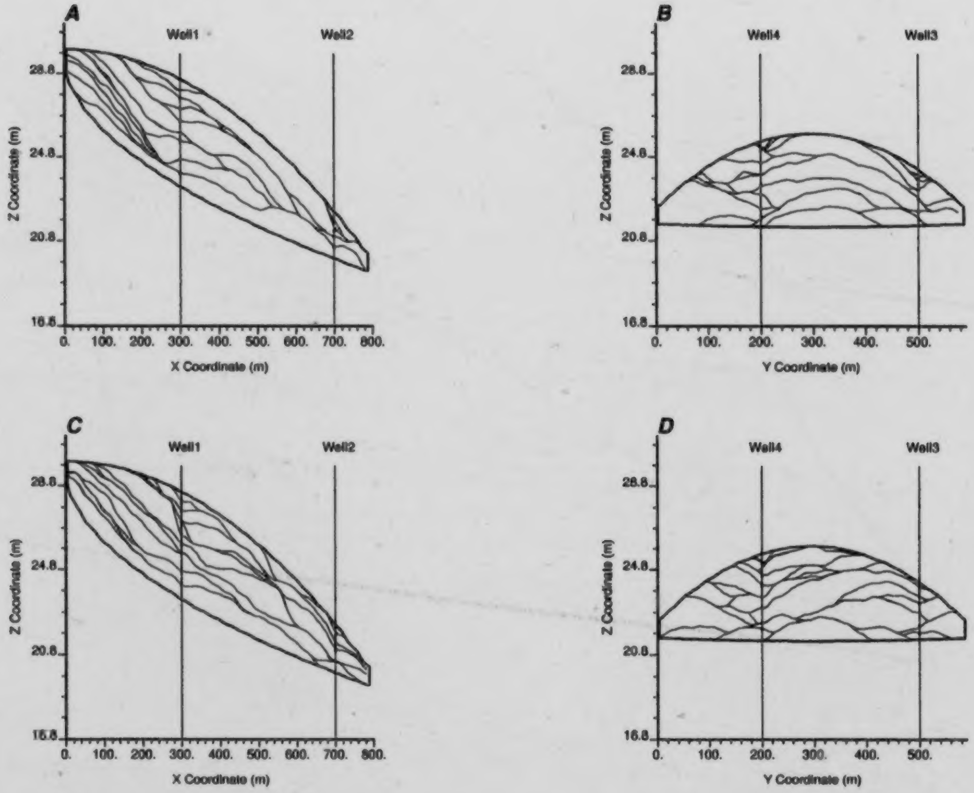
A
Well1
Well2
28.8
24.8
20.8
16.8
Z Coordinate (m)
0. 100. 200. 300. 400. 500. 600. 700. 800.
X Coordinate (m)
B
Well4
Well3
28.8
24.8
20.8
16.8
Z Coordinate (m)
0. 100. 200. 300. 400. 500.
Y Coordinate (m)
C
Well1
Well2
28.8
24.8
20.8
16.8
Z Coordinate (m)
0. 100. 200. 300. 400. 500. 600. 700. 800.
X Coordinate (m)
D
Well4
Well3
28.8
24.8
20.8
16.8
Z Coordinate (m)
0. 100. 200. 300. 400. 500.
Y Coordinate (m)

Figure 4.24: The lobe geometry, vertical well locations and sections for the demonstration of stochastic surface-based flow events within a lobe: A - first realization long section $A - A'$, B - first realization cross section $B - B'$, C - second realization $A - A'$ and D - second realization cross section $B - B'$ long section.

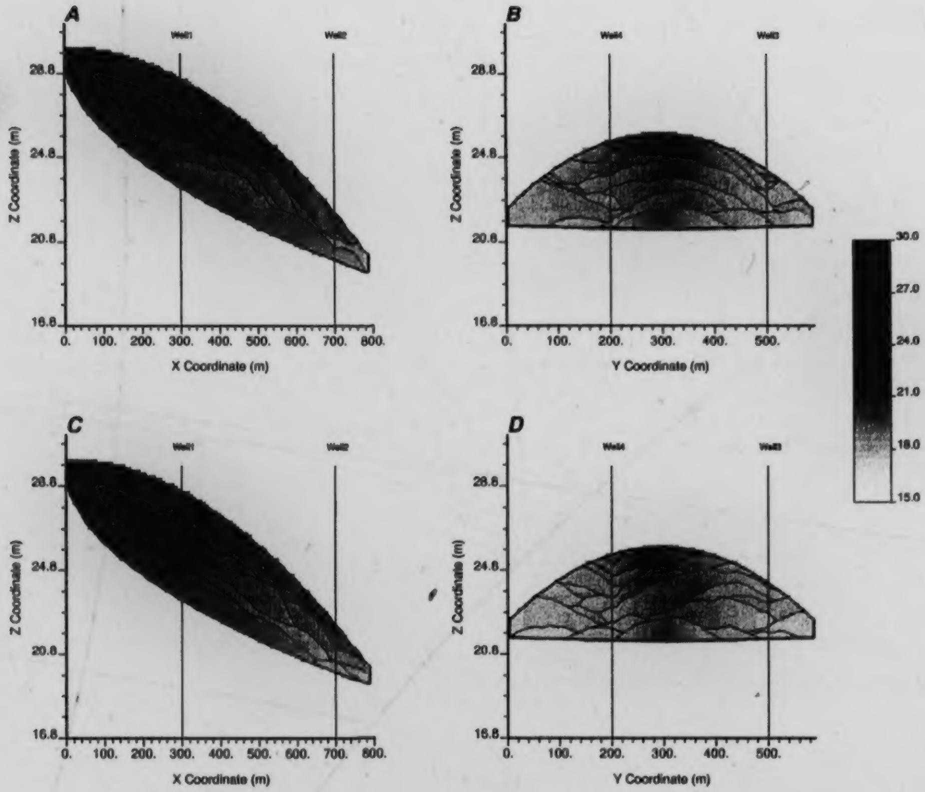

Figure 4.25: Two example realizations of flow events in a depositional lobe with hierarchical trend models: A - first realization long section $A-A'$, B - first realization cross section $B-B'$, C - second realization $A-A'$ and D - second realization cross section $B-B'$ long section. The property units are percent porosity.

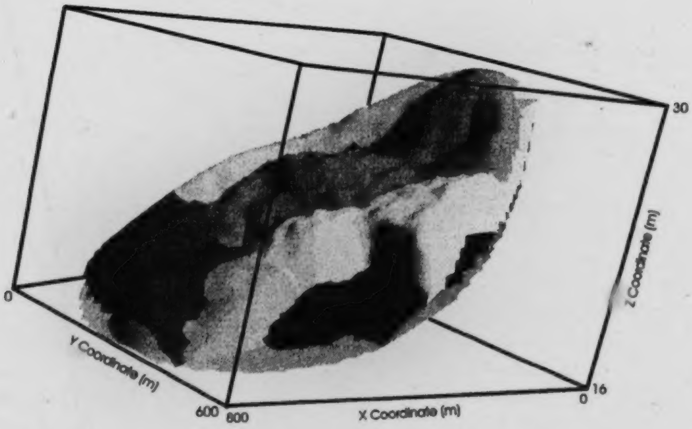
30
Z Coordinate (m)
0
Y Coordinate (m)
600
800
X Coordinate (m)
0
16

Figure 4.26: A screen capture from Gocad of the first ten flow event surfaces.

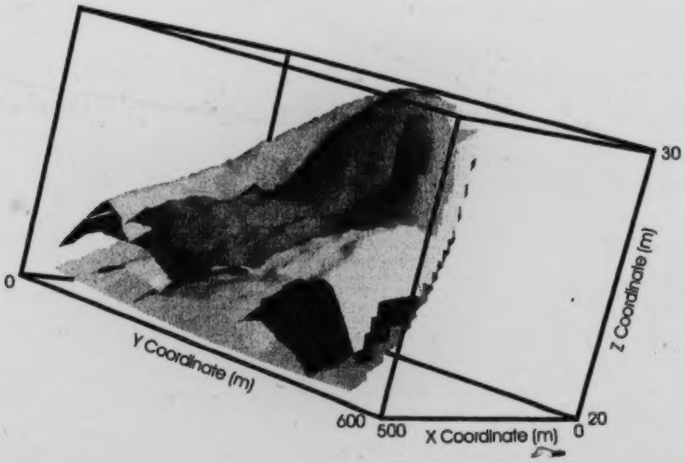
30
Z Coordinate (m)
0
Y Coordinate (m)
600
500
X Coordinate (m)
0
20

Figure 4.27: A screen capture from Gocad of the first ten flow event surfaces with a cut away view to reveal internal structure.

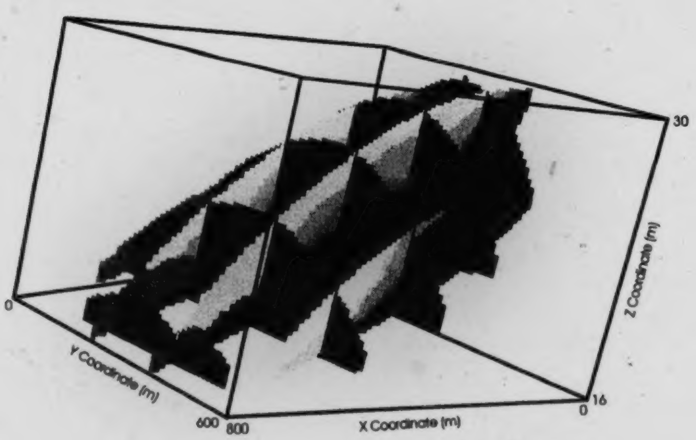

Figure 4.28: A fence plot of the discretized architectural element model from Gocad.

fining upwards trend, while the $3^{rd}$ lobe shows a coarsening upward trend. These trends would be expected in a prograding system of individual Bouma sequences within a turbidite lobe (Bouma, 1962)[6]. These models may be corrected to honor vertical and areal trends.

A target areal and vertical trend was constructed. For the purpose of demonstration these trends were assumed. The initial areal and vertical trends from the hierarchical trend model and the target areal and vertical trends are shown in Figure 4.29 and Figure 4.30, respectively.

The hierarchical trend model was corrected for vertical and areal trends (see Section 4.2.2). A smoothing volume of 1/5 the model volume and 5,000 iterations were applied. The algorithm required less than five minutes on a modest 2003 vintage PC. The areal and vertical trends of the corrected trend model are shown in Figure 4.31.

Comparison of corrected trend model and the target areal and vertical trends reveals that the large scale features are imported into the hierarchical trend model and that the global mean is reproduced. The mismatch (corrected-target) of the areal and vertical trends was calculated (see Figure 4.32).

The trend correction methodology has adjusted the 3-D trend model to honor the target vertical and areal trends. An increase in the number of iterations and a decrease in the convergence tolerance would result in even closer reproduction. The vertical trend shows slight dimples. This could be removed by decreasing the size

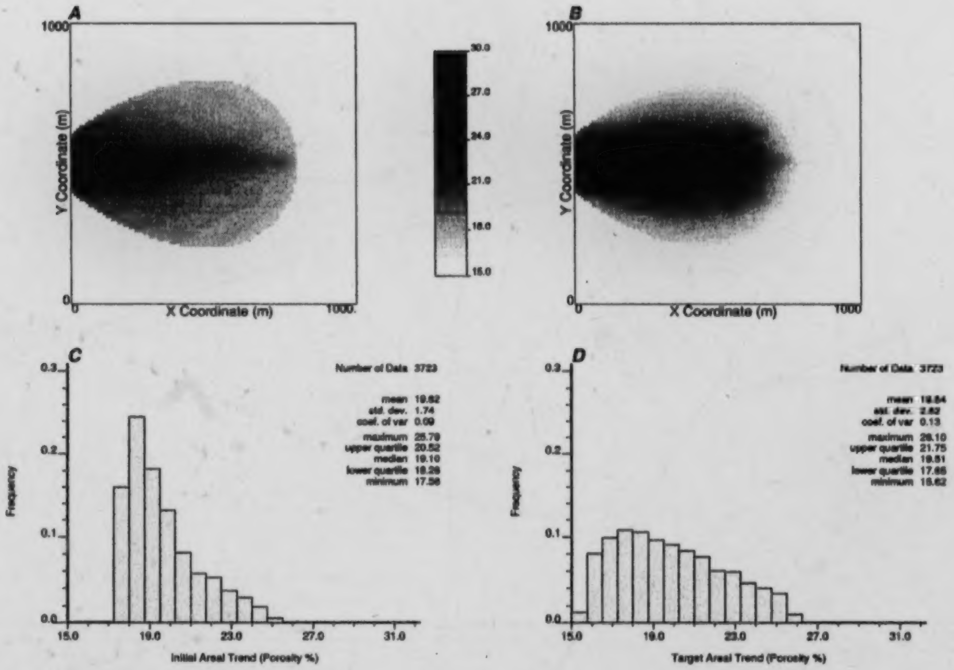

Figure 4.29: Areal trend models: A - the initial areal trend model from the hierarchical trend model, B - the target areal trend based on assumed conditioning, C - the distribution of the initial areal trend and D - the distribution of the target areal trend. The property units are percent porosity.

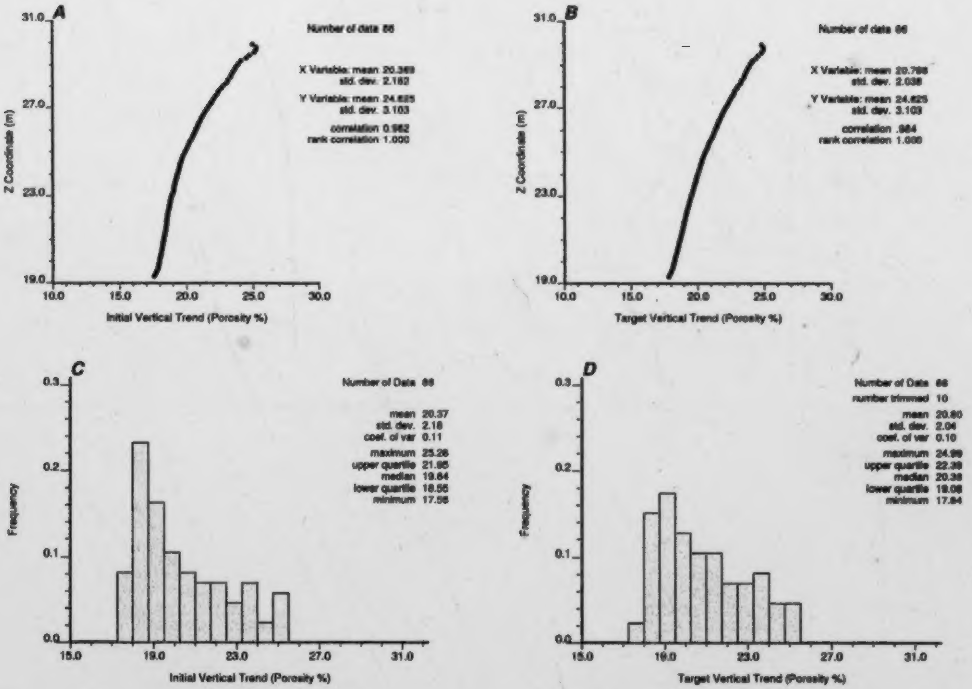

Figure 4.30: The vertical trend models: A - the initial vertical trend model from the hierarchical trend model, B - the target vertical trend based on assumed conditioning, C - the distribution of the initial vertical trend and D - the distribution of the target vertical trend. The property units are percent porosity. Note the target vertical trend has a lower variance and is more linear than the initial vertical trend.

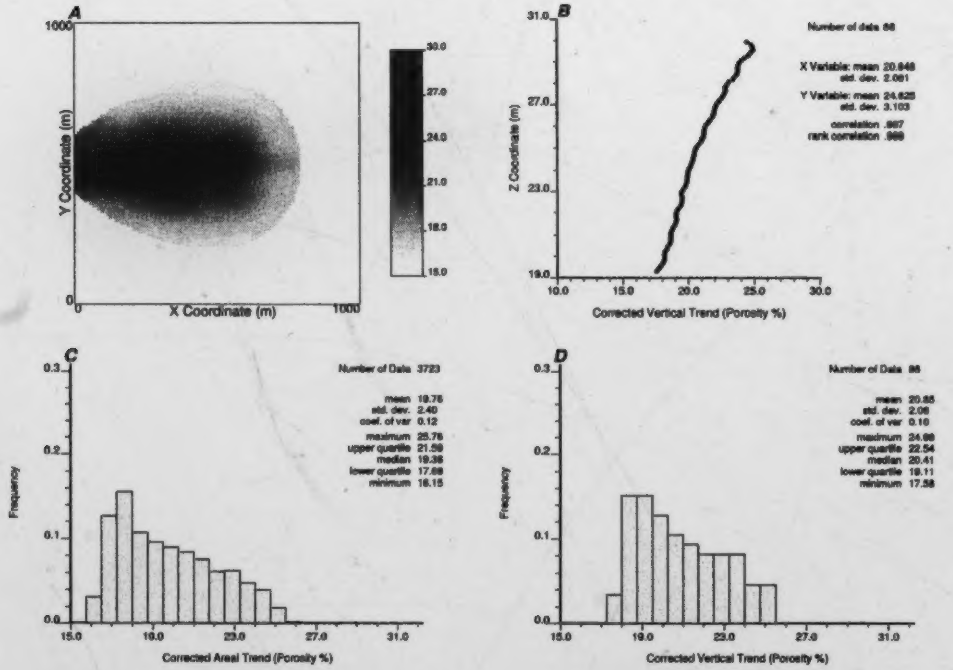

Figure 4.31: The areal and vertical trend of the corrected trend model: A - corrected areal trend, B - corrected vertical trend, C - the distribution of the corrected areal trend and D - the distribution of the corrected vertical trend. The property units are percent porosity.

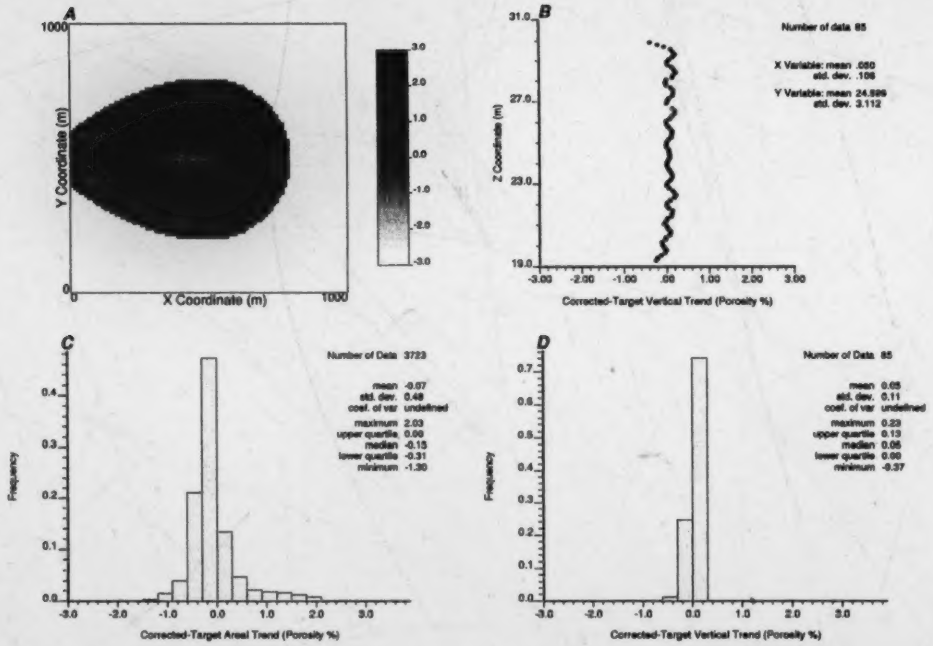

Figure 4.32: The mismatch between the corrected and target areal and vertical trends: A - corrected - original areal trend, B - corrected - original vertical trend, C - the distribution of the corrected - original areal trend and D - the distribution of the corrected - original vertical trend. The property units are percent porosity.

of the maximum factor and increasing the number of iteration.

A series of long sections (see Figure 4.33) and fence diagrams of the surface-based model, the initial trend model and the correction trend model (see Figure 4.34) are included. This illustrates that the correction to honor areal and vertical trends and maintains the small scale trends based on the surface constrained hierarchical trend model.

## 4.6 Turbidite Case Study

This synthetic case study is based on Lobe VII of the Cengio Turbidite System (Italy) of the Tertiary Piedmont Basin (Cazzolo et al., 1985)[13]. Lobe VII is dominated by compensational cycles that constrain the distribution of lithofacies. There are many other well studied modern and ancient examples that contain signifi-

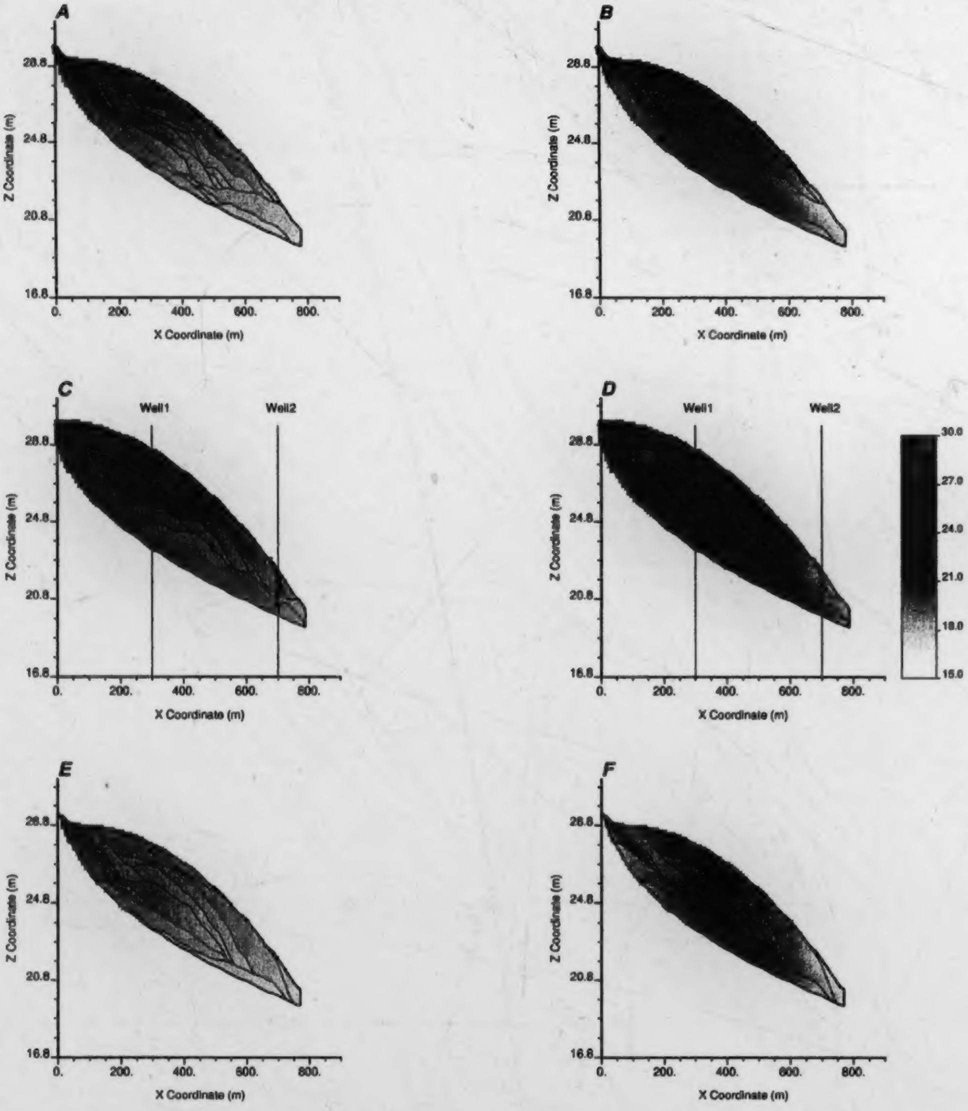

Figure 4.33: Long sections of the hierarchical trend model before and after correction to honor areal and vertical trend model: A & B - long section 400 before and after correction, C & D - long section 500 before and after correction and E & F - long section 600 before and after correction. Note that the large scale correction preserves small scale trend features. The property units are percent porosity.

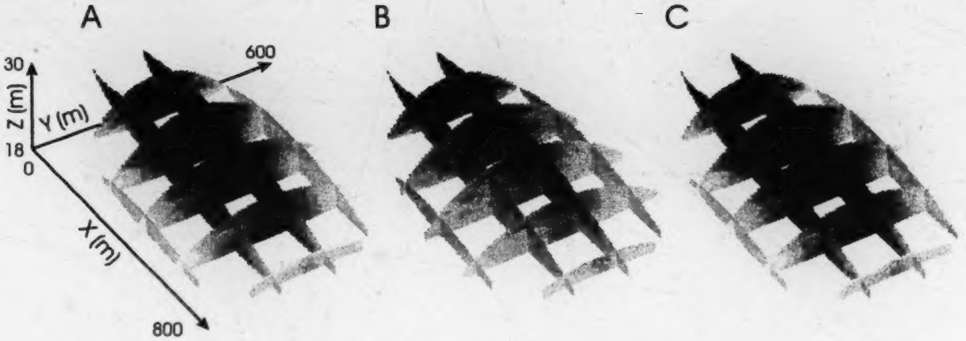

Figure 4.34: Fence diagrams of: A - the initial surfaced-based model, B - the initial trend model and C - the corrected trend model. This demonstrates that the correction to honor areal and vertical trends preserves the small scale features imparted by the construction of the hierarchical trend model. The property units are percent porosity with the same grey scale as Figure 4.33.

cant compensational cycles including Mississippi Middle Miocene (M4) (De Vray et al.)[31], Gottero Turbidite System, Italy (Nilsen and Abbate, 1985)[81] and Tanqua Karoo Subbasin, South Africa (Dudley et. al, 2000)[33]. The Cengio turbidite system is comprised of eight tabular lobes with thickness ranging between five to 25 meters. Lobe VII is roughly 20 meters thick and extends for about six kilometers and is bounded on the west to north by a slope mudstone.

The subsequent flows may be separated by mud drapes and have persistent internal lithofacies trends. The mudstone facies are thinly bedded and are not laterally persistent (Cazzolo et al., 1985)[13]. Even with limited continuity these shales may act as baffles to fluid flow. The modeling of these compensational cycles is an important step in assessing the impact on reservoir response of shale baffles and the other related lithofacies trends.

### 4.6.1 The Data

The top and bottom of the lobe is correlated between wells and may be interpolated with the aid of seismic information. The initial bathymetry is defined as a deterministic surface that approximates fault-bounded, southwest-northeast-trending submarine depression described by Cazzolo et al. (1985)[13] (see Figure 4.35).

It is assumed that seven vertical wells are available, as indicated in Figure 4.35.

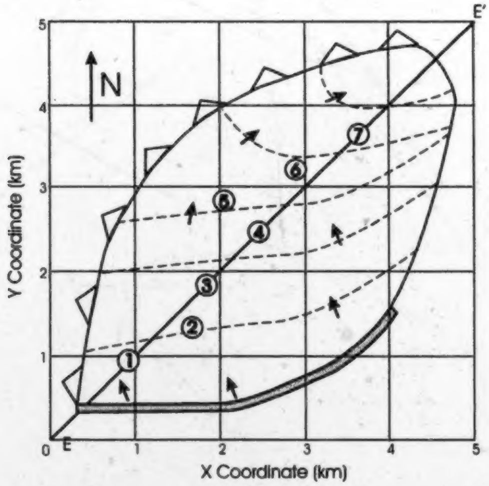
N
E'
E
Y Coordinate (km)
X Coordinate (km)
0
1
2
3
4
5
1
2
3
4
5
①
②
③
④
⑤
⑥
⑦

Figure 4.35: A schematic of the initial bathymetry loosely based on a study of Cengio turbidite system Italy (Cazzolo et al., 1985)[13]. The dark gray section represents the source for flow events. The fan lobe onlaps a mudstone slope along the west, northwest and north. The vertical well locations and the paleocurrents are indicated. The study area is 25 square kilometers.

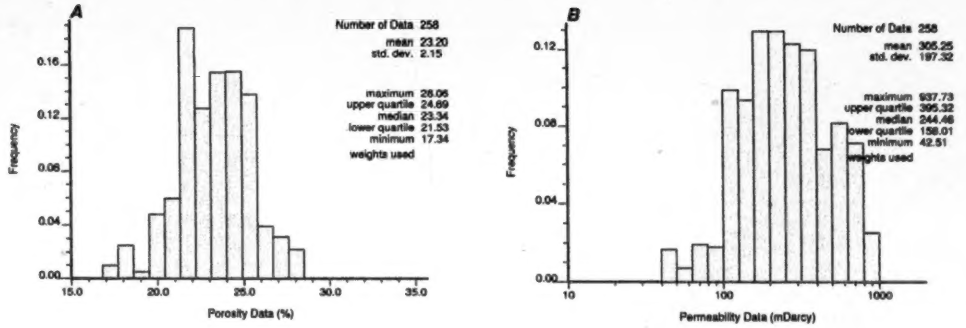

Figure 4.36: The distribution of synthetic A - porosity and B - permeability from well log.

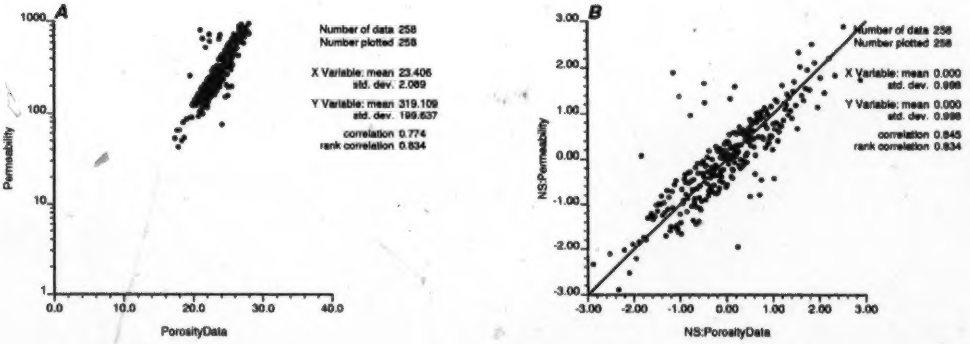

Figure 4.37: The scatter plots of synthetic well permeability and porosity, A - before Gaussian transform and B - and after Gaussian transform. The permeability is in mD and the porosity is in percent.

Seven wells were chosen as a reasonable high level of conditioning in a typical deepwater reservoir study of this areal extent. Note this is conservative since this modeling procedure performs better with less conditioning (see Section 4.5). The contacts of the flow events are assumed along the wells with a similar density observed in the Cazzolo et al. (1985)[13] case study. Also, porosity and permeability along the wells are assumed. The data distributions are shown in Figure 4.36 and the scatter plot of permeability and porosity is shown in Figure 4.37. The sections that are used for visualization are shown Figure 4.38.

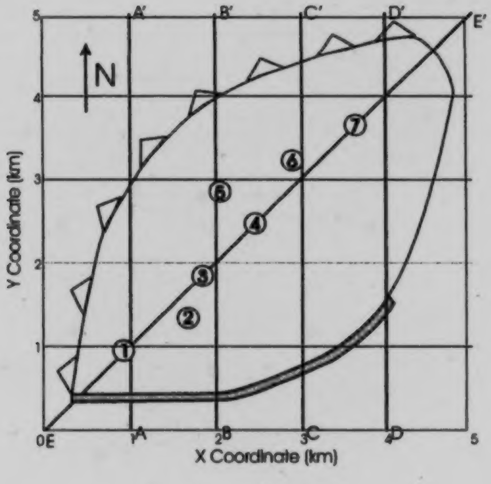

Figure 4.38: The locations of the North-South sections (A through D) and the long section (E).

### 4.6.2 Geostatistical Work Flow

The application of stochastic surface based simulation is demonstrated within a geostatistical workflow for the modeling of petrophysical properties within Lobe VII. A common geostatistical workflow is to model: (**1**) reservoir geometry, (**2**) lithofacies and (**3**) petrophysical properties constrained by lithofacies. These models are conditional to all available data and analog information (Deutsch, 2002)[21].

#### Model of Reservoir Geometry

Often reservoir geometry is provided by seismic information calibrated to well logs. Seismic resolution is a function of the source frequency content, rock sonic properties and the depth of the trace. There is commonly a significant level of uncertainty associated with respect to the reservoir geometry. This uncertainty may be carried through the stochastic workflow through the use of multiple reservoir geometry realizations or scenarios. These scenarios may be the result of simulated surfaces conditioned to well contacts or based of expert judgment of professional geologists. For each realization or scenario of reservoir geometry, a realization of facies and petrophysical properties may be calculated (Pyrcz et al., 2004)[103]. For this case study a single reservoir geometry was used.

| Category | Dominant Lithology | Bedding |
|---|---|---|
| Facies 1 | sandstone | thick - massive, crudely graded |
| Facies 2 | sandstone | thin - medium, subtly graded |
| Facies 3 | mudstone | thinly bedded sandstone |
| Facies 4 | mudstone | devoid of sandstone |

Table 4.7: A summary of the lithofacies identified by Cazzolo et al. (1985)[13].

### Lithofacies Models

There are four lithofacies types identified by Cazzolo et al. (1985)[13]. They are summarized in Table 4.7. There are significant trends in the facies including: (**1**) higher fraction of sandier amalgamated sandstone bodies along the center axis, (**2**) fining to the distal and (**3**) capping of sandy flows with sandy mudstone. It was decided not to explicitly model lithofacies. Instead porosity and permeability are constrained by trend models that account for these lithofacies trends. This is reasonable since these lithofacies represent a natural continuum of reservoir quality from high porosity and permeability sandstone to low porosity and permeability mudstone.

### Petrophysical Properties

Porosity and permeability are modeled by the following steps: (**1**) calculate surfaces representing stochastic flow events within the lobe, (**2**) construct a hierarchical porosity trend model that characterizes the observed trends in lithofacies constrained to the surface based model, (**3**) simulate porosity conditional to well logs and with the hierarchical porosity trend model as a local variable mean model (Deutsch and Journel, 1998)[23] and (**4**) simulate permeability with the porosity realization as secondary data for collocated cokriging (Deutsch and Journel, 1998)[23].

It is recommended that a single realization of surface-based trend be coupled with a realization of porosity and permeability to produce a single reservoir realization, rather than a combinatorial of matched trend and property realizations. The former is a more computationally efficient method to sample the model space of uncertainty and is applied in this case study (Pyrcz et al., 2004)[103].

This methodology honors the available porosity and permeability data from well log and core, the trend in the porosity and permeability informed by geologic information on the transition in lithofacies, the compensational cycle geometry and the relationship between porosity and permeability. The associated steps are demonstrated and discussed in detail.

The methodology for generating stochastic flow events has been discussed and demonstrated previously. Implementation of this procedure with this specific case study requires; (**1**) the characterization of the lobe geometry and (**2**) the assignment of flow event parameter distributions. The construction of the reservoir geometry has been previously discussed. The flow event parameter distributions should be determined from well data and analog information. The size distributions should be consistent with the lobe geometry. If the distribution of flow event sizes is too small then the distal section of the lobe may not be filled. In this case, the algorithm should be modified to allow for disconnected lobes.

For this case study, the parameter distributions were drawn from Gaussian and uniform distributions (see Table 4.8). The length of the flow events $L$ is drawn from a Gaussian distribution with mean of 5,000 meters and standard deviation of 1,000 meters. This parameter was set based on consistency with the $3^{rd}$ order lobe. The length to the position of maximum width $l$ is drawn from a uniform distribution of 40% to 70% of $L$, the maximum lobe width $W$ is drawn from a uniform distribution of 10% to 30% of $L$ and the width of the source $w$ is assigned as 40% of $W$. These areal geometric parameters result in a wide variety of lobe morphologies and reflect the uncertainty in their assignment given the limited areal information available in the outcrop study (Cazzolo et al., 1985)[13]. The difficulty in assigning small scale areal geometric parameters was discussed in Section 4.5.1. The width to height ratio was selected to reproduce the nominal flow event thickness of 1.0 m observed in the outcrop.

Two surface based realizations were simulated, based on the reservoir geometry and the distribution of flow event parameters indicated above. The first and second realizations are comprised of 121 and 71 flow events, respectively. The long section for two realizations is shown in Figure 4.39 and the north-south sections for the first realization are shown in Figure 4.40.

Each surface based realization honors the identified contacts along the wells. This is demonstrated in Figure 4.39. Between the wells and at locations along the wells with missing information the realizations may vary greatly while honoring the

| Parameter | Distribution |
|---|---|
| $L$ | $N\{m = 5,000, \sigma = 1,000\}$ |
| $l$ | $U\{0.4 \cdot L, 0.7 \cdot L\}$ |
| $W$ | $U\{0.1 \cdot L, 0.3 \cdot L\}$ |
| w | $0.4 \cdot W$ |
| w:h ratio | 2,500 |

Table 4.8: Lobe parameter distributions applied in the example case study. All units are in meters.

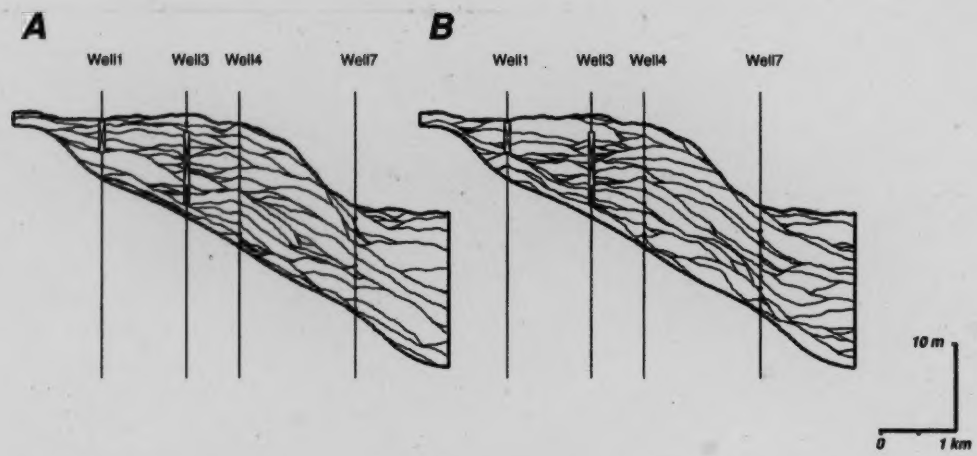
A
Well1
Well3
Well4
Well7
B
Well1
Well3
Well4
Well7
10 m
0
1 km

Figure 4.39: Two surface realizations (long section $E$ - $E'$): A - the first surface realization and B - the second surface realization.

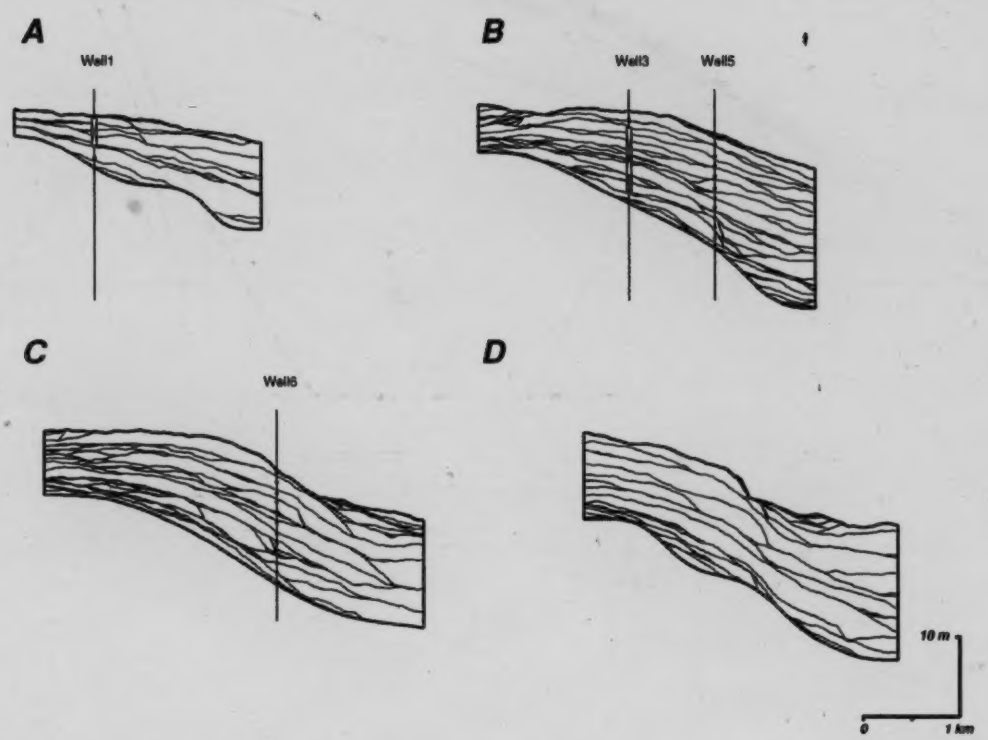
A
Well1
B
Well3
Well5
C
Well6
D
10 m
0
1 km

Figure 4.40: One surface realization: A - section $A - A'$, B - section $B - B'$, C - section $C - C'$ and D - section $D - D'$.

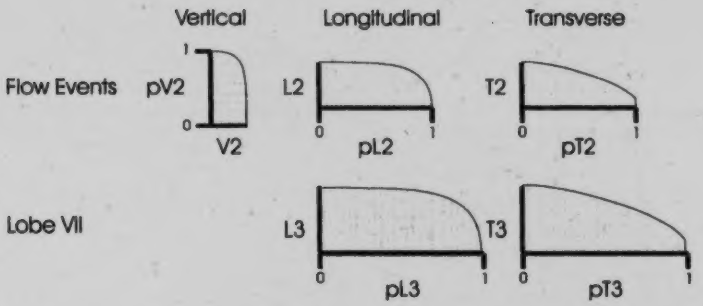

Figure 4.41: The porosity trends inferred from the lithofacies study of the Cengio Turbidite System, Italy (Cazzolo et al., 1985)[13]. The flow events have subtle grading and are often capped by fine grained facies. Flow events and the lobes demonstrate an increase in fine facies towards the distal and are coarsest along the primary axis of flow.

flow event geometry and the compensational stacking pattern.

The lithofacies trends were quantified as functions describing the porosity trend in the depositional coordinate system. The functions describing these trends are shown in Figure 4.41. Mud drapes are represented by a sharp decrease in the porosity trend near the top of the flow events and fining towards the peripheries is indicated in the longitudinal and transverse trend functions. The resulting hierarchical trend models based on the two surface based simulations (refer to Figure 4.39) are shown in Figure 4.42 and a fence diagram of the first trend model is shown in Figure 4.43.

These trend models may be applied as local variable mean models for SGSIM (Deutsch and Journel, 1998)[23] of porosity conditioned to well log. SGSIM requires the modeling of semivariograms of the Gaussian transform of the data. The experimental semivariograms were calculated in the plane of the flow events (near horizontal) and orthogonal to the flow events (near vertical). The porosity semivariograms and their associated models are shown in Figure 4.44. The semivariograms were modeled by a spherical structure with a nugget effect of 0.2. This high nugget effect in the experimental semivariogram of the residual may indicate that some of the spatial structure is captured in the hierarchical porosity trend model. Over fitting of the trend is avoided, since the trend model is based on a stochastic model and multiple trend models are applied to construct multiple property realizations. The experimental semivariograms may vary between realizations of hierarchical trend

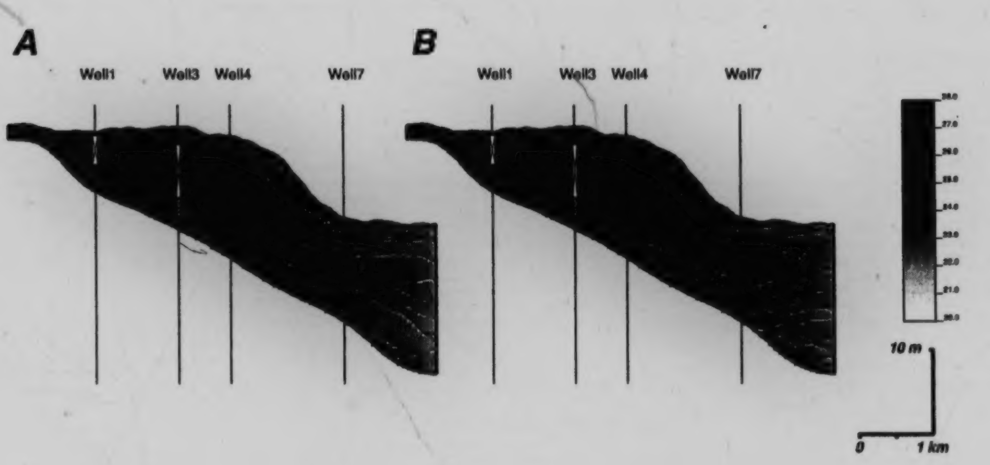
A
B
Well1
Well3
Well4
Well7
Well1
Well3
Well4
Well7
28.0
27.0
26.0
25.0
24.0
23.0
22.0
21.0
20.0
10 m
0
1 km

Figure 4.42: Two porosity (percent) hierarchical trend models (Section E-E'): A - the first hierarchical porosity trend model and B - the second hierarchical porosity trend model. The trends described in Figure 4.41 are reproduced and the trend model mean is corrected to the declustered mean from the well logs.

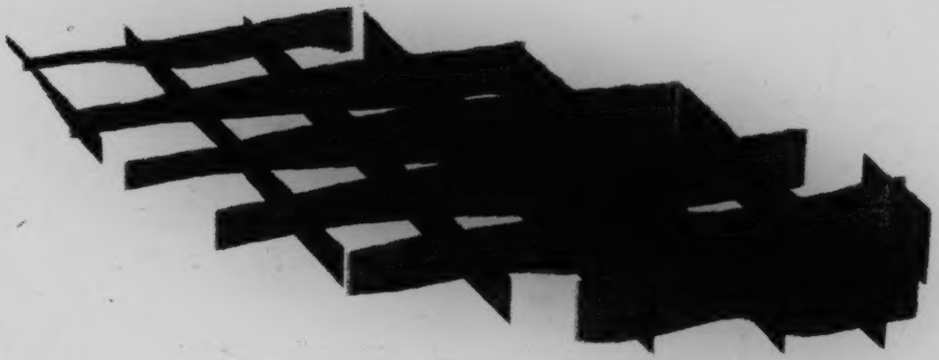

Figure 4.43: A fence diagram of the first realization of the porosity hierarchical trend model (30 times vertical exaggeration). Grey scale is the same as in Figure 4.42.

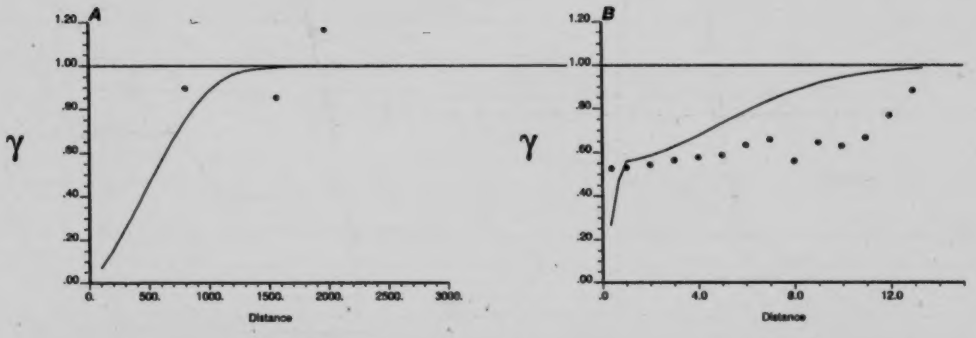

Figure 4.44: The semivariograms of the Gaussian transform of the porosity residual (well log data - hierarchical trend model): A - the horizontal semivariogram and B - the vertical semivariogram.

model. It is assumed that this difference is not significant; therefore the experimental semivariograms are only calculated once.

Two realizations of porosity were calculated each paired with a local variable mean model (refer to Figure 4.42). These realizations reproduce the porosity conditioning from well log, the declustered porosity distribution and the porosity trends constrained to the stochastic surfaces (see Figures 4.45 and 4.46). At the sampled locations along the wells the porosity realizations are the same, but away from the wells the realizations may be quite different, while honoring the local variable trend model and stationary semivariogram. This represents the increasing uncertainty away from the wells.

It is assumed that permeability inferred from log and core is available at the wells (refer to Figure 4.36). The correlation coefficient between the Gaussian transform of porosity and permeability may be inferred from the available conditioning (refer to Figure 4.37) and from analogue. The experimental permeability semivariograms were calculated in the plane of the flow events (near horizontal) and orthogonal to the flow events (near vertical). The permeability semivariograms and their associated models are shown in Figure 4.47.

Two realizations of permeability were simulated with the associated porosity realizations applied as collocated secondary data in a collocated cokriging context (Deutsch and Journel, 1998)[23] (see Figure 4.48 and Figure 4.48).

These realizations of reservoir petrophysical properties may be applied for reser-

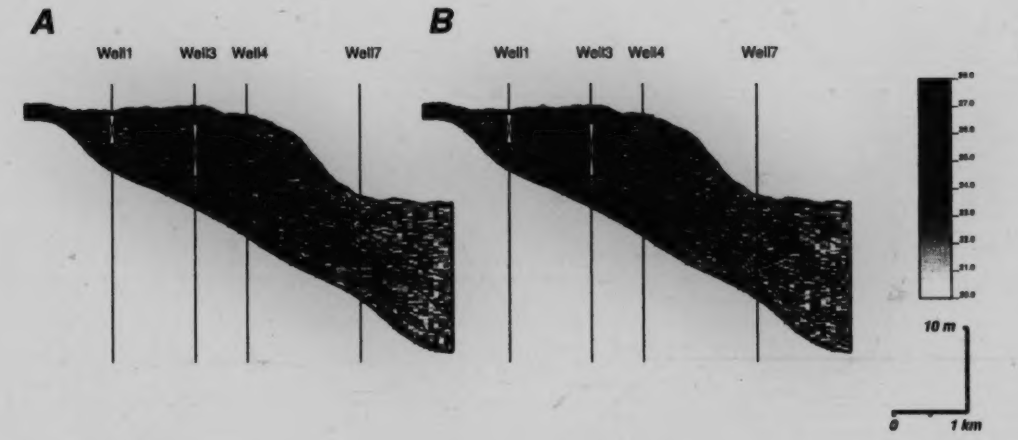

Figure 4.45: Two realizations of porosity (percent) constrained to the surface based hierarchical trend model and conditioned to well logs (Section E-E'): A - the first porosity realization and B - the second porosity realization.

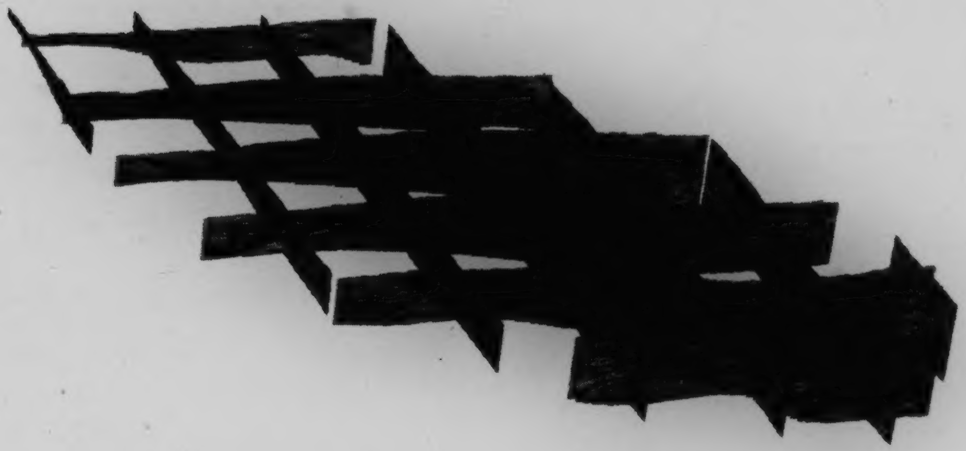

Figure 4.46: A fence diagram of the first porosity realization based on the porosity hierarchical trend model (30 times vertical exaggeration). The units are porosity percent and the grey scale is the same as Figure 4.45.

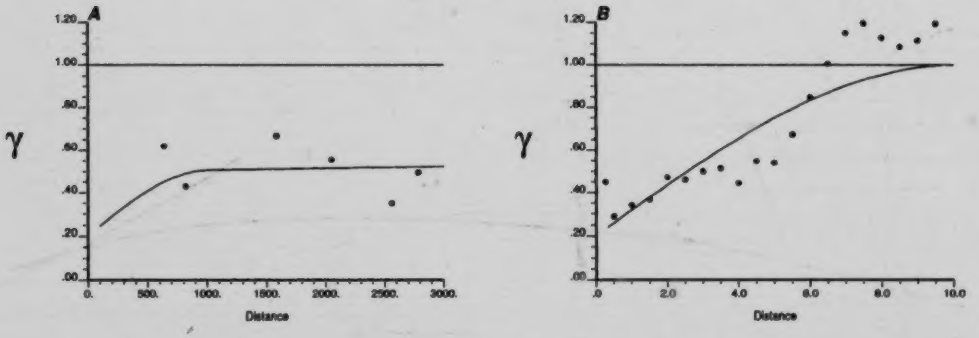

Figure 4.47: The semivariograms of the Gaussian transform of the permeability well log data: A - the horizontal semivariogram and B - the vertical semivariogram.

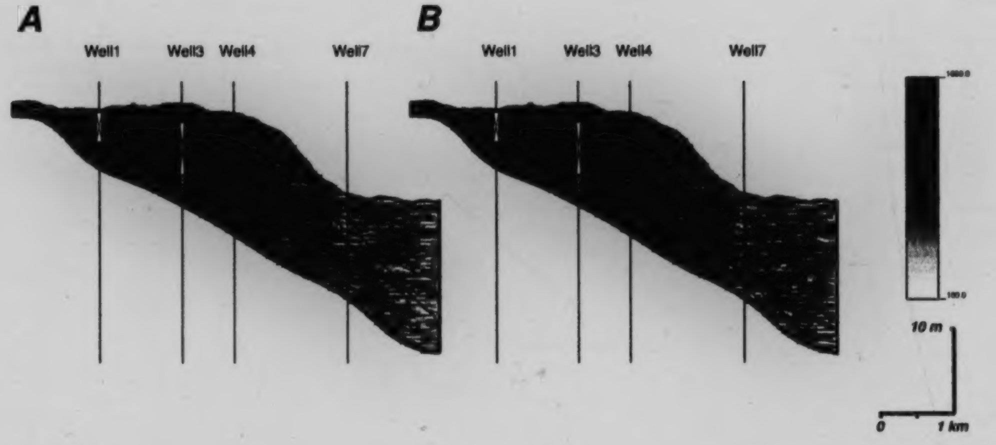
A
Well1
Well3
Well4
Well7
B
Well1
Well3
Well4
Well7
10 m
0
1 km

Figure 4.48: Two realizations of permeability correlated to the paired porosity realizations and conditioned to well logs (Section E-E'): A - the first realization and B - the second realization.

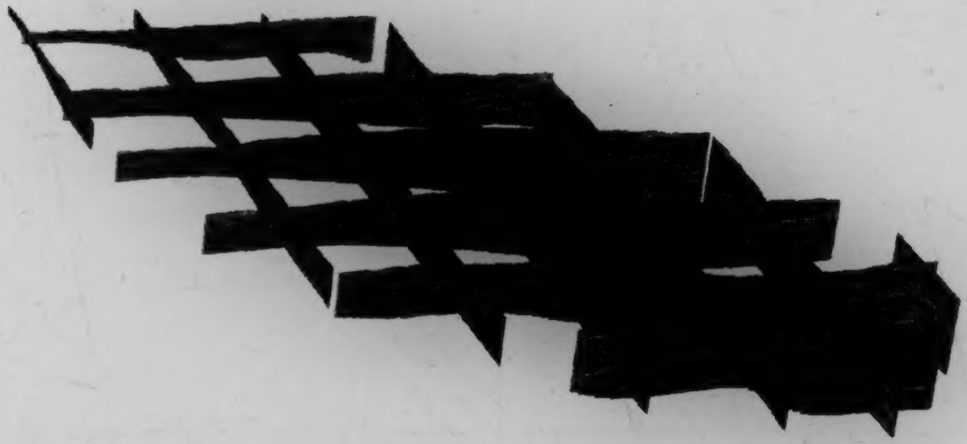

Figure 4.49: A realization of permeability correlated to the paired porosity realization and conditioned to well logs. Grey scale is the same as in Figure 4.48.

voir development planning. A suite of realizations may be subjected to flow simulation or other transfer functions to assess the uncertainty in a response variable such as production rate. For example, porosity × thickness (PhiH) 6 maps may be calculated for each realization to calculate reservoir volume (Figure 4.50).

### 4.6.3 Comments on the Surface Based Turbidite Model

There are many statistical models that could be applied to this geologic setting. This surface based model is one particular statistical model that was developed because it: (**1**) mimics compensational related features that are often observed in turbidite lobes, that are often below the data resolution, may influence reservoir response and (**2**) retains the ability to be conditional to a realistic level of conditioning. The features specific to this model should be compared with the geologic reality to determine appropriateness. Some of these features include (**1**) the absence of erosion, (**2**) stationarity in the distributions, (**3**) steepest gradient primary flow axis and (**4**) flow event vertical position anchored to the primary flow axis.

#### Absence of Erosion

The `TURBSIM` algorithm does not account for erosion. This may be reasonable is low energy distal settings. In proximal settings high energy turbidity flows may scour

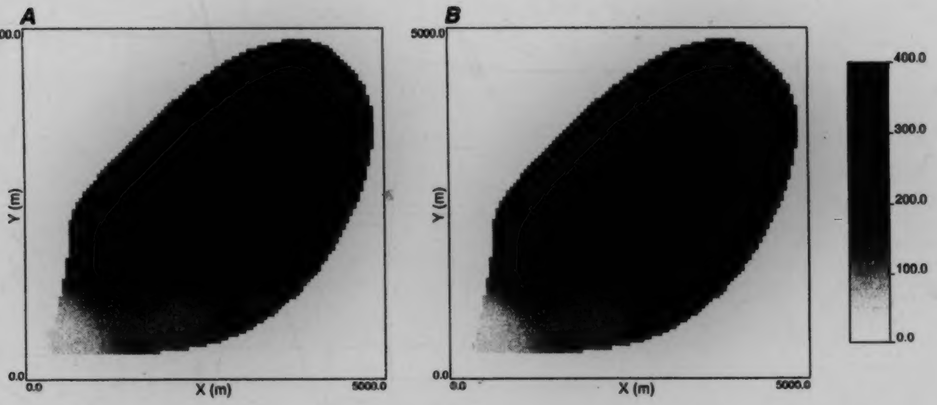

Figure 4.50: Porosity·thickness maps for two realizations of porosity (%m): A - the first realization and B - the second realization.

meters of substrate. This erosional tendency is demonstrated by the presence of sharp bases and scour and tool marks (Walker, 1992) [135].

The addition of erosional processes would compromise the ability of the `TURBSIM` algorithm to honor conditioning at wells. The previous surface $\mathcal{U}^{\ell}_{\psi^{\ell}}(\mathbf{u})$ is conditioned to all available well contacts. Erosion in the vicinity of wells during the placement of subsequent surfaces place the surface below the well contacts. A couple of solutions could include (**1**) accounting for subsequent erosion in surface $\mathcal{U}^{\ell}_{\psi^{\ell}}(\mathbf{u})$ by honoring a location above the well contact or (**2**) not allowing erosion at well locations. Both of these methods may lead to artifacts.

### Stationarity in the Distributions

The `TURBSIM` algorithm assumes that all distributions are stationary. The length of the flow axis and geometry of the flow event deposits are drawn from Gaussian distributions that remain constant over the model. Progradation may result in thickening upward sequences with more extensive flow event deposits in latter stages of lobe development. The periods of terrigenous hiatus with pelagic sedimentation between flow events are not random events. Longer hiatus may lead to thicker fine-grained drapes. Also, all flow events are assumed to be unconfined and attached to the source location. The integration of channel elements would be difficult given the erosional limitation and the difficulty of surface based approaches to represent multiple architectural element types simultaneously.

Nonstationarity in the flow event deposit extent may be accounted for with the implementation of a distribution schedule. The parameters of the flow path and geometry distributions may be varied based on surface number, average elevation of the last surface or percent of volume filled.

### Steepest Gradient Primary Flow

The compensational stacking pattern is reproduced by application of steepest gradient flow axis. This simple methodology does not account for effects related to momentum and flow stripping (Posamentier, 2003)[93].

### Anchoring Flow Events to the Flow Axis

The `TURBSIM` algorithm calculates the vertical location of the surface relative to the nearest location on a 3-D spline fit to the flow axis. This causes the surfaces to reflect bathymetric relief along the spline while being independent of bathymetric relief elsewhere under the lobe. Other methods for vertical positioning surface geometries would result in varying influence of bathymetry on the surface geometry (see Section 4.2).

Adequate horizontal discretization is required. If the gradient in the bathymetry is high and the horizontal discretization is coarse then sharp edges result at the peripheries of the flow events. In the case study with a maximum gradient of one degree a 100 × 100 grid was applied without edge artifacts.

In addition, there are limits in the conditioning of this model. As the level of conditioning increases or the flow event size increases, it is more unlikely to match conditioning. This results in more rejected flow event geometries; therefore, greater computational effort to calculate realizations. In this example only about twenty percent of geometries were rejected and less than ten minutes was required for each realization. In the extreme case, a very tight tolerance and dense conditioning may result in the algorithm failing to calculate appropriate surface geometries.

## 4.7 Discussion

Compensational cycles are common in distal lobes frontal splays of turbidite systems, which are significant reservoir targets. These features are due to the preferential filling of topographic lows and the smoothing out of topographic relief and cycles of deposition and hiatus. This stacking pattern is seen as repeating thickening upward sequences in wells.

Small-scale features such as compensational cycles may significantly constrain reservoir response and are often below seismic resolution. Petrophysical property distributions may be constrained by trends related to these small-scale features. In distal settings hemipelagic mud drapes may be preserved along the tops of flow event deposits and may act as barriers or baffles to flow. These small-scale features are often not resolved by available data.

Methodologies for surface based simulation and hierarchical trend models have been described. A specific methodology and algorithm for modeling compensational cycles with surface based simulation is proposed that reproduces the geometries and stacking patterns. This algorithm is demonstrated within a geostatistical workflow for the construction of stochastic turbidite models that honor the available conditioning data, reproduce trends in petrophysical properties due to compensational cycles and reproduce the relationship between porosity and permeability as characterized by the linear correlation coefficient.

Similar features are observed in other dispersive sedimentation settings such as alluvial fans and deltas. The presented surface based algorithm and geostatistical workflow may be tailored to a variety of other depositional settings.

# Chapter 5

# Training Images

A training image is a numerical model that represents heterogeneities that are expected in a specific area of interest. Input statistics for subsequent geostatistical modeling may be borrowed from a training image in the absence of sufficient conditioning data for the inference of these statistics. A training image may be constructed from available geologic information and professional geologist judgement and then quantified with multiple-point statistics, recovery factors, connected geo-objects and other transfer functions.

This chapter explores the application of training images to improve the geologic realism of stochastic models. Section 5.1 discuses the dependence of multiple-point geostatistics on training images. Section 5.2 summarizes the suite of training images in the static training image library. This library is expected to develop and expand over time. Section 5.3 discuses a technique for the flexible construction of deepwater training images based on streamline based simulation method from Section 3.2. Section 5.4 presents a set of Fortran programs to tailor training images and to calculate multiple-point statistics. Section 5.5 discusses the potential applications for the static and dynamic training images. Static training images are a set of numerical models that span a set of potential geologic scenarios, while the dynamic training images are algorithms to construct training images based on geometric parameters and geologic assumptions.

## 5.1 Multiple Point Techniques

Semivariogram based geostatistics is limited to two-point statistics. These techniques are unable to reproduce curvilinear geometries that are often present in reservoir geology. Object and surface based models reproduce complicated geometries but may lack flexibility to efficiently honor a variety of conditioning data. Settings with dense data relative to the object size pose difficult optimization problems that are computational intensive to solve (see Section 4.5). High resolution seismic information may be difficult to integrate with such techniques.

The omission of curvilinear features may result in numerical reservoir models that misrepresent the reservoir response quantified by flow simulation. This limitation has motivated research in geostatistical methods that integrate multiple-point statistics beyond the semivariogram.

An introduction to multiple-point geostatistics is provided in Section 2.2.6. While these techniques are able to reproduce complicated geometries, characterization of the required multiple-point statistics is often an impossible inference problem. The requirement of consistent or positive definite multiple-point statistics is satisfied by borrowing these statistics from exhaustive training images.

Training images contain information on the geometries and interrelationships between geologic categories. These categories may represent lithofacies or truncated continuous petrophysical properties. Training images may be constructed in a variety of ways, including outcrop mapping, conceptual models from professional geologic judgment and stochastic algorithms. In the latter case, the most efficient approach may be to apply of the stochastic algorithm in a conditional mode instead of conditioning by multiple-point methods.

## 5.2 Training Image Library

A library of training images is developed for fluvial and deepwater depositional settings. These training images are based on marked point processes, fluvial and deepwater models and are constructed with code developed for this thesis and the `FLUVSIM` algorithm from Deutsch and Tran(2002)[25]. The training images represent a range of NTG ratios and a variety of depositional styles.

Fortran routines required to modify, format and tailor the training images and to extract multiple-point statistics are provided. This code allows the practitioner to match site specific features and to utilize this library in a variety of applications.

There is a wide range of anticipated applications for this training image library beyond a source for multiple-point statistics. This library may be utilized in comparative flow studies, as type-models for demonstration and training and to aid in scenario based uncertainty studies, see Section 5.5 for anticipated applications.

### 5.2.1 The Static Training Images

This library includes training images from (**1**) marked point processes, (**2**) `FLUVSIM` (Deutsch and Tran, 2002)[25] models, (**3**) surface based models (see Section 4.5) and (**4**) streamline based models (see Section 3.2). Model parameters have been set to represent a variety of potential features. For example, each model is generated with a NTG ratio of 0.2, 0.4, 0.6, and 0.8 and channelized models include narrow, median and wide channels. Model parameters are discussed, but details of the algorithms are left in the original references. This static training image was originally developed in Pyrcz and Deutsch (2004)[99].

The training image scale was selected to be representative of nominal reservoir scale. The models represent a volume of 4,000 meters × 4,000 meters × 20 meters. It is anticipated that these models are relevant over a wide range of scales from 10% to 1,000% of this volume depending on the level of scale invariance in the specific depositional setting.

The model resolution was chosen as a balance between adequately characterizing the simulated features for export of multiple-point statistics and portability, computation and storage requirements. Additionally, the rapid increase in available computational power was considered. The models are discretized by 256 × 256 × 128 with resulting 8.6 million cells (see Figure 5.2). A summary of the models in the training image library is provided in Figure 5.1. A total of 498 training images are provided.

#### Marked Point Training Images

These training images are based on concepts from stochastic geometry (Stoyan et al, 1987)[119]. A Poisson point process with or without stationary intensity may be applied to position germs. Primary grains, or parameterized objects, are then positioned relative to the germs.

| Model Type | Number of Models | Categories | Schematic |
|---|---|---|---|
| Marked Point | | | |
| Lobe | 12 | Object<br>Matrix | 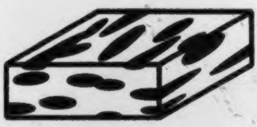 |
| Ellipse | 12 | | |
| Bar | 12 | | |
| FLUVSIM | | | |
| Channel | 108 | Channel<br>Levee<br>Splay<br>Overbank fine | 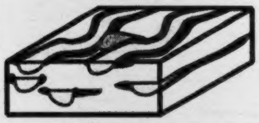 |
| Channel and Levee | 108 | | |
| Channel, Levee and Splay | 108 | | |
| Surface Based | | | |
| Compensational Cycles of Lobest | 36 | Lobe<br>Shale | 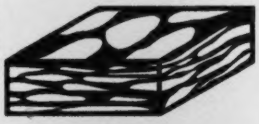 |
| Streamline Based | | | |
| Channel Complex | 81 | Abandoned Channel<br>Point Bar<br>Levee<br>Crevasse Splay<br>Overbank fine | 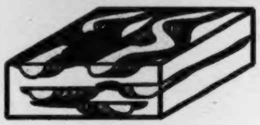 |

Figure 5.1: Summary of the training image library with schematic representations of the models.

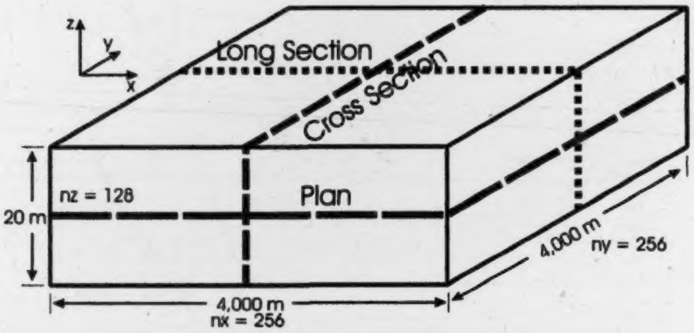

Figure 5.2: The nominal training image size, the level of discretization and the model origin. The plan, long and cross sections used in subsequent visualizations are indicated. In subsequent figures these sections are denoted A, B and C respectively.

| **Parameter** | **Distribution** |
|---|---|
| Scale | $T[0.8, 1.0, 1.2]$ |
| Azimuth | $T[-30°, 0°, 30°]$ |
| Dip | $T[-3°, 0°, 3°]$ |
| Rake | $T[-5°, 0°, 5°]$ |

Table 5.1: The distributions of stochastic geometry transforms applied to the primary grains. The distributions are triangular parameterized by lower limit, mode and upper limit. These parameters are illustrated in Figure 5.4.

| **NTG** | **Scale (m)** | **Geometry** |
|---|---|---|
| 0.2 | 500 | Ellipse |
| 0.4 | 1000 | Lobe |
| 0.6 | 1500 | Bar |

Table 5.2: The parameters for the marked point process scenarios. The training images include all combinations of parameters.

The marked point training images are binary models with stationary intensity of germs and a variety of primary grains representing ellipsoids, bars and lobes. Geometric templates characterize the primary grains (the associated geometries are shown in Figure 5.3).

Lobes and ellipsoidal mounds commonly occur in the distal deepwater setting. They may form stacked sets at reservoir scale and larger (Stow, 1996; )[118]. Bars commonly occur within channel bedforms (i.e. DA elements)(Miall, 1996)[73].

The germ locations are drawn from a uniform distribution of the training image space. The associated orientation and scale are drawn from triangular distributions (tabulated in Table 5.1 and illustrated in Figure 5.4). The scenarios are indicated in Table 5.2.

Example training images are shown in Figures 5.5 and 5.6. Primary grains are stochastically added until the NTG ratio is met. The results are smoothed by the maximum a-posteriori selection (MAPS) (Deutsch, 1998a)[20] method to remove discretization artifacts.

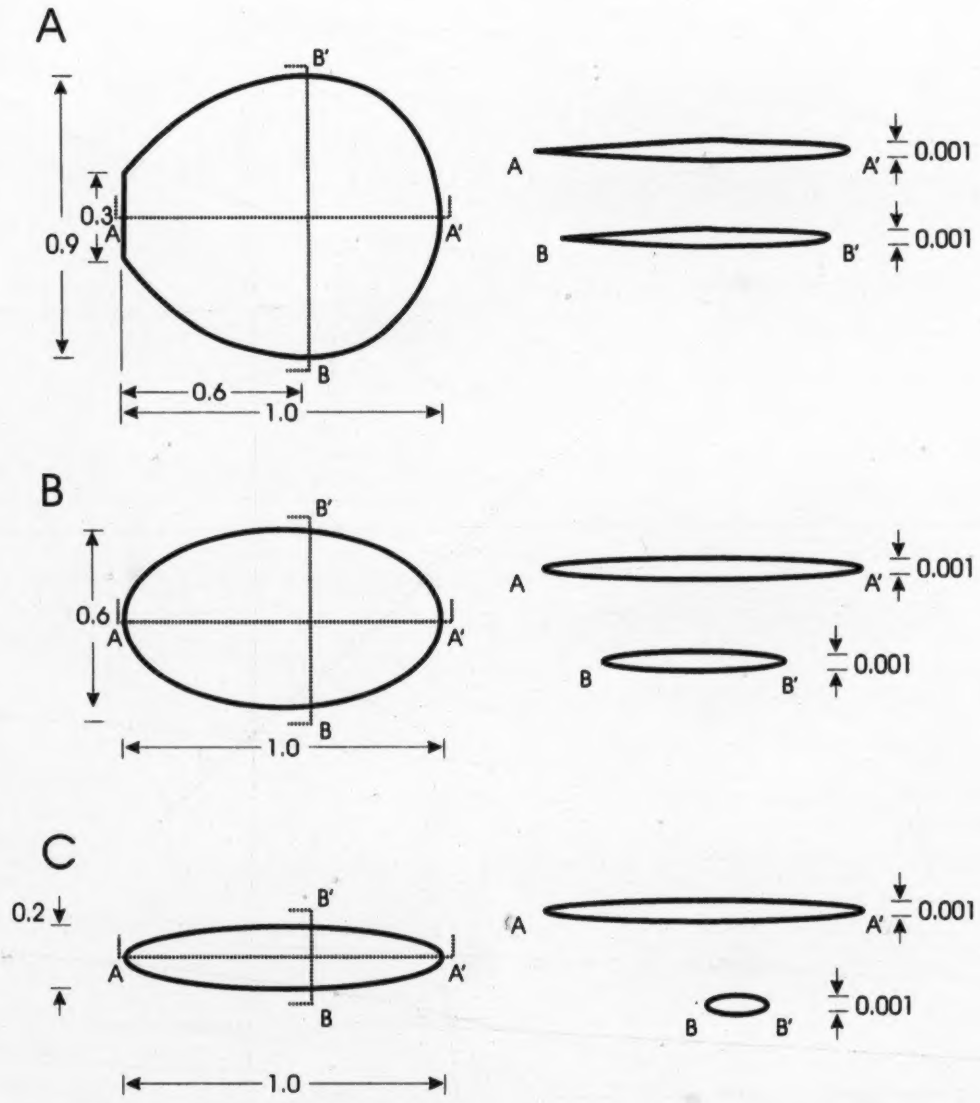
A
B'
0.3
A
0.9
A'
B
0.6
1.0
A
A'
0.001
B
B'
0.001
B
B'
0.6
A
A'
B
1.0
A
A'
0.001
B
B'
0.001
C
0.2
B'
A
A'
B
1.0
A
A'
0.001
B
B'
0.001

Figure 5.3: The templates for the marked point processes: A - lobe, B - ellipsoid and C - bar. The units are in the fraction of the randomly assigned scale (see Table 5.2). Schematic is not to scale.

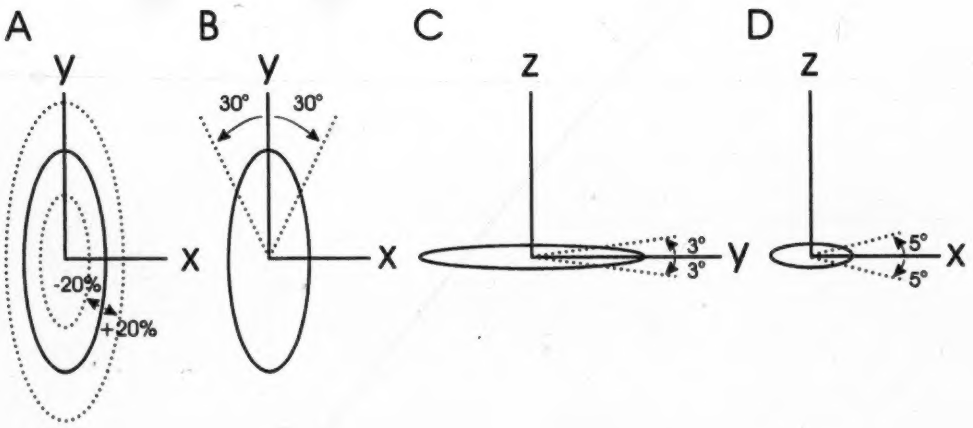

Figure 5.4: The limits of the triangular distributions for: A - scale, B - azimuth, C - dip and D - rake. Schematic is not drawn to scale.

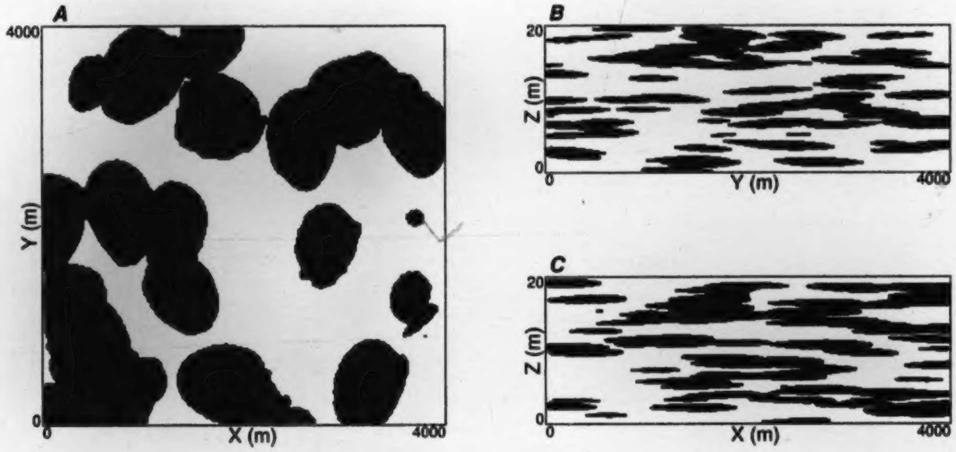

Figure 5.5: An example marked point training image - small lobes with a NTG ratio of 0.6. Sections include: A - plan section, B - cross section and C - long section.

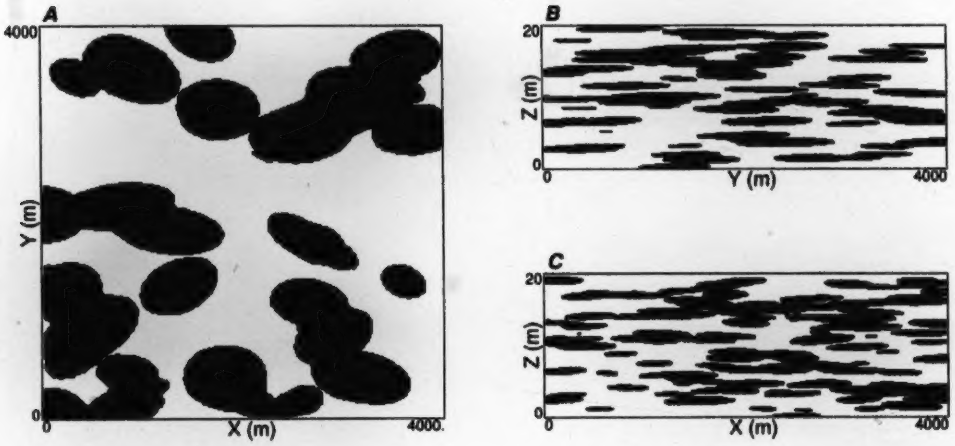

Figure 5.6: An example marked point training image - small ellipses with a NTG ratio of 0.8. Sections include: A - plan section, B - cross section and C - long section.

### `FLUVSIM` Training Images

The development of fluvial object based models is outlined in Section 2.2.8. `FLUVSIM` is a convenient public domain fluvial object based algorithm. The algorithm generates a channel centerline RF and fits stochastic channel and related architectural element geometries to the RF. The `FLUVSIM` geologic model is based on ribbon sandbodies from typically low net-to-gross systems with primary reservoir quality encountered in sinuous to straight channels and secondary reservoir rock based on levees and crevasse splays embedded in overbank fines (Galloway and Hobday, 1996; Miall, 1996)[39, 73]. The model represents Miall's PV type fluvial reservoirs (Miall, 1996)[73] (see Section 3.1.4).

These ribbon sandbodies are commonly characterized by relatively low width to depth ratios (often less than fifteen) and ribbon thickness of less than ten meters (Colinson, 1996)[15]. A schematic of the `FLUVSIM` model in shown in Figure 5.7. Training images with channel only, channel and levee and channel, levee and splay were calculated (see example training images in Figures 5.8, 5.9 and 5.10).

### Channel Only

Ribbon sandbodies may be highly sinuous to straight. A series of training images were simulated with FLUVSIM to span the scenarios listed in Table 5.3. An example training images is shown in Figure 5.8.

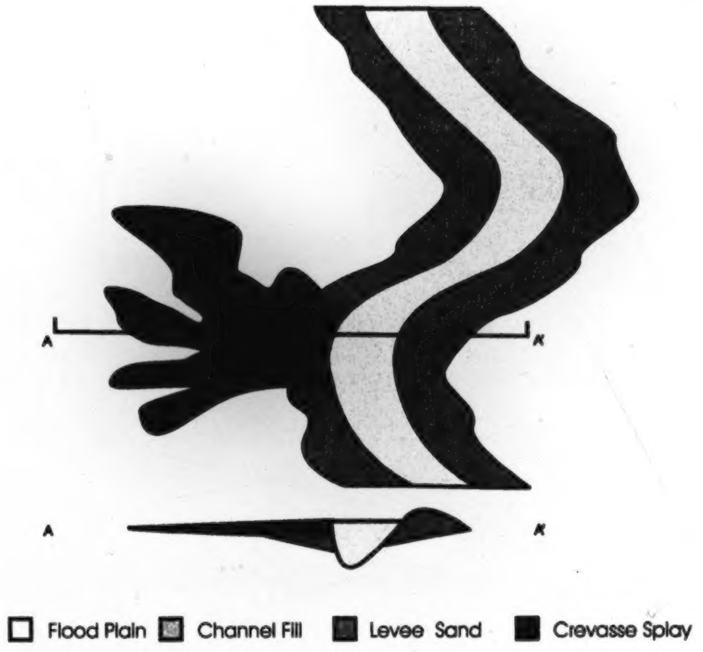
A
A'
A
A'
Flood Plain
Channel Fill
Levee Sand
Crevasse Splay

Figure 5.7: A schematic of the FLUVSIM model (based on Deutsch and Tran (2002)[25]).

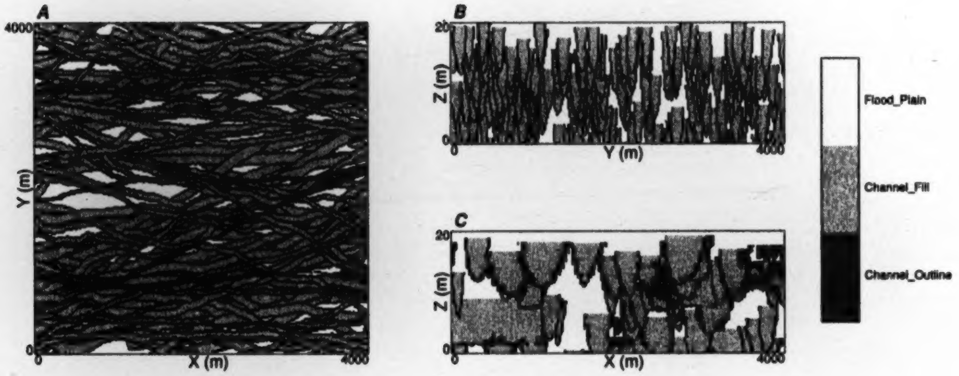

Figure 5.8: An example FLUVSIM training image - channel only, channel width to thickness ratio of 20, low sinuosity and NTG of 0.8. Sections include: A - plan section, B - cross section and C - long section.

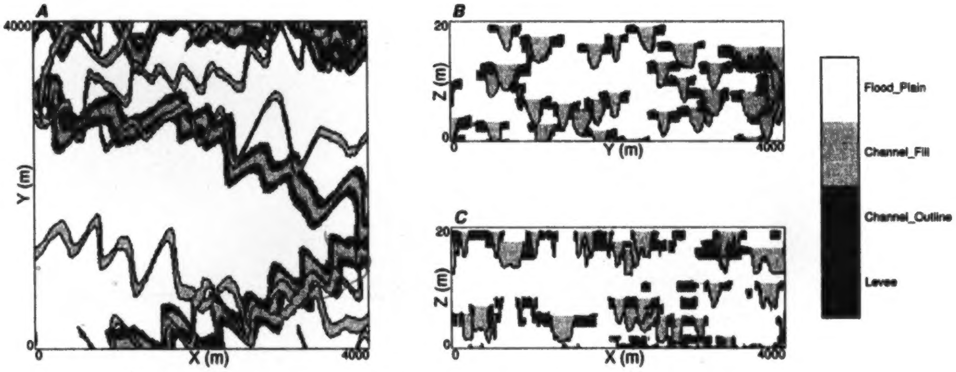
A
4000
Y (m)
0
X (m)
4000
B
20
Z (m)
0
Y (m)
4000
C
20
Z (m)
0
X (m)
4000
Flood_Plain
Channel_Fill
Channel_Outline
Levee

Figure 5.9: An example `FLUVSIM` training image - channel and levee, channel width to thickness ratio of 50, high sinuosity and NTG of 0.4. Sections include: A - plan section, B - cross section and C - long section.

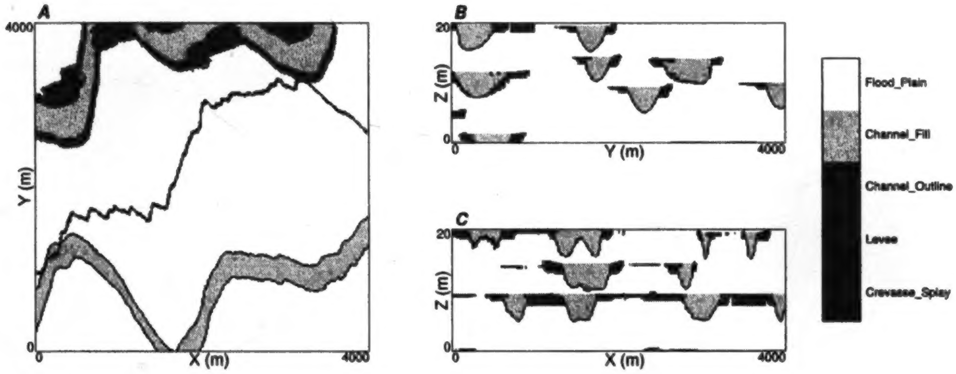
A
4000
Y (m)
0
X (m)
4000
B
20
Z (m)
0
Y (m)
4000
C
20
Z (m)
0
X (m)
4000
Flood_Plain
Channel_Fill
Channel_Outline
Levee
Crevasse_Splay

Figure 5.10: An example `FLUVSIM` training image - channel, levee and crevasse splay, width to thickness ratio of 100, median sinuosity and NTG of 0.2. Sections include: A - plan section, B - cross section and C - long section.

| NTG | Channel Thickness (m) | Channel Width: Thickness | Sinuosity |
|---|---|---|---|
| 0.2 | 2 | 20 | 1.0 |
| 0.4 | 4 | 50 | 1.5 |
| 0.6 | 7 | 100 | 2.0 |
| 0.8 | | | |

Table 5.3: The scenarios for the channel only ribbon sandbody training images. The training images include all combinations of parameters.

| NTG | Channel Thickness (m) | Channel Width: Thickness | Sinuosity | Levee Fraction |
|---|---|---|---|---|
| 0.2 | 4 | 20 | 1.0 | 0.2 |
| 0.4 | | 50 | 1.5 | 0.5 |
| 0.6 | | 100 | 2.0 | 0.8 |
| 0.8 | | | | |

Table 5.4: The scenarios for the channel with levee ribbon sandbody training images. The training images include all combinations of parameters.

### Channel and Levee

Significant net facies may be represented in levees (Miall, 1996, p. 172)[73]. For the median channel thickness case ribbon sandbodies with levees were simulated. These cases are shown in Table 5.4. The levee fraction reported in the table is the fraction of the net facies.

The levee size is determined by a calibration within the `FLUVSIM` program. The CH and LV elements are placed until the target CH proportion is exceeded. Then the proportion of LV is calculated and compared with the target LV proportion. The LV geometry is scaled to approximately correct the LV proportion. An example training images is shown in Figure 5.9.

### Channel, Levee and Crevasse Splay

Crevasse splay may represent a significant fraction of net facies. For the median

| NTG | Channel Thickness (m) | Channel Width: Thickness | Sinuosity | Levee Fraction | Crevasse Splay Fraction |
|---|---|---|---|---|---|
| 0.2 | 4 | 20 | 1.0 | same | 0.2 |
| 0.4 |  | 50 | 1.5 | as | 0.5 |
| 0.6 |  | 100 | 2.0 | channel | 0.8 |
| 0.8 |  |  |  |  |  |

Table 5.5: The scenarios for the channel with levee and crevasse splay ribbon sandbody training images. The training images include all combinations of parameters.

channel thickness case ribbon sandbodies with levees fraction the same as channel fraction a variety of scenarios were simulated with crevasse splays. These cases are shown in Table 5.5. The crevasse splay fraction is the fraction of the net and the remaining net is divided evenly between channel and levee.

The levee and crevasse splay size is determined by the same calibration as applied in CH and LV models with the addition of scaling of the CS elements. An example training images is shown in Figure 5.10.

### `FLUVSIM` and Sinuosity

Sinuosity is not an input in the `FLUVSIM` algorithm. The inputs related to sinuosity are maximum channel deviation from channel axis and the correlation length of the 1-D RF that characterizes channel deviation. To characterize the relationship between sinuosity and these parameters the channel generation subroutine was iterated for a variety of deviations and deviation correlation lengths. To minimize the impact of ergodic fluctuations the expected sinuosity was calculated over ten realizations. There is a clear relationship between sinuosity and the `FLUVSIM` channel parameters, deviation and deviation correlation length (see Figure 5.11). `FLUVSIM` was modified to more closely reproduce the NTG ratio in the initial object seeding step and the initial temperature in the annealing schedule was set to zero, with the maximum iterations set to twenty. With these parameters the `FLUVSIM` results are based on maximum a posteriori selection (MAPS) and not simulated annealing. Since only global proportions are being honored and there is no well data and trends, the initial calibration and a few MAPS iterations are sufficient to construct the training images.

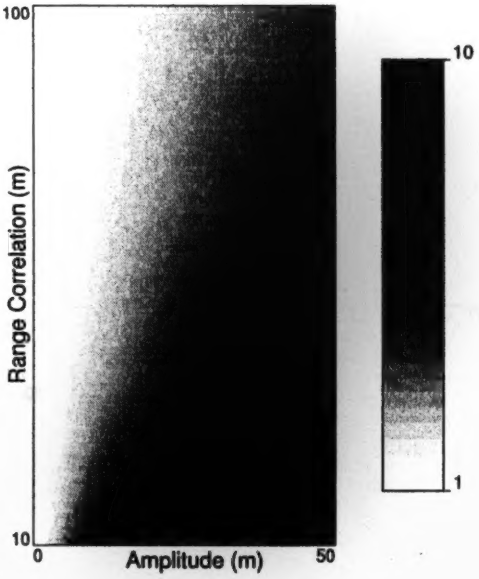

Figure 5.11: The relationship between deviation, deviation correlation length and sinuosity in the `FLUVSIM` channel model. The units are in sinuosity (the ratio of length along the streamline to the length from head to tail).

| NTG | Surface Correlation | Lobe Size |
|---|---|---|
| 0.2 | Low | Small |
| 0.4 | Medium | Medium |
| 0.6 | High | Large |

Table 5.6: The scenarios for the surface based turbidite lobe training images. The training images include all combinations of parameters.

### Surface Based Training Image

Surface based models are a variation of object based models, although they focus on the object skin or bounding surfaces. These methods are amenable to reproducing planar geometries and bed stacking patterns. Surface based techniques are introduced in Section 2.2.7. Pyrcz and Deutsch (2003)[96] developed a surface based algorithm for modeling compensational cycles within turbidite lobes. This algorithm is explained in detail in Section 4.5. This model is applied to construct turbidite lobe training images with varying lobe size, NTG ratios and range of surface correlation (see Table 5.6 and see example training images in Figures 5.12 and 5.13). The range of surface correlation controls the regularity of the lobes, with high correlation leading to smooth lobes. The surfaces enclosing the lobes are coded as shale and then the `MAPS` algorithm is applied to correct the facies proportions to the specific NTG ratio.

### Streamline Based Fluvial Model Training Images

The version of the streamline based fluvial model applied in the static training image library shares the same geometries applied in `FLUVSIM` with the exception of (**1**) channel streamlines generated by the disturbed periodic model and fit to cubic splines that allow for high sinuosity features, (**2**) channel migration and the realistic generation of lateral accretion (point bar) deposits and (**3**) the formation of abandoned channels and oxbow lakes. A more advanced version of the streamline based algorithm is presented in Section 3.2. The advanced version includes channel branching and improved architectural elements.

This model is representative of mixed load to suspended load fluvial systems (Galloway and Hobday, p. 400, 1996; Miall, p. 484, 1996)[39, 73]. The model is

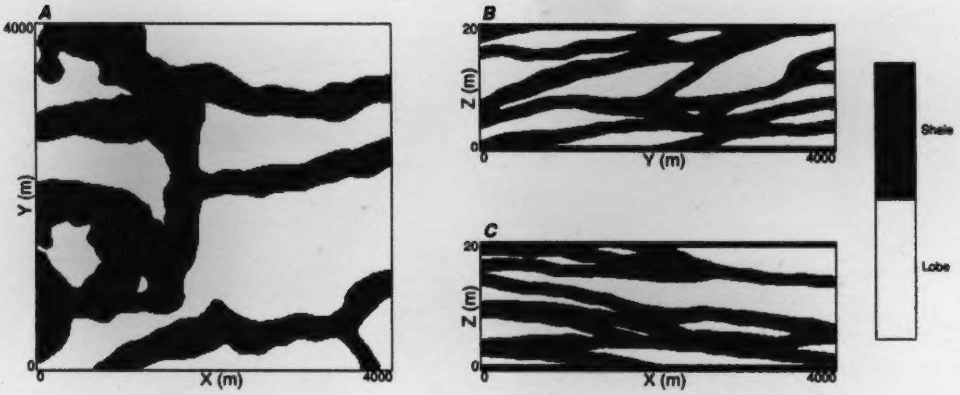
A
4000
Y (m)
0
0
X (m)
4000
B
20
Z (m)
0
0
Y (m)
4000
C
20
Z (m)
0
0
X (m)
4000
Shale
Lobe

Figure 5.12: An example surface based training image - large lobes, low correlation and NTG of 0.4. Sections include: A - plan section, B - cross section and C - long section.

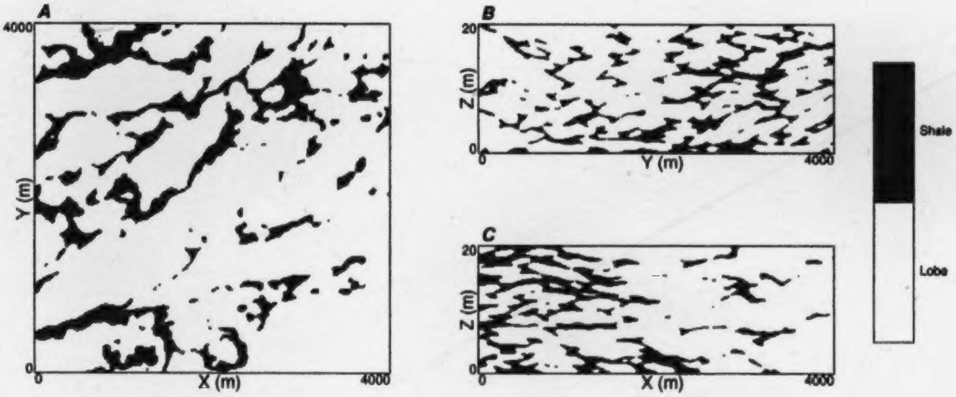
A
4000
Y (m)
0
0
X (m)
4000
B
20
Z (m)
0
0
Y (m)
4000
C
20
Z (m)
0
0
X (m)
4000
Shale
Lobe

Figure 5.13: An example surface based training image - small lobes, high correlation and NTG of 0.8. Sections include: A - plan section, B - cross section and C - long section.

| NTG | Channel Thickness (m) | Channel Width: Thickness | Sinuosity | Amalgamation |
|---|---|---|---|---|
| 0.2 | 4 | 20 | 1.0 | Low |
| 0.4 | | 50 | 1.5 | Medium |
| 0.6 | | 100 | 2.0 | High |

Table 5.7: The scenarios for the streamline based training images. The training images include all combinations of parameters.

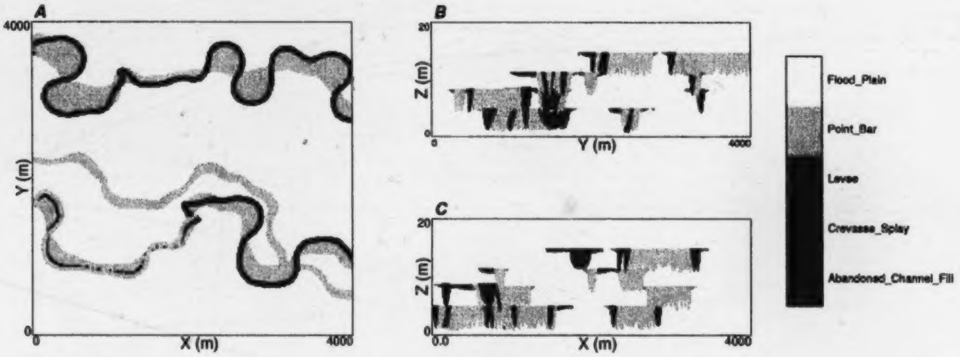

Figure 5.14: An example streamline based training image - high degree of amalgamation, channel width to thickness ratio of 20, median sinuosity and NTG of 0.2. Sections include: A - plan section, B - cross section and C - long section. Note alternating course and fine grained channel fills.

indicative of the CB reservoir type from Miall (1996)[73] and more specifically, the labyrinth reservoir type from Weber and van Geuns (1990)[137]. Training images with variable NTG ratio, channel width to thickness ratio, initial sinuosity and degree of channel belt amalgamation were calculated (see Table 5.7) and example training images are shown in Figures 5.14 and 5.15).

### 5.2.2 Correction of Global Category Proportions

Due to ergodic fluctuations and a limited number of training images, the NTG ratio requires correction. The global proportions may be corrected to precisely match the representative statistics of the reservoir being modeled by applying the `MAPS`

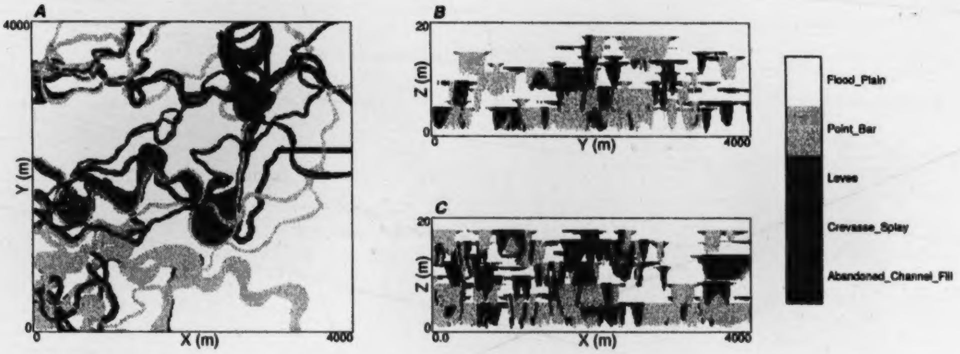

Figure 5.15: An example streamline based training image - low degree of amalgamation, channel width to thickness ratio of 20, high sinuosity and NTG of 0.4. Sections include: A - plan section, B - cross section and C - long section. Note the alternating course and fine grained channel fills.

program.

### 5.2.3 Selection of the Appropriate Training Image

This static training image library provides a set of training images with a wide variety of fluvial and deepwater features. They may be tailored to represent the geologic features in a broad variety of reservoir settings. The following are some example settings.

Compensation cycles are ubiquitous in distal submarine lobes (Mutti and Sonnino, 1981)[79]. These features occur in significant exploration targets in the off shore Gulf of Mexico, West Africa and the North Sea. The surface based training images may be applied to represent these compensational features.

Significant resources are available in fluvial reservoirs in areas such as the North Sea (Clemetsen et al., 1990)[14], and East Texas (Galloway and Hobday, 1996)[39]. There are a variety of recognized settings. PV type reservoirs with characteristic shoe-string sands in a matrix of overbank and CB type reservoirs with lateral accretion lenses and channel fill mud plugs have been identified in various forms. The `FLUVSIM` and streamline based model images may be applied to represent these fluvial settings.

Low to high sinuosity channels and levee complexes have been recognized in deepwater settings. There are some differences between subaqueous and subaerial channels. For example, deepwater channels decrease in width and depth toward the distal due to flow stripping (Flood and Damuth, 1987)[37]. Yet, many of the same features are observed in subaqueous and subaerial channels (Leeder, 1999)[60]. The `FLUVSIM` and streamline based training images may be applied to channelized deepwater settings as found in Gulf of Mexico, West Africa and North Sea.

The marked point training images may be applied to a variety depositional settings. This may include bars in coastal settings and lobes in deepwater settings. These training images may be applied directly or may be merged into other training images. For example, bars may be merged into the channel facies of a fluvial training image to represent down stream accretion channel macroforms (Miall, 1996)[73].

The static training image library is useful, although greater flexibility is available through the construction of a dynamic training image library. A dynamic deepwater training image library is discussed in the next section.

## 5.3 Turbidite Style Training Image Generating Algorithms

The set of C++ classes for the flexible construction of deepwater training images is called the dynamic deepwater training image library. Recent high resolution seismic studies of the deepwater have uncovered features such as highly sinuous and braided channels, meander development and LA architectural elements that were previously believed to exclusively exist in the subaerial settings (for example Peakall et al., 2000; Posamentier, 2003)[93, 91]. With limited modification the techniques developed for fluvial streamline based simulation (see Section 3.2) may be applied for the construction of deepwater training images.

### 5.3.1 Turbidite Style Training Image Architectural Elements

The same architectural elements developed for the streamline based simulation technique in Section 3.2 are applied. In addition, an architectural element denoted as *lobe* was added. This architectural element has the same areal geometry as the lobe element applied in Section 4.5. This geometry taken from `LOBESIM` algorithm by Deutsch and Tran (1999)[26]. The geometry in the vertical direction is controlled by depth to width ratio to capture the erosional component and height to width ratio to capture the aggradational component. The parametrization may be adjusted to represent the geometries associated with frontal splays (FS), sheets (SH) and ponds (PD) architectural elements (see Figure 5.16).

All architectural elements may be fit to any portion of a streamline and to low or high sinuosity streamlines. Frontal splays form when turbidite channels lose confinement; therefore, frontal splays typically form lobate shapes at the ends of channels (Stow et al., 1996)[118]. Ancient and modern examples of FS elements indicate a large range in scales. Individual FS elements may have widths of hundreds to thousands of meters, slightly elongated with thicknesses from meters to tens of meters (Hobday and Galloway, 1996, Stow et al., 1996)[39, 118]. FS elements include well graded medium to thickly beds turbidite sequences.

SH elements form adjacent to the CH, LV and FS elements. These elements are characterized as parallel sided and laterally extensive. SH elements typically have a thickness of meters (Stow et al., 1996)[118]. In modern examples SH elements extend up to kilometers from the channel system (Walker, 1992)[135]. SH elements are composed of medium to thinly bedded turbidites. PD elements result from the filling of a bathymetric low. These elements are composed of medium to thickly bedded turbidites.

### 5.3.2 Turbidite Dynamic Training Images in C++

The object oriented approach of C++ is advantageous in the design of an algorithm for the flexible construction of turbidite training images. Within the C++ programming language, the user may design self contained classes with associated variables, constructors, destructor and member functions. Another class may create, modify and destroy objects within this class in a very flexible manner.

In Section 3.2 the building blocks approach to streamline based simulation identifies the 3-D streamline and associated properties as the basic building block. A streamline class was coded for the C++ implementation a streamline class was coded. The streamline operations avulsion (proximal and within the model), aggradation and meander migration and the architectural elements CH, LV, LA, FS, PD and SH are member functions of the streamline class. The copy constructor was designed to allow for "deep copies" of the streamline so that a copy becomes an independent object. All information related to streamline and architectural properties

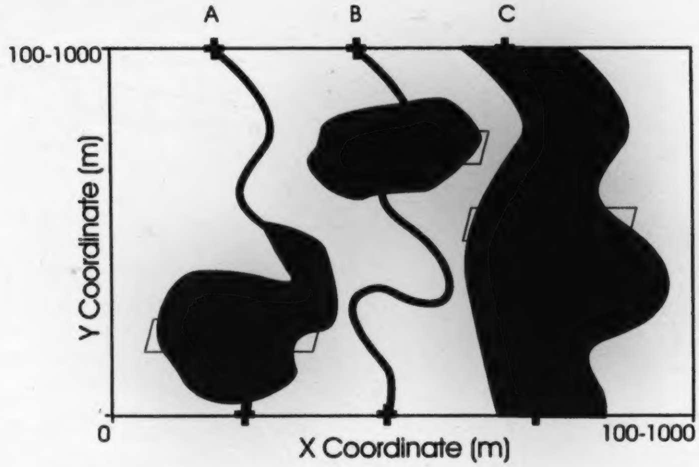

Figure 5.16: The lobe architectural element. The geometric parameters may be tailored to represent three common architectural elements in the deepwater; A - frontal splay, B - pond and C - sheet. The potential streamline is represented as the center line and cross sections illustrate erosional and aggradational components.

are private within the streamline class.

This streamline class may be utilized by a training image construction class. Classes were written to construct turbidite training images tailored to the (**1**) channel and levee complex and (**2**) channelized sheet complex turbidite styles. The training image construction classes proceed by (**1**) reading user specified geometric parameters and proportions, (**2**) calibration to correct element geometries to improve match with target proportions, (**3**) generation and positioning of streamline objects and streamline associations based on a schedule and stacking model and (**4**) placement of architectural elements associated with streamline objects based on a model of architectural element associations. Each of the training image construction classes are now discussed with reference to these steps.

### 5.3.3 Channel and Levee Complex

Channel and levee complexes commonly form in the proximal of turbidite systems. These systems are often confined within submarine canyons. Isolated CH elements may form in nested patterns and may include extensive LV elements (see schematic A in Figure 5.17)(Walker, 1992)[134].

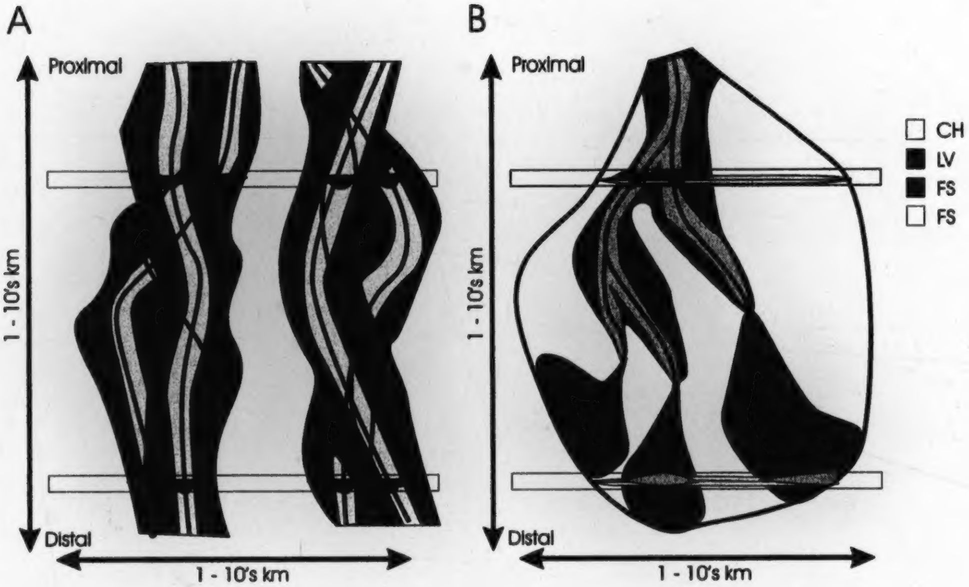
A
B
Proximal
Distal
1 - 10's km
1 - 10's km
Proximal
Distal
1 - 10's km
1 - 10's km
☐ CH
■ LV
■ FS
☐ FS

Figure 5.17: A schematic of the: A - channel and levee complex and B - channelized sheet complex turbidite styles. Both are plan view with two cross sections superimposed.

**Parameters**

The parameters include geometric parameters for the CH and LV architectural elements (see Section 3.2.4) and parameters to control the degree of nesting and the spacing of nested channel groups. The LV architectural elements have additional asymmetry and distal thinning parameters. Channel nesting is discussed later.

LV asymmetry controls the level of asymmetry of LV elements on the cut bank and point bar side of a streamline. LV asymmetry is set between 0 and 1. For a value of 0 the LV elements on the cut bank and point bar side are symmetric. For a value of 1 the LV elements width is doubled on the cut bank side and halved on the point bar side of the streamline at the location of maximum curvature. The LV asymmetry smoothly changes along the streamline as a function of streamline curvature (see Equations 5.1 and 5.2 for the left and right side).

$$LV_{width}(\mathbf{s}) = 1.0 + factor \cdot \left| \frac{c(\mathbf{s})}{max(c)} \right| \cdot \overline{LV_{width}} \tag{5.1}$$

$$LV_{width}(\mathbf{s}) = 1.0 - factor \cdot \left| \frac{c(\mathbf{s})}{max(c)} \right| \cdot \overline{LV_{width}} \tag{5.2}$$

where $factor$ is the strength of asymmetry parameter, $c(\mathbf{s})$ is the curvature at location $\mathbf{s}$ along the streamline,$max(c)$ is the maximum curvature along the streamline and $\overline{LV_{width}}$ is the average LV width drawn from the user specified distribution.

The LV thinning parameter integrates the effect of flow stripping on LV development. The loss of the mud component in turbidity flows, attenuates LV elements towards the distal. For a LV thinning parameter of 0 the LV elements maintain a constant width. For a LV thinning of 1 the LV elements have twice the width at the proximal edge and smoothly decrease to zero width at the distal end of the LV element (see Equation 5.3).

$$LV_{width}(\mathbf{s}) = \overline{LV_{width}} \cdot \left[ 1 + 2 \cdot factor \cdot \left( 0.5 - \left| \frac{\mathbf{s} - \mathbf{s}_t}{\mathbf{s}_h - \mathbf{s}_t} \right| \right) \right] \tag{5.3}$$

where $factor$ is the strength of thinning parameter, $\mathbf{s}$ is the distance along the streamline, $\mathbf{s}_h$ and $\mathbf{s}_t$ are the distances along the streamline of the start and end of the LV element and $\overline{LV_{width}}$ is the average LV width drawn from the user specified distribution.

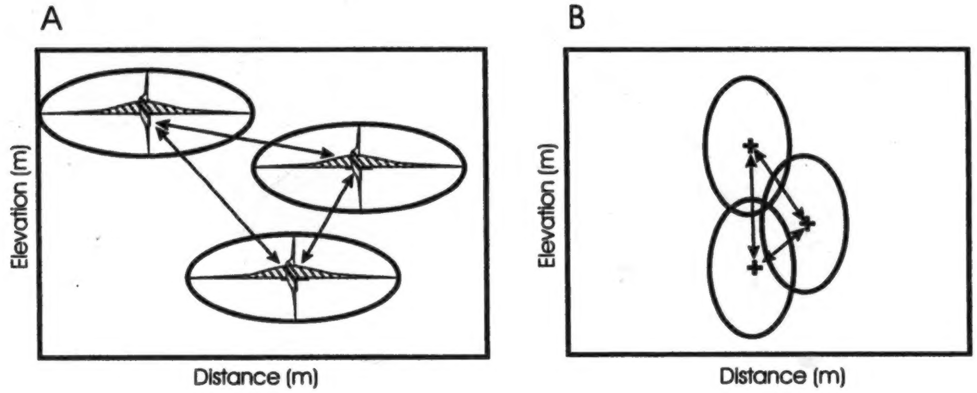

Figure 5.18: Nested associations of streamlines parameterized by mean and standard deviation of spacing between streamline associations in the vertical and horizontal and standard deviation of streamline dispersion about the centroid of the nested association. A - isolated streamline associations with a high degree of avulsion and low rate of aggradation. B - amalgamated streamline associations with high rate of aggradation and low degree of avulsion.

### Calibration

The calibration method is similar to the technique in the `FLUVSIM` algorithm. The CH and LV elements are placed until the target CH proportion is exceeded. Then the proportion of LV is calculated and compared with the target LV proportion. The LV width is then scaled to approximately correct the LV proportion.

### Creation and Positioning Streamline Associations

The streamlines are grouped into nested streamline associations. These associations are parameterized by a vertical and horizontal standard deviation (biGaussian distribution) and the association centroid. The spacing between streamline associations is parameterized by mean and standard deviation spacing in the horizontal and vertical locations. This is illustrated in Figure 5.18.

The nested association centroids are calculated by constructing a Poision point process with acceptance criteria. The first germ is placed randomly in the plane representing proximal edge of the model. Subsequent germs are randomly placed. For each, the nearest neighbour germ is found and the new germ is accepted with

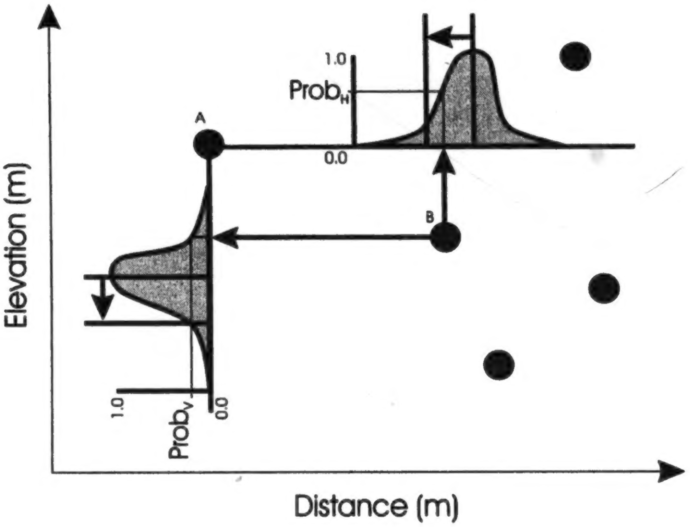

Figure 5.19: The acceptance criteria applied to calculated the centroids for the nested streamline associations. A - the new centroid and B - the nearest neighbour centroid.

probability defined by:

$$Prob\{accept\} = Prob_V \cdot Prob_H \tag{5.4}$$

the assumption of independence is applied to combine the probabilities from the Gaussian pdfs for horizontal and vertical spacing.

$$Prob\{accept\}(\Delta_V, \Delta_H) = \frac{g_{m_{\Delta_V},\sigma_{\Delta_V}}(|\Delta_V|)}{g_{m_{\Delta_V},\sigma_{\Delta_V}}(m_{\Delta_V})} \cdot \frac{g_{m_{\Delta_H},\sigma_{\Delta_H}}(|\Delta_H|)}{g_{m_{\Delta_H},\sigma_{\Delta_H}}(m_{\Delta_H})} \tag{5.5}$$

where $g$ is the Gaussian pdf, $m_V$ and $\sigma_V$ defines the spacing in the vertical and $m_H$ and $\sigma_H$ defines the spacing in the horizontal direction of the streamline association centroids. $\Delta_V$ and $\Delta_H$ are the difference vertically and horizontally between the new and nearest neighbour centroid. If the vertical and horizontal spacing between the new and nearest neighbour centroid were equal to the mean ($\Delta_V = m_V$ and $\Delta_H = m_H$) then the probability of accepting the new centroid is 1.0. If the spacing is outside three standard deviations of the Gaussian distribution for either horizontal or vertical then the probability of accepting the new centroid is effectively 0.0. These probabilities are shown schematically in Figure 5.19.

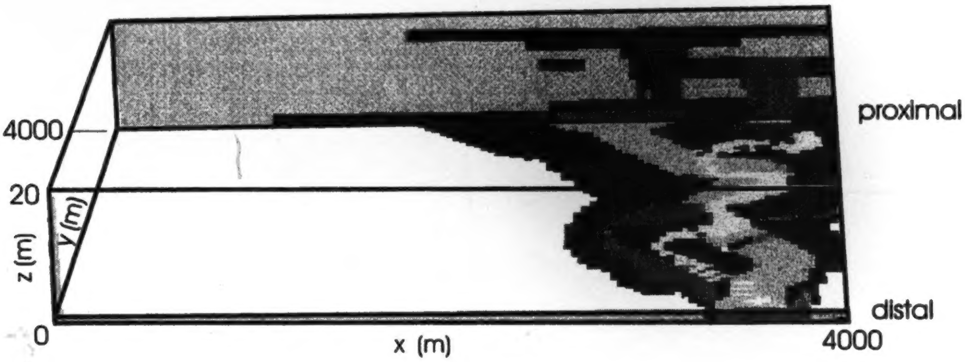

Figure 5.20: Example channel and levee complex training image. There are two streamline associations stack on top of each other. The CH elements have a mean width of 400 meters and a sinuosity of 1.3. The LV elements have a nominal width of 500 meters and a LV thinning factor of 1.0.

For each streamline, the source location along the proximal edge of the model is drawn in a two step process. First the streamline association is drawn from a uniform pdf and then the location of the position within the streamline association is drawn from a bivariate Gaussian distribution (refer to Figure 5.18). Example channel and levee complex training images is shown in Figures 5.20 and 5.21.

### 5.3.4 Channelized Sheet Complex

Channelized sheet complexes commonly form in the distal of turbidite systems. These systems are characterized by confined CH within LV with flow stripping attenuating the LV elements toward the distal (Peakall et al., 2000; Posamentier, 2003)[91, 93]. This attenuation leads to a transition to unconfined FS elements. SH elements form along the peripheries of the system (see schematic B in Figure 5.17).

#### Parameters

The parameters include user specified geometric parameters for the architectural elements, the frequency of branching, the type of source and the stacking parameter.

The architectural elements include CH, LV, FS and SH. The CH and LV geo-

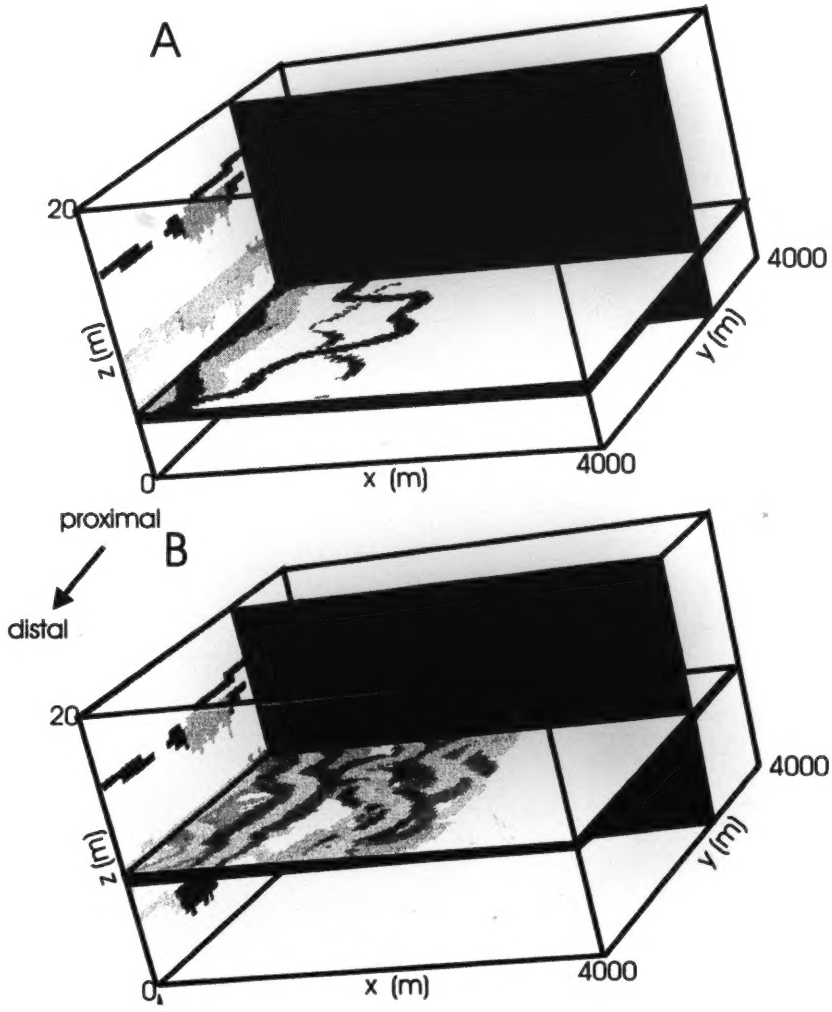
A
20
z (m)
0
x (m)
4000
4000
y (m)
proximal
distal
B
20
z (m)
0
x (m)
4000
4000
y (m)

Figure 5.21: Example channel and levee complex training image. There are six streamline associations with a large degree of aggradation and avulsion. The CH elements have a mean width of 400 meters and a sinuosity of 1.5. The LV elements have a nominal width of 500 meters and a LV asymmetry factor of 0.6. A - horizontal slice at z =5 meters and B - horizontal slice at z=10 meters.

metric parameters are discussed in Section 3.2.4. The FS and SH elements are based on the lobe parameters from Section 4.5.1. For the FS element the proximal width, $w$ is set to the channel width at the start location on the streamline object. The maximum width, $W$, length to the maximum width, $l$, and the total length $L$ are drawn from Gaussian distributions with mean and standard deviation specified by the user. For the SH element all parameters are specified by the user. The widths should be set larger than the widths of the CH and LV elements so the SH element persists to the peripheries.

Streamlines are grouped into streamline associations composed of stem and branch streamlines. The stem streamline is the first streamline after a proximal avulsion. The branch streamlines are copies of the stem streamline with an avulsion event within the model. The level of branching is specified by the mean and standard deviation of the number of branches for each stem.

### Calibration

The channelized sheet complex class applies calibration to scale the architectural element geometries in the same manner as the channel and levee complex class. In addition, calibration establishes the mean vertical separation between streamline associations. To reproduce the compensational stacking pattern these models are constructed in sequence from the bottom up.

### Creation and Positioning Streamline Associations

The elevation of the stem channel and associated branches is set as the previous elevation (or bottom of the model for the first placement) plus an aggradation step drawn from a Gaussian distribution with mean from calibration and user specified standard deviation. The horizontal location along the proximal edge of the model is drawn from a Gaussian distribution with mean of the mid point and with user specified standard deviation. A small source standard deviation results in a point source system, while a large standard deviation results in an apron or linear source system as found on the shelf edge (Hobday and Galloway, 1996)[39]. The stem and branch streamlines are parameterized by mean and standard deviation of sinuosity.

The primary azimuth of the stem channels is parameterized by mean and standard deviation. A low standard deviation will result in parallel to sub parallel streamlines as found in a shelf edge setting while a higher standard deviation will

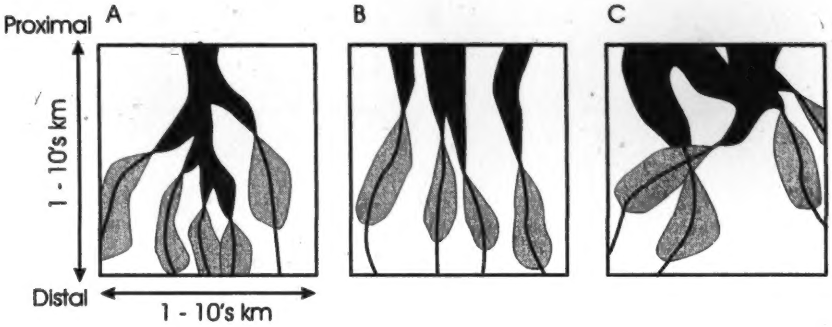

Figure 5.22: The influence of source and primary azimuth distribution on streamline associations: A - point source canyon, B - line source, shelf edge and C - delta front (Hobday and Galloway, 1996)[39]. All views are plan sections.

result in a dispersive system as in a delta front system (see schematic in Figure 5.22). Example training images with point and apron sources are shown in Figure 5.23.

An approximate model of compensational stacking is applied in this class (see illustration in Figure 5.24). The target location for each stem channel is drawn from a weighted distribution of all locations along the distal edge of the model. Initially the distribution is uniform. The distribution is modified to reduce the weight of locations near the previously drawn target. The modification is based on a linear function with user specified "compensation range". The distribution is standardized after each modification to prevent the eventual occurrence of negative weights. The result is stacked streamline associations that mimic compensational stacking with respect to each other (see Figure 5.25).

### 5.3.5 Comments on Training Image Generating Algorithms

As with the static training image library, the dynamic training image library represents a first version. It is anticipated that future feedback and iteration will lead to the improved integration of geologic information. The established building blocks and example deepwater training image construction classes will be an asset in this future work.

Another approach to the dynamic construction of training images is the application of deductive models (see Section 2.1.8). While these models do represent complex geologic features, their chaotic nature renders them difficult to constrain

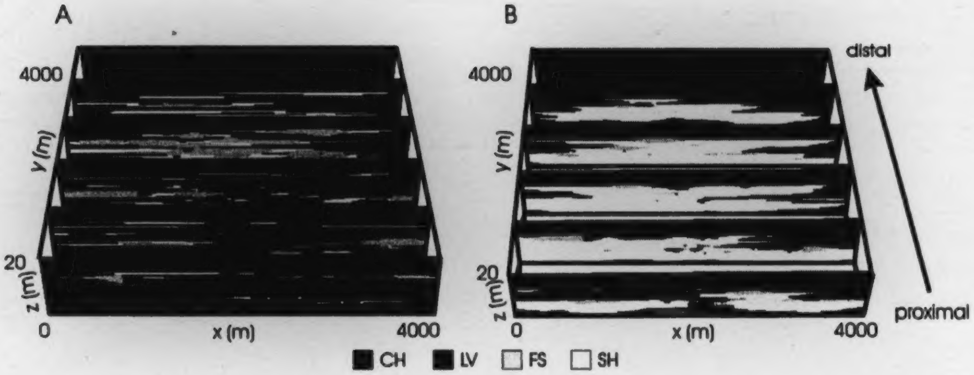

Figure 5.23: Cross sections of two example channelized sheet complex training images. A - apron source, high frequency of branching and thin SH elements and B - point source, low frequency of branching and thick SH elements.

to the available geologic information. The presented streamline based models may be efficiently tailored to site specific information related to geometry and interrelationships.

## 5.4 Associated Code for Training Image Library

Fortran programs are included to extract statistics from the training images, perform model operations for the tailoring of training images to specific sites. These programs are described below.

### 5.4.1 Extraction of Multiple-point Statistics from the Training Images

A program called `MPSTAT` was written to extract multiple-point statistics from the training images. The following statistics may be extracted; (**1**) multiple point histograms, (**2**) transition probabilities, (**3**) distributions of runs and (**4**) connected geo-objects. Other statistics such as histograms and indicator semivariograms may be calculated with `GSLIB` programs (Deutsch and Journel, 1998)[23].

Multiple-point statistics are calculated over a specified multiple-point configuration. This configuration is defined by lag vectors, $\mathbf{h}_1, \ldots, \mathbf{h}_N$, with $\mathbf{h}_1 = 0$ by convention. This is known as a template. The selection of the appropriate template

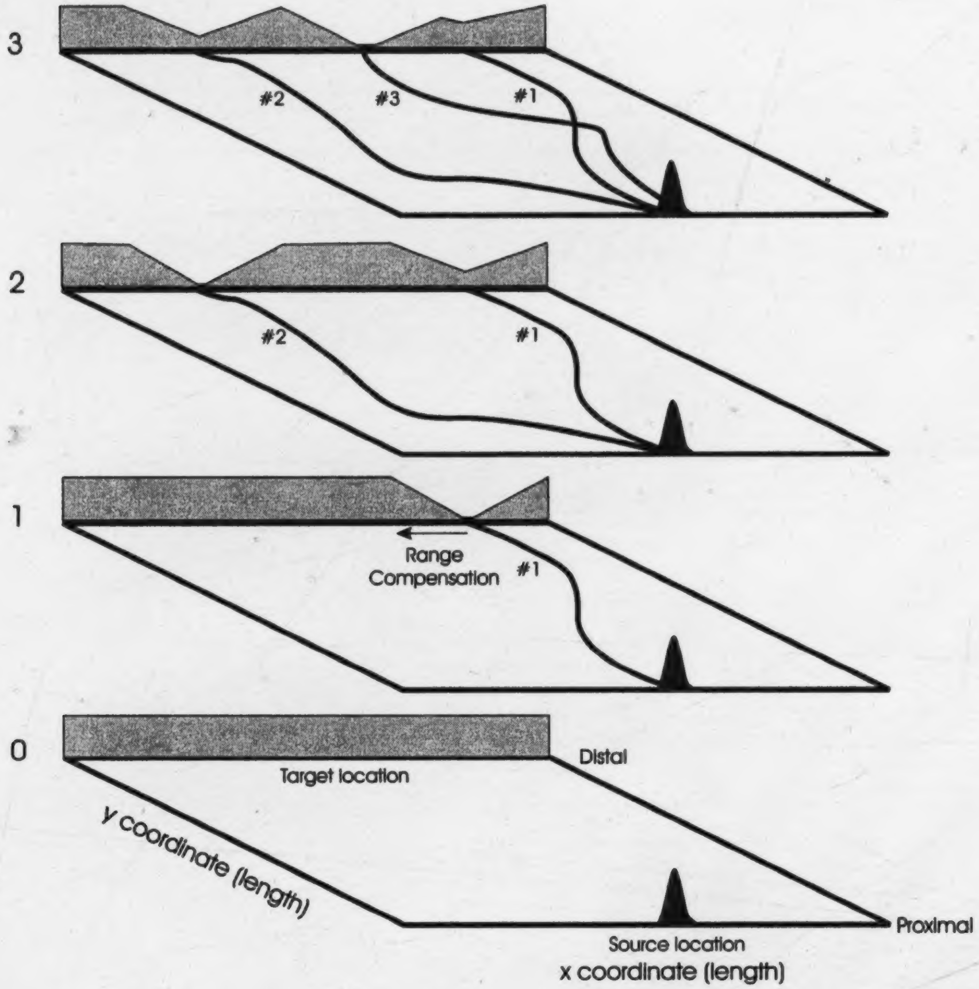
3
#2
#3
#1
2
#2
#1
1
Range Compensation
#1
0
Target location
Distal
y coordinate (length)
Proximal
Source location
x coordinate (length)

Figure 5.24: A method for integrating a compensational stacking pattern into streamline association placement. The source and target distributions are indicated at the proximal and distal edges respectively. At time step 0 the target distribution is uniform. Source and target locations are drawn and a streamline is placed. The target distribution is updated.

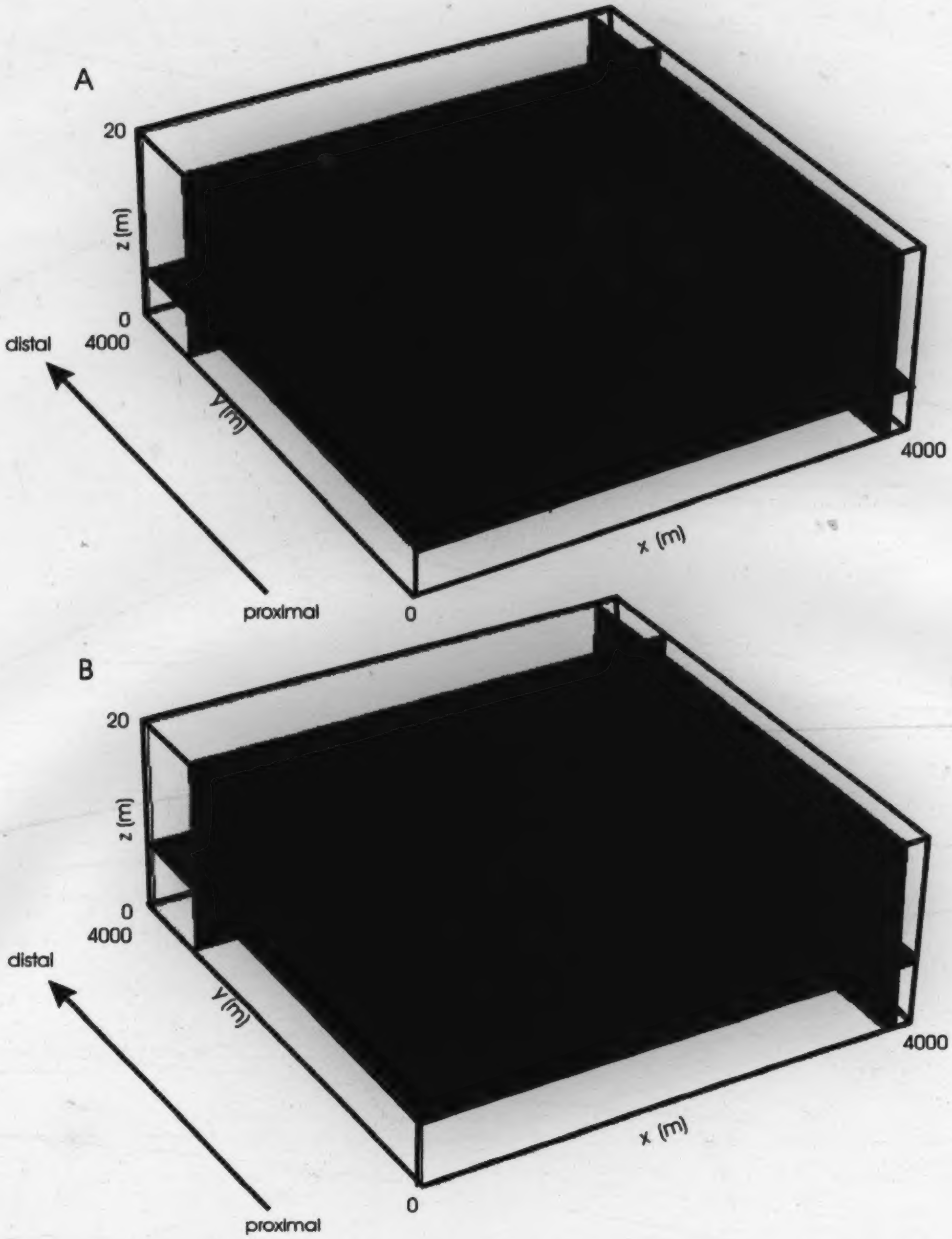
A
20
z (m)
0
distal
4000
y (m)
proximal
0
x (m)
4000
B
20
z (m)
0
distal
4000
y (m)
proximal
0
x (m)
4000

Figure 5.25: Example channelized sheet complex training image. Two horizontal slices A and B show the influence of compensational stacking between streamline associations.

is a function of the available computational resources, and the character and scale of the salient features in the training image (Strebelle, 2002)[120].

### Multiple Point Histogram

The multiple-point histogram is a multiple-point probability density function (pdf) as defined below and represents the probability of a specific configuration of categories, $1,\ldots,K$, existing at the template locations, $\mathbf{h}_1,\ldots,\mathbf{h}_N$.

$$f(\mathbf{h}_1,\ldots,\mathbf{h}_N;k_1,\ldots,k_K) = Prob\{Z(\mathbf{u}+\mathbf{h}_1) \in \mathit{category}\ k_1,\ldots \qquad (5.6)$$

$$,Z(\mathbf{u}+\mathbf{h}_N) \in \mathit{category}\ k_N\}$$

where $k_1,\ldots,k_K = 1,\ldots,K, \forall \mathbf{u} \in A$.

It is convenient to calculate an index representing as possible configurations of categories, $z(\mathbf{u}+\mathbf{h}_i)$, for template locations, $1,\ldots,N$, that may take classes, $1,\ldots,K$ (Deutsch, 1992)[19].

$$index = 1 + \sum_{i=1}^{N}[z(\mathbf{u}+\mathbf{h}_i) - 1] \cdot K^{i-1} \qquad (5.7)$$

where $index = 1,\ldots,K^N$.

The multiple-point histogram may then be represented as a table of the frequency of each index when the template is scanned over the training image. An example five-point template that may be applied to calculate a multiple-point histogram is shown in Part A of Figure 5.26.

### Transition Probability

The transition probability is a subset of the multiple point histogram for the specific case of two points, where the two points are typically adjacent. The transition probability from $k_1$ to $k_2$ for lag $\mathbf{h}$ is the probability that given $Z(\mathbf{u})$ is category $k_1$ that $Z(\mathbf{u}+\mathbf{h})$ is in category $k_2$.

$$f(\mathbf{h};k_1,\ldots,k_K) = Prob\{Z(\mathbf{u}) \in \mathit{category}\ k_1,\ldots,Z(\mathbf{u}+\mathbf{h}) \in \mathit{category}\ k_N\} \qquad (5.8)$$

where $k_1,\ldots,k_K = 1,\ldots,K, \forall \mathbf{u} \in A$.

This statistic is summarized as a $K \times K$ matrix. This is an intuitive method for visualization of interrelationships of facies. The matrix may not be symmetric

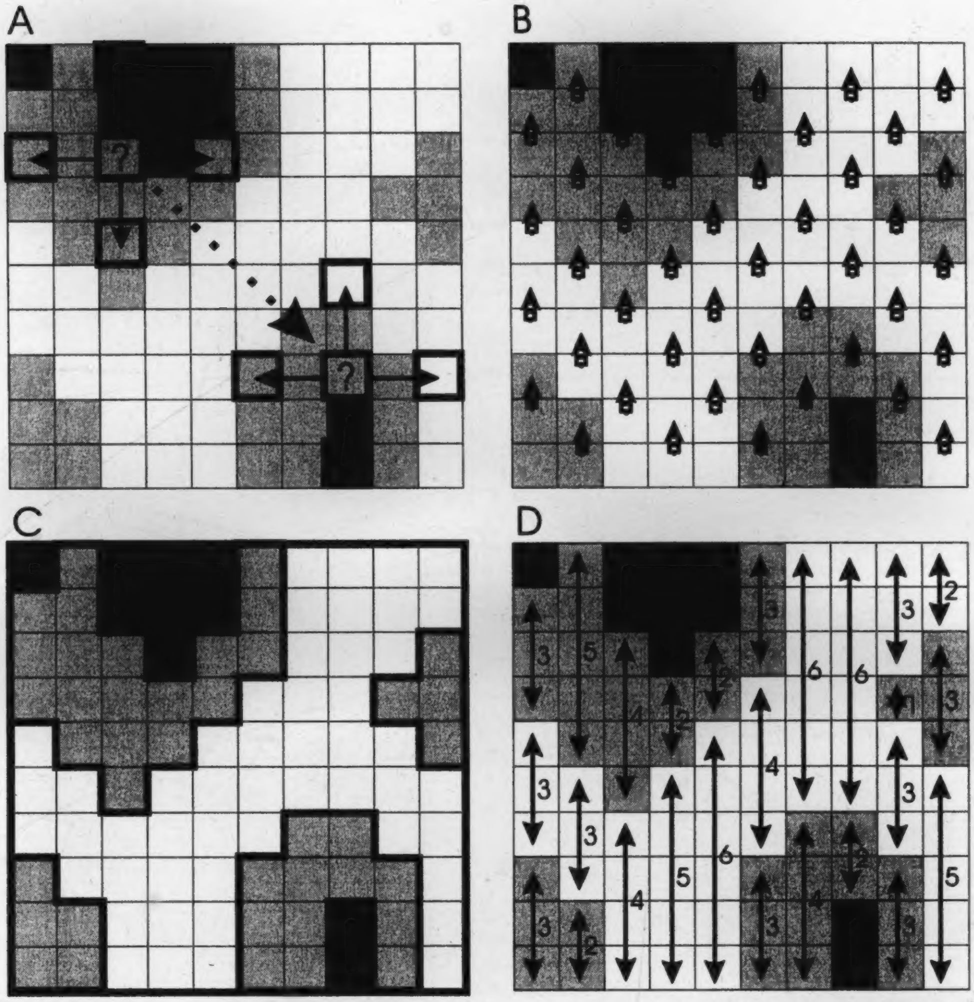

Figure 5.26: A schematic representation of the multiple point statistics calculated with the `MPSTATS` program. A - n-point histograms, a template is scanned through the image and the frequency of specific configurations is stored, B - transition probabilities are the probability of contact between two facies, note to avoid clutter only every second transition is shown, C - connectivity functions, the image is divided into connected geo-objects and D - the distribution of runs.

due to the lag effect. The transitions for $\mathbf{h} = (0,1)$ are illustrated in Part B of Figure 5.26.

### Connectivity Function

The connectivity function calculates geo-objects approximated as connected regions for the identified net categories. The output is the original training image categories and the associated geo-object index, set as null for non-net categories. A fast algorithm is applied that allows the user to specify whether edges and corners allow for communication (algorithm from Deutsch, 1998b)[20]. The distribution of runs is illustrated for $\mathbf{h} = (0,1)$ in Part C of Figure 5.26.

### Distribution of Runs

For the categorical case, a run is defined as a sequence of locations with the same category. A single run is parameterized by its length. A specific lag vector, $\mathbf{h}$ identifies the configuration of 1-D strings within the training image, $Z(\mathbf{u} + m \cdot \mathbf{h})$ for $\mathbf{u} \in A$ and $m$ is any integer such that $\mathbf{u} + m \cdot \mathbf{h} \in A$. All possible strings are extracted and the distribution of runs is calculated. The associated probability may be shown as:

$$Prob\{Run\ of\ Length\ M\} = Prob\{Z(\mathbf{u}) \in category\ k_i, \tag{5.9}$$
$$Z(\mathbf{u} + m \cdot \mathbf{h}) \in category\ k_i, \ldots, Z(\mathbf{u} + M \cdot \mathbf{h}) \in category\ k_i\}$$

where $k_i = 1, \ldots, K, \forall\ \mathbf{u} \in A$.

The statistic is summarized as table with the length of run and associated frequency. The distribution of runs is illustrated for $\mathbf{h} = (0,1)$ in Part D of Figure 5.26.

### `MPSTATS` Parameter File

The parameter file associated with the `MPSTATS` program is shown below and a summary of the input parameters is included in Table 5.8.

```
Parameters for MPSTATS
 1.  model.dat         -file with model
 2.  1                 -column
 3.  256 256 128       -nx,ny,nz
 4.  3 1 2 3           -number of facies, facies:1,...,nfacies
```

```
5.  1 2               -number of pay facies, pay: 1,...,npay (option
                       3 only)
6.  1                 -option (1-np hist.,2-trans. prob.,3-conn.
                       func.,4-runs)
7.  4                 -number of cells in template (option 1)
                       or number of lags (option 2 and 4)
8.  -1 -1  0          - cell #1 in template / lag #1: x,y,z relative
9.  0  1  0           - cell #2 in template / lag #2: x,y,z relative
10. 1  0  0           - cell #3 in template / lag #3: x,y,z relative
11. -1  0             - cell #4 in template / lag #4: x,y,z relative
12. 1 1               -testedge, testcorner (option 3 only)
13. mpstats.out       -output file
```

Multiple-point histogram output is in GEOEAS format, with $K^N$ rows, and columns with the indices (see Equation 5.7), the categories at locations $\mathbf{h}_1, \ldots, \mathbf{h}_N$, the frequency and the conditional probability, $Prob\{z(\mathbf{h}_1)|z(\mathbf{h}_2), \ldots, z(\mathbf{h}_N)\}$. These conditional probabilities may be read directly into a multiple point simulation algorithm.

The transition probabilities output is a $K \times K$ matrix with the probability of transition. This output may be applied directly to infer quantitative interrelationships as required by truncated Gaussian methods.

The output for the connectivity function is the original training image with the connected object index number appended in GEOEAS format. This index may be applied to visualize and quantify connected geo-objects. This information may be applied to assess recovery factors and morphologies for object based simulation.

The distribution of runs output is in GEOEAS format, with $N$ rows (where $N$ is the maximum run length), and columns with the length of run and the frequency. This output may be applied as soft information on connectivity or as input to simulation algorithms that consider the distribution of runs (Ortiz, 2003)[86].

### 5.4.2 Model Operations

A program called `MODELOPS` is provided to tailor the training images to a specific site. This program performs operations such as: **(1)** arithmetic operations on multiple models, **(2)** merging two models, **(3)** extracting subsets and **(4)** grouping facies. The program reads in multiple models from any number of files and then performs model operations sequentially. The output may represent the entire model or a subset of the model (see an example parameter file below and Table 5.9 for a description of

| Line | Description |
|---|---|
| 1 | input file. The file should be in GEOEAS format and GSLIB grid convention. |
| 2 | column number with the associated categorical data. |
| 3 | size of the input model (see Figure 5.2). |
| 4 | number of facies and the associated indices. |
| 5 | number of pay facies and the associated indices. This is only used for the calculation of the connectivity function. |
| 6 | type of calculation: Option #1 - multiple point histogram, Option #2 - transition probabilities, Option #3 - connectivity function and Option #4 - distribution of runs |
| 7 | number of cells in the template (option 1) or the lags (option 2 and 4). Note for multiple point histograms the locations 0 is assumed at 0,0,0; therefore, a template with 4 cells defines a 5 point histogram. For transition probabilities and distribution of runs results are calculated for each lag separately. |
| 8 to 11 | relative locations of the template nodes / lags. These are integers representing number of cells relative to location 0. |
| 12 | logical switches for accounting for edge and corner connections. This is only used for the calculation of the connectivity function. |
| 13 | output file. |

Table 5.8: A summary of the `MPSTATS` parameter file.

the parameters).

```
Parameters for MODELOPS
 1.  2 2 -1.0 100.0    -nfile,nop,tmin,tmax
 2.  data1.dat         -datafl#1
 3.  1 1               -datafl#1: ndata, cols
 4.  data2.dat         -datafl #2
 5.  1 1               -datafl#2: ndata, cols
 6.  256 256 128       -nx,ny,nz
 7.  1 2 1 3           -operation#1: d1, d2, op, d3
 8.  1 3 1 4           -operation#2: d1, d2, op, d3
 9.  modelops.out      -output file
 10. 4 1 2 3 4         -nout, values
 11. 1 256             -osx,osx
 12. 1 256             -osy,osy
 13. 1 128             -osz,oez

 1:d1+d2,2:d1-d2,3:d3*d4,4:d3/d 4,5:d3**d4
 6:d1 merge into d2 if d3,7:group f1 and f2 in d1 as f3
```

MODELOPS operation parameters are further illustrated for an example with two data files, with two data from the first file and one from the second. The first selected column from file #1 is $data_1$, the second selected column is $data_2$ and the selected column from file #2 is $data_3$. The following example operations are performed:

```
 2 1 7 3                - Operation#1: cat1,cat2,op,data1
 1 2 1 4                - Operation#2: data1,data2,op,data3
 3 4 3 5                - Operation#3: data1,data2,op,data3
```

Categories 1 and 2 are grouped as category 2 in $data_3$. $data_1$ and $data_2$ are added together and become $data_4$. Product of $data_3$ and $data_4$ become $data_5$. Any combination of data1 through $data_5$ may be included in output file.

Coordinates may be added to the training images with the ADDCOORD program from GSLIB (Deutsch and Journel, 1998)[23]. The ADDCOORD source may be modified to adjust the format and order for input to a variety of software packages.

## 5.5 Anticipated Applications

There is a wide variety of anticipated applications for the fluvial and deepwater training image library. (1) Primarily, these training images may be applied to aid

| Line | Description |
|---|---|
| 1 | number of input data files, number of operations to perform and the trimming limits. If any data is trimmed then that model location is set as null for all output. |
| 2 to 5 | the input data files, the number of data from each file and the associated columns. The input data are indexed in logical order, for example is there are two data files each with two data then: $data_1$ and $data_2$ are the first and second data from the first file and $data_3$ and $data_4$ are the first and second data from the second file. |
| 6 | size of the input models |
| 7 and 8 | list of operations, the format generally follows this format, $data_1^i$ $operation^i$ $data_2^i$ equals $data_3^i$: Operation #1: addition ($d_1+d_2 = d_3$), Operation #2: subtraction ($d_1 - d_2 = d_3$), Operation #3: multiplication ($d_1 d_2 = d_3$), Operation #4: division ($d_1/d_2 = d_3$), Operation #5: exponent ($d_1^{d_2} = d_3$), Operation #6: merge two categories ($d_2$ set to $d_1$ if $d_2 = d_3$), Operation #7: group (set $cat_1$ and $cat_2$ as $cat_1$ in $d_3$). Note: for this operation the parameters are: $cat_1$ $cat_2$ op $d_3$. |
| 9 | the output file |
| 10 | the number of data to write out and a list of their indices |
| 11 to 13 | the output model size. In this example the original model is written out. This allows subsets to be written out. |

Table 5.9: A summary of the `MODELOPS` parameters file.

in the inference to input statistics for conventional semivariogram and multiple-point based geostatistical models. (**2**) They may be utilized in comparative flow studies, for the calculation of recovery factors for reserves, to assess connectivity and to quantify geo-objects for input into object based simulation methods. (**3**) This library provides a documented set of "type-models" that demonstrate the capabilities and limits of geostatistical models and may be applied to help newcomers understand the techniques, tools and algorithms available in geostatistics. (**4**) This library provides scenarios for uncertainty analysis that are especially useful in frontier reservoirs.

### 5.5.1 Inference of Input Statistics

The primary application of these training images is to aid in the inference of input statistics for conventional semivariogram based and multiple-point geostatistical models. Training images may be chosen from the existing library or tailored by merging a variety of training images, such that spatial features deemed relevant to the site being characterized are represented.

The indicator semivariogram model is an important input for pixel based categorical geostatistics. The inference of the indicator semivariogram model is often problematic because of sparse data. Analysis of the experimental indicator semivariograms from the appropriate training images may provide information on the nested structures, associated shapes and range of correlation, in the principal directions. This information combined with the available experimental indicator semivariograms will result in improved indicator semivariogram model inference.

The need for training images in multiple-point geostatistical algorithms has been discussed. This training library provides a variety of high resolution training images and the tools to tailor them to a specific site and to extract the required consistent multiple-point statistics. This library makes the application of multiple-point geostatistics more practical.

To demonstrate this application a streamline based training image with 60% NTG, high sinuosity channels, high amalgamation and 20:1 channel width to depth ratio was applied to calculate (**1**) indicator semivariograms, (**2**) transition probabilities and (**3**) n-point histogram. Three sections through the training image are shown in Figure 5.27. The resulting statistics are shown in Figure 5.28.

The indicator semivariograms may be applied in the inference of semivariogram models for semivariogram based `SISIM`. The transition probabilities may be applied

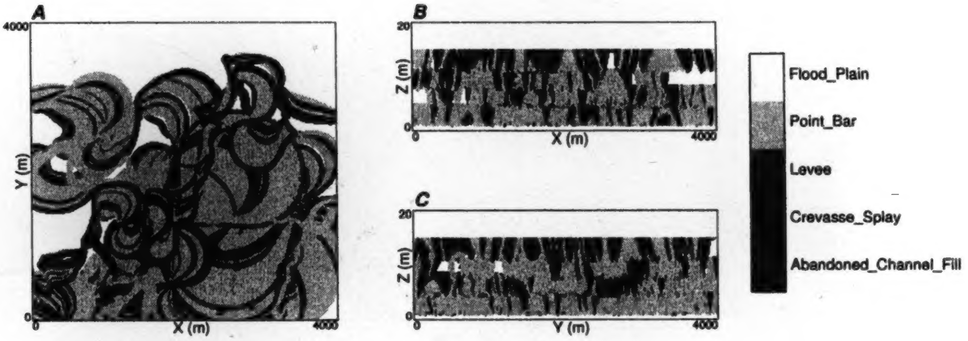
A
4000
Y (m)
0
0
X (m)
4000
B
20
Z (m)
0
0
X (m)
4000
C
20
Z (m)
0
0
Y (m)
4000
Flood_Plain
Point_Bar
Levee
Crevasse_Splay
Abandoned_Channel_Fill

Figure 5.27: Example training image for the inference of statistics. A - plan, B - long section and C - cross section. Note the alternating course and fine grained channel fills.

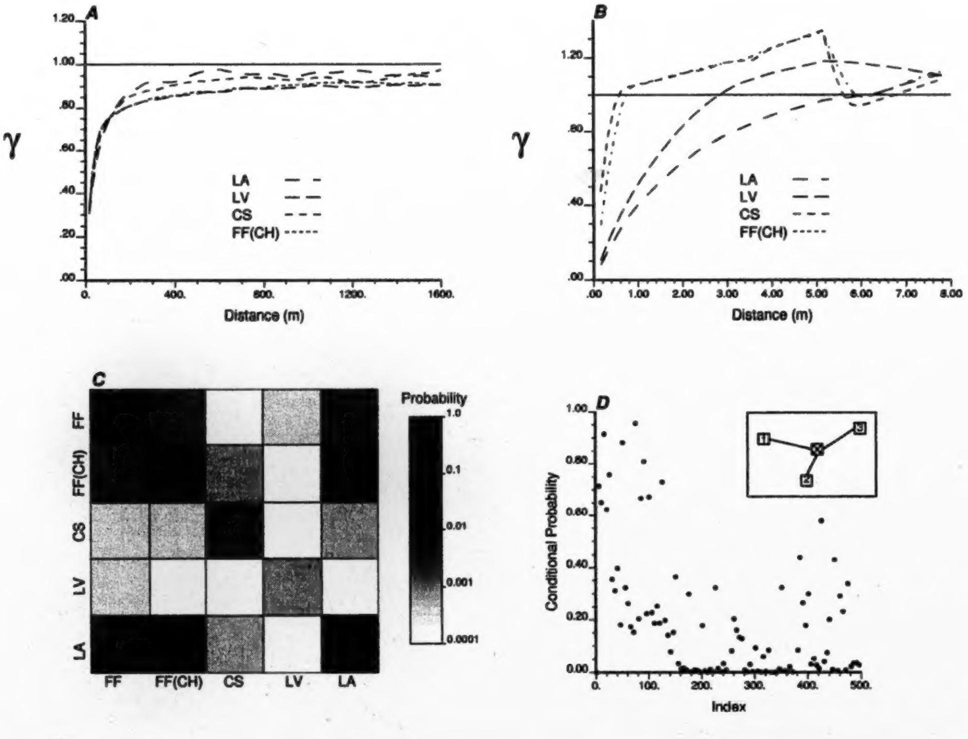

Figure 5.28: Statistics inferred from the example training image. A - horizontal indicator semivariograms calculated in the x positive direction, B - vertical indicator semivariograms, C - the transition probabilities pooled for the x, y and z directions and D - an example 3-point histogram for the indicated template.

to assess ordering relationships for `GTSIM`. For example, LV elements are more likely to be adjacent to FF elements than any other element. The n-point histogram provides the conditional probability of an element occurring at null location, $\mathbf{u}_1$, given a specific configuration at location, $\mathbf{u}_i, i = 2, ..., N$. The index is based on Equation 5.7 and the template is shown in Part D of Figure 5.28.

### 5.5.2 Comparative Flow Studies

In practice, only a small fraction of reservoirs are subjected to full flow simulation studies. In the absence of full flow simulation, these training images may be applied to aid in the inference of recovery factors and to quantify the connectivity, geometries and features that may constrain reservoir response.

Recovery factors are an important unknown parameter in the exploratory stage of reservoir development. The training images may be applied to calculate the potential recovery factors given the recovery method and expected geologic features. The resulting distribution of recovery factors may be applied to aid in reservoir management decisions.

Connectivity and geometry may significantly constrain reservoir response. The training images provide various models that contain characteristic fluvial and deepwater features that may be analyzed for the formation of barriers, baffles and conduits. Connected geo-objects may be calculated to assess the potential for compartmentalization. In addition, the identified geo-objects may be quantified and integrated into an object based simulation algorithm.

### 5.5.3 Documented "Type Models"

These training images represent documented type models that demonstrate features that geostatistical models are able to reproduce and their associated limits. The features reproduced in these training images may be compared and contrasted with other spatial models, such as fractals, neural nets, genetic algorithms and other pattern recognition techniques and may aid in the integration of secondary data such as seismic and production data. Also, these type models may be applied as training tools.

All models have unique underlying assumptions that may significantly affect the simulated distribution of response variables after a transfer function. For example, the multi-Gaussian (MG) distribution assumption results in maximum disorder of the extremes. Models based on the MG distribution may result in exaggerated dispersive flow and may under represent the presence of conduits, barriers and baffles to flow. The training image models may be compared with models generated by other algorithms to assess the impact of model assumptions after the application of a transfer function.

These training images represent different object and surface based geostatistical algorithms. These training images demonstrate a wide variety of input statistics and parameters that may be reproduced by geostatistical algorithms; therefore, they may be applied as a training tool for geologists, engineers, geophysicists and other professionals that are involved in reservoir characterization. Some of these algorithms reproduce complicated geometries and interrelationships; this may inspire additional research into the integration of geologic information into geostatistical models.

### 5.5.4 Library for Scenario Based Uncertainty Study

There is often a high degree of uncertainty with respect to reservoir morphologies and geometries (e.g. lobes or channels), and their associated properties (large or small lobes or channels). This uncertainty may be quantified through the assignment of scenarios with their associated probabilities based on the available data, analogue information and expert judgment. The uncertainty in reservoir morphologies may be modeled by calculating multiple realizations with training images drawn from the identified scenarios (Pyrcz et. al, 2004)[103].

An example scenario tree is shown in Figure 5.29. For this example there is uncertainty with respect to the depositional setting, architectural elements and the scale of the sandbodies. Conditional probabilities are assigned for each decision and the probability of each scenario is calculated (recall Equation 5.10):

$$Prob\{A,B,C\} = Prob\{C|A,B\} \cdot Prob\{B|A\} \cdot Prob\{A\} \tag{5.10}$$

Training images may be selected that meet these criteria. Then realizations based on a multiple point stochastic algorithm may be calculated with training images drawn from the selected scenarios.

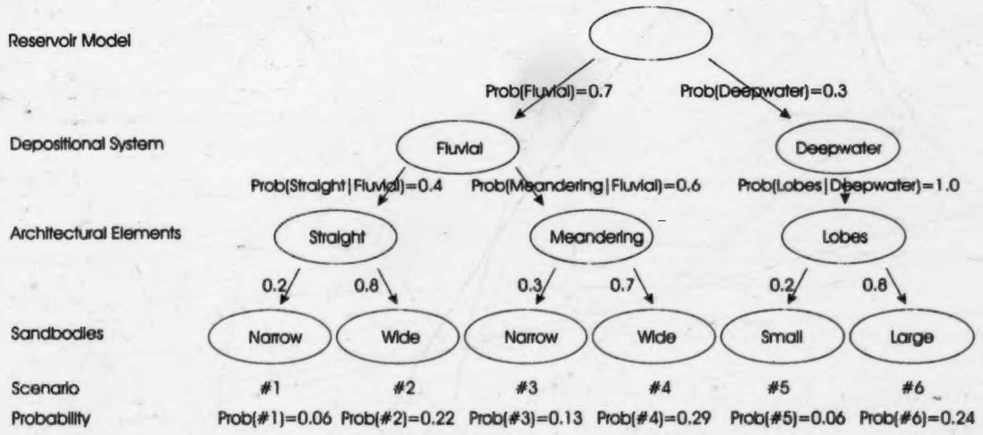
Reservoir Model
Prob(Fluvial)=0.7
Prob(Deepwater)=0.3
Depositional System
Fluvial
Deepwater
Prob(Straight|Fluvial)=0.4
Prob(Meandering|Fluvial)=0.6
Prob(Lobes|Deepwater)=1.0
Architectural Elements
Straight
Meandering
Lobes
0.2
0.8
0.3
0.7
0.2
0.8
Sandbodies
Narrow
Wide
Narrow
Wide
Small
Large
Scenario
#1
#2
#3
#4
#5
#6
Probability
Prob(#1)=0.06
Prob(#2)=0.22
Prob(#3)=0.13
Prob(#4)=0.29
Prob(#5)=0.06
Prob(#6)=0.24

Figure 5.29: A potential scenario tree for a reservoir model with uncertainty with respect to the depositional system, architectural elements and sandbody geometry. The resulting probabilities for each scenario may be applied for drawing training images

## 5.6 Discussion

This chapter has presented the static training image library for fluvial and deepwater reservoirs and provided an algorithm for the flexible construction of deepwater training images. The many potential applications of these training images have been discussed. A major application is the exportation of multiple point statistics. An algorithm has been provided for the calculation of multiple point statistics. These training images provide an important tool to improving the geologic realism within geostatistical fluvial and deepwater reservoir models.

# Chapter 6

# Gridding and Building Blocks

Quantitative models based on irregular grids more efficiently represent subsurface heterogeneity. The limitation of regular grids to represent heterogeneity with a limited number of cells is illustrated in Figures 6.1 and 6.2. The ability of irregular grids to capture complex features with few model cells is illustrated in Figure 6.3. The application of irregular grids within geostatistics may result in more realistic models and reduced numerical dispersion in flow simulation. Direct sequential simulation allows for efficient population of irregular grids.

This chapter covers the theory and methods required for simulation directly to irregular grids and presents the necessary code and example case studies. Section 6.1 briefly reviews a variety of gridding schemes and their associated advantages, limitations and some implementation details. Section 6.2 covers the direct sequential simulation (`DSSIM`) with histogram reproduction algorithm. Section 6.3 presents the building blocks for `DSSIM`. These building blocks are Fortran subroutines that perform the operations required by `DSSIM` in a CPU efficient manner. Section 6.4 presents example applications of the `DSSIM` algorithm to simulate directly to a two gridding schemes and discusses related implementation details.

## 6.1 Gridding

The following is based on a review of gridding implications for geostatistical models by Deutsch (2003)[22]. A grid network must be assigned to the reservoir volume to allow for the modeling of geologic heterogeneity and to apply transfer functions such as flow simulation. The gridding scheme should consider the need to resolve geo-

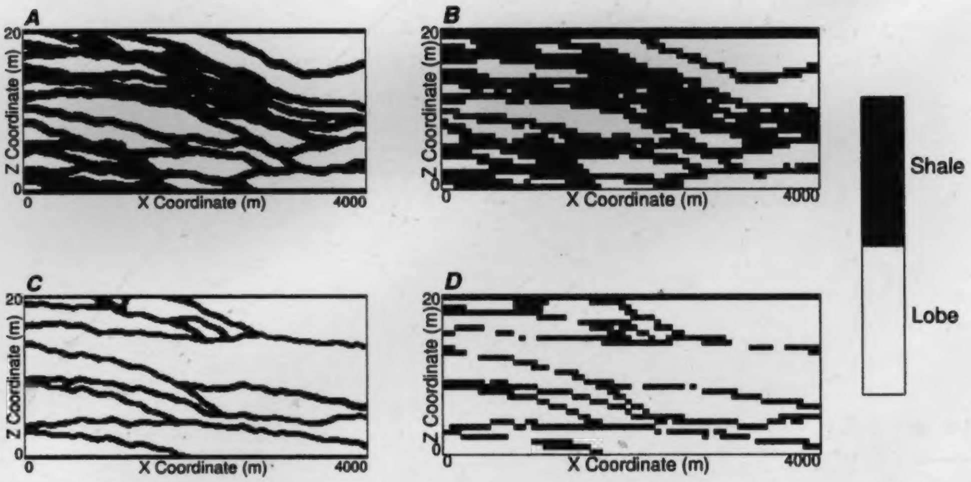

Figure 6.1: Cross sections of stochastic mud drape models upscaled for flow simulation. Low NTG model: A - high resolution model eight million cells, B - upscaled for flow simulation two hundred thousand cells. High NTG model: C - high resolution model eight million cells, D - upscaled for flow simulation two hundred thousand cells. These upscaled models on regular grids lose important features such as continuous mud drape barriers.

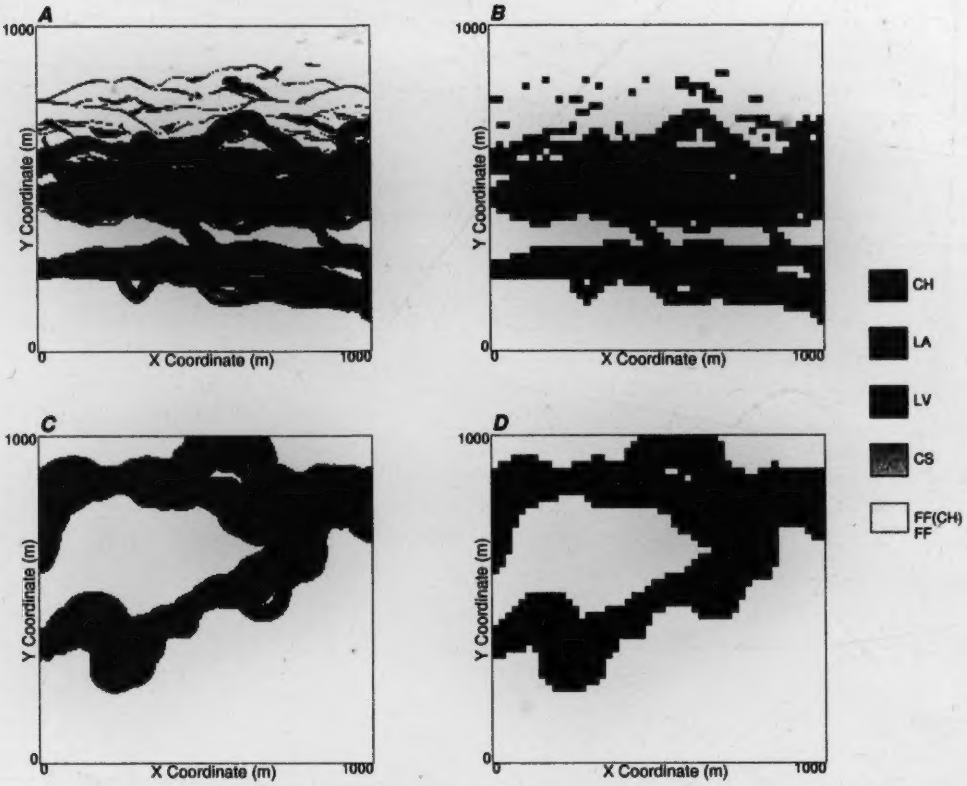
A
B
C
D
1000
0
Y Coordinate (m)
X Coordinate (m)
CH
LA
LV
CS
FF(CH)
FF

Figure 6.2: Plan views of streamline based stochastic models upscaled for flow simulation on regular Cartesian grids. CB type jigsaw fluvial model: A - high resolution model eight million cells, B - upscaled for flow simulation two hundred thousand cells. CB type labyrinth model: C - high resolution model eight million cells, D - upscaled for flow simulation two hundred thousand cells. These upscaled models on regular grids lose important features such as connected channel sands.

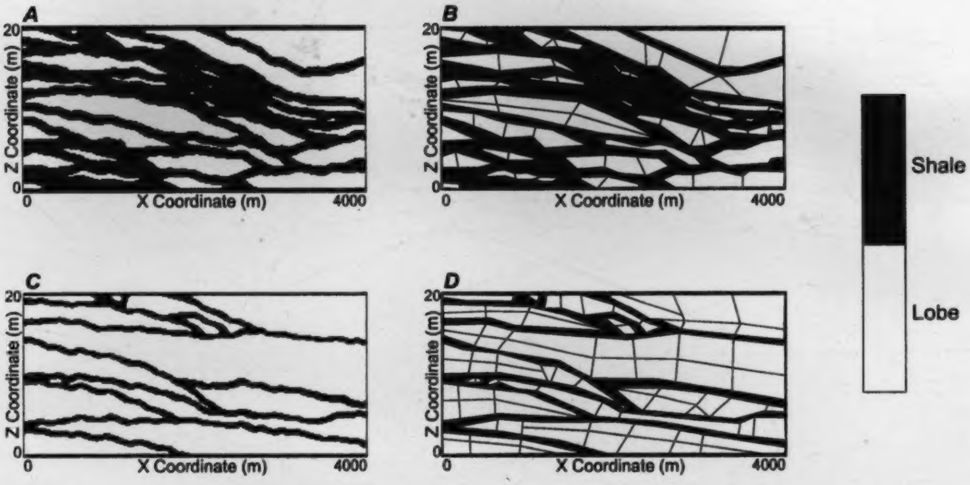
A
B
C
D
20
0
Z Coordinate (m)
X Coordinate (m)
4000
Shale
Lobe

Figure 6.3: Cross sections of stochastic mud drape models upscaled for flow simulation on Voronoi grids. Low NTG model: A - high resolution model eight million cells, B - schematic of a upscaled model on Voronoi grids with perhaps a couple thousand cells. High NTG model: C - high resolution model eight million cells, D - schematic of a upscaled model on Voronoi grids with less than a thousand cells.

logic feature such as reservoir boundaries, faults, stratigraphic surfaces and within sequence facies changes, trends in petrophysical properties and engineering constraints related to flow simulation such as flow paths and gradients. Gridding represents a modeling decision dependent on the available computer resources and the goals of the reservoir study. If the purpose of the study is the calculate volumetrics then a coarse and simple gridding scheme should be sufficient. If the goal is to assess the effect of thinly bedded shales on reservoir response then a finer and more complicated gridding scheme may be required.

The general principle is to choose the simplest and coarsest grid that meets the reservoir study goals, although this is a difficult problem. This will save professional and computational time. The grid should represent significant heterogeneities. Significance may be checked by comparing models with and without the specific geologic feature. Significance should always be measured by the impact on the results after the application of the transfer function. In addition, the resolution of the model should account for changes in the reservoir study goals and the potential need to scale up the grid for flow simulation. Long term studies may consider the future increase in available computational power.

Implementation details and examples are presented below for regular and irregular grids, including regular Cartesian, tartan, nested, Voronoi and general corner point grids. The following brief discussion focuses on the advantages and limitations associated with each gridding scheme.

### 6.1.1 Regular Cartesian Grids

Regular Cartesian grids are commonly applied. These grids are characterized by few parameters and allow for simple indexing and fast locating (see Figure 6.4 for an example regular grid). Only nine parameters are required to characterize a regular Cartesian grids 3-D grid: number of cells, origin and size of the cells for each dimension. The parameters for a GSLIB (Deutsch and Journel, 1998)[23] Cartesian grid are shown in Table 6.1.

The level of discretization may be different in each direction but is constant over the entire model. This may result in wasted computational effort to finely resolve unimportant or relatively homogeneous subsets of the model at the same level of precision required by subsets that are more significant or highly heterogeneous. Regular Cartesian grids require a high resolution in order to represent complicated

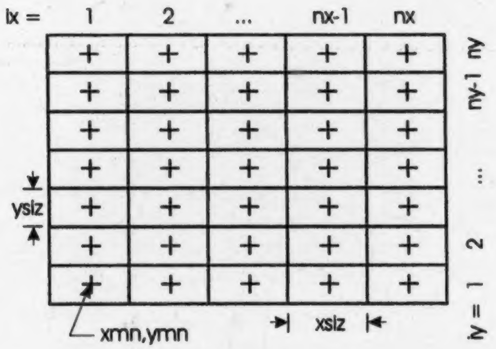

Figure 6.4: An example regular Cartesian grid and the associated parameters. This schematic is based on Figure II.1 from Deutsch and Journel, 1998.[23]

| | **X** | **Y** | **Z** |
|---|---|---|---|
| Number of Cells | $nx$ | $ny$ | $nz$ |
| Origin | $xmn$ | $ymn$ | $zmn$ |
| Cell Size | $xsiz$ | $ysiz$ | $zsiz$ |

Table 6.1: The parameters required to define a regular Cartesian grid.

geologic structures. Geostatistics is commonly applied with regular Cartesian grids because of increased complexity in simulating to irregular grids.

Regular Cartesian grids are often coupled with prior stratigraphic coordinate calculation and the application of straightening and rotation transformations. This improves the ability of regular Cartesian grids to conform to geologic and engineering constraints. These calculations and transformations are discussed by Deutsch (2003)[22].

### 6.1.2 Irregular Grids

Irregular grids may be populated either by **(1)** simulation to a small scale regular grid and scaling up or by **(2)** simulation directly to the irregular grid. The issues related to simulation to irregular grids are covered in Section 6.2.

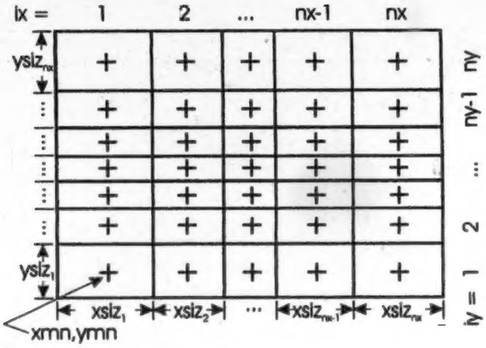

Figure 6.5: An example tartan grid and the associated parameters.

| | X | Y | Z |
|---|---|---|---|
| Number of Cells | $nx$ | $ny$ | $nz$ |
| Origin | $xmn$ | $ymn$ | $zmn$ |
| Cell Size | $xsiz_i, i = 1, \ldots, nx$ | $ysiz_i, i = 1, \ldots, ny$ | $zsiz_i, i = 1, \ldots, nz$ |

Table 6.2: The parameters required to define a tartan grid.

### Tartan Grids

Tartan grids are the simplest form of irregular grids. They retain simple parametrization, indexing and locating and provide limited control over the local level of discretization (see Figure 6.5 for an example tartan grid). The application of tartan grids is demonstrated in Section 6.4. Tartan grid parametrization requires the addition of a size parameter for each row of cells in each dimension (see Table 6.2).

### Nested Grids / Local Grid Refinements

Nested grids are inserted to further refine a grid to capture important local geologic or engineering information. A common example is the application of nested redial grids around a well to reduce discretization artifacts in flow simulation due to radial flow and step gradients (see Figure 6.6 for an example nested grid).

Often the coarse grid may be regular Cartesian or tartan. In this case the nodes in the regular grid retain the simple search and indexing, while the nested nodes may require more complicated search and indexing. The use of nested grids may represent a compromise between regular and irregular grids.

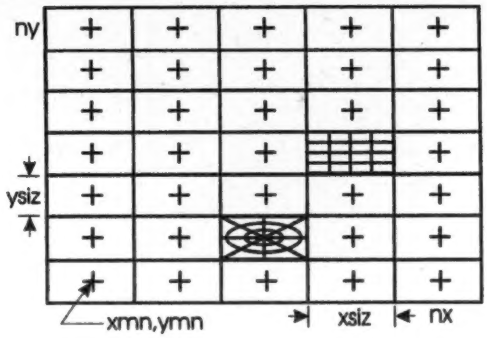

Figure 6.6: An example tartan grid and the associated parameters; note the inclusion of two nested redial grids.

An efficient methodology for working with nested grids is to account for the hierarchical relationship between the global and nested grid. For example, a point, **u**, may be located relative to the global grid and then if the specified node is refined with a nested grid, the location within the nested grid is calculated. For direct simulation, the regionalized property may be calculated over the global grid, then over the local grid refinements with the collocated simulated value as conditioning (see Section 6.4.1 for an example and further details).

### Voronoi Grids

The Voronoi grid is constructed by choosing control nodes and constructing Voronoi blocks defined by perpendicular bisectors. Voronoi block represents the subset within a domain that is closest to a specific control node (see Figure 6.7 for a schematic of a Voronoi grid).

Voronoi grids are flexible. The grid node location may be chosen independent of each other. Voronoi grids may freely conform to geologic features and engineering constraints and may vary in local discretization density (Palagi and Aziz, 1991)[89].

In addition, Voronoi grids may be designed to represent any other grid types (e.g. Cartesian, tartan, and local grid refinements). For example, a regular mesh of control points results in a regular Cartesian grids. Hybrids of gridding schemes may also be applied. Voronoi grid represent a natural methodology to connect local grid refinements within a coarse grid (Forsyth, 1989)[38].

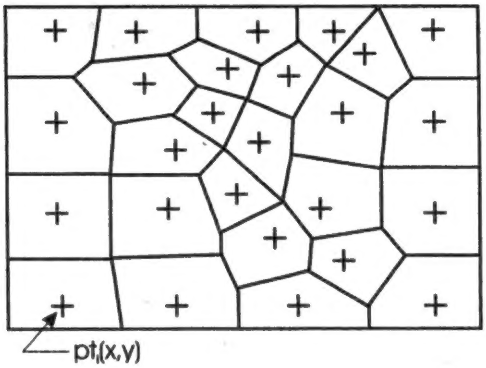

Figure 6.7: An example Voronoi grid and associated parameters.

## 6.2 Concepts Related to Direct Sequential Simulation

Reservoir simulation is often performed on irregular non-Cartesian grids. A common methodology for building the input reservoir models is to simulate geostatistical reservoir models on a fine grid and then to average up to the coarser unstructured grid.

The procedure for simulating a fine Cartesian grid and upscaling to an arbitrary grid is classical. Any type of averaging including non-linear averages and flow based averaging could be used. There are, however, two good reasons to be interested in simulation directly to irregular grids.

1. It may be more efficient to directly populate an unstructured grid than to simulate to a fine grid and upscale. This will depend on the range of block sizes within the irregular grid, since the fine grid should have at least three cells in each dimension in each coarse irregular grid block (Journel and Huijbregts, 1978)[59]. If there are very small blocks in the irregular grid the required regular grid will have a very fine resolution uniformly over the entire domain.

   The CPU time and memory requirements may be large for very fine regular 3-D grids. Multiple realizations are required for uncertainty analysis and risk assessment. The proposed method to directly populate irregular grids performs most calculation upfront and subsequent realizations have reduced CPU intensities (see Section 6.4). Nevertheless, this reason alone would not be sufficient given the efficiency of regular grid simulation for most practical problems. There may be little or no speed advantage to directly populate irregular grids.

2. Consideration of input data at multiple scales requires the same elementary calculations as those required to simulate directly to irregular grids. Current geostatistical practice is to assume that secondary data such as seismic or inverted production data is at the fine scale of modeling. This is incorrect. If the data is accounted for at their correct scale and precision then the ultimate grid might as well be populated directly. This link is explained below.

In simulation to irregular grids the areas/volumes of the cells being populated must be accounted for; larger volume cells have less variability. Direct simulation (Journel, 1986)[55] must be employed, since variables do not average linearly after Gaussian transformation. Implicit to linear estimation (see Equation 2.17) and mean covariance values (see Equation 2.22) is the assumption or arithmetic averaging, that is, the variable averages linearly. Some variables, such as permeability do not average linearly. The power law transform may be applied to transform the variable so that it averages linearly (see Section 2.2.10) (Deutsch, Zanon and Nguyen, 2002 and Deutsch, Pyrcz and Tran, 2002)[30, 24].

The direct sequential simulation (`DSSIM`) paradigm proceeds in the same manner as sequential Gaussian simulation (see Section 2.2.5), except (**1**) there is a non-Gaussian distribution assumption so the appropriate shape of the local conditional cumulative distribution function (ccdf) must be calculated, (**2**) support size of the grid nodes and the conditioning data are accounted for through the application of mean covariance values (see Section 2.2.5) and (**3**) the resulting models assume homoscedasticity unless heteroscedasticity is explicitly modeled. The following is a discussion of the methodologies applied to accomplish these requirements. Further implementation details are provided in the discussion on the building blocks (see Section 6.3).

### 6.2.1 Local CCDF in Direct Space

The kriging system, which is at the heart of most pixel based simulation algorithms, provides an estimate and the estimation variance. When working in Gaussian ($Y$) space these two parameters are sufficient to characterize the local distributions of uncertainty, since the local distributions are Gaussian in shape. The consistent ap-

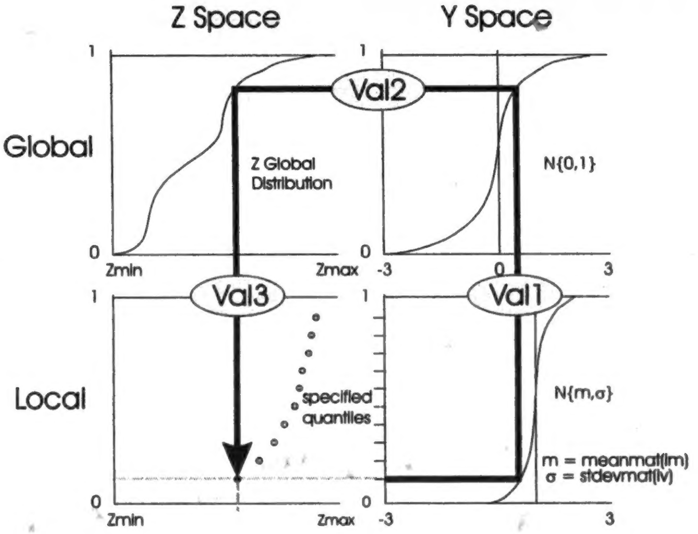

Figure 6.8: An schematic demonstrating the utilization of the link between global direct and Gaussian global distributions to construct the direct space local distribution from Gaussian space local distribution.

plication of Gaussian distributions ensures that the global distribution is reproduced. In the `DSSIM` framework, the local distributions are not sufficiently characterized by the kriging estimate and the estimation variance.

Any local distribution with the correct mean and variance will allow for reproduction of the covariance, but will not reproduce the correct global distribution. A method to determine the shape of the local distributions, such that the global is reproduced is illustrated in Figure 6.8 (Deutsch et al., 2001; Deutsch et al., 2002; Oz et al., 2003)[27, 24, 88]. This is a quantile transform from local $Y$ or Gaussian space to local $Z$ or direct space that utilizes the link between direct space ($Z$ space) and Gaussian space ($Y$ space) global distributions.

Given a specific quantile of a local $Y$ space distribution with mean ($m$) and standard deviation ($\sigma$) a $Z$ space quantile may be calculated by the following procedure. The inverse of the specific quantile is calculated as the inverse of the nonstandard Gaussian function.

$$Val1 = G^{-1}_{(m,\sigma)}(q) \tag{6.1}$$

where $G^{-1}_{(m,\sigma)}$ is the Gaussian function with the specific local mean and standard deviation from kriging, and $q$ is any quantile. The associated probability is calculated from the standard Gaussian distribution,

$$Val2 = G_{(0,1)}(Val1) = G_{(0,1)}(G^{-1}_{(m,\sigma)}(q)) \tag{6.2}$$

where $G_{(0,1)}$ is global $Y$ space distribution. The link between the global $Y$ space and global $Z$ space distributions is utilized to move into $Z$ space. The value in $Z$ space associated to the probability $Val2$ is then calculated from the $Z$ space global distribution.

$$Val3 = F^{-1}(Val2) = F^{-1}(G_{(0,1)}(G^{-1}_{(m,\sigma)}(q))) \tag{6.3}$$

where $Val3$ is the $Z$ space quantile of a local distribution of uncertainty associated with the probability value $q$.

This procedure is repeated for a series of quantiles to characterize the full distribution. The mean and variance of the $Z$ space distribution is not known prior to characterization of the distribution; therefore, it is not possible to directly determine the $Z$ space local distribution for a specific mean and variance provided from the kriging system.

A practical approach is to construct a reference table of valid local ccdfs that span a range of mean of variances. The ccdf table is constructed by repeating the above procedure to calculate valid local $Z$ space ccdfs over a range of $Y$ space means and variances. A sufficient number of discretizations should be applied in both $Y$ space mean and variances. Then, for a required $Z$ space mean and variance from the kriging system the nearest distribution is extracted from the ccdf look up table. An affine correction is applied to correct the exact mean and variance to the mean and variance from the kriging system.

Too few discretization points may result in large corrections applied to the extracted distributions. The affine correction assumes no shape change and is only considered valid over small changes in variances (Isaaks and Srivastava, 1989)[51]; therefore, the corrected realizations will be less reliable and the global histogram reproduction may be less precise. Too many discretizations will unnecessarily increase the computational intensity of the algorithm.

An example ccdf table was generated with a bimodal $Z$ space distribution, and the $Y$ space discretized into 100 equally spaced entries in both mean and variance

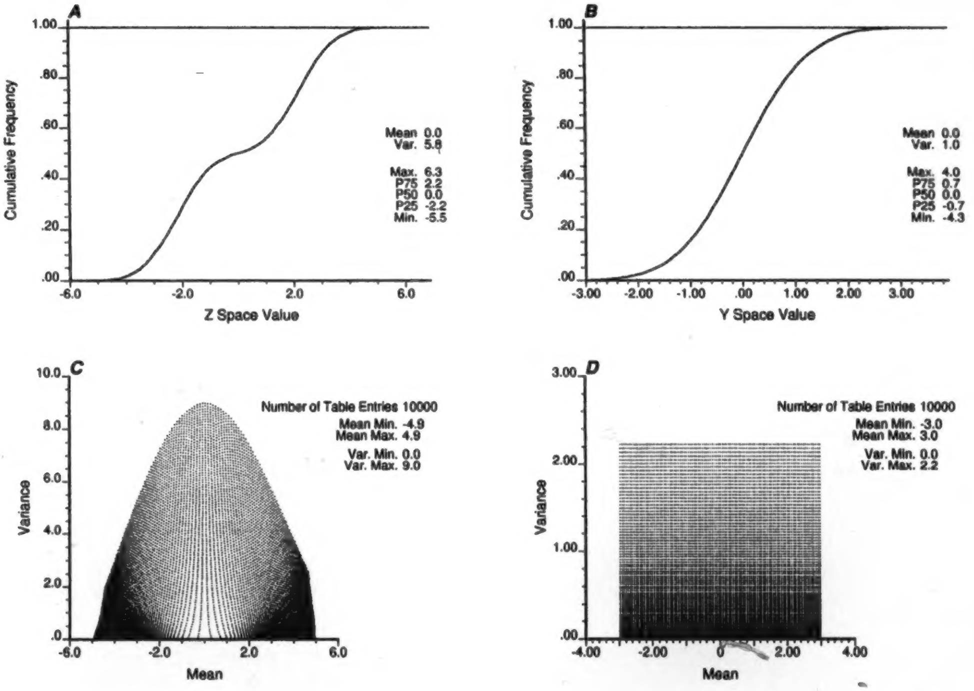

Figure 6.9: Example $Y$ and $Z$ global distributions and the resulting ccdf table entries. A - the $Z$ space reference distribution is set as a bimodal distribution and B - the $Y$ space is the required standard normal distribution. D - the regular series of means and variances for which local distributions were calculated are shown along with C - the resulting means and variances of the $Z$ space entries.

(see Figure 6.9). The resulting $Z$ space ccdf look up table is very densely populated. For practical problems fewer discretizations may be applied.

### 6.2.2 Accounting for Support Size in Direct Space

The volumes of the conditioning data and estimated or simulated locations may be explicitly accounted for with mean covariances (see Equation 2.22) applied in the simple kriging equations (see Equation 2.21).

A numerical approximation of the mean covariance between two volumes ($v_1$ and $v_2$) is calculated by discretizing the volumes and then averaging the point covariance over all possible combinations of discretized nodes between $v_1$ and $v_2$ (see Equation 6.4:

$$\overline{C}(v_1, v_2) \approx \frac{1}{n \cdot n'} \sum_{i=1}^{n} \sum_{j=1}^{n'} C(\mathbf{u}_i, \mathbf{u}_j) \tag{6.4}$$

It has been found that in 3-D the maximum number of discretizations required is four in each direction (Journel and Huijbregts, pg.97, 1978)[59]. Thus, a single mean covariance between two 3-D blocks may require up to $4^6 = 16,384$ covariance calculations. Three discretizations require $3^6 = 729$ covariance calculations for each mean covariance. This great number of covariance calculations will increase CPU effort. To keep run times under control either the number of discretizations ($n$ and $n'$) should be limited or the calculation of $C(\mathbf{u}, \mathbf{u}')$ should be sped up by some other means.

### Previous Approach to Reduce CPU Intensity of Mean Covariance Calculations

Previous work by Xie and Deutsch (2001)[141] addressed these issues by (**1**) avoiding redundant calculations of the covariance, $C(\mathbf{u}, \mathbf{u}')$ where $\mathbf{u} \in v_1$ and $\mathbf{u}' \in v_2$, (**2**) calculating $\overline{C}(v_1, v_2)$ by regression and (**3**) applying a semivariogram look up table.

The $n^6$ covariance calculations may include redundant calculations (especially if $v_1$ and $v_2$ have the same size and shape). These occur when the covariance, $C(\mathbf{h})$ is repeatedly calculated for the same lag vector translated, $\mathbf{h}$ (see Figure 6.10). The Xie and Deutsch (2001)[141] method was to identify redundant covariance calculations based on the geometries of each volume. While this technique may substantially decrease CPU intensity of the mean covariance calculation, it is very difficult to generalize.

A regression algorithm may be applied to calculate the approximate mean covariance as opposed to the previous CPU intensive discrete solution (refer to Equation 6.4)(Xie and Deutsch, 2001)[141]. Neural networks were applied because of their ability to fit nonlinear regression problems (Bishop, 1995)[4]. The mean covariance was modeled as a function of the following following parameters; (**1**) separation lag vector, (**2**) orientation of $v_1$ and $v_2$ and (**3**) extents of $v_1$ and $v_2$.

Errors in the mean covariance approximation from the neural networks result in instability within the kriging matrices. This may result in unreliable kriging estimates and variances. In addition, the application of neural networks results in additional complexity and computational effort for design and training of a neural

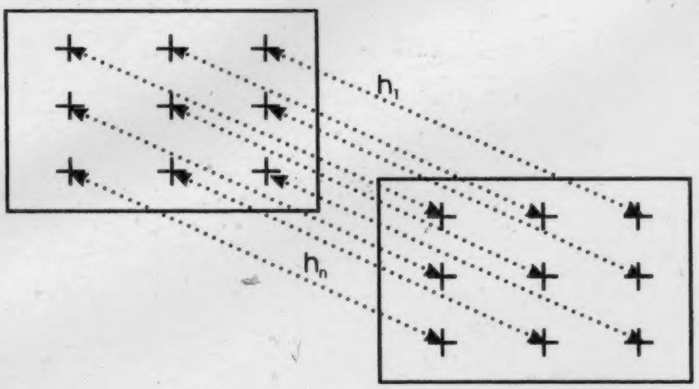

Figure 6.10: An example setting with redundant covariance calculations. Note that for each one of these point covariances that the lag **h** between volumes $v_1$ and $v_2$ are the same.

network.

### Proposed Approach to Reduce CPU Intensity of Mean Covariance Calculations

An alternative methodology for reducing the CPU intensity of mean covariance calculations with the application of (1) semivariogram tables and (2) a nonstationary covariance table. This methodology is applied in the building blocks algorithms (see Section 6.3).

The semivariogram calculations may be computational expensive (see Deutsch and Journel (1998))[23] for permissible semivariogram models). For example an exponential model is shown below:

$$\gamma(\mathbf{h}) = c \cdot \left[1 - exp\left(-\frac{3\mathbf{h}}{a}\right)\right] \tag{6.5}$$

where $c$ is the contribution, $a$ is the range and **h** is the lag vector.

A less computationally intensive method would be to construct a table with the semivariogram model for each structure and for each discretized lag distances (Xie and Deutsch, 2001)[141]. Then during estimation or simulation an index may be quickly calculated from the lag distance and applied to look up the associated semivariogram values from the table. If the table is sufficiently discretized (on the order of 1000 bins over the range) the results are sufficiently precise. This is

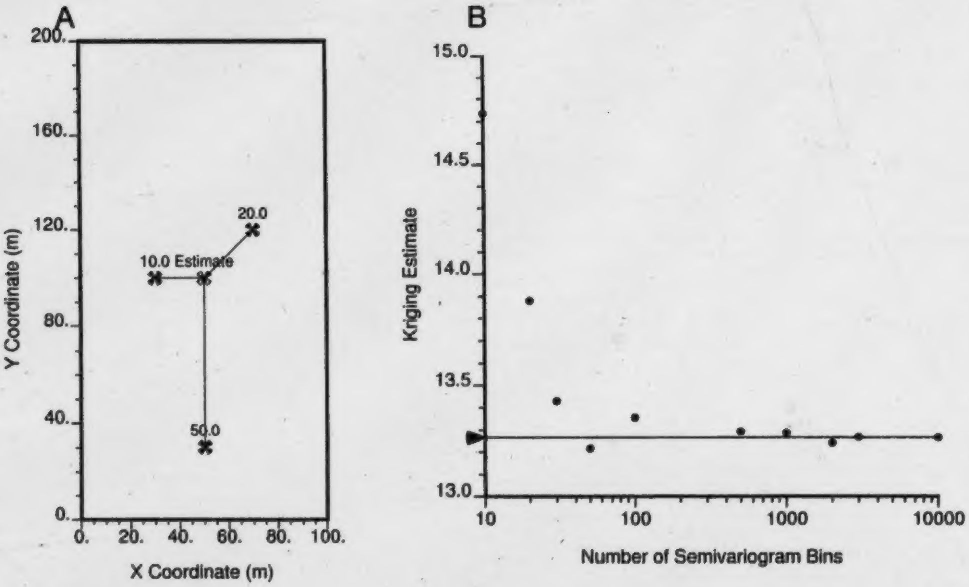

Figure 6.11: An example to demonstrate the sensitivity of kriging estimate to the number of bins in the semivariogram look up table. A - the conditioning data and estimate location. An isotropic spherical semivariogram with a range of 100 meters was applied. B - the kriging estimates with respect to the number of bins in the semivariogram look up table. The kriging estimate based on the actual semivariogram values is indicated by the horizontal line.

demonstated with a simple example with three conditioning data and simple kriging applied to estimate at an unknown location (see Figure 6.11). Note the change in the kriging estimate is becomes very small after 500 bins for this configuration.

To further reduce redundant calculations a nonstationary mean covariance table is built. The mean covariance between all volumes within the range of correlation of each other is calculated and stored prior to simulation. The nonstationary mean covariance table is sorted and a pointer array is constructed. This combines the search and mean covariance calculation into a single step prior to simulation. This results in an increased computational expense initially but greatly reduces the required computational effort to calculate subsequent realizations. Further implementation details are provided in Section 6.3.3.

### 6.2.3 Accounting for Heteroscedasticity in Direct Space

A heteroscedastic distribution is one for which the local variance varies as a function of local mean while homoscedasticity assumes local mean and local variance are independent. In natural phenomenon with positively skewed distributions it is common for the conditional variance to systematically increase as the local mean increases. This feature is called the proportional effect (see Goovaerts, 1997; Journel and Huijbregts, 1978[43, 59] for a discussion on the proportional effect).

In Gaussian simulation the Gaussian transform is applied prior to the application of kriging. The Gaussian distribution is homoscedastic, hence the Gaussian transform removes heteroscedasticity and the homoscedastic assumption of kriging is reasonable. The back transform after simulation from Gaussian to direct space generally replaces heteroscedastic features.

`DSSIM` does not apply a Gaussian transform; therefore, the results are homoscedastic unless heteroscedasticity is modeled explicitly. This may represent a significant limitation. This issue is not dealt with in this dissertation. This has been addressed by Oz and Deutsch (2002)[87].

## 6.3 Implementation with the Building Blocks Subroutines

The previously outlined methods allow for the direct simulation of irregular grid stochastic models. The building blocks are Fortran subroutines that perform the previously described tasks required by `DSSIM` in an computationally efficient manner. These tasks include:

1. Calculate valid local distributions of uncertainty in $Z$ space:
   (a) construct a local ccdf look up table
   (b) locate and correct local ccdfs
2. Calculate the average covariance between two blocks $v_1(\mathbf{u})$ and $v_2(\mathbf{u}')$:
   (a) construct semivariogram look up tables
   (b) non-stationary covariance lookup table

These building blocks are essential for many aspects of `DSSIM` with regular and unstructured grids. Clean, well documented, and tested code has been prepared. These algorithms should be fast in comparison with the brute force method of simulating on a fine grid and averaging a posteriori to an irregular grid.

It is common when simulating directly to irregular grids to encounter spurious kriging weights as a result of the screening effect and limitations in precision. Techniques for addressing this problem are also presented.

### 6.3.1 Local CCDF Look Up Table

The local ccdf look up table is constructed by the Fortran subroutine `PRECDIST`. The inputs include the specified number of quantiles, means, and variances, and the range of means and variances in $Y$ space, and the global ccdf. The mean and variance of the $Z$ space local ccdfs are calculated. The resulting quantiles are stored in a ccdf list array and the associated $Z$ space mean and variance for each distribution are stored in separate arrays. A super block search (arbitrarily set to 20 x 20) over the ccdf table is set up to increase to speed of subsequently finding the ccdf entry with the closest $Z$ space mean and variance to a required mean and variance calculated by kriging. The super block search was adapted from the `SETSPR` subroutine from GSLIB (Deutsch and Journel, 1998)[23].

The arrays required for the generation of the ccdf lookup table are dimensioned as allocatable in the `DISTMODULE` module and are then allocated at the beginning of the `PRECDIST` subroutine.

The series of quantile transforms to move from the local $Y$ space distribution to local $Z$ space distribution is applied as described previously in Section 6.2.1. The flow chart for this procedure within the `PRECDIST` subroutine is shown in Figure 6.12. An additional expanded flow chart is shown in Figure 6.13 that provides further detail on the application of the quantile transformation.

The `PRECDIST` subroutine establishes the framework required for the calculation and rapid retrieval of valid local distributions of uncertainty. The `GETCDIST` subroutine retrieves a distribution from this table given a target $Z$ space mean and variance. This subroutine may be called any number of times after the `PRECDIST` subroutine has been executed. The flowchart of this subroutine is shown in Figure 6.14.

The tasks of the `GETCDIST` subroutine are divided into two main operations: **(1)** find the ccdf table entry nearest to the called mean and variance and **(2)** correct the

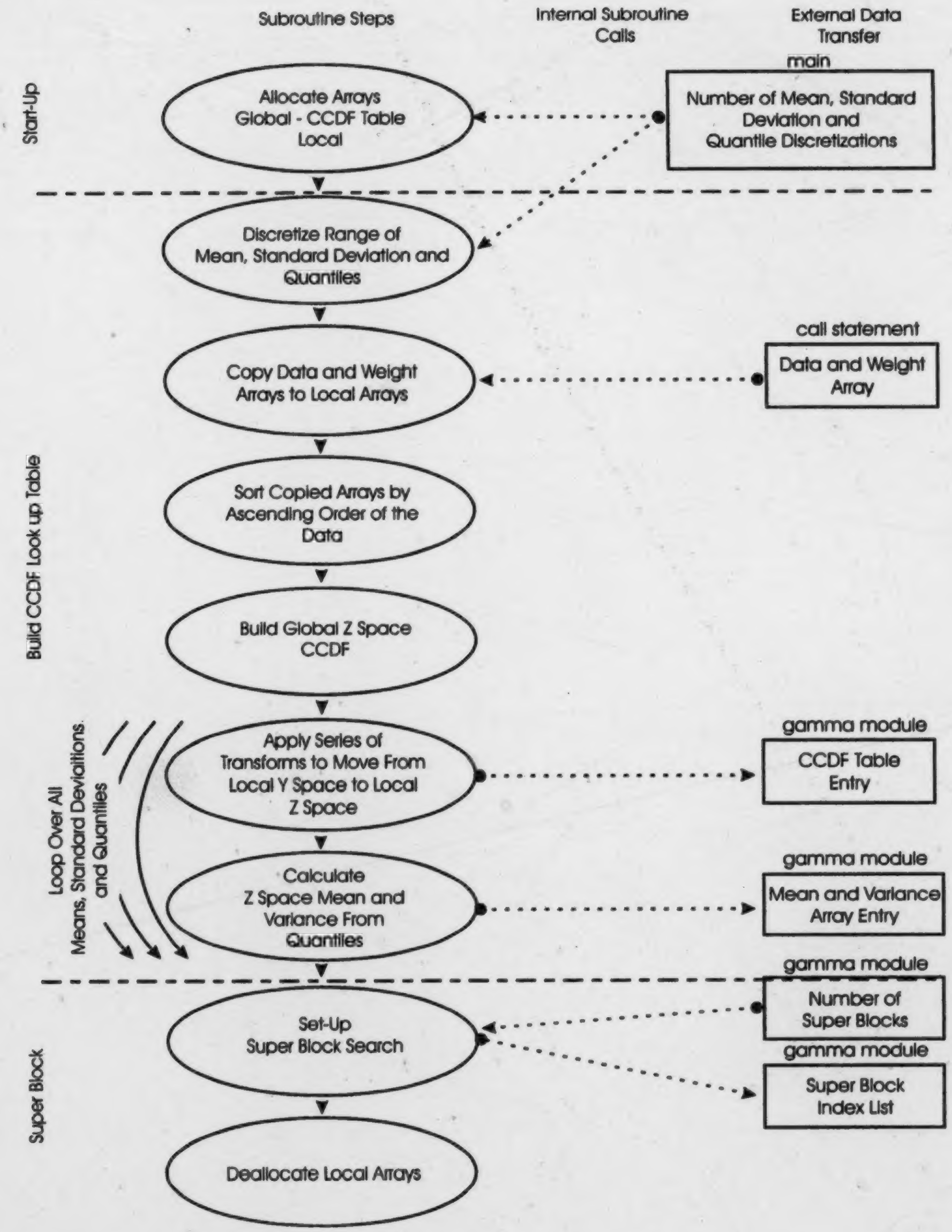
Subroutine Steps
Internal Subroutine Calls
External Data Transfer
Start-Up
main
Allocate Arrays Global - CCDF Table Local
Number of Mean, Standard Deviation and Quantile Discretizations
Discretize Range of Mean, Standard Deviation and Quantiles
call statement
Copy Data and Weight Arrays to Local Arrays
Data and Weight Array
Build CCDF Look up Table
Sort Copied Arrays by Ascending Order of the Data
Build Global Z Space CCDF
Loop Over All Means, Standard Deviations and Quantiles
gamma module
Apply Series of Transforms to Move From Local Y Space to Local Z Space
CCDF Table Entry
gamma module
Calculate Z Space Mean and Variance From Quantiles
Mean and Variance Array Entry
gamma module
Number of Super Blocks
Super Block
Set-Up Super Block Search
gamma module
Super Block Index List
Deallocate Local Arrays

Figure 6.12: The main PRECDIST subroutine flow chart. This subroutine builds a table of local ccdf and then sets up a super block search to facilitate the locating of the nearest ccdf entry to a required mean and variance.

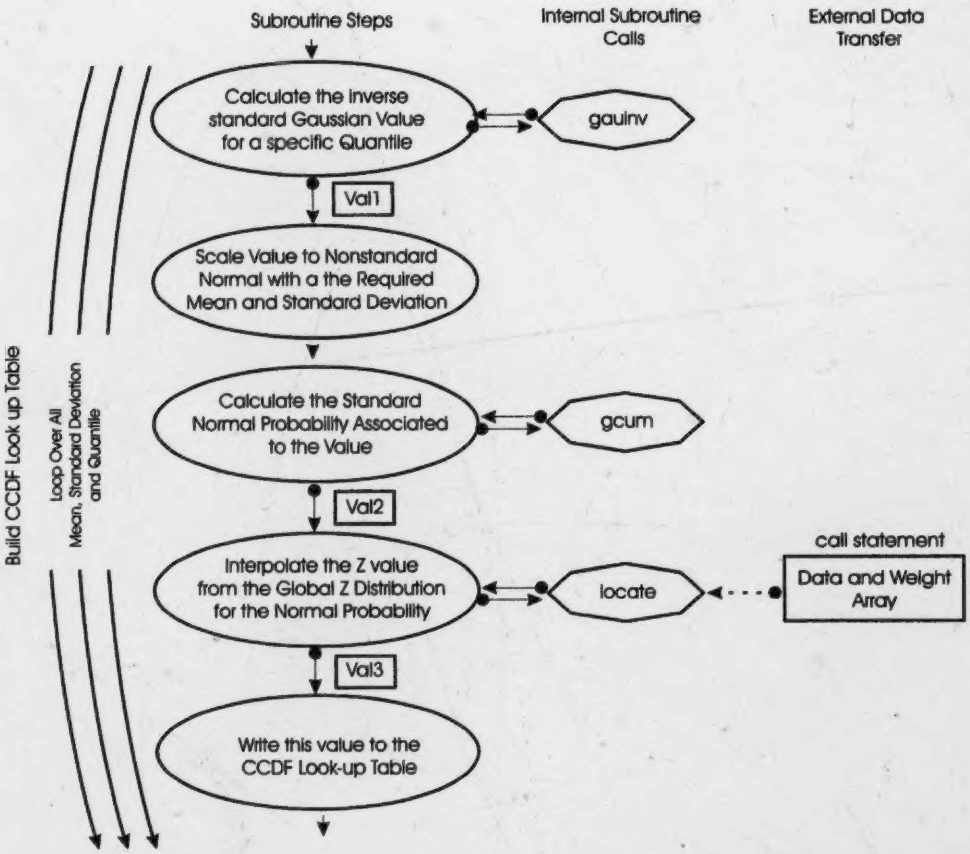
Subroutine Steps
Internal Subroutine Calls
External Data Transfer
Calculate the inverse standard Gaussian Value for a specific Quantile
gauinv
Val1
Scale Value to Nonstandard Normal with a the Required Mean and Standard Deviation
Calculate the Standard Normal Probability Associated to the Value
gcum
Val2
call statement
Interpolate the Z value from the Global Z Distribution for the Normal Probability
locate
Data and Weight Array
Val3
Write this value to the CCDF Look-up Table
Build CCDF Look up Table
Loop Over All Mean, Standard Deviation and Quantile

Figure 6.13: The transforms to move from $Y$ space to $Z$ space in the `PRECDIST` subroutine. These steps are illustrated graphically in Figure 6.8. Variables denoted in boxes are the same variables labelled in Figure 6.8.

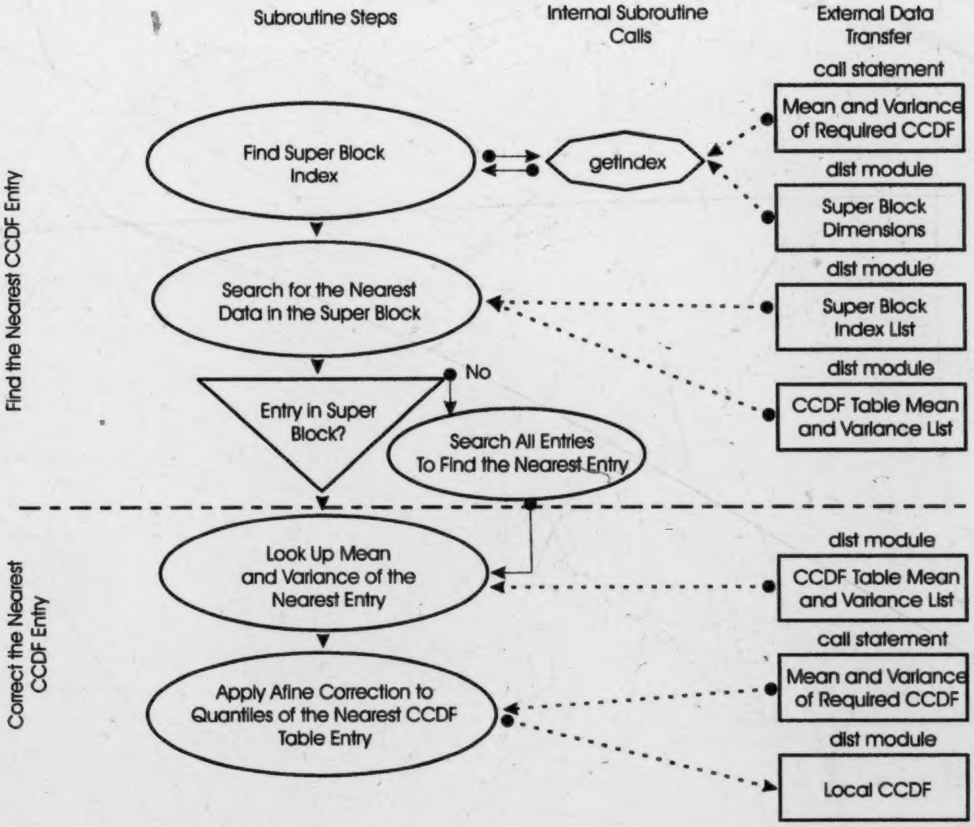
Subroutine Steps
Internal Subroutine Calls
External Data Transfer
Find the Nearest CCDF Entry
Correct the Nearest CCDF Entry
call statement
Mean and Variance of Required CCDF
Find Super Block Index
getindex
dist module
Super Block Dimensions
dist module
Search for the Nearest Data in the Super Block
Super Block Index List
dist module
No
Entry in Super Block?
Search All Entries To Find the Nearest Entry
CCDF Table Mean and Variance List
dist module
Look Up Mean and Variance of the Nearest Entry
CCDF Table Mean and Variance List
call statement
Mean and Variance of Required CCDF
Apply Afine Correction to Quantiles of the Nearest CCDF Table Entry
dist module
Local CCDF

Figure 6.14: The **GETCDIST** subroutine flow chart. Given a required mean and variance a super block search is used to find the nearest ccdf table entry. Affine correction is then applied to forced the returned ccdf to have the exact mean and variance required.

retrieved distribution to the kriging mean and variance. The super block search (see Section 6.3.1)is applied to speed the search of the table. If the specific super block has no entries then a search over all entries is performed. Although this global search requires more time, this situation will occur infrequently. The second operation is to correct the retrieved distribution to have exactly the required mean and variance. This is achieved through the affine correction of each quantile.

$$q_t = \sqrt{\frac{\sigma_t^2}{\sigma_o^2}}(q_o - m_o) + m_t \tag{6.6}$$

where $m_o$ and $\sigma_o^2$ are the mean and variance of the ccdf from the look up table and $m_t$ and $\sigma_t^2$ are the target mean and variance identified by the kriging system.

Affine correction is commonly applied to correct distributions for change in support size (see Deutsch and Journel, 1998)[23]. The underlying assumption is that the shape does not change and the distribution is shifted and multiplicatively scaled. This assumption is generally acceptable for small changes in mean and variance. A high level of discretization in the ccdf look up table may be applied to ensure that correction is minimal.

After affine correction, each quantile is checked to ensure that it remains within the range of the global distribution. Values outside this range are truncated to the distribution minimum or maximum. Severe cases may result in spikes in the retrieved ccdf.

### 6.3.2 Mean Covariance Calculation

All required global variables for the mean covariance calculation, such as the number of lag discretizations, and the semivariogram table array, are declared in the Fortran module, `GAMMAMODULE`. The `PREGBAR` subroutine builds a semivariogram look up table for each semivariogram structure over all direct and cross semivariograms (in the case of cokriging). The flow chart for `PREGBAR` is shown in Figure 6.15.

This subroutine should be executed once prior to mean covariance calculations or geometric distance calculations. There are two components to this subroutine, the first builds the rotation matrices required to calculated geometric distances. This step is applied in GSLIB's (Deutsch and Journel, 1998)[23] semivariogram based algorithms. These are standardized such that the ranges of all structures are set to 1.0. Then the standardized covariances are calculated and entered into the

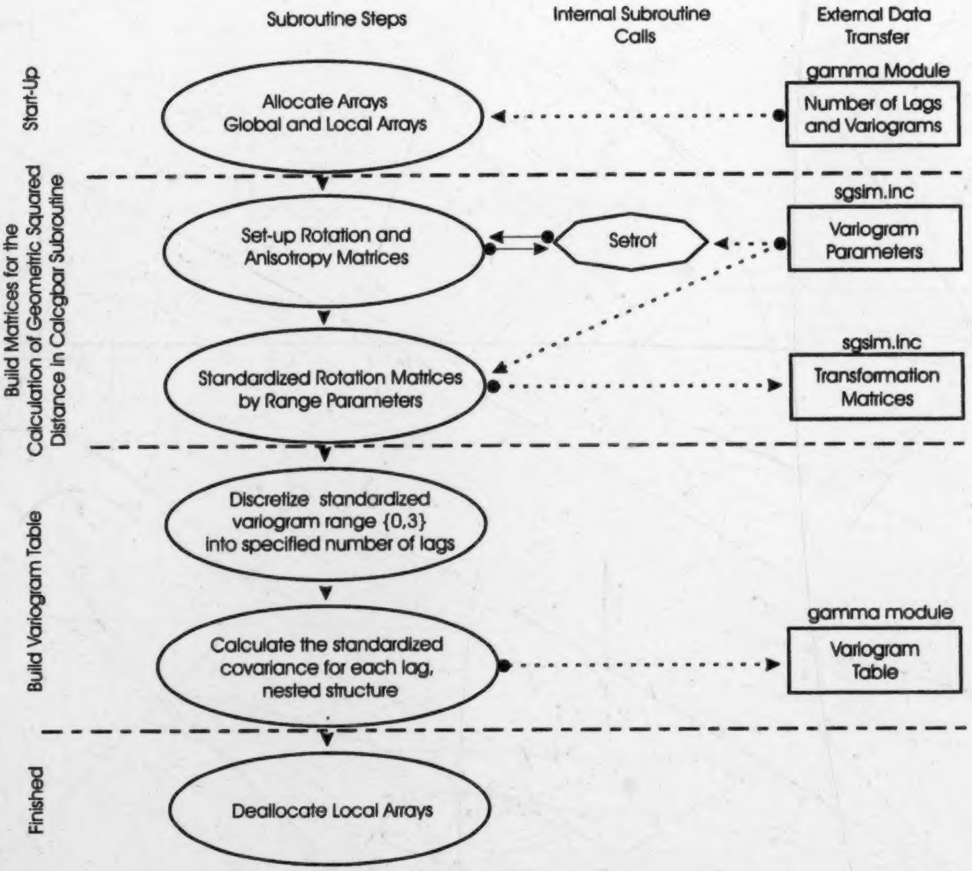
Subroutine Steps
Internal Subroutine Calls
External Data Transfer
Start-Up
Allocate Arrays Global and Local Arrays
gamma Module
Number of Lags and Variograms
Build Matrices for the Calculation of Geometric Squared Distance in Calcgbar Subroutine
sgsim.inc
Set-up Rotation and Anisotropy Matrices
Setrot
Variogram Parameters
sgsim.inc
Standardized Rotation Matrices by Range Parameters
Transformation Matrices
Build Variogram Table
Discretize standardized variogram range {0,3} into specified number of lags
gamma module
Calculate the standardized covariance for each lag, nested structure
Variogram Table
Finished
Deallocate Local Arrays

Figure 6.15: The **PREGBAR** subroutine flow chart. This subroutine uses the semivariogram parameters to build standardized rotational matrices and then to build a semivariogram lookup table.

semivariogram table.

The `CALCGBAR` subroutine may then be executed any number of times to calculate the mean covariance between any two volumes. This subroutine requires the semivariogram table and rotational matrices from the `PREGBAR` subroutine. Also, the shape (extents and orientation) and separation vector of the two volumes. This requires subroutines specific to the applied gridding scheme.

There are two options available for the calculation of the mean covariance, (**1**) the traditional discretization approach (see Equation 6.4) and (**2**) a new approach of randomly sampling the point covariance between volumes $v_1$ and $v_2$ and assigning the sample mean as an approximation of the mean covariance. The sample mean covariance will be unbiased, and for most circumstances a close approximation may be acquired with as few as 30 samples. This random sampling method results in a drastic decrease in the computational effort required to calculate the mean covariance (compare to $3^6 = 729$ calculations for the traditional discretization approach). The application of approximate mean covariance values does result in increased instability issues in kriging matrix solution. This is demonstrated in the tartan grid case study (see Section 6.4.1).

The `CALCGBAR` subroutine flow chart is shown in Figure 6.16. The procedure loops over discretized combinations or random locations $v_1(\mathbf{u})$ and $v_2(\mathbf{u}')$ and calculates the geometric distance between these locations and then finds the point covariance between these locations. If the geometric distance is very close to 0 then the maximum covariance minus the nugget effect is assigned as the covariance.

$$C(0)' = C(0) - c_0 \tag{6.7}$$

where $c_0$ is the contribution of the nugget effect. This has the same practical result as applying a infinitesimal shift to offset coincidental discretizations. This prevents a bias in the mean covariance calculations due to the zero effect (Journel and Huijbregts, pg.96, 1978)[59].

### 6.3.3 Nonstationary Covariance Table

The subroutine that builds the nonstationary covariance table is called `NONSTATCOVTABLE`. This algorithm scans the irregular grid for all volumes and data combinations within the range of correlation of each other. For each of these instances

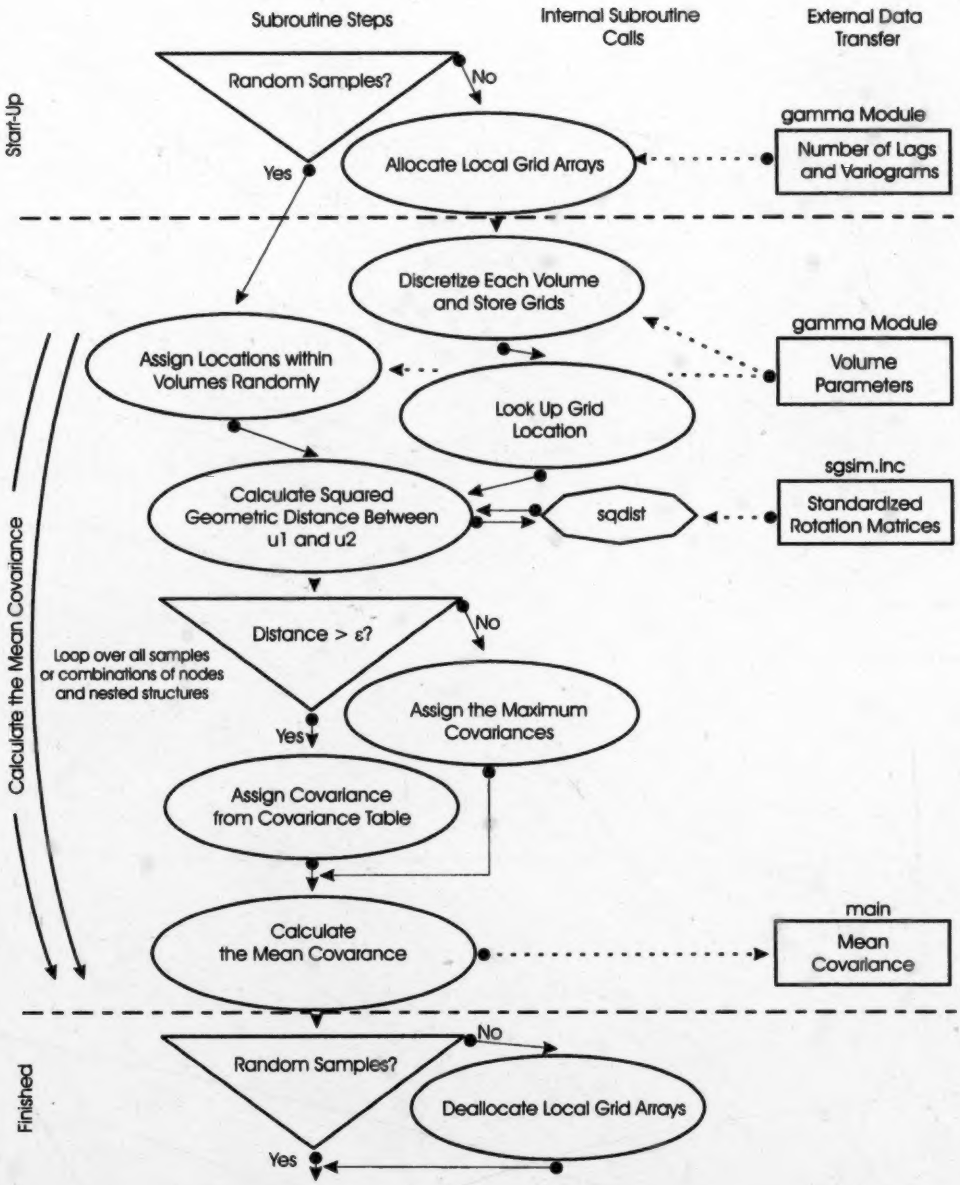
Subroutine Steps
Internal Subroutine Calls
External Data Transfer
Start-Up
Random Samples?
No
Yes
Allocate Local Grid Arrays
gamma Module
Number of Lags and Variograms
Discretize Each Volume and Store Grids
gamma Module
Volume Parameters
Assign Locations within Volumes Randomly
Look Up Grid Location
sgsim.inc
Calculate Squared Geometric Distance Between u1 and u2
sqdist
Standardized Rotation Matrices
Calculate the Mean Covariance
Distance > ε?
No
Loop over all samples or combinations of nodes and nested structures
Yes
Assign the Maximum Covariances
Assign Covariance from Covariance Table
main
Calculate the Mean Covarance
Mean Covariance
Finished
Random Samples?
No
Deallocate Local Grid Arrays
Yes

Figure 6.16: The **CALCGBAR** subroutine flowchart. The rotational matrices and semivariogram lookup table calculated in **PREGBAR** are applied to calculate the mean covariance between two rectangular volumes. This is accomplished by averaging point covariances over discretized node combinations or random locations.

the mean covariance is calculated and stored in the nonstationary covariance table.

Separate nonstationary covariance tables ares constructed for: (**1**) node to node, (**2**) data to data and (**3**) node to data mean covariance. Each table has a single column with mean covariance values $\overline{C}(v_i(\mathbf{u}_i), v_j(\mathbf{u}_j)$ cycling $i = 1, \ldots,$ number of nodes or data and $j = 1, \ldots,$ number of nodes or data within the range of correlation. This redundancy (the table will include $\overline{C}(v_i(\mathbf{u}_i), v_j(\mathbf{u}_j))$ and $\overline{C}(v_j(\mathbf{u}_j), v_i(\mathbf{u}_i)))$ increases the size of the table and the number of initial mean covariance calculations, but this method allows for the use of fast index look up. For each $i$ index location all the $j$ neighbor entries are sorted in the order of decreasing mean covariance, and the table location of each of these subsets is recorded in a separate pointer array. By applying this pointer array any subsequent search for nearest nodes and conditioning data only requires that the table is checked until maximum number of data or previously simulated nodes are found. This is faster than typical search methods, such as super block search.

A simple data set and grid are provided to illustrate the construction of a nonstationary covariance table (see Figure 6.17). The grid cells are denoted as volumes $A, B, \ldots, F$ and the conditioning data are are denoted $1, 2, \ldots, 5$. The nonstationary covariance table associated with grid nodes would be ordered $\overline{C}(A, A)$, $\overline{C}(A, B)$, $\overline{C}(A, D)$, $\overline{C}(A, E)$, $\overline{C}(A, C)$, $\overline{C}(A, F)$, $\overline{C}(A, G)$, $\overline{C}(A, H)$, $\overline{C}(A, I)$, $\overline{C}(B, B)$, $\overline{C}(B, A)$ ,$\overline{C}(B, C)$, $\overline{C}(B, E), \ldots$. This order is based on decreasing covariance and the assumption of an isotropic semivariogram model.

The nonstationary covariance table associated with conditioning data would be ordered $\overline{C}(1, 1)$, $\overline{C}(1, 4)$, $\overline{C}(1, 2)$, $\overline{C}(1, 5)$, $\overline{C}(2, 2)$, $\overline{C}(2, 3)$, $\overline{C}(2, 4)$, $\overline{C}(2, 5)$, $\overline{C}(3, 4)$, $\overline{C}(3, 1)$, $\overline{C}(3, 2)$ ,$\overline{C}(3, 5)$, $\overline{C}(4, 4), \ldots$. The nonstationary covariance table associated with conditioning data and conditioning data would be ordered $\overline{C}(A, 1)$, $\overline{C}(A, 4)$, $\overline{C}(A, 3)$, $\overline{C}(A, 2)$, $\overline{C}(A, 5)$, $\overline{C}(B, 2)$, $\overline{C}(B, 1)$, $\overline{C}(B, 3)$, $\overline{C}(B, 4)$, $\overline{C}(B, 5)$, $\overline{C}(C, 2)$ ,$\overline{C}(C, 3)$, $\overline{C}(C, 1), \ldots$. The flow chart for this subroutine is shown in Figure 6.18.

### 6.3.4 Search Considerations

While simulating irregular volumes, screening can cause extreme weights. This phenomenon was described by Xie et al. (2001)[29]. Figure 6.19 demonstrates a variety of settings which result in extreme weights.

These extreme weights may result in negative kriging variances (refer below to the kriging variance equation):

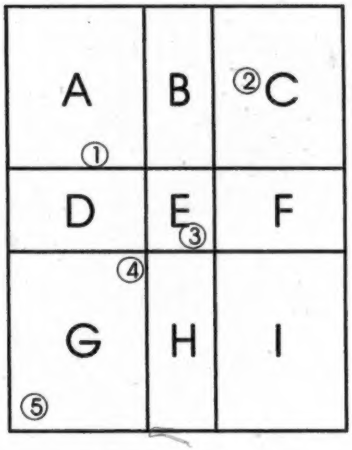

Figure 6.17: An example tartan grid and well data to demonstrate the construction of a nonstationary covariance table.

$$\sigma^2_{SK} = \overline{C}(v(\mathbf{u}), v(\mathbf{u})) - \sum_{\alpha=1}^{n} \lambda_\alpha \overline{C}(v_\alpha(\mathbf{u}_\alpha), v(\mathbf{u})) \tag{6.8}$$

Given a positive definite covariance model and correctly calculated mean covariances the resulting kriging variance should be non-negative. The cause of these negative variances is precision limitations in the solution of the kriging matrix being magnified by large weights. Extreme weights are rare when simulating directly to a regular grid. An example is illustrated (see Figure 6.20) of a tartan simulation to model with equal volumes for each cell. A realization with the same semivariogram and reference histogram but with an irregular grid is shown in Figure 6.21. This setting resulted in frequent extreme weights.

The problem of extreme weights may be addressed by (**1**) template screening, (**2**) iterative kriging and (**3**) octant search.

Template screening is based on preemptively preventing screening by rejecting any conditioning datum that is shadowed by closer data. This is accomplished by applying a shadow template. When a datum is selected to condition an unknown location a shadow template is positioned with the apex on the datum and oriented away from the unknown location. All locations within this template are set to 'unavailable' and may not be subsequently selected as conditioning data for this estimate.

Figure 6.22 shows an example application of shadow templates. The application

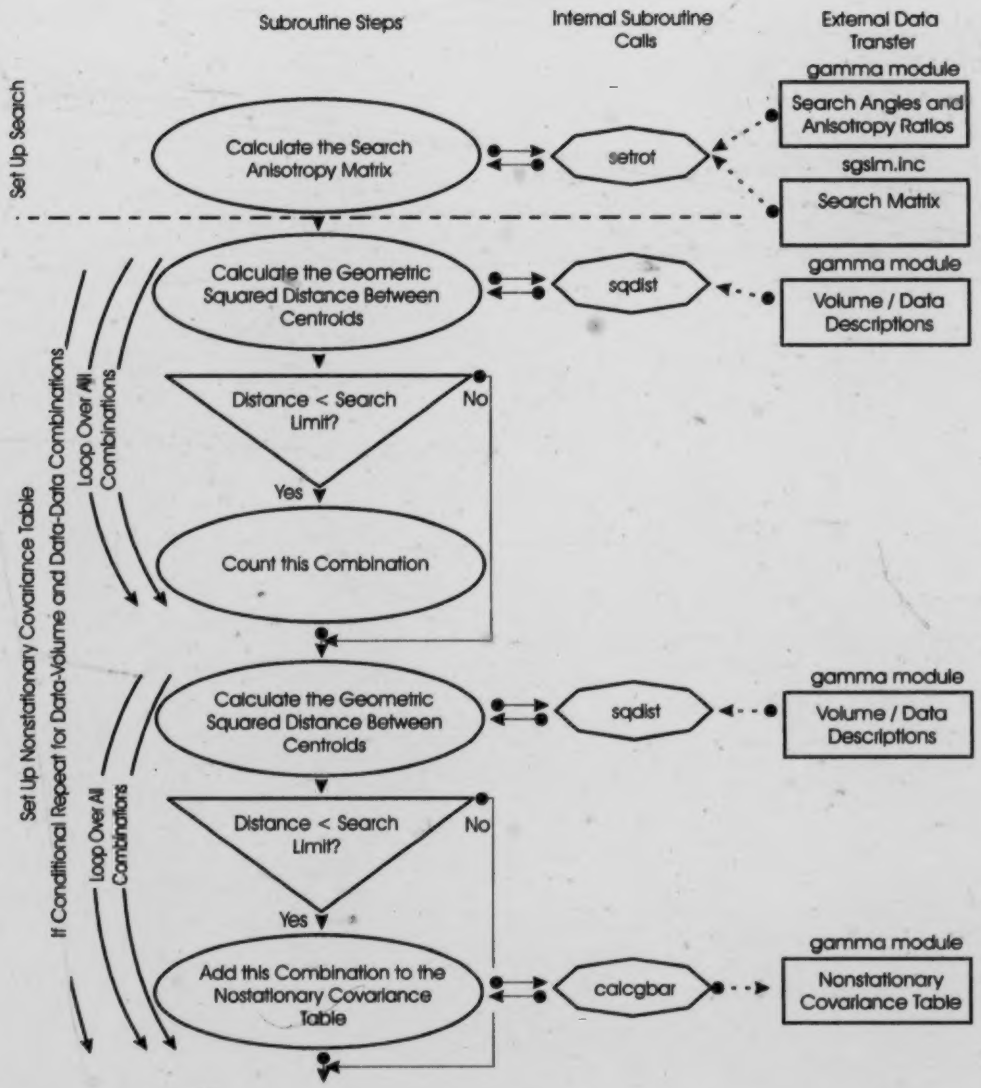
Subroutine Steps
Internal Subroutine Calls
External Data Transfer
Set Up Search
gamma module
Search Angles and Anisotropy Ratios
Calculate the Search Anisotropy Matrix
setrot
sgsim.inc
Search Matrix
Set Up Nonstationary Covariance Table
If Conditional Repeat for Data-Volume and Data-Data Combinations
Loop Over All Combinations
Calculate the Geometric Squared Distance Between Centroids
sqdist
gamma module
Volume / Data Descriptions
Distance < Search Limit?
No
Yes
Count this Combination
Loop Over All Combinations
Calculate the Geometric Squared Distance Between Centroids
sqdist
gamma module
Volume / Data Descriptions
Distance < Search Limit?
No
Yes
Add this Combination to the Nostationary Covariance Table
calcgbar
gamma module
Nonstationary Covariance Table

Figure 6.18: The `NONSTATCOVTABLE` subroutine flowchart. Mean covariances are stored for all combinations of data and volumes that are correlated with each other.

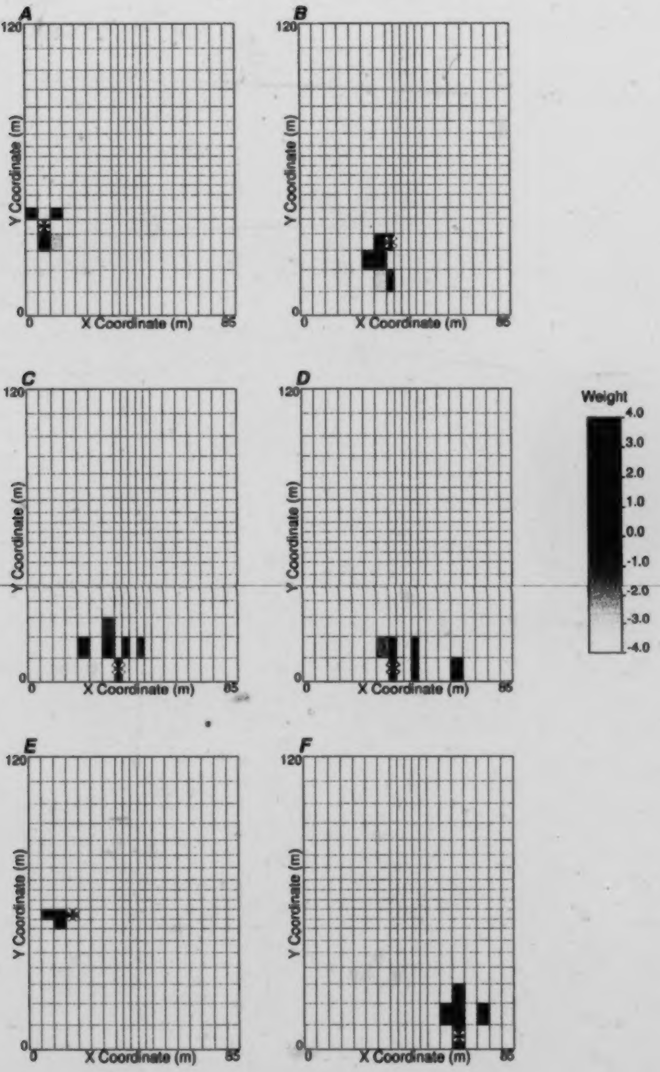

Figure 6.19: A variety of estimation settings that result in extreme weights. The estimation location coded with a weight of 0.0 and a white 'X' and the conditioning data (previously simulated nodes) are colored according to their weights.

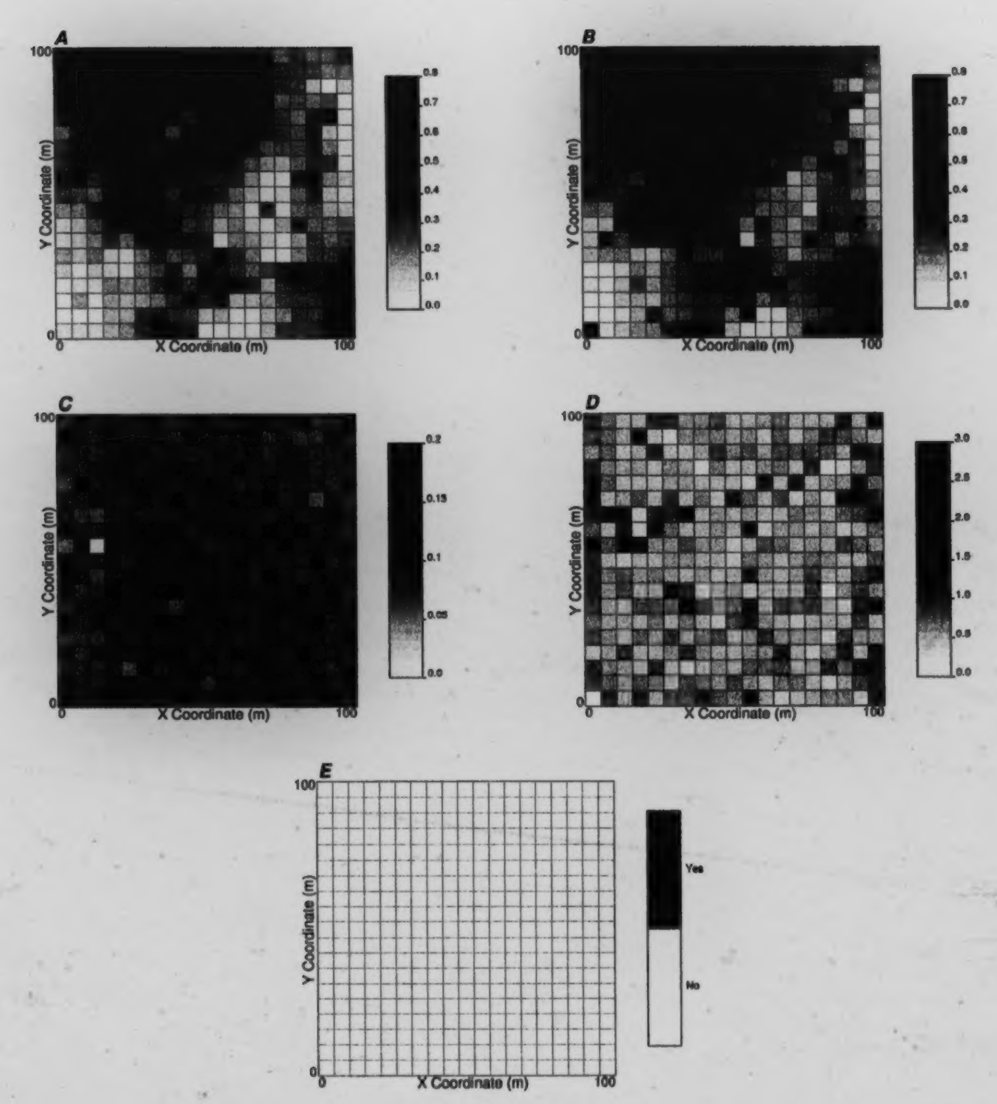

Figure 6.20: `TARTANSIM` on a regular grid with an isotropic semivariogram (spherical, range = 50) and a reference distribution: A - a simulated realization, B - e-type estimate, C - kriging standard deviation, D - maximum absolute kriging weight and E - map of negative variances. The realization appears well behaved, the local realizations are within the reference distribution and the weights and the maximum kriging weights are reasonable.

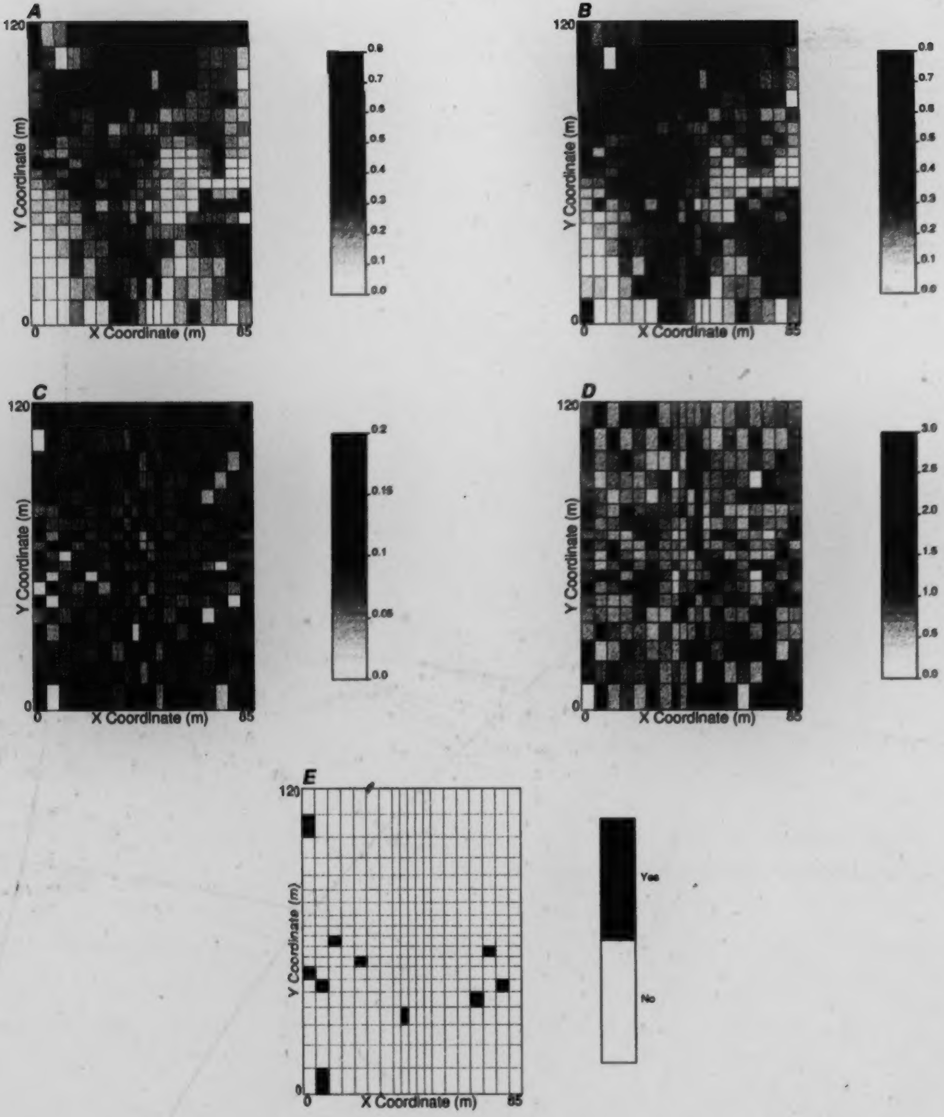

Figure 6.21: `TARTANSIM` on a irregular grid with an isotropic semivariogram (spherical, range = 50) and a reference distribution. A - the simulated realization, B - e-type estimates, C - kriging standard deviation, D - maximum absolute kriging weight and E - map of negative variances. There are many large weights and some negative variances present.

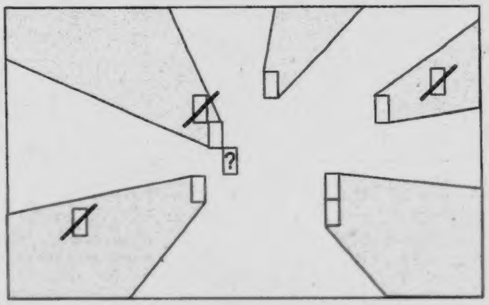

Figure 6.22: The shadow template that is applied to filter screened data. This is a 2-D example where four data have already been chosen as conditioning (rectangles). The shadow templates (grey areas) are located with their apexes on the chosen data and radiate away from the unknown location at the center square. These templates are like exaggerated shadows cast by the chosen data if the unknown location was a light source (indicated with a question mark).

of the shadow template removes screening and extreme weights. This technique is computationally expensive since trigonometric operations are required to build each shadow. In addition, this method leads to a significant increase in the level of complexity of the local data search algorithm.

In the iterative kriging method, the kriging weights are checked for large values. If an absolute weight larger than a threshold is encountered then the least correlated conditioning datum is removed and the kriging matrix is solved again. This process is iterated until all absolute weights are below the threshold. The results from this technique are shown in Figure 6.23. The frequency of negative variances is decreased as the weight threshold is decreased, although many negative variances remain with a threshold of 1.0.

This technique does not add significantly to the complexity of the current algorithm and is computationally cheap if anomalous weights are infrequent. Also, this technique is a self healing method, since the correction is only applied when required, the level of correction is tailored to the need and there is no need for parameter tweaking.

Another possible technique would be to apply the octant search method. This method is commonly applied in simulation (applied in programs such as `SGSIM` from GSLIB (Deutsch and Journel, 1998)[23]) to prevent all conditioning data from

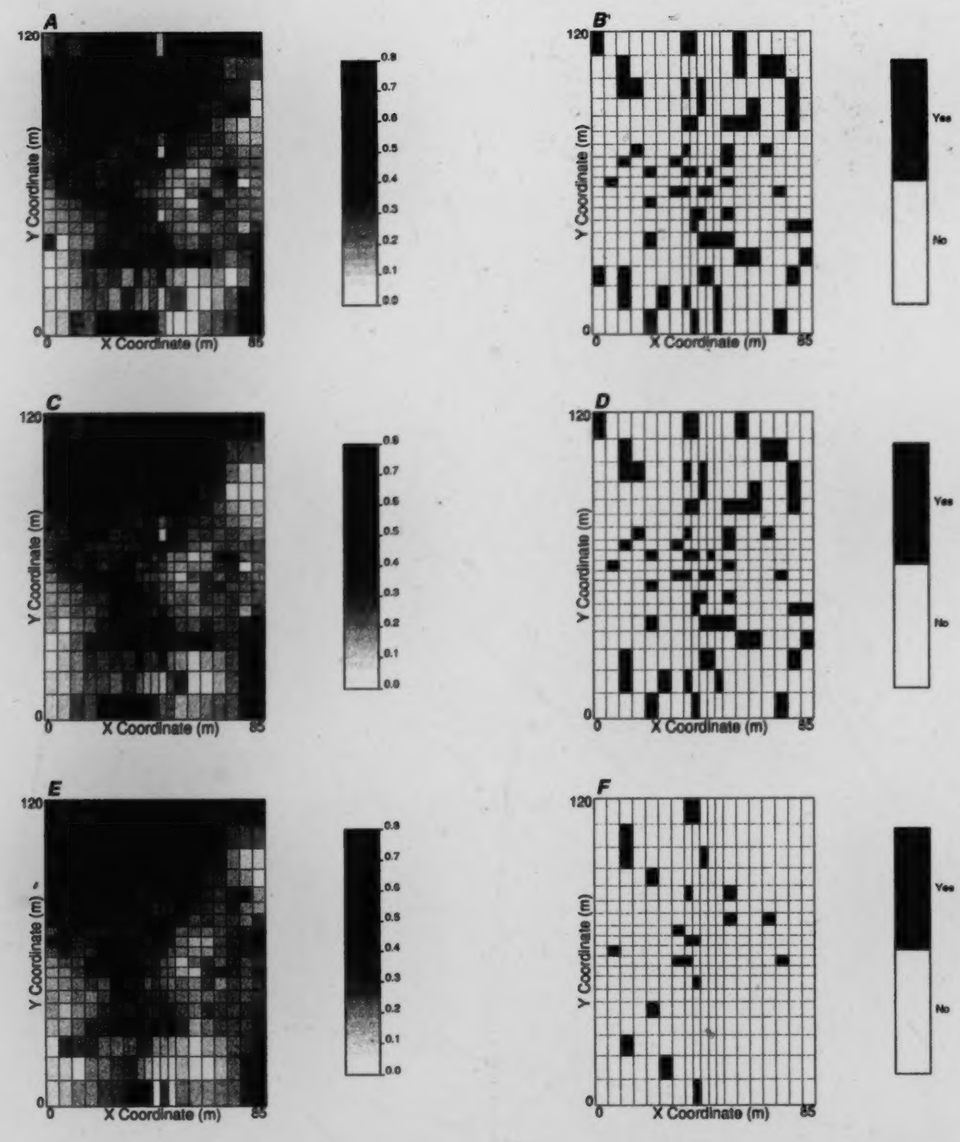

Figure 6.23: Three `TARTANSIM` realizations with the same parameters, but with different kriging weight thresholds. A and B - kriging weight threshold of 5.0: realization and locations with negative kriging variances. C and D - kriging weight threshold of 3.0: realization and locations with negative kriging variances. E and F - kriging weight threshold of 1.0: realization and locations with negative kriging variances. Decreasing the kriging weight threshold reduces the incidence of negative variances.

originating from a single well or drill hole. In this setting, screening could be avoided by only accepting the nearest conditioning data from each octant. The rationale is similar to template screening. This technique may unnecessarily limit the available conditioning.

These methods may affect the kriging estimate and the kriging variance. It is common practice in geostatistics to constrain the number of data applied to condition a local estimate or simulated realization. It is assumed that less correlated data are screened and will have reduced influence on the estimate and that the application of all available conditioning needlessly increases the computational intensity. There are other search issues related to conditional bias that are not discussed here (see McLennan and Deutsch, 2003[71]).

There are cases in which "screened" data may carry important information content. When a hole effect semivariogram is applied then the previously discussed methods are not applicable. A datum that falls in the shadow of a closer datum may actually be more correlated with the estimation or simulation location. Also, screening often results in negative weights. This allows kriging to extrapolate outside the data interval. In this case the information content of the screened datum may be significant (Deutsch and Journel, 1998)[23].

## 6.4 Applications of Simulation in Direct Space

The following are examples of applications of the methods and subroutines to simulate directly to irregular grids. The building blocks outlined in Section 6.3 have been applied in the coding of algorithms to directly simulate to regular grids `DSSIM`, tartan grids `TARTANSIM` and Voronoi grids (called atomic grids in the example) `ATOMSIM`. The following is a discussion on the `TARTANSIM` and `ATOMSIM` algorithms.

### 6.4.1 Direct Sequential Tartan Grid Simulation (TARTANSIM) with Radial Nested Grids

A Fortran program, `TARTANSIM`, is presented that performs simulation directly to tartan grids. A module is included in this algorithm to insert locally refined radial grids.

The program is based on building block subroutines discussed in Section 6.3. This section presents the general algorithm flow and provides some example output. Results are discussed and the algorithm is validated by comparison to the theoretically established block averaged sequential Gaussian simulation (`SGSIM`).

In addition to the building blocks, there have been added specific subroutines which interpret tartan and radial grids. A modified `PIXELPLT` program from GSLIB (Deutsch and Journel, 1998)[23], called `TARTANPIX` is included which is applied to visualize the resulting tartan and nested radial grid simulations. All illustrations of `TARTANSIM` output were generated with this program.

### The TARTANSIM Parameters

The `TARTANSIM` algorithm is based on `SGSIM` from the GSLIB code (Deutsch and Journel, 1998)[23]. The general flow, parameter file format and annotation have followed the same form. An example parameter file is shown below. The new parameters in addition to the standard `SGSIM` parameters are indicated by an '*'.

```
Parameters for TARTANSIM
 data.dat               -file with data
 1 2 0 6 0 0            - columns for X,Y,Z,vr,wt,sec.var.
 -100.0 1.0e21          - trimming limits
 1 500 10000            *CBAR: random samples(1-yes,0-discr.),ndis,nl
 100 100 100 3.0 1.5    *CCDF Table: nm,nv,nq,limmean,limstd
 0                      -consider ref. dist(0=no, 1=yes)
 refdist.dat            - file with ref. dist distribution
 1 0                    - columns for vr and wt
 -3.0 3.0               -zmin,zmax(tail extrapolation)
 1 -3.0                 - lower tail option,parameter
 1  3.0                 - upper tail option,parameter
 0                      -debugging level: 0,1,2,3
 tartansim.dbg          -file for debugging output
 tartansim.out          -file for tartan simulation output
 201                    -number of realizations to generate
 5 0.0 6 2 1 2 6        *tnx,originx,dx(ix),ix=1,...,nx
 5 0.0 6 2 1 2 6        *tny,originy,dy(iy),iy=1,...,ny
 1 0.5 1                *tnz,originz,dz(iz),iz=1,...,nz
 69069                  -random number seed
 0 8                    -min and max original data for sim
 12                     -number of simulated nodes to use
 1 3                    -multiple grid search (0=no, 1=yes),num
 0                      -maximum data per octant (0=not used)
 20 20 1                -maximum search radii (hmax,hmin,vert)
 0.0 0.0 0.0            -angles for search ellipsoid
 0 0.0 1.0              -ktype:0=SK,1=OK,2=LVM,3=EXDR,4=COLC
 ../data/cluster.dat    -  file with LVM,EXDR or COLC variable
```

```
1                    -  column for secondary variable
1 0.0                -nst, nugget effect
1 1.0 0.0  0.0  0.0  -it,cc,ang1,ang2,ang3
      10.0 10.0 10.0 -a_hmax,a_hmin,a_vert
```

The *CBAR* parameters are applied by the `PREGBAR` and `CALCGBAR` subroutines that deal with the calculation of mean covariances. The *randomsamp* parameter determines whether random samples are applied to calculate the mean covariance. If set to 0 then the traditional discretization method is applied. The *ndis* parameter is the number of random samples or the number of discretizations and *nl* is the number of discretizations applied to the semivariogram model. The *CCDF* parameters are applied in the `PRECDIST` program to build the ccdf lookup table for the purpose of accessing valid $Z$ space local ccdfs. The first three parameters, *nm*, *nv*, and *nq* indicate the number of descritizations used in the CCDF lookup table and the parameters *limmean*, and *limstd* control the limits of the descritization in Gaussian space. The gridding scheme applied in `TARTANSIM` is illustrated in Section 6.1.2. Unlike traditional GSLIB, the origin is set at the lower, bottom left corner of the data space. Also, note that for true 2-D realizations the thickness in the $Z$ direction should be set to 0.0 or vertical volume will be considered. For all other parameters refer to Deutsch and Journel (1998)[23].

### The Program Flow

The `PRECDIST` subroutine is called to build the ccdf look up table. Unconditional realizations must have a reference distribution. The `PREGBAR` subroutine is called to build the geometric search matrices and the semivariogram lookup table. For accurate results many ($> 1,000$) bins should be applied to the semivariogram model (see discussion in Section 6.2.2).

A subroutine unique to `TARTANSIM`, called `TARTANINTERPRET`, is called next. It translates the tartan grid parameters into a table with block information for each node in the model. This information includes the extents in x,y,z directions and the center location. These parameters are illustrated in Figure 6.5. Next, the nonstationary covariance table is constructed.

During simulation and at each location the `MATRIXBUILD` subroutine searches the nonstationary covariance tables and builds the kriging matrix in the format required by the standard GSLIB matrix solution subroutine, `KSOL` (Deutsch and Journel, 1998)[23]. If there any weights above a threshold (hard coded as +/-1.5) then the associated data is removed and the kriging is repeated.

For each location the local ccdf is calculated with the `GETCDIST` subroutine given the calculated kriging mean and variance and Monte Carlo drawing is applied as usual. In this manner all nodes are visited randomly.

### Computational Intensity of `TARTANSIM`

All of the computationally intensive steps are completed prior to simulation. The ccdf lookup table is calculated and indexed for a super block search, and all the mean covariances are stored in indexed tables with pointer arrays. This computational effort required for this initial setup is a function of the grid size, the search range, and the level of discretization applied to the ccdf table and the mean covariance calculations. During simulation the only significant calculation is the solving of the kriging matrix. In the following example, the first realization of block averaged `SGSIM` required less than a seconds while the `TARTANSIM` equivalent required ten seconds (on a Pentium III, 1.5 GHz). For a suite of 101 realizations `TARTANSIM` requires twenty seconds whiles block averaged `SGSIM` requires 75 seconds. The additional 100 realizations from `TARTANSIM` require only ten seconds! The following should be considered.

1. The speed advantage becomes more pronounced when the number of realizations is increased. For example, 1001 realizations would require about 1 minute for `TARTANSIM` and about 6 minutes for `SGSIM`.
2. The smallest tartan grid node decreases. Then a finer grid would be required for scale up.

Nevertheless, the speed advantage for the calculation of many realizations may be a moot point. Modern geostatistical studies account for uncertainty in the model parameters and do not only rely solely on ergodic fluctuations for a measure of uncertainty. In this case only one or a few realizations for each parameter set will be calculated and direct simulation may be at a disadvantage.

### Unconditional Example

Unconditional simulations generated by `SGSIM` and `TARTANSIM` were compared (see Figures 6.24 and 6.25). The `SGSIM` realizations were simulated on a 100 × 100 grid and then block averaged to a 15 × 15 tartan grid. The semivariogram was set as a single isotropic spherical structure with a range equal to $\frac{1}{5}$ of the size of the model.

The covariance between adjacent blocks was checked. The actual mean covariance calculated with the semivariogram model was compared to the empirical covariance between adjacent blocks over 201 realizations. Also, the empirical covariance of `TARTANSIM` and `SGSIM` were compared (see Figure 6.26). In this example the covariance are similar between `TARTANSIM` and `SGSIM` and in general the actual covariance is reproduced.

### Conditioned Example

The *cluster.dat* 2-D data set (from Deutsch and Journel, 1997 [23]) was applied as conditioning. The Gaussian transformation was applied to remove heteroscedasticity and no declustering was applied. See Figure 6.27 for the distribution and location map of the transformed data set.

201 realizations where generated with `SGSIM` with 100 × 100 cells. These realizations were block averaged to a tartan grid (see Figure 6.28 for some example realizations). The same conditioning data were used in `TARTANSIM` for simulation directly to the tartan grid (see Figure 6.29 for some example realizations).

The e-type estimate (the expected value of multiple local realizations) was calculated over the 201 realizations for both `TARTANSIM` and block averaged `SGSIM` results (see Figure 6.30). The e-type maps indicate that the conditional means from `TARTANSIM` are similar to the `SGSIM` results.

Some example local distributions of uncertainty were compared (see Figure 6.30). The local distributions of uncertainty generated with `TARTANSIM` are very similar to the `SGSIM` distributions. The covariance between adjacent blocks was once again checked (see Figure 6.32). The `TARTANSIM` results closely agree with the `SGSIM` results.

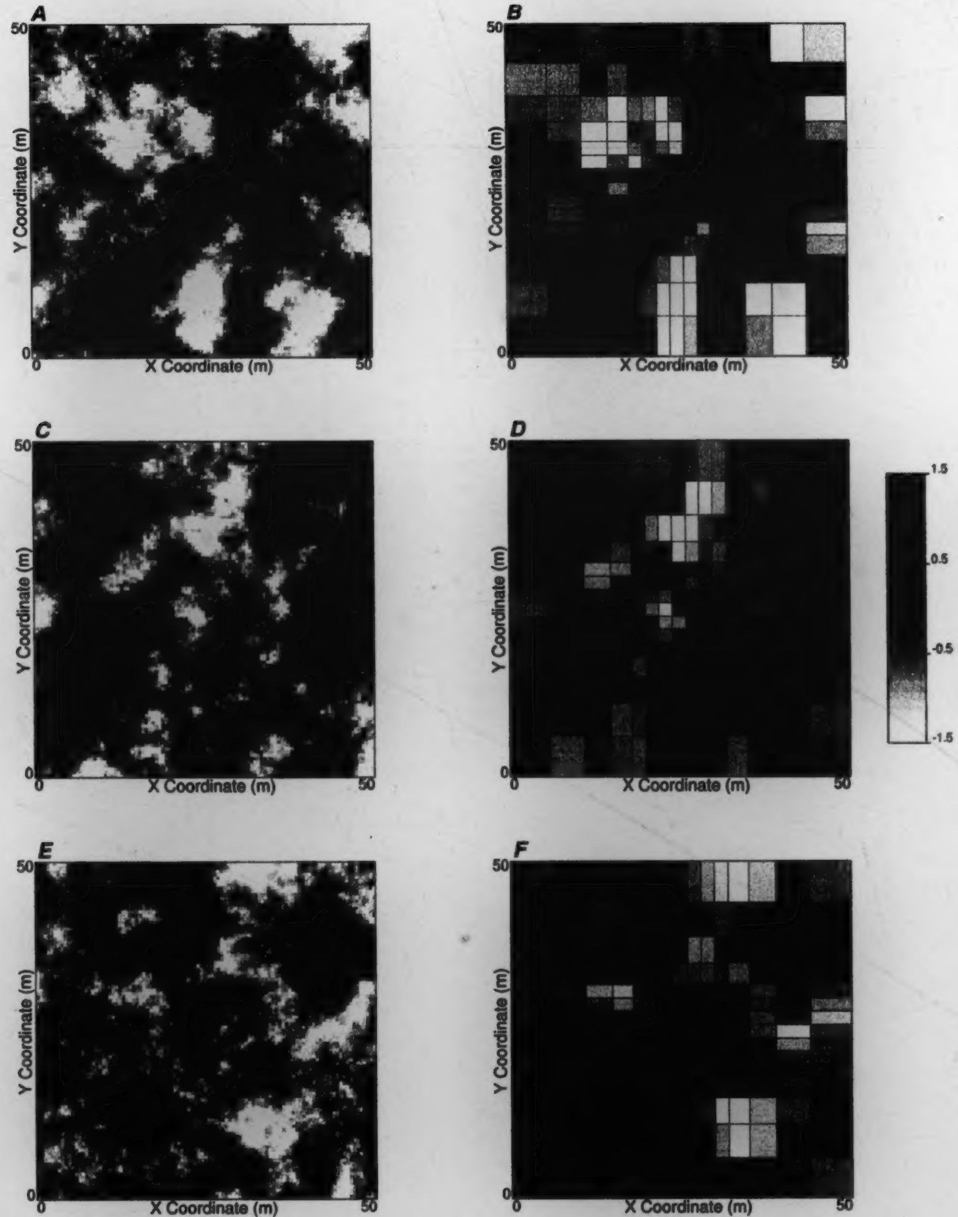

Figure 6.24: Example unconditional SGSIM realizations and the associated block averaged results. A and B - first realization and block averaged results, C and D - second realization and block averaged results and E and F - third realization and block averaged results.

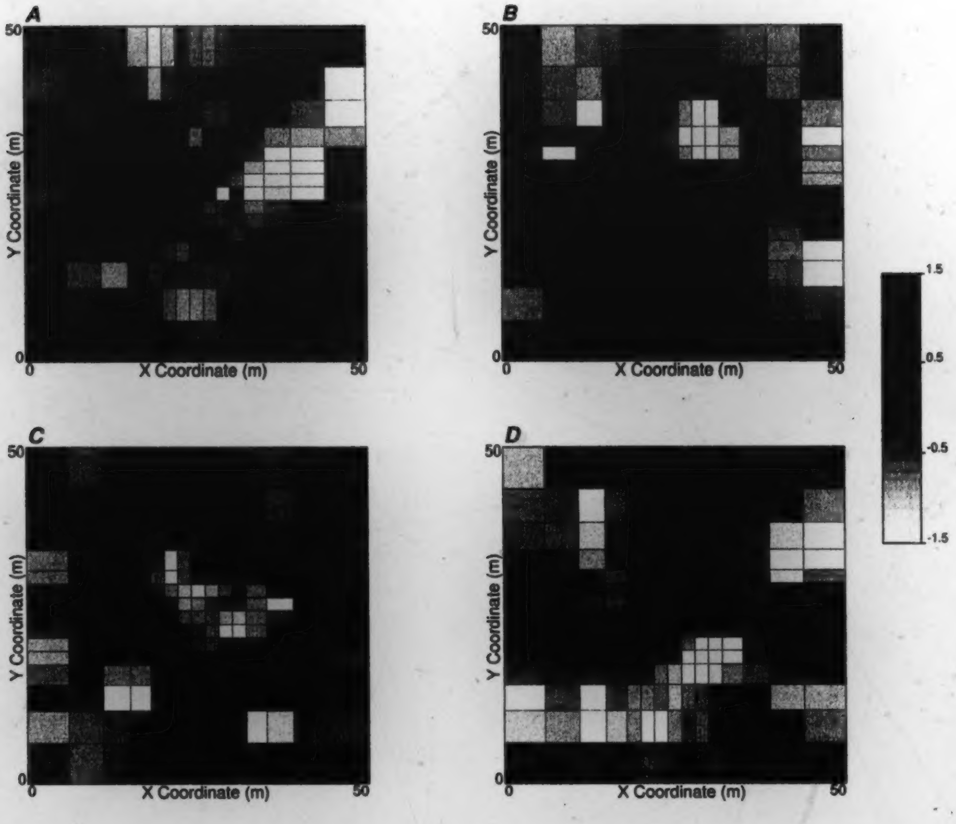

Figure 6.25: Example unconditional `TARTANSIM` realizations: A - first realization, B - second realization, C - third realization and D - fourth realization.

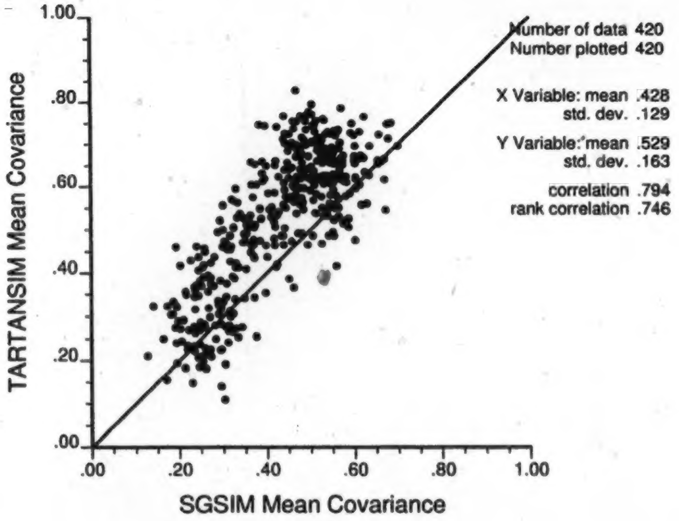

Figure 6.26: Scatter plots of the covariance for `TARTANSIM` and block averaged `SGSIM` for the unconditional case.

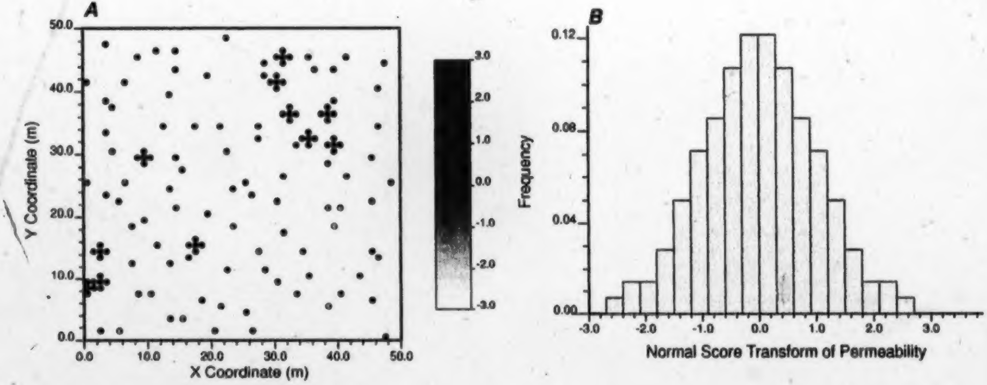

Figure 6.27: The data locations and Gaussian transformed distribution. A - location map and B - distribution. Values are normal score transform of permeability.

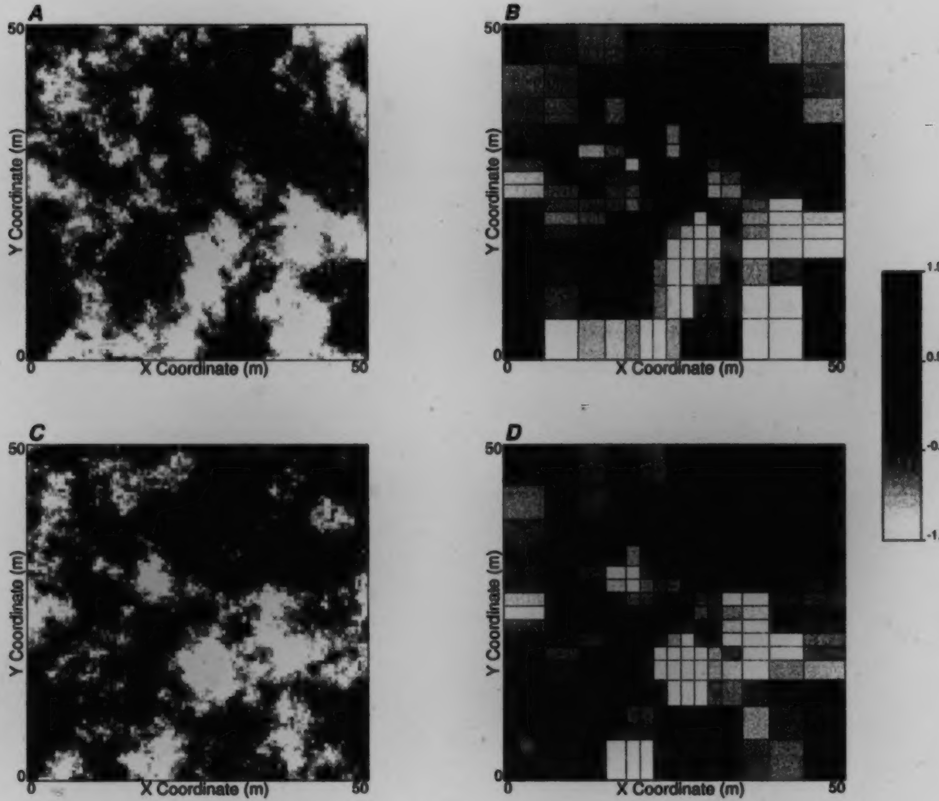

Figure 6.28: Example unconditional SGSIM realizations and the associated block averaged results. A and B - first realization and block averaged results and C and D - second realization and block averaged results.

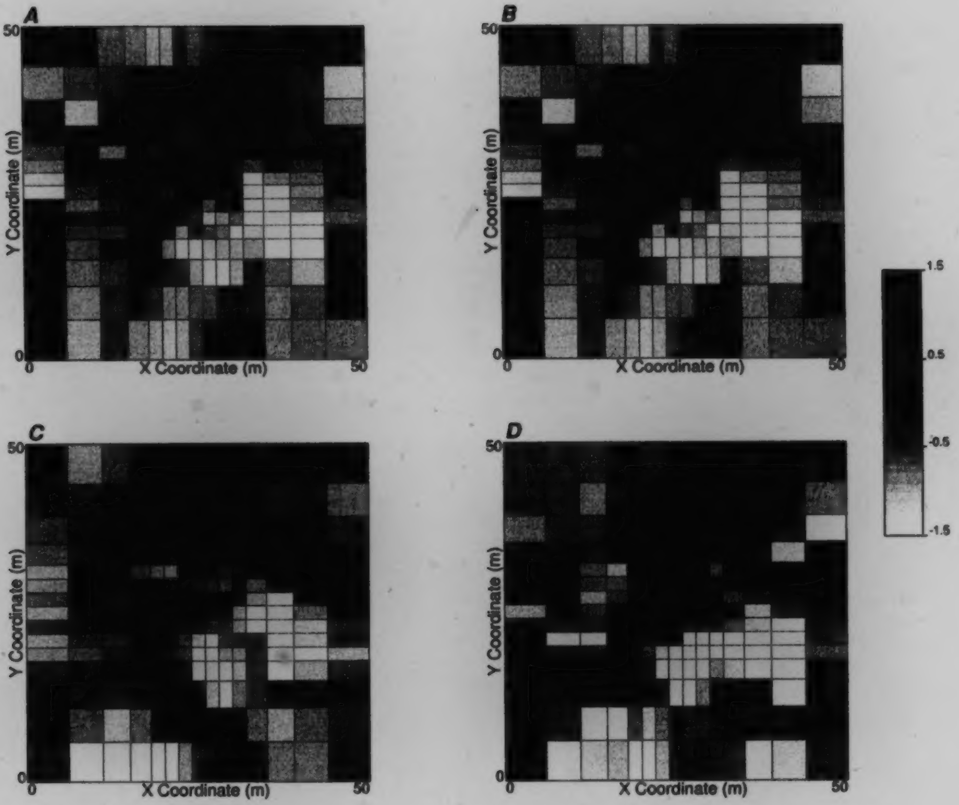

Figure 6.29: Example unconditional `TARTANSIM` realizations: A - first realization, B - second realization, C - third realization and D - fourth realization.

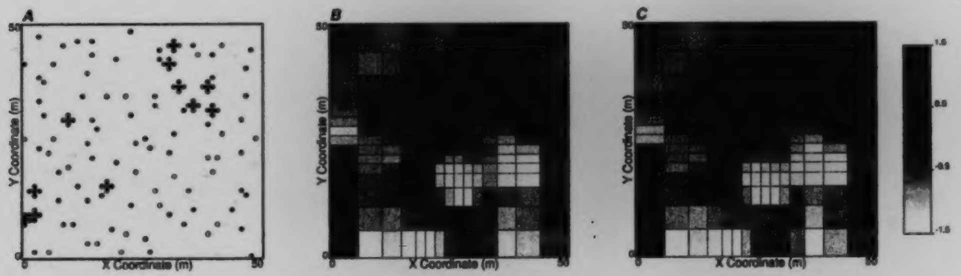

Figure 6.30: E- type estimated: A - the conditioning data locations and the e-type estimates over 201 realizations for both B - `TARTANSIM` and C - block averaged `SGSIM`.

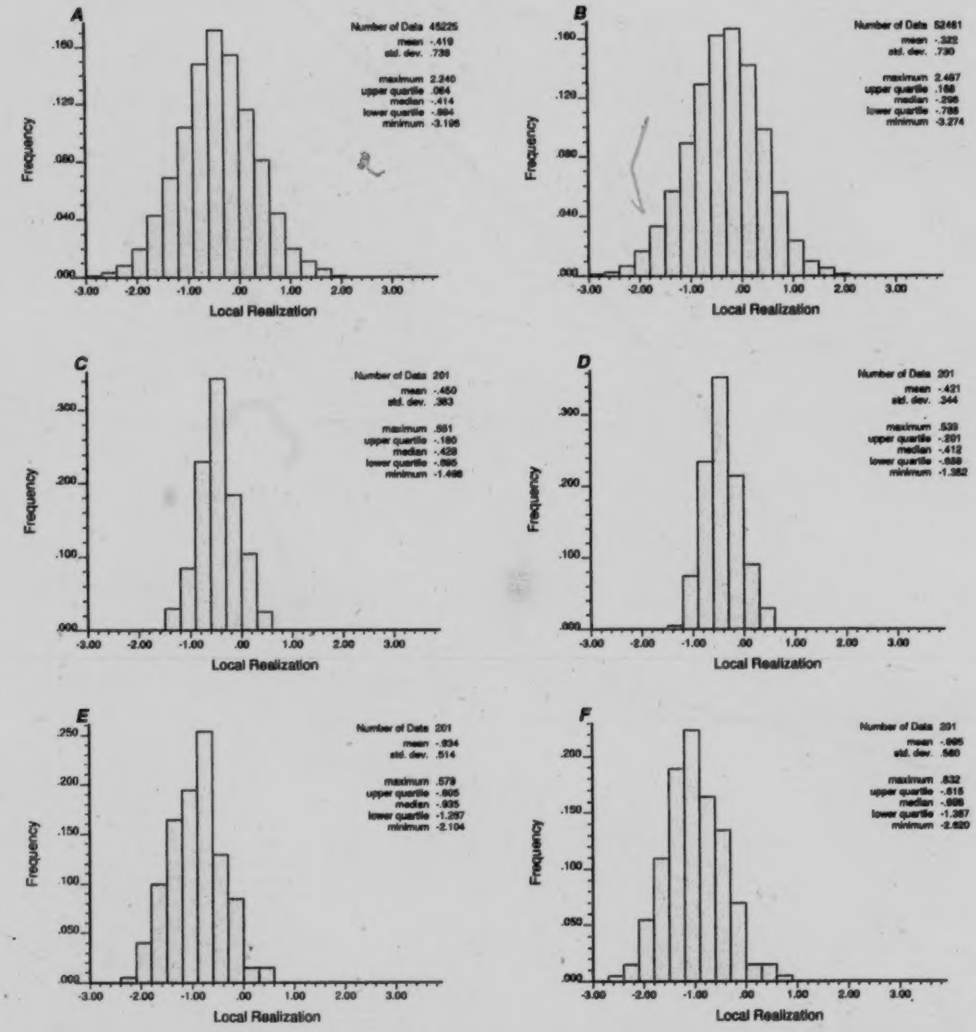

Figure 6.31: Three example local distributions of uncertainty compared between `SGSIM` block averaged and `TARTANSIM`. A and B - `SGSIM` block averaged and `TARTANSIM` distributions for first location, C and D - `SGSIM` block averaged and `TARTANSIM` distributions for second location and E and F - `SGSIM` block averaged and `TARTANSIM` distributions for third location.

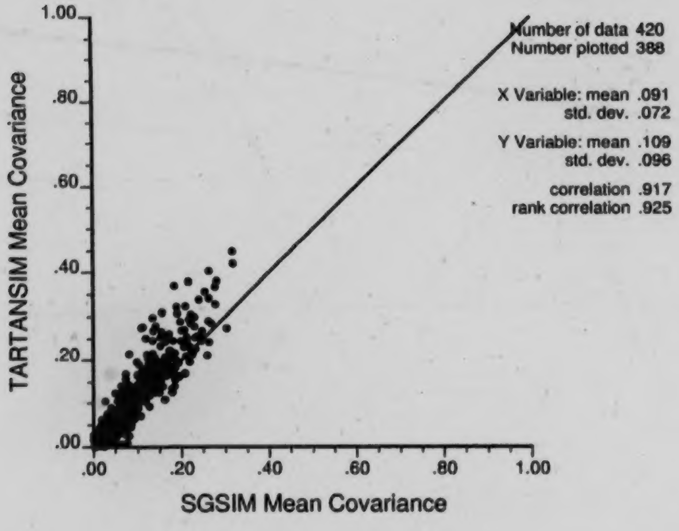

Figure 6.32: Scatter plots of the covariance for TARTANSIM and block averaged SGSIM for the conditional case.

### Radial Nested Grids

A module is included with TARTANSIM for the simulation of radial nested grids. The gird parameters and format are illustrated in Figure 6.33. Activation of this module requires the addition of a line at the end of the parameter file with a 1, the number of radial grids and the list of indexes where the radial grids will be placed. The radial grids are simulated after the tartan grid has been simulated. Only the simulated value for the coincidental tartan grid block is retained as conditioning. The method for simulation is similar to that of TARTANSIM. An adapted nonstationary covariance table subroutine called RADIALNONSTATCOVTABLE, and a matrix building subroutine called RADIALMATRIXBUILD is used. Since all the mean covariances are precalculated and stored in a 2-D matrix the search and construction of the kriging matrices is very rapid. An example with the previous conditioned data set and 6 nested radial grids is shown in Figure 6.34. It may be relevant to also consider the simulated values for adjacent nodes in the tartan grid as conditioning.

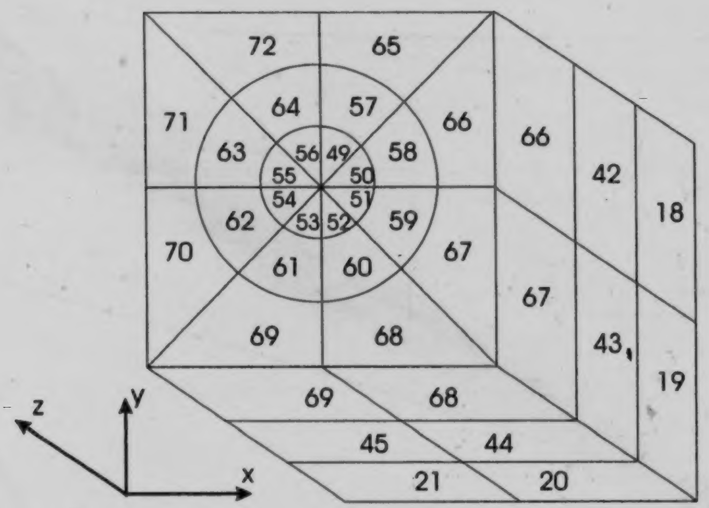
72
65
71
64
57
66
63
56
49
58
55
50
54
51
62
53
52
59
70
61
60
67
69
68
66
42
18
67
43
19
69
68
45
44
21
20
z
y
x

Figure 6.33: The nested radial grid format. The index proceeds first by sectors, then by tracks, and then by levels. The index begins at $Y$ axis and moves clockwise, the tracks begin on the inside and move outward and the levels begin at the bottom and move upwards.

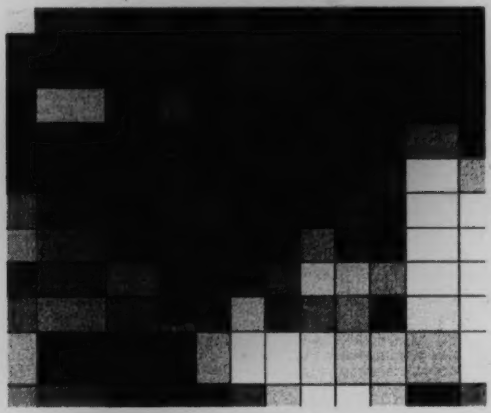

Figure 6.34: Example conditioned `TARTANSIM` realization with six nested radial grids. The same tartan grid realization from Figure 6.29 is used. The figure is cropped to improve visibility of the nested radial grids.

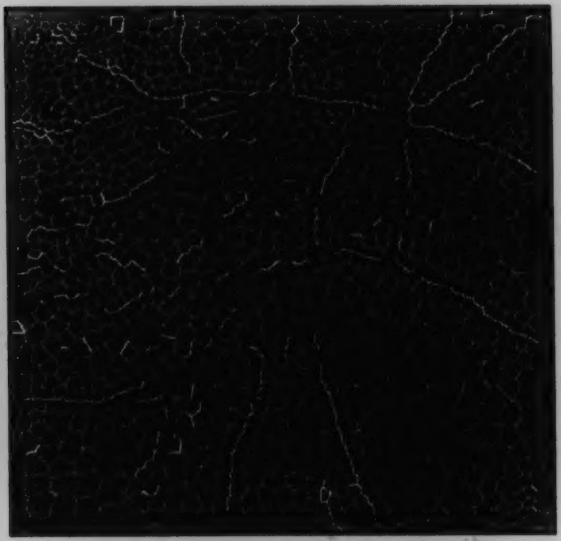

Figure 6.35: An atomic grid provided by D. Hale, Landmark Graphics (2002)[46].

**Remarks on `TARTANSIM`**

This section has demonstrated the viability and efficiency of direct simulation to irregular grids. `DSSIM` with nonstationary covariance tables and ccdf look up tables has been shown to be robust, and to calculate results comparable to the theoretically established `SGSIM` algorithm.

### 6.4.2 Atomic Grid Example

An atomic grid generated to account for geophysical data and engineering constraints including mapped faults is shown in Figure 6.35(courtesy of D. Hale, Landmark Graphics)[46]. The problem of populating the grid will be considered.

A simplified dataset was generated by constructing Voronoi polygons from the provided point coordinates (1603 nodes with locations from 0 to 255 in both $X$ and $Y$ directions).

The largest polygon is about 50 times larger than the smallest polygon. Assuming constant variability within the polygons would be an error. One approach would be to simulate a fine scale Cartesian mesh and upscale. A grid of about $10^5$ cells would be required to ensure that nine simulated values are in the smallest grid cell (Assume $3 \times 3$ discretizations required in the minimum cell size of 2.6, if the

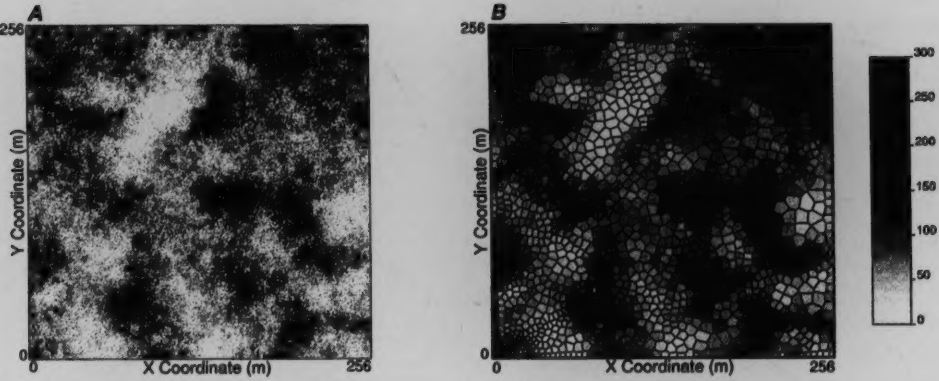

Figure 6.36: A - a fine scale simulation for upscaling to the atomic grid. B - this fine mesh realization is averaged within the Voronoi polygons to yield the upscaled realization.

cell is nearly square then it is 1.6 × 1.6 length units in size. Thus we would need 3 nodes in 1.6 length units, or about a 500 × 500 discretization). This is two orders of magnitude more than 1603 and it would be inefficient and cumbersome to deal with the fine grids and the required upscaling. A 256 × 256 simulation of a regular Cartesian grid is shown below in Figure 6.36 for demonstration. A finer grid would be required in practice.

A realization was generated with a point-scale lognormal distribution of permeability (mean of 100 mD and standard deviation of 100 mD) and a spherical semivariogram model with a range of 64 units. The point and block scale histogram are shown in Figure 6.37. The minimum block value is twice the minimum point value, the maximum block value is one half the maximum point value and the variance has decreased by more than 25%.

## Methodology and Results

The direct simulation of the Voronoi mesh could be undertaken sequentially with `DSSIM` or all at once with a matrix method. A sequential formalism is often used because it permits very large grids, but given the relatively small size of this grid a matrix method is considered (see for example `LUSIM` in Deutsch and Journel, 1998[23]). There are $n = 1603$ blocks of different size to assign. The $n \times n$ covariance matrix of average covariance between the grid blocks is required (see Equation 2.22).

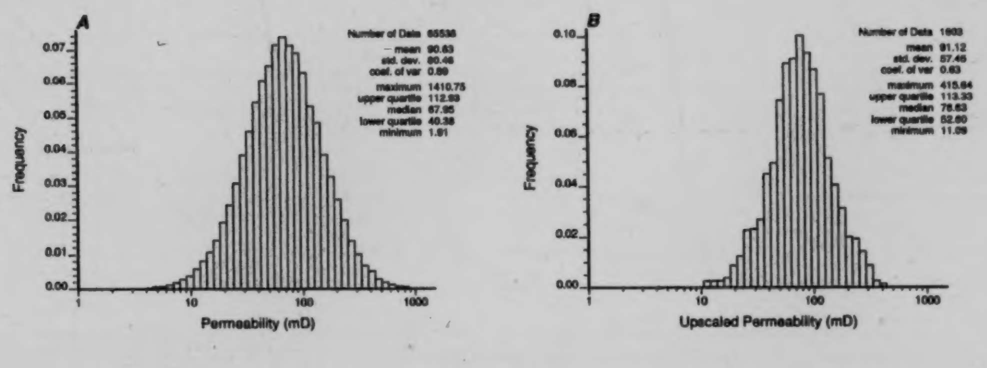

Figure 6.37: The distributions at the support size of A - the fine regular grid and B - the Voronoi grid. The precise relationship between the point and block values depends on the block scale and on the semivariogram.

These can be calculated once by applying the speed enhancements described in Section 6.2.2. Then simulation comes down to inverting this $n \times n$ covariance matrix, generating random vectors, and simple multiplication. Conditioning data (wells, seismic, production and other types of conditioning) add to the size of the matrix, but we can integrate that data in one step. The covariance between all grids (1603 × 1603) was calculated. This was accomplished by applying the same level of discretization applied in the previous upscaled method. The `LUSIM` matrix simulation algorithm (Deutsch and Journel, 1998) was modified to load the grid node covariance table directly. A single realization was generated in just over a minute (see Figure 6.38). Additional realizations were generated in a couple seconds each.

## 6.5 Discussion

The application of irregular grids improves the ability of geostatistical models to represent geologic heterogeneity. Simulation directly to irregular grids may be more computationally efficient than upscaling from fine, regular grids, but most importantly it allows for improved integration of data of different support sizes.

The building blocks include efficient subroutines for the simulation directly to irregular grids. The construction of semivariogram tables and nonstationary covariance tables increase the initial computational intensity, but allow for the efficient calculation of multiple realizations. The construction of a ccdf lookup tables al-

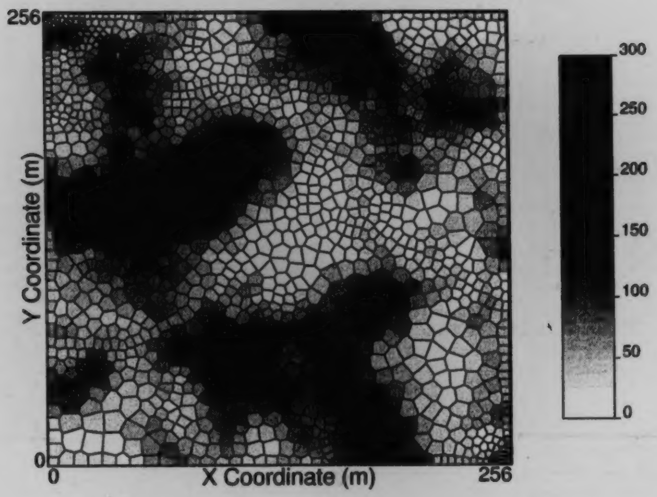

Figure 6.38: A direct simulation based on the LUSIM matrix method.

lows for the efficient calculation of local distributions of uncertainty that allow for reproduction of the global histogram.

The building blocks were demonstrated with sequential simulation to a tartan grid and `LUSIM` applied to an atomic grids. These building blocks may be readily adapted into current simulation algorithms such those included in GSLIB.

# Chapter 7

# Concluding Remarks

Stochastic simulation is used to construct reservoir models that capture small scale heterogeneity and provide an assessment of uncertainty. Current stochastic modeling algorithms lack the flexibility to integrate the diverse range of available geologic information. The available information is specific to the depositional environment and systems tract and may include, internal and external geometries and interrelationships of architectural elements including associations and stacking patterns. Methodologies have been developed for the construction of improved stochastic fluvial and deepwater reservoir models and training images with improved integration of this information.

## 7.1 Summary

The goal of this thesis is to develop a variety of tools to improve the integration of geologic information in geostatistical models. The original contributions of this dissertation include; (**1**) the advanced development and implementation of surface based simulation, (**2**) the development of building blocks for streamline based models, (**3**) the development of methodologies for the construction of hierarchical trend models, (**4**) the development of building block subroutines for the efficient simulation directly to irregular grids and (**5**) the construction of a flexible training image library for fluvial and deepwater reservoirs.

### 7.1.1 Surface Based Simulation

Surface based simulation has been advanced in Section 4.3 of this dissertation. The techniques and algorithms developed in this dissertation may be applied to construct conditional surface based models for strataform sediments with gradational, erosional and missing well data contacts (see Section 4.4). In addition, a surface based simulation algorithm tailored to distal turbidite lobes is developed in Section 4.5. This algorithm accounts for the geometry and stacking pattern of small scale turbidite flow event deposits within turbidite lobes.

### 7.1.2 Streamline Based Simulation

Streamline based simulation was introduced for fluvial reservoir models in Section 3.2 and extended to deepwater reservoir training images in Section 5.3.1. This technique is based on the characterization of architectural elements in these depositional settings by primary flow axes. This technique allows for the reproduction of complicated geologic features efficiently and with simple parametrization. The flexibility of this building block approach allows for the construction of realistic fluvial and deepwater reservoir models (see Sections 3.3.3 and 5.3.1 respectively). The resulting models may be updated to honor well conditioning in an efficient manner (see Section 3.4).

### 7.1.3 Hierarchical Trend Models

Hierarchical trend models provides an intuitive method for integrating a variety of geologic information related to the hierarchy of trends in reservoir properties in characteristic depositional directions (see Section 4.2). Geologists may quantify these trends with trend functions and combine these trends in composite trend models. A smooth correction method has been demonstrated to correct hierarchical trend models to honor large scale areal and vertical trends in reservoir properties (see Section 4.2.2).

### 7.1.4 Building Blocks for Direct Simulation to Irregular Grids

A set of building blocks have been developed for the direct simulation to irregular grids in Section 6.3. Irregular grids allow for flexible characterization of geologic heterogeneity. The application of these building blocks may provide a computational advantage over traditional methods of simulation to a small scale regular grid and scaling up. Perhaps of greater importance, these building blocks apply procedures required to account directly for data and model support size. This allows for the direct integration of geologic information data sources with a variety of support sizes.

### 7.1.5 Training Images

A suite of training images and algorithms for the dynamic construction of training images have been developed in Sections 5.2 and 5.3.2, respectively. In addition, algorithms for the customization of training images and the calculation of statistics such as transition probabilities and n-point histograms are provided (see Section 5.4). The training images are based on stochastic models that integrate a variety of geologic information in the geometry and interrelationships of architectural elements. These training images may be applied in training image based geostatistics and flow studies to improve decision making (see Section 5.5).

### 7.1.6 Implementation

These developments have been presented in a variety of peer reviewed and conference publications during this Ph.D (Deutsch et al., 2002, Pyrcz and Deutsch, 2001, Pyrcz and Deutsch, 2003, Pyrcz and Deutsch, 2004a, Pyrcz and Deutsch, 2004b, Pyrcz and Deutsch, 2004c, Pyrcz and Deutsch, 2004d, Pyrcz and Deutsch, 2004e, Pyrcz and Deutsch, 2004f, Pyrcz et al., 2004)[24, 95, 96, 97, 98, 99, 100, 101, 102, 103] There has been a strong interest in the oil and gas industry in the application of these methodologies. Specific interest has been generated among developers of offshore reservoirs in fluvial and turbidite settings with: (**1**) sparse data, (**2**) high cost associated with the collection of additional data, (**3**) complicated geologic features that are not well captured with traditional geostatistical models and (**4**) analog information with regard to geologic features. In this situation the integration of additional geologic data is a particularly valuable tool for improved geostatistical models.

## 7.2 Future Work

There is a variety of additional work that may be considered in the development of geostatistical techniques that allow for the improved integration of geologic infor-

6

mation. The following are some ideas for future research.

### 7.2.1 Additional Depositional Settings

Additional depositional settings may be addressed. This dissertation focused on fluvial and deepwater systems. The former has been a favorite target of geostatistical research and the latter has recently received attention. Carbonates represent a significant source of hydrocarbon production. Deltaic, eolian, lacustrine, estuary and coastal environments also represent significant reservoir targets. These depositional settings are the product of well understood depositional processes that result in predictable geometries and interrelationships that may be explicitly accounted for in stochastic models. Geostatistical methodologies should be developed to account for information specific to these depositional settings.

### 7.2.2 Diagenesis

Diagenesis is not addressed by the techniques presented in this dissertation. This dissertation has focused on reservoir heterogeneity as a function of sedimentary processes. Diagenesis may significantly alter reservoir heterogeneity after sedimentation. Future work is required to account for the impact diagenesis on reservoir heterogeneity. Diagenetic processes should be quantified and integrated into stochastic reservoir models.

### 7.2.3 Trend Models

There is a paucity of information available in the geostatistical literature on the construction and implementation of trend models in geostatistical models. Limited discussion is available in Deutsch (2003), Deutsch and Journel (1998) and Leuangthong and Deutsch (2003)[22, 23, 62]. Some issues require further elicitation, such as (**1**) methods for constructing 3-D trends from areal and vertical trends, (**2**) the application of the semivariogram of the variable or the residual and (**3**) the integration of soft analog information in trend models and the resulting stochastic nature of the trend models (as proposed in Section 4.5.2).

The hierarchical trend model technique developed and demonstrated in this dissertation allows for the construction of trend models based on characteristic depositional trends for a variety of hierarchies and depositional directions (see Section 4.2).

Qualitative information on trends in a variety of depositional settings is published by authors such as Allen and Allen (1990), Galloway and Hobday (1996), Miall (2000), Reading (1996) and Walker and James (1992)[2, 39, 74, 104, 136].

A compiled library of quantified trend functions is required. This library of trends functions on various case studies and available models of the depositional processes would be a valuable tool for the construction trend of models. It should include approximate trend shapes and strengths in principle depositional directions for a variety of systems tracts, depositional settings and associated hierarchies of architectural elements.

### 7.2.4 Improved Conditioning

Further research is required to develop flexible and conditional stochastic models. The constraint of conditioning well data reduced the flexibility of the turbidite surface based simulation model (see Section 4.5). Methodologies for conditioning streamline based simulations are demonstrated (see Section 3.4). Further development is required to construct robust algorithms for conditioning streamline based models to a variety of architectural elements identified at along wells.

Methods to directly honor well data are often overly complicated and ad hoc while attempts to constrain the initial and boundary conditions of forward modeling do not hold much promise given the chaotic nature of dynamical problems. Two methods that have great flexibility for conditioning are simulated annealing (Deutsch, 1992)[19] and multiple point geostatistics (Strebelle, 2002)[21].

With the increased computational power available, it may be time to resurrect simulated annealing (Deutsch, 1992)[19]. Simulated annealing has the ability to reproduce a variety of two point and multiple point statistics and interactions between lithofacies (transition matrices) and architectural elements through attraction and repulsion functions while reproducing conditioning data. It would be beneficial to develop a suite of programs and functions for simulation of a variety of geologic settings with simulated annealing.

Multiple point geostatistics has recently been advanced and applied to reservoir studies (Strebelle et al., 2002)[122]. This method has the ability to reproduce nonlinear features from training images. The ability to integrate information directly from training images that are constructed with all available geologic information and to honor local conditioning in an efficient manner is attractive. Future research is required to improve the ability of multiple point techniques to reproduce complicated geometries and interactions between architectural elements.

### 7.2.5 Surface Based Models

Basic methodologies for surface based simulation were introduced in Section 4.3 and tailored to the distal deepwater environment in Section 4.5. Additional depositional settings should be explored for further implementation. Also, more general algorithms may be developed with surface templates that may be easily tailored. This may be accomplished by allowing the user to input the geometry in the major and minor axis and then applying the same technique developed in Pyrcz and Deutsch (2004)[98] for the calculation of a consistent covariance table to calculate smooth surface template.

In the general surface based modeling approach (see Section 4.3) a variety of stacking patterns may be reproduced by applying probability fields for the horizontal positioning of the surface geometries. For example, a probability proportional to available accommodation will tend to a compensational stacking pattern.

Techniques should be developed for the efficient conditioning of surface based models. The current technique becomes inefficient as the ratio of areal size of candidate surface relative to data spacing increases. Also, techniques for accounting for erosion have not been developed in the conditional framework.

### 7.2.6 Implementation of Irregular Grids

Irregular grids are often based on engineering considerations or large-scale structural controls. Engineering objectives are to minimize discretization effects and improve CPU efficiency of flow simulation. Geologic objective include a desire to characterize significant geologic features. Irregular grids may be fit to subsurface heterogeneity to avoid averaging out important subsurface features and to improve CPU efficiency. Important subsurface features may be characterized stochastically. It may be necessary to construct multiple realizations of unstructured grids matched to subsurface property realizations. The efficient construction of irregular grids from stochastic realizations should be explored.

The simulation of categorical variables to irregular grids is problematic. Change of support size may require the consideration of mixtures of facies. Implementation details and work flows should be explored, since facies distributions are often required in geostatistical models to constrain property distributions.

The relative computational cost of direct sequential simulation compared with the traditional fine scale simulation and scale up should be further explored. Some general comments have been made concerning this matter in this dissertation, but it would be valuable to test CPU efficiency in a variety of realistic settings.

### 7.2.7 Application with Flow Simulation

The simulated realizations are only an intermediate step. The real concern is the response of the numerical model to flow simulation and the associated model of uncertainty. These results are the basis for reservoir development decisions. This dissertation does not address the application of transfer functions such as flow simulation. It would be valuable to apply flow simulation to assess the impact of the further integration of geologic information. If this impact is not significant in a specific setting then the additional effort may not be justified and traditional geostatistical methods may suffice.

# Bibliography

[1] A. Allaby and M. Allaby. *Dictionary of Earth Sciences.* Oxford, New York, 1999.

[2] P. A. Allen and J. R. Allen. *Basin Analysis Priciples and Applications.* Blackwell Scentific Publications, London, 1990.

[3] G. T. Bertram and N. J. Milton. Seismic stratigraphy. In D. Emery and K. J. Myers, editors, *Sequence Stratigraphy*, pages 45–60. Blackwell Science, 1996.

[4] C. M. Bishop. *Neural Networks for Pattern Recognition.* Oxford University Press, Oxford, 1995.

[5] S. Boggs. *Principles of Sedimentology and Stratigraphy.* Prentice-Hall, Toronto, 2001.

[6] A. H. Bouma. *Sedimentation of Some Flysch Deposits: a Graphical Approach to Facies Interpretation.* Elservier Publishing Company, New York, 1962.

[7] A. H. Bouma. Fine-grained , mud-rich tubidite systems; model and comparison with coarse-grained, sand-rich systems. In A. H. Bouma and C. G. Stone, editors, *Fine-grained Turbidite Systems, AAPG Memoir 72 / SEPM Special Publication No. 68*, pages 9–19. American Association of Petroleum Geologists, 2000.

[8] A. C. Brayshaw, G. W. Davis, and P. W. M. Corbett. Depositional controls on primary permeability and porosity at the bedform scale in fluvial reservoir sandstones. In P. Carling and M. R. Dawson, editors, *Advances in Fluvial Dynamics and Stratigraphy*, pages 373–394. John Wiley & Sons Ltd., 1996.

[9] C. S. Bristow and J. L. Best. Braided rivers: Perspective and problems. In *Braided Rivers*, pages 1–11, San Antonio, TX, 1993. Geologic Society of London. Special Publication 75.

[10] L. F. Brown and W. L. F. M. Mitchum. Seismic stratigraphic intepretation of depositional systems: Examples from brazilian rift pull apart basins. In C. E. Payton, editor, *Seismic Stratigraphy - Applications to Hydrocarbon Exploration, AAPG Memoir 26*, pages 213–248. American Association of Petroleum Geologists, 1977.

[11] M. Carr and M. H. Gardner. Portrait of a basin-floor fan for sandy deep-water systems, Permian Lower Bushy Canyon Formation, West Texas. In A. H. Bouma and C. G. Stone, editors, *Fine-grained Turbidite Systems, AAPG Memoir 72 / SEPM Special Publication No. 68*, pages 215–231. American Association of Petroleum Geologists, 2000.

[12] O. Catuneanu. *Sequence Stratigraphy of Clastic Systems*. Geologic Association of Canada, Edmonton, 2003.

[13] C. E. Cazzolo and B. Vigna. Cengio turbidite system, italy. In W. R. Normark and N. E. Barnes, editors, *Submarine Fans and Related Turbidite Systems*, pages 179–183. Springer-Verlag, 1985.

[14] R. Clemensten, A. R. Hurst, R. Knarud, and H. Omre. A computer program for evaluation of fluvial reservoirs. In Buller et al., editors, *North Sea Oil and Gas Reservoirs II*. Graham and Trotman, London, UK, 1990.

[15] J. D. Collinson. Alluvial sediments. In H. G. Reading, editor, *Sedimentary Environments: Processes, Facies and Stratigraphy*, pages 37–82. Blackwell Science, 1996.

[16] P. W. M. Corbett. *Reservoir Characterization of a Laminated Sediment: the Rannoch Formation, Middle Jurassic, North Sea*. PhD thesis, Heriot-Watt University, Edinburgh, UK, 1993.

[17] P. W. M. Corbett, S. Zheng, M. Pinisetti, A. Mesmari, and G. Stewart. The integration of geology and well testing for improved fluvial reservoir characterisation. In *1998 SPE International Conference and Exhibition*, Beijing, China, November 1998. Society of Petroleum Engineers.

[18] T. A. Cross and J. W. Harbaugh. Quantitative dynamic stratigraphy: A workshop, a philosophy, a methodology. In T. A. Cross, editor, *Quantitative Dynamic Stratigraphy*, pages 3–20. Prentice-Hall, 1990.

[19] C. V. Deutsch. *Annealing Techniques Applied to Reservoir Modeling and the Integration of Geological and Engineering (Well Test) Data.* PhD thesis, Stanford University, Stanford, CA, 1992.

[20] C. V. Deutsch. Fortran programs for calculating connectivity of 3-d numerical models. *Computers and Geosciences*, 24:69–76, 1998.

[21] C. V. Deutsch. *Geostatistical Reservoir Modeling.* Oxford University Press, New York, 2002.

[22] C. V. Deutsch. *Fundamental of Geostatistics: Principles and Hands on Practice Short Course.* University of Alberta, Edmonton, 2003.

[23] C. V. Deutsch and A. G. Journel. *GSLIB: Geostatistical Software Library and User's Guide.* Oxford University Press, New York, 2nd edition, 1998.

[24] C. V. Deutsch, M. J. Pyrcz, and T. T. Tran. Geostatistical assignment of reservoir properties on unstructured grids. In *2002 SPE Annual Technical Conference and Exhibition*, San Antonio, TX, October 2002. Society of Petroleum Engineers.

[25] C. V. Deutsch and T. T. Tran. Fluvsim: A program for object-based stochastic modeling of fluvial depositional systems. *Computers & Geosciences*, 28, 2002.

[26] C. V. Deutsch and T. T. Tran. Simulation of deepwater lobe geometries with object based modeling: LOBESIM. In *Report 5, Centre for Computational Geostatistics*, Edmonton, May 2003.

[27] C. V. Deutsch, T. T. Tran, and Y.-L. Xie. A preliminary report on: An approach to ensure histogram reproduction in direct sequential simulation. In *Report 3, Centre for Computational Geostatistics*, Edmonton, September 2001.

[28] C. V. Deutsch and L. Wang. Hierarchical object-based stochastic modeling of fluvial reservoirs. *Mathematical Geology*, 28(7):857–880, 1996.

[29] C. V. Deutsch, Y. Xie, and A. S. Cullick. Surface geometry and trend modeling for integration of stratigraphic data in reservoir models. In *2001 Society of Petroleum Engineers Western Regional Meeting*, Bakersfield, CA, March 2001. Society of Petroleum Engineers.

[30] C. V. Deutsch, S. Zanon, and H. Nguyen. Power-law averaging for inference of effective permeability. In *Canadian International Petroleum Conference 2002*, Calgary, Alberta, 2002. The Petroleum Society of the Canadian Institute of Mining, Metallurgy and Petroleum.

[31] J. C. DeVay, D. Risch, E. Scott, and C. Thomas. A Mississippi-sourced, Middle Miocene (M4), Fine-grained Abyssal Plain Fan Complex, Northeastern Gulf of Mexico. In A. H. Bouma and C. G. Stone, editors, *Fine-grained Turbidite Systems, AAPG Memoir 72 / SEPM Special Publication No. 68*, pages 109–118. American Association of Petroleum Geologists, 2000.

[32] M. Diaz-Molina. Geometry of lateral accretion in meander loops: Examples from the Upper Oligocene - Lower Miocene, Loranca Basin, Spain. In M. Marzo and C. Puigdefabregas, editors, *Alluvial Sedimentation - Special Publication #17*. International Association of Sedimentology, 1993.

[33] P. R. C. Dudley, D. E. Rehmer, and A. H. Bouma. Reservoir-scale characteristics of fine-grained sheet sands, Tanqua Karoo, South Africa. In *20th Annual Research Conference*. Gulf Coast Section, Society of Economic Paleontologists and Mineralogists Foundation Proceedings, 2000.

[34] D. J. Easterbrook. *Principles of Geomorphology*. McGraw-Hill, New York, 1969.

[35] D. Emery and K. J. Myers. *Sequence Stratigraphy*. Oxford Science Publications, Oxford, 1996.

[36] R. I. Ferguson. Disturbed periodic model for river meanders. *Earth Surface Processes*, 1:337–347, 1976.

[37] R. D. Flood and J. E. Damuth. Quantitative characteristics of sinuous distributary channels on the amazon deep-sea fan. *Geologic Society of American Bulletin*, 98:728–738, 1987.

[38] P. A. Forsyth. A control volume finite elemient mathod for local mesh refinement. In *10th Symposium on Reservoir Simulation*, Houston, TX, February 1989. Society of Petroleum Engineers.

[39] W. E. Galloway and D. K. Hobday. *Terrigenous Clastic Depositional Systems.* Springe, New York, 1997.

[40] F. Georgsen and H. Omre. Combining fibre processes and gaussian random functions for modeling fluvial reservoirs. In A. Soares, editor, *Geostatistics Troia 1992*, volume 2, pages 425–440. Kluwer, 1993.

[41] B. Ghosh and D. R. Lowe. The archiecture of deep-water channel complexes, Cretaceous Venado Sandstone Member, Sacramento Valley, CA. In S. A. Graham and D. R. Lowe, editors, *Advances in the Sedimentary Geology of the Great Valley Group, Sacramento Valley, CA.* Pacific Section, Society of Economic Paleontologists v. 73, 1993.

[42] J. Gleick. *Chaos Making a New Science.* Penguin Books, New York, 1987.

[43] P. Goovaerts. *Geostatistics for Natural Resources Evaluation.* Oxford University Press, New York, 1997.

[44] E. Gringarten and C. V. Deutsch. Accounting for multiple-point continuity in geostatistical modeling. In *Sixth International Geostatistics Congress*, Cape Town, September 2000.

[45] R. Gundesø and O. Egeland. SESIMIRA - a new geologic tool for 3-d modeling of heterogeneous reservoirs. In Buller et al., editors, *North Sea Oil and Gas Reservoirs II.* Graham and Trotman, London, UK, 1990.

[46] D. Hale. Atomic meshes: from seismic imaging to reservoir simulation. In *Proceedings of the 8th European Conference on the Mathematics of Oil Recovery*, Freiberg, Germany, September 2002. Institute of Mathematics.

[47] A. S. Hatløy. Numerical facies modeling combining deterministic and stochastic method. In J. M. Yarus and R. L. Chambers, editors, *Stochastic Modeling and Geostatistics: Principles, Methods, and Case Studies*, pages 109–120. AAPG Computer Applications in Geology, No. 3, 1995.

[48] R. N. Horne. *Modern Well Test Analysis. A Computer-Aided Approach.* Petroway Inc, 926 Bautista Court, Palo Alto, CA, 94303, 1995. Second Edition.

[49] K. Hove, G. Olsen, S. Nilsson, M. Tonnesen, and A. Hatløy. From stochastic geological description to production forecasting in heterogeneous layered reservoirs. In *SPE Annual Conference and Exhibition, Washington, DC*, Washington, DC, October 1992. Society of Petroleum Engineers.

[50] A. D. Howard. Modeling channel migration and floodplain sedimentation in meandering streams. In P. A. Carling and G. E. Petts, editors, *Lowland Floodplain Rivers*, pages 1–42. John Wiley and Sons, 1992.

[51] E. H. Isaaks and R. M. Srivastava. *An Introduction to Applied Geostatistics.* Oxford University Press, New York, 1989.

[52] J. L. Jensen, P. W. M. Corbett, G. E. Pickup, and P. S. Ringrose. Permeability semivariograms, geological structure and flow performance. In *Meeting of the International Association of Mathematical Geology*, Banff, October 1994.

[53] Y. Jin, D. Liu, and C. Luo. Development of daqing oil field by waterflooding. *Journel Petroleum Technology*, pages 269–274, February 1985.

[54] S. D. Johnson, F. Stephen, D. Hinds, and H. D. Wickens. Anatomy, geometry and sequence stratigraphy of basin floor to slope turbidite systems. *Sedimentology*, 48:987–1023, 2001.

[55] A. G. Journel. Direct sequential simulation. Class notes for a course in Geostatistics, 1986.

[56] A. G. Journel and F. G. Alabert. Focusing on spatial connectivity of extreme valued attributes: stochastic indicator models of reservoir heterogeneities. 1988.

[57] A. G. Journel and F. G. Alabert. Non-Gaussian data expansion in the earth sciences. *Terra Nova*, 1:123–134, 1989.

[58] A. G. Journel and C. V. Deutsch. Entropy and spatial disorder. *Mathematical Geology*, 25(3):329–355, April 1993.

[59] A. G. Journel and C. J. Huijbregts. *Mining Geostatistics.* Academic Press, New York, 1978.

[60] M. R. Leeder. *Sedimentology and Sedimentary Basins: from Turbulence to Tectonics.* Blackwell, Oxford, 1999.

[61] O. Leuangthong. *Stepwise Conditional Transformation for Multivariate Geostatistical Simulation.* PhD thesis, University of Alberta, Edmonton, 2003.

[62] O. Leuangthong and C. V. Deutsch. Stepwise conditional transformation for simulation of multiple variables. *Mathematical Geology*, 35:155–173, 2003.

[63] H. Li and C. D. White. Geostatistical models for shales in distributary channel point bars (Ferron Sandstone, Utah): From ground penetrating radar data to three-dimensional flow modeling. *American Association of Petroleum Geologists, Bulletin*, 87(12):1851–1868, 2003.

[64] J. Y. Liu. Sea floor morphology and sediment paths of the North Gulf of Mexico Deepwater. In A. H. Bouma and C. G. Stone, editors, *Fine-grained Turbidite Systems, AAPG Memoir 72 / SEPM Special Publication No. 68*, pages 33–45. American Association of Petroleum Geologists, 2000.

[65] S. Lopez, A. Galli, and I. Cojan. Fluvial meandering channelized reservoirs: a stochastic and process-base approach. In *2001 Annual Conference of the IAMG*, Cancun, Mexico, September 2001. Society of Petroleum Engineers.

[66] G. Lyall and C. V. Deutsch. Geostatistical modeling of multiple variables in presence of complex trends and mineralogical constraints. In *Sixth International Geostatistics Congress*, Cape Town, September 2000.

[67] A. C. MacDonald and J. O. Aasen. A prototype procedure for stochastic modeling. In J. M. Yarus and R. L. Chambers, editors, *Stochastic Modeling and Geostatistics: Principles, Methods, and Case Studies*, pages 91–108. AAPG Computer Applications in Geology, No. 3, 1995.

[68] G. Matheron. *Random Sets and Integral Geometry.* John Wiley and Sons Co., New York, 1975.

[69] G. Matheron. *Estimating and Choosing: An Essay on Probability in Practice.* Springer-Verlag, New York, 1989.

[70] G. Matheron, H. Beucher, H. de Fouquet, A. Galli, D. Guerillot, and C. Ravenne. Conditional simulation of the geometry of fluvio-deltaic reservoirs. SPE paper # 16753, 1987.

[71] J. A. McLennan and C. V. Deutsch. Conditional bias of geostatistical simulation for estimation of recoverable reserves. *CIM Bulletin*, May 2003.

[72] A. D. Miall. Architectural-element analysis: a new method of facies analysis applied to fluvial deposits. *Earth Sciences Review*, 22:261–308, 1985.

[73] A. D. Miall. *The Geology of Fluvial Deposits.* Springer, New York, 1996.

[74] A. D. Miall. *Principles of Sedimentary Basin Analysis.* Springer, New York, 2000.

[75] R. M. Mitchum. Seismic stratigraphy and global changes of sea level, part 11: Glossary of terms used in seismic stratigraphy. In C. E. Payton, editor, *Seismic Stratigraphy - Applications to Hydrocarbon Exploration, AAPG Memoir 26*, pages 205–212. American Association of Petroleum Geologists, 1977.

[76] G. D. Mossop and P. D. Flach. Deep channel sedimentation in the lower cretaceous mcmurray formation. *Sedimentology*, 30:493–509, 1983.

[77] E. Mutti and W. R. Normark. Comparing examples of modern and ancient turbidite systems: Problems and concepts. In J. K. Legget and G. G. Zuffa, editors, *Marine Clastic Sedimentology: Concepts and Case Studies*, pages 1–38. Graham and Trotman, 1987.

[78] E. Mutti and W. R. Normark. An integrated approach to the study of turbidite systems. In P. Weimer and M. H. Link, editors, *Seismic Facies and Sedimentary Processes of Submarine Fans and Turbidite Systems*, pages 75–106. Springer-Verlag, 1991.

[79] E. Mutti and M. Sonnino. Compensational cyles: a diagnostic feuature of turbidite sandstone lobes. In *2nd European Regional Meeting Abstracts*, Bologna, Italy, March 2001. International Association of Sedimentologists.

[80] E. Mutti, R. Tinterri, E. Remacha, N. Mavilla, S. Angella, and L. Fava. *An Introduction to the Analysis of Ancient Turbidite Basins from and Outcrop Perspective.* American Association of Petroleum Geologists, Tulsa, 2002.

[81] T. Nilsen and E. Abbate. Gottero turbidite system, Italy. In W. R. Normark and N. E. Barnes, editors, *Submarine Fans and Related Turbidite Systems*, pages 199–204. Springer-Verlag, 1985.

[82] K. P. Norrena and C. V. Deutsch. Using the critical temperature to improve the speed of geostatistical applications of simulated annealing. In *Sixth International Geostatistics Congress*, Cape Town, September 2000.

[83] R. A. Olea, editor. *Geostatistical Glossary and Multilingual Dictionary.* Oxford University Press, New York, 1991.

[84] H. Omre. Heterogeneity models. In *SPOR Monograph: Recent Advances in Improved Oil Recovery Methods for North Sea Sandstone Reservoirs*, Norway, 1992. Norwegian Petroleum Directorate.

[85] N. Oreskes, K. Shrader-Frechette, and K. Belitz. Verification, validation, and confirmation of numerical models in the earth sciences. *Science*, 263:641–646, February 1994.

[86] J. Ortiz. *Characterization of High Order Correlation for Enhanced Indicator Simulation.* PhD thesis, University of Alberta, Edmonton, 2003.

[87] B. Oz and C. V. Deutsch. A short note on the proportional effect and direct sequential simulation. In *Report 4, Centre for Computational Geostatistics*, Edmonton, May 2002.

[88] B. Oz, C. V. Deutsch, T. T. Tran, and Y. Xie. A Fortran 90 program for direct sequential simulation with histogram reproduction. *Mathematical Geology*, 29:39–51, 2003.

[89] C. L. Palagi and K. Aziz. Use of Voronoi grid in reservoir simulation. In *66th Annual Technical Conference and Exhibition*, pages 77–91, Dallas, TX, October 1991. Society of Petroleum Engineers.

[90] C. Paola. Quantitative models of sedimentary basin filling. *Sedimentology*, 47:121–178, 2000.

[91] J. Peakall, W. D. McCaffrey, B. C. Kneller, C. E. Stelting, T. R. McHargue, and W. J. Schweller. A process model for the evolution of submarine fan channels: Implications for sedimentary architecture. In A. H. Bouma and C. G.

Stone, editors, *Fine-grained Turbidite Systems, AAPG Memoir 72 / SEPM Special Publication No. 68*, pages 73–87. American Association of Petroleum Geologists, 2000.

[92] K. T. Pickering, J. D. Clark, R. D. A. Smith, R. N. Hiscott, F. R. Lucchi, and N. H. Kenyon. Architectural element analysis of turbidite systems and selected topical problems for sand-prone deep-water systems. In K. T. Pickering, R. N. Hiscott, N. H. Kenyon, F. R. Lucchi, and R. D. A. Smith, editors, *Atlas of Deepwater Envrionments: Archictectural Styles in Turbidite Systems*, pages 1–10. Chapman and Hall, 1995.

[93] H. W. Posamentier. Integration of seismic geomorphology and seismic stratigraphy: Principles and applications. In *2003 CSPG / CSEG Convention*. Canadian Society of Petroleum Geologists, 2003.

[94] H. W. Posamentier and G. P. Allen. *SEPM Concepts in Sedimentology and Paleontology No. 7*. Society for Sedimentary Geology, New York, 1999.

[95] M. J. Pyrcz and C. V. Deutsch. Two artifacts of probability feild simulation. *Mathematical Geology*, 33(7):775–799, 2001.

[96] M. J. Pyrcz and C. V. Deutsch. Stochastic surface modeling in mud-rich, fine-grained turbidite lobes. In *AAPG Annual Meeting*, Salt Lake, UT, May 2003. American Association of Petroleum Geologists.

[97] M. J. Pyrcz and C. V. Deutsch. Conditioning complex curvilinear lithfacies models. In *Seventh International Geostatistics Congress*, Banff, September 2004.

[98] M. J. Pyrcz and C. V. Deutsch. Geometric semivariogram models. *Submitted to Mathematical Geology*, 2004.

[99] M. J. Pyrcz and C. V. Deutsch. A library of training images for fluvial and deepwater reservoirs and associated code. *Submitted to Computers & Geosciences*, 2004.

[100] M. J. Pyrcz and C. V. Deutsch. Spectral corrected semivariogram models. *Submitted to Mathematical Geology*, 2004.

[101] M. J. Pyrcz and C. V. Deutsch. Stocahastic surface-based simulation of turbidite lobes. *Submitted to AAPG Bulletin*, 2004.

[102] M. J. Pyrcz and C. V. Deutsch. Stochastic inclined heterolithic stratification with the bank retreat model. In *CSPG/CWLS/CHOA Joint Convention (ICE 2004)*, Calgary, June 2004.

[103] M. J. Pyrcz, E. Gringarten, P. Frykman, and C. V. Deutsch. Representative input parameters for geostatistical simulation. In T. C. Coburn, editor, *Stochastic Modeling II*. American Association of Petroleum Geologists, 2004.

[104] H. G. Reading. *Sedimentary Environments: Processes, Facies and Stratigraphy*. Blackwell Science, London, 1996.

[105] W. Ren, L. Cunha, and C. V. Deutsch. Preservation of multiple point structure when conditioning by kriging. In *Sixth International Geostatistics Congress*, Banff, September 2004.

[106] D. F. Ritter, R. C. Kochel, and J. R. Miller. *Process Geomorphology*. McGraw-Hill, Boston, 2002.

[107] D. J. Rozman. Characterization of a fine-grained outer submarine fan deposit, Tanqua-Karoo Basin, South Africa. In A. H. Bouma and C. G. Stone, editors, *Fine-grained Turbidite Systems, AAPG Memoir 72 / SEPM Special Publication No. 68*, pages 279–290. American Association of Petroleum Geologists, 2000.

[108] N. Satur, A. Hurst, B. T. Cronin, G. Kelling, and K. Gurbuz. Sand body geometry in a sand-rich, deep-water clastic system. *Marine and Petroleum Geology*, 17:239–252, 2000.

[109] G. Shanmugam. 50 years of the turbidite paradigm (1950s-1990s): Deep-water processes and facies models - a critical perspective. *Marine and Petroleum Geology*, 17:285–342, 2000.

[110] P. V. Sharma. *Geophysical Methods in Geology*. Elsevier, New York, 1986.

[111] L. Shmaryan and C. V. Deutsch. Object-based modeling of fluvial/deepwater reservoirs with fast data conditioning: Methodology and case studies. In

*1999 SPE Annual Technical Conference and Exhibition*, Houston, TX, October 1999. Society of Petroleum Engineers.

[112] R. M. Slatt, G. H. Brown, R. J. Davis, G. R. Clemenceau, J. R. Colbert, R. A. Young, H. Anxionnaz, and R. J. Spang. Out-crop-behind outcrop characterization of thin-bedded turbidites for improved understanding of analog reservoirs: New Zealand and Gulf of Mexico. In *Ninth SPE Symposium on Reservoir Simulation*, New Orleans, LA, October 1998. Society of Petroleum Engineers.

[113] D. G. Smith. *Modern Analogues of the McMurray Formation Channel Deposits, Sedimentology of Meso-tidal-influenced Meandering River Point Bars with Inclined Beds of Alternating Mud and Sand.* Alberta Oil Sands Technology and Research Authority, Calgary, 1985.

[114] K. O. Stanley, K. Jorde, N. Raestad, and C. P. Stockbridge. Stochastic modeling of reservoir sand bodies for input to reservoir simulation, Snorre Field, northern North Sea. In Buller et al., editors, *North Sea Oil and Gas Reservoirs II.* Graham and Trotman, London, UK, 1990.

[115] C. E. Stelting, A. H. Bouma, and C. G. Stone. Fine-grained grained turbidite systems: Overview. In A. H. Bouma and C. G. Stone, editors, *Fine-grained Turbidite Systems, AAPG Memoir 72 / SEPM Special Publication No. 68*, pages 1–8. American Association of Petroleum Geologists, 2000.

[116] D. A. V. Stow and M. Johansson. Deep-water massive sands: Nature, origin and hydrocarbon implications. *Marine and Petroleum Geology*, 17:145–174, 2000.

[117] D. A. V. Stow and M. Mayall. Deep-water sedimentary systems: New models for the 21st century. *Marine and Petroleum Geology*, 17:125–135, 2000.

[118] D. A. V. Stow, H. G. Reading, and J. D. Collinson. Deep seas. In H. G. Reading, editor, *Sedimentary Environments: Processes, Facies and Stratigraphy*, pages 395–453. Blackwell Science, 1996.

[119] D. Stoyan, W. S. Kendall, and J. Mecke. *Stochastic Geometry and its Applications.* John Wiley & Sons, New York, 1987.

[120] S. Strebelle. Conditional simulation of complex geological structures using multiple-point statistics. *Mathematical Geology*, 32(9):2937–2954, 2002.

[121] S. Strebelle and A. G. Journel. Dynamic data structure. In *Sixth International Geostatistics Congress*, Cape Town, September 2000.

[122] S. Strebelle, K. Payrazyan, and J. Caers. Modeling of a deepwater turbidite reservoir conditional to seismic data using multiple-point geostatistics. In *Ninth SPE Symposium on Reservoir Simulation*, San Antonio, TX, October 2002. Society of Petroleum Engineers.

[123] T. Sun, P. Meakin, and T. Josang. A simulation model for meandering rivers. *Water Resources Research*, 32(9):2937–2954, 1996.

[124] D. M. Tetzlaff. Limits to the predictive ability of dynamic models the simulation clastic sedimentation. In T. A. Cross, editor, *Quantitative Dynamic Stratigraphy*, pages 3–20. Prentice-Hall, 1990.

[125] R. G. Thomas, D. G. Smith, J. M. Wood, J. Visser, A. Calverley-Range, and E. H. Koster. Inclined heterolithic stratification - terminology, description, interpretation and significance. *Sedimentary Geology*, 53:123–179, 1987.

[126] H. Tjelmeland and H. Omre. Semi-markov random fields. In A. Soares, editor, *Geostatistics Troia 1992*, volume 2, pages 493–504. Kluwer, 1993.

[127] T. T. Tran. Improving variogram reproduction on dense simulation grids. *Computers & Geosciences*, 20(7):1161–1168, 1994.

[128] K. Tyler, A. Henriquez, F. Georgsen, L. Holden, and H. Tjelmeland. A program for 3d modeling of heterogeneities in a fluvial reservoir. In *3rd European Conference on the Mathematics of Oil Recovery*, pages 31–40, Delft, June 1992.

[129] K. Tyler, A. Henriquez, A. MacDonald, T. Svanes, and A. L. Hektoen. MOHERES - a collection of stochastic models for describing heterogeneities in clastic reservoirs. In *3rd International Conference on North Sea Oil and Gas Reservoirs III*, pages 213–221. 1992.

[130] L. Vincent. Morphology algorithms. In E. R. Dougherty, editor, *Mathematical Morphology in Image Processing*, pages 255–288. Marcel Dekker Inc., 1993.

[131] S. Viseur. *Stochastic Object-based Simulation of Fluvial Deposits.* PhD thesis, Institut National Polytechnique de Lorraine, Nancy, France, 2001.

[132] S. Viseur, A. Shtuka, and J.-L. Mallet. New fast, stochastic, boolean simulation of fluvial deposits. In *1998 SPE Annual Technical Conference and Exhibition*, pages 697–709, New Orleans, LA, September 1998. Society of Petroleum Engineers.

[133] J. C. V. Wagoner, R. M. Mitchum, K. M. Campion, and V. D. Rahmanian. *Siliclastic Sequence Stratigraphy in Well Logs, Cores, and Outcrops: Concepts for High-Resolution Correlation of Time Facies.* The American Association of Petroleum Geologists, Tulsa, Oklahoma, 1990.

[134] R. G. Walker. Facies models and modern stratigraphic concepts. In R. G. Walker and N. P. James, editors, *Facies Models Responce to Sea Level Change*, pages 1–14. Blackwell Science, 1992.

[135] R. G. Walker. Turbidites and submarine fans. In R. G. Walker and N. P. James, editors, *Facies Models Responce to Sea Level Change*, pages 239–263. Blackwell Science, 1992.

[136] R. G. Walker and N. P. James. *Facies Models: Response to Sea Level Change.* Geological Association of Canada, St. John's, 1992.

[137] K. J. Weber and L. C. V. Geuns. Framework for constructing clastic reservoir simulation models. *Journal Petroleum Technology*, 42:1248–1297, 1990.

[138] L. J. Wietzerbin and J. L. Mallet. Parameterization of complex 3d heterogeneities: A new CAD approach. In *1993 SPE Annual Technical Conference and Exhibition*, Houston, TX, October 1993. Society of Petroleum Engineers.

[139] B. J. Willis. Interpretation of bedding geometry with ancient point-bar deposits. In M. Marzo and C. Puigdefabregas, editors, *Alluvial Sedimentation - Special Publication #17.* International Association of Sedimentology, 1993.

[140] Y. Xie and C. V. Deutsch. Surface-geometry and trend modeling for integration of stratigraphic data in reservoir models. In *Sixth International Geostatistics Congress*, Cape Town, September 2000.

[141] Y. Xie and C. V. Deutsch. Preliminary research toward direct geostatistical simulation of unstructured grids. In *Report 3, Centre for Computational Geostatistics*, Edmonton, May 2001.

[142] W. Xu. Conditional curvilinear stochastic simulation using pixel-based algorithms. *Mathematical Geology*, 28(7):937–949, 1996.

# Appendix A

# Algorithms and Abbreviations

The following list of abbreviations and algorithms applied in this dissertation.

`ADDCOORD` - adds coordinates to model files, from GSLIB (Deutsch and Journel, 1998)[23]

***AOI*** - area of interest

`ALLUVSIM` - streamline based alluvial simulation

`ALLUVSIMCOND` - streamline based alluvial simulation with well conditioning

`ATOMSIM` - direct simulation to atomic or Voronoi grids

`CALCGBAR` - subroutine that calculates mean covariances

***CCDF*** - conditional cumulative distribution function

***CDF*** - cumulative distribution function

***CH type*** - channel belt type fluvial reservoir

***CH*** - channel fill, fluvial or turbidite architectural element

$CH'$ - channel fill architectural element without specification of channel fill, lateral accretion or abandoned channel fill.

***CR*** - crevasse channel, fluvial architectural element

***CS*** - crevasse splay, fluvial architectural element

***DA*** - downstream-accretion macroform, fluvial architectural element

`DISTMODULE` - module required for `PRECDIST` and `GETCDIST` subroutines

`DSSIM` - direct sequential simulation

***FF*** - flood plain fines, fluvial architectural element

***FF(CH)*** - abandoned channel, fluvial architectural element

***FFT*** - fast Fourier transform

`FLUVSIM` - simulated annealing driven object based PV reservoir type modeling algorithm (Deutsch and Wang, 1996; Deutsch and Tran, 2002)[28, 25]

***FR*** - forced regression

***FS*** - frontal splay, turbidite architectural element

***FSST*** - falling stage systems tract

`GAMMAMODULE` - module required for `PREGBAR` and `CALCGBAR` subroutines

***GB*** - gravel bars and bedforms, fluvial architectural element

`GETCDIST` - subroutine that extracts a valid local ccdf from a ccdf look up table

***GSLIB*** - geostatistical library (Deutsch and Journel, 1998)[23]

`GTSIM` - Gaussian truncated simulation, from GSLIB (Deutsch and Journel, 1998)[23]

`HIERTREND` - hierarchical trend model calculated for generic categorical models

***HO*** - scour hollows, fluvial architectural element

***HST*** - highstand systems tract

***IHS*** - inclined heterolithic stratification

***LA*** - lateral accretion, fluvial or turbidite architectural element

***LMC*** - linear model of coregionalization

***LMR*** - linear model of regionalization

`LOBESIM` - turbidite channel and frontal splay simulated annealing driven object based model, algorithm by Deutsch and Tran (1999)[26]

***LS*** - laminated sand sheet, fluvial architectural element

***LST*** - lowstand systems tract

`LUSIM` - lower upper decomposition simulation, from GSLIB (Deutsch and Journel, 1998)[23]

***LV*** - levee, fluvial or turbidite architectural element

`MAPS` - maximum a posteriori selection

***MG*** - multi-Gaussian

`MODELOPS` - modify a model (algebraic operations, merge and combine categories)

***MPS*** - multiple point statistics

`MPSTATS` - calculate multiple point statistics from a 3-D categorical model

***MG*** - massive sand facies association

`NONSTATCOVTABLE` - subroutine that sets up a nonstationary covariance table

***NR*** - normal regression

***NTG*** - net-to-gross fraction

***OK*** - ordinary kriging

`PFSIM` - probability field simulation

***PD*** - ponds, turbidite architectural element

`PIXELPLT` - regular grid plotting utility, from GSLIB (Deutsch and Journel, 1998)[23]

`PRECDIST` - subroutine that sets up a local ccdf look up table

`PREGBAR` - subroutine that constructs a semivariogram look up table

***PV type*** - paleovalley type fluvial reservoir

***QDS*** - quantitative dynamic stratigraphy

`RADIALMATRIXBUILD` - subroutine that sets up a kriging matrices for radial nested grids

`RADIALNONSTATCOVTABLE` - subroutine that sets up a nonstationary covariance table for radial nested grids

***RF*** - random function

***RV*** - random variable

***SB*** - sandy bedforms, fluvial architectural element

`SETSPR` - subroutine that sets up super a block search, from GSLIB (Deutsch and Journel, 1998)[23]

***SH type*** - sheet type fluvial reservoir

***SG*** - sedimentary gravity flow, fluvial architectural element

`SGSIM` - sequential Gaussian simulation, from GSLIB (Deutsch and Journel, 1998)[23]

`SISIM` - sequential indicator simulation, from GSLIB (Deutsch and Journel, 1998)[23]

***SK*** - simple kriging

`SURFSIM` - surface based simulation

`SURFTREND` - hierarchical trend model calculation for a surface based model model

***T-R*** - transgression - regression

`TARTANPIX` - tartan grid plotting utility

`TARTANSIM` - direct sequential simulation to tartan grids

`TRENDCOR` - correct a 3-D trend model to honor areal and vertical trends

`TURBSIM` - surface based simulation of compensational cycles in turbidite lobes

***TST*** - transgressive systems tract